Molecular Beam Epitaxy grown Molybdenum Oxide Nanostructures: Growth, Characterizations and Applications

By

Paramita Maiti

(PHYS07201304005)

Institute of Physics, Bhubaneswar

A thesis submitted to the
Board of Studies in Physical Sciences

In partial fulfillment of requirements
for the Degree of

DOCTOR OF PHILOSOPHY
of
HOMI BHABHA NATIONAL INSTITUTE

July, 2019

STATEMENT BY AUTHOR

This dissertation has been submitted in partial fulfillment of requirements for an advanced degree at Homi Bhabha National Institute (HBNI) and is deposited in the Library to be made available to borrowers under rules of the HBNI.

Brief quotations from this dissertation are allowable without special permission, provided that accurate acknowledgement of source is made. Requests for permission for extended quotation from or reproduction of this manuscript in whole or in part may be granted by the Competent Authority of HBNI when in his or her judgment the proposed use of the material is in the interests of scholarship. In all other instances, however, permission must be obtained from the author.

Paramita Maiti

DECLARATION

I, Paramita Maiti, hereby declare that the investigation presented in the thesis has been carried out by me. The work is original and has not been submitted earlier as a whole or in part for a degree / diploma at this or any other Institution / University.

Paramita Maiti

List of Publications arising from the thesis

Journal

[1] Microscopy and spectroscopy study of nanostructural phase transformation from β-MoO_3 to Mo under UHV – MBE conditions.
P. Maiti, P. Guha, H. Hussain, C. Nicklin and P. V. Satyam, *Surf. Sci.* **2019**, *682*, 64.

[2] Optical band gap, local work function and field emission properties of MBE grown β-MoO_3 nanoribbons.
P Maiti, P Guha, R Singh, J K Dash and P V Satyam, *Appl. Surf. Sci.* **2019**, *476*, 691.

[3] Growth of molybdenum trioxide nanoribbons on oriented Ag and Au nanostructures: a scanning electron microscopy (SEM) study.
P Maiti, A Mitra, R R Juluri, A Rath and P V Satyam, *Microsc. and Microanal.* **2019** DOI: 10.1017/S1431927619014648.

[4] Determination of Oxygen concentration in Molybdenum oxide nanostructures: a resonant RBS study.
P Maiti, B. Sundaravel and P V Satyam, (*to be submitted*).

[5] Vacuum dependent annealing effect on structural, optical, local work function and field emission properties of Molybdenum oxide thin films.
P Maiti, R Singh and P V Satyam, (*to be submitted*).

Chapters in books and lectures notes

Conferences

[1] Structural study of β-MoO_3 nano-ribbons grown by molecular beam epitaxy technique (*Poster presented*)
An International Conference on Electron Microscopy "Electron Microscope Society of India - 2017 (EMSI2017)" jointly organized by Electron Microscope Society of India (EMSI), Indira Gandhi Centre for Atomic Research, Kalpakkam (IGCAR, Kalpakkam) and Indian Institute of Technology, Madras (IITM) during 17th - 19th July, 2017 at Mahabalipuram, Tamil Nadu.

[2] Temperature dependent shape transition of the Ge nanostructures grown on Si (110) surface by MBE technique
(*Oral presented*)
10th International Conference on Advanced Nano Materials (ANM-2017), University of Surray, Guildford, England during 11th – 13th September, 2017.

[3] Temperature dependent morphological evolution and phase transition of MoO_3 grown by molecular beam epitaxy technique.
(*Oral presented*)
International Conference on Nanotechnology: Ideas, Innovations & Initiatives-2017 (ICN:3I-2017), IIT Roorkee during 06th – 08th December, 2017.

[4] Growth and characteristics of Molecular Beam Epitaxy (MBE) grown β-MoO_3 nanoribbons
(*Oral presented*)
XIX International Workshop on Physics of Semiconductor Devices (IWPSD-2017) jointly organized by Solid State Physics Laboratory, Delhi; Defence Research & Development Organization and IIT Delhi, New Delhi during 11th – 15th December, 2017.

[5] Nanostructural Phase Transformation from β-MoO_3 to Mo under UHV – MBE Conditions
(*Poster presented*)
An International Conference on Electron Microscopy “Electron Microscope Society of India - 2018 (EMSI2018)”, Mayfair Convention Center, Bhubaneswar, Odisha during 18th - 20th July, 2018. Nadu.

Paramita Maiti

DEDICATED TO ALL MY FAMILY MEMBERS

Acknowledgments

Now, at the end of the research period for my PhD thesis, I want to show my sincere gratitude to those who have helped me finishing this thesis work in different regards. Please forgive me if I forget to mention someone unconsciously or unwittingly.

First and foremost, I would like to convey my heartfelt gratitude and indebtedness to Prof. P V Satyam as my supervisor for providing me an opportunity to work in his group. I am incredibly grateful for his invaluable guidance, constant encouragement and supervision to complete this work. He has given me full freedom to carry out research works in my own interest, which I have enjoyed a lot. It is my proud privilege to show my appreciation to him for his continuous support both academically and socially whenever I needed. I would like to thank him for giving me a very well equipped setup and also for arranging several necessary experiments for this thesis work through his contacts and collaborations. I have learnt various skills such as technical, writing and communication from him which I needed to develop not only for this thesis work but also for my ensuing future. I consider myself very fortunate in having been associated with such an enthusiastic scientist.

I am grateful to the Director, IOPB for all the help I received from him during my stay here.

I would like to thank Prof. Chris Nicklin and Dr. Hadeel Hussain, Diamond Light Source (DLS), UK as collaborator for the *in-situ* X-ray photoelectron spectroscopy (XPS) measurements.

I am very thankful to Prof. Raynald Gauvin and Dr. Jillian Yuan, McGill University, Canada Ffor their assistance in theoretical calculations using CASINO software.

I am gratified to Prof. B. Sundaravel (IGCAR, Kalpakkam) and his group for allowing me and helping me to carry out Rutherford backscattering spectrometry (RBS) measurements in their laboratory and it's my great pleasure to work with them.

I am really grateful to Saha Institute of Nuclear Physics (SINP), India especially to Dr. M K Mukhopadhyay, Dr. A B Dey and Dr. A Bhattacharyya for facilitating and accomplishing the experiments at Photon Factory, Japan.

I would like to acknowledge Prof. T Som (IOP, BBSR) and his group members specially Mr. Ranveer Singh for carrying out several measurements e.g., UV-vis, electron field emission, KPFM for many times. I wish to thank Dr. D Topwal (IOP, BBSR) and his student Mr. Pronoy Nandi for XRD and PL measurements for several times whenever I needed. I would like to thank Prof. S Varma (IOP, BBSR) and her student Mr. Ashis Manna for allowing me to do Raman measurements. My good wishes to Mr. R Singh, Mr. P Nandi and Mr. Ashis Manna for their research works. I feel privileged to Mr. Mihir Ranjan Sahoo (IIT, BBS) for DFT calculations. I want to thank Dr. Chhayabrita Maji (Institute of Chemical Technology, Indian Oil Odisha Campus) for fundamental discussions on XPS. Her invaluable suggestions and continuous support help me in carrying out XPS analysis.

Sincere thanks go to Prof. S Varma, Prof. S K Patra and Prof. T Som as my thesis committee members for their beneficial suggestions, continuous cooperation, support and colossal advices throughout my research tenure at IOP.

It has given me immense pleasure to spend more than 4 years at IOP. I wish to acknowledge all the members in our group for their respective help and support. I would like to acknowledge the individual help and support from our MBE-STM, HR-TEM and FE-SEM group members. They have provided with a friendly and an excellent research atmosphere. I genuinely convey my cordial gratefulness to all my lab fellow workers Dr. Jatis K Dash, Dr. Ashutosh Rath, Dr. Raghavendra R Juluri, Dr. Arnab Ghosh, Dr. A Bhukta and Dr. Puspendu Guha. Everyone has helped me one way or the other. My innermost acknowledgement to Jatisda and Anjanda for their tireless support since the days I have started my research life. Their incredible levels of skill, expertise, knowledge and experience have enriched me to a great extent.

I am really thankful to our group postdoctoral fellows Dr. T Arun, Dr. B Rakshit, Dr. S S Ram and Dr. A Mitra for their assistances in all aspects. A very special thanks goes to my seniors Dr. Puspendu Guha, and Dr. Arijit Mitra, without their help I couldn't able to complete my thesis works in time. Thank you very much Arijitda and Puspenduda da for their enormous and continuous cooperation in every regards right from idea, experiments, data analysis to paper writings.

I would like to thank Mr. B K Dash and Mr. S R Mohanty as our proficient scientific assistants for providing each and every requirement. A very special thank goes to Mr. B K Dash for his continuous, quick and reliable assistance in both academic and non-academic contests whenever I required.

Thanks to my friends, batch mates, seniors, juniors for making enjoyable and memorable experience during my whole stay here. We have shared joys and struggling in tough times.

I would like to thank all my teachers who taught me in the pre-doctoral course work and all the experimental condensed matter group faculties at IOP, for their generous support.

I acknowledge the excellent library and computer facilities provided by the IOP and all the members of IOP for their direct or indirect help in many cases.

Last but not the least, I am deeply indebted to my parents where the basic source of my energy resides and all family members for their love, affection and support. I must acknowledge my husband Mr. Arnab Mandal for his constant encouragement and being cooperative in every situation through this tough journey of my PhD life. Without their constant sacrifice and guidance, this accomplishment would have never been completed. They always believed in me and continuously motivated me to move forward. Thanks to all of you.

CONTENTS

Synopsis

The thesis work involves an extensive study on the growth of molybdenum oxide (MoO_x) nanostructures (NSs) by molecular beam epitaxy (MBE) technique under ultra-high vacuum (UHV) conditions with varying parameters, such as, substrates, substrate temperature, film thickness, etc. and their applications as very good field emitters. Well-ordered, highly crystalline, defect free nanostructures (NSs) are very important for technological applications due to their interesting physical, chemical and mechanical properties at the nano or subatomic scale [1-3]. However, to synthesize well-ordered and oriented 1-D or 2-D NSs (e.g. nanorods, nanobelts, nanotubes, nanoribbons and nanoplates) by simple growth methods have proven to be a great challenge from the last two three decades [4,5]. NSs of transition metal oxides (TMO) (for example, WO_3, MnO_2, SnO_2, TiO_2, MoO_3, etc.) have attracted the research community in applied science due to their promising application in electronic and energy devices such as, solar cell [6], gas sensing [7], ultrasensitive plasmonic biosensing [8] lithium storage [9], electro chromic devices [10], photo chromic devices [11], light emitting diodes [12], field emission [13], electrocatalytic hydrogen evolution [14], resistive switching [15] and many more. Among the transition metal oxides, molybdenum oxide plays a very important role as it can be made transparent, light, flexible and possibly can be alternative solution to organic semiconductors which degrade quickly in the ambient conditions [16]. It can exist in many different phases (e,g, MoO_3, Mo_8O_{23}, Mo_9O_{26}, Mo_4O_{11}, and MoO_2) depending on the oxidation state of Mo (+6, +5, +4, +3 and +2). This allows for band gap engineering of these materials: from the wide band gap of MoO_3 (≈ 3.2 eV) [17] to the more conducting MoO_{3-x} [18] and then to semi-metallic MoO_2 (≈ 2.6 eV) [19] and finally to the metallic system (in the form of metal – Mo). The growth of MoOx nanostructures and their enhanced field emission properties have been studied in detail. Further, the phase change variation dues vacuum dependent annealing/growth parameters has been studied. As the oriented nanostructure growth depends on the catalysts for their growth, the results discussed here, show that oriented Au nanostructures work as better catalyst agents than Ag nanostructures for the growth of MoO_x nanostructures.

There exists three possible polymorphs of molybdenum tri-oxide (MoO_3), stable orthorhombic α-MoO_3, metastable β-MoO_3 and metastable hexagonal h-MoO_3. Most of the α-MoO_3 nanostructures are grown using many methods, such as, physical vapor deposition, chemical vapor deposition [13]. But high quality β-MoO_3 nanostructures are very difficult to achieve due to its metastable phase formation. *This thesis work is focused on the growth and characteristics of defect free, mixed phase free metastable molybdenum trioxide (β-MoO_3) on varied substrates and MoO_2 and then the phase transition from β-MoO_3 to MoO_2 to Mo by simple thermal reduction process in ultra-high vacuum (UHV) condition by molecular beam epitaxy (MBE) technique. Effect of different thickness of molybdenum oxide nanostructures and vacuum level, on the optical band gap, local work function and field emission have also been covered.*

This thesis is constituted of eight chapters. In the chapter one of the thesis, a brief introduction and motivation to the need of growing molybdenum oxide nanostructures (NSs) in ultra-high vacuum (UHV) condition and their properties with possible applications have been described. The past and present status of different molybdenum oxide NSs have also been included. Temperature, substrate, vacuum, thickness dependent effects on the NSs have been emphasized.

In chapter 2, different experimental methods with their basic operating principles that are employed for the growth, characterizations and applications of the materials, have been discussed briefly. Epitaxial growth technique like molecular beam epitaxy (MBE) is used mainly to grow the NSs. Besides the epitaxial method, other thermal evaporation techniques like physical vapor deposition (PVD) and chemical vapor deposition (CVD) have been exploited to synthesize and anneal the thin films. The mechanism of the characterization techniques, such as, field emission gun based scanning electron microscope (SEM) with energy dispersive x-ray analysis (EDS), transmission electron microscope (TEM) capable with high resolution mode coupled with selected area electron diffraction (SAED), scanning tunneling microscope (STM), reflection high energy electron diffraction (RHEED), Rutherford backscattering spectrometry (RBS), grazing incidence X-ray diffraction (GIXRD), X-ray photoelectron spectroscopy (XPS), UV-Vis-NIR spectroscopy, Kelvin probe force microscopy (KPFM) are briefly presented. For application of the NSs, field emission (FE) procedure is also outlined.

The thickness, composition, growth mode and structural aspects of the molybdenum oxide thin film deposited on the surface either at different substrate temperature and thicknesses or post anneal at different ambience have been studied in Chapter 3 using Rutherford backscattering spectrometry (RBS) method both in random and aligned conditions [20]. RBS experiments are very useful for determining the atomic masses (or composition) at nanometer (*nm*) depth resolution. Its sensitivity is poor for low atomic number target atoms, in particular when these are surrounded by high atomic number matrix. We present the use of ion scattering under resonance conditions (using 3.04 MeV He ions from 1.7 MV Tandetron Accelerator) to determine the concentration of oxygen in MBE and PVD grown thin film oxide nanostructures, such as, MoOx and compare the same with TEM, XRD and XPS measurements. Based on the experimental observations, compositional depth profile analysis and the thickness of NSs and thin films were investigated using SIMNRA software package [21].

Chapter 4 reports nanostructural phase and morphology transformation from molybdenum tri-oxide (β-MoO_3) nanoribbons (NRs) phase to MoO_2 nanoparticles (NPs) and then followed to Mo (elemental), grown on reconstructed Si(100) substrate by thermal annealing in ultra-high vacuum (UHV) condition using molecular beam epitaxy (MBE) epitaxy technique. For the growth, molybdenum trioxide (α-MoO_3) powder (99.995% purity from Alfa-aeser) and atomically cleaned Si(100) (*n-type*, phosphorus doped, resistivity ≈ 1-20 Ω–cm) were used as source material and substrates, respectively. Ultra clean or reconstructed silicon surfaces acts as clean surfaces (without any oxide at the surface and the interfaces) .To remove the native oxide on surfaces, substrates were degassed at 600 °C by direct heating (DH) for 12-15 hours. After that they were flashed at 1200 °C repeatedly for few minutes. A ≈ 10 nm thick molybdenum oxide film was deposited on the reconstructed Si substrates at different substrate temperature with a deposition rate ≈ 1 Å/min, keeping the source temperature at 670 °C. At 350 °C substrate temperature, NRs like structures are formed. Grazing incidence (GIXRD), selected area electron diffraction (SAED) pattern, high resolution TEM (HRTEM) results reveal that the monoclinic phase of MoO_3 (β-MoO_3) is grown under ultra-vacuum conditions. After raising the substrate temperature to 400 °C with ≈ 10 nm MoO_3 deposition (i.e. MoO_3 deposited at 400 °C, the 10nm here represent the effective thickness of the film deposited, obtained using the bulk density of MoO_3 and usually this is obtained using the Rutherford backscattering spectroscopy methods), morphology changes from NRs to NPs. From microscopy measurements, we have observed that all the as-grown samples having substrate temperature ranging from 400 °C to 600 °C, exhibit similar morphology (i.e. monoclinic

MoO_2). Decrease in average particle size, coverage area and increasing in areal density with increasing the substrate temperature have been observed. For in-situ XPS study, NRs sample has been taken. After measuring XPS of NRs sample, anneal the sample at subsequent temperatures, cool down and taking XPS data. From this experiment, it is found that Mo 3d peak shifts from 232.35 eV (for Mo^{6+} $3d_{5/2}$) to 228.77 eV (for Mo^{4+} $3d_{5/2}$) to 227.25 eV (for Mo^{0+} $3d_{5/2}$) whereas lattice oxygen peak generated for MoO_3 cases gradually decreasing with increasing temperature and vanishes when MoO_3 converts to Mo at 750°C. The *ex-situ* KPFM measurements showed a decrease in the local work function (Φ) from ≈ 5.27 ± 0.05 eV (for β-MoO_3 NRs) to ≈ 4.83 ± 0.05 eV (for Mo bimodal NPs) with increasing substrate temperature. A gradual reduction of the band gap from ≈ 3.32 eV for β-MoO_3 NRs to zero band gap for Mo NPs is also observed from UV-Vis-NIR spectrometry during the annealing up to 750 °C [22].

In chapter 5, growth of defect free, mixed phase free metastable monoclinic molybdenum trioxide (β-MoO_3) NRs on various substrates, such as, on Si(100), Si(5512) and fluorine-doped tin oxide (FTO) by molecular beam epitaxy (MBE) technique under ultra-high vacuum (UHV) condition has been studied. This exercise was carried out to find out the dependence of substrate on the formation of ordered MoOx nanostructures. The dependence of substrate *conditions* and the effective thickness of MoO_3 films on the morphology of nanostructures and their structural aspects are also reported. From electron microscopy observations, all NRs are found to be out of plane, oriented with an average angle of ±24° with the substrate normal along <011>, preferentially growth direction and restricted in <200>. From the growth of NRs on different substrates, it has been observed that out of plane unidirectional growth of the NRs structures is a substrate independent phenomena. Different effective thickness of MoO_3 films, starting from 5, 10, 15, 20 and 30 nm have been deposited on Si(100) with native oxide layer substrate. Here, one needs to keep in mind that the growth of MoOx nanostructures formed as there was no wetting phenomena occurred and hence no uniform continuous films are formed. With increasing effective thickness, length and the aspect ratio of nanostructures increase by 260% without any significant change in the width. This result has been explained in the light of quantum size effect. We have also shown how quantum size effects and thickness dependency will play a role on band gap, local work function and field emission properties of β-MoO_3 NRs. With increasing effective film thickness from 5 nm to 30 nm, the optical band gap decreased from 3.38± 0.01eV to 3.17± 0.01eV. A liner relationship exists between band gap (Eg) and $1/(\text{thickness }(t))^2$. From the slope of band gap versus $1/t^2$ plot, effective mass of electron in MoO_3 has been calculated and found to be

0.0191m_e which is same as the previously reported theoretical value. By knowing electron effective mass, de Broglie wavelength (λ) =7 nm was obtained which is of the order of effective film thickness. Local work function increases from 5.397 ± 0.025 eV to 5.757 ± 0.030 eV with increasing film thickness from 5 nm to 30 nm. Field emission (FE) behavior strongly influenced by two parameters, one is structure (composition, tip diameter and aspect ratio) and other is work function (Φ) of the emitters. Here, with increasing film thickness from 5 nm to 30 nm, aspect ratio (length/width) increases from 3.9±0.1 to 14.1±0.5. So the FEF increases from 1.1×10^4 to 5.9×10^4 in the low field region and from 3.3×10^3 to 7.4×10^3 in high field regime. *The self-assembled grown β-MoO_3 NRs sample (30 nm thickness) reported here, exhibits lowest turn-on field (2.5 V/µm for10 µA/cm^2) and highest FEF among all the previously reported other types of molybdenum oxide nanostructures [23].*

Growth of molybdenum trioxide NRs on oriented silver (Ag) and gold (Au) nanostructures (NSs) are covered in Chapter 6. This is an important aspect as if a catalysts is found for the growth of MoO_x nanostructures, then it would enable to fabricate aligned and ordered nanostructures. The work presented here clearly show that oriented Au nanostructures act as good catalysts. For the growth of Ag nanostructures that are used as possible catalyst agents are grown on substrates using MBE conditions. For this purpose, silver films of effective thickness of about 2 nm has been deposited at different growth temperatures (using UHV-MBE) on atomically cleaned Si(100), Si(110) and Si(111) substrates. The experiments reported here show that a minimum temperature of 650 °C is necessary to grow epitaxial Ag film on various reconstructed Si substrates. For faceted Au NSs, a ≈50 nm Au has been deposited (using high vacuum thermal evaporation) on Si(100) substrate with native oxide layer at the interface and annealed the sample in low vacuum (≈ 10^{-2} mbar) and at high temperature (≈ 975 °C) [24]. Either Ag nanostructures grown using MBE conditions or oriented Au nanostructures grown in high vacuum condition are used as catalysts for the growth of MoO_3 nanostructures. Growth of MoO_3 NRs by MBE technique under UHV condition, 99.995% purity MoO_3 powder has been used as source material and kept the source temperature at 670 °C so that the deposition rate is ≈ 0.1nm/min. From energy dispersive X-ray spectroscopy (EDS) elemental mapping and line scan it is found that MoO_3 nanostructures are uniformly distributed on Ag microstructures as well as Si substrate for MoO_3/Ag films, whereas interestingly, in case of MoO_3/Au films the density of MoO_3 nanostructures is very high on top of the faceted Au structures. [25]. Simple SEM-EDS measurements shown that Au nanostructures act as better catalysts for the growth of MoO_3 nanostructures.

In chapter 7, works are involved on the vacuum dependent annealing of molybdenum oxide thin films and their morphological, optical and field emission (FE) studies. A ≈ 250 nm thick molybdenum trioxide film was deposited at room temperature (RT) on Si(100) substrates with native oxide layer at ≈ 1 Å/sec deposition rate by physical vapor deposition (PVD) technique with base pressure of 1.8×10^{-6} mbar. Then the films have been annealed at 650 °C under different ambient conditions viz air, low vacuum (LV) and ultra-high vacuum (UHV) and their resultant outcomes have been discussed in this chapter. SEM and atomic force microscopy (AFM) images depict layered like structures after annealing in air whereas plate like microstructures and granular structures are formed for post anneal (PA) in LV and UHV respectively. X-ray diffraction (XRD) confirms the orthorhombic phase of molybdenum trioxide (α-MoO_3) for layered like and monoclinic phase of MoO_2 for granular structures. Mixed states of β-MoO_3 and η-Mo_4O_{11} exist for microplates after annealing in LV. How the ambience plays an important role on the morphology and phase of different oxidation states of molybdenum is the main focus of this chapter. To explore the optical band gap, UV-VIS spectroscopy measurements are done on the annealed samples. Optical band gap decreased from 3.22 ± 0.01 eV (for α-MoO_3, PA in Air) to 3.00 ± 0.01 eV (for mixed phase of β-MoO_3 and η-Mo_4O_{11}, PA in LV) to 2.6 ± 0.01 eV (for MoO_2, PA in UHV). The *ex-situ* KPFM measurements show a decrease in the local work function (Φ) from ≈ 5.764 ± 0.029 eV for layered α-MoO_3 microstructures to ≈ 5.123 ± 0.026 eV for granular MoO_2 structures. Here with increasing vacuum level from air to UHV, aspect ratio (length/width) decreases. So the FEF decreases from 3.8×10^4 to 3.3×10^3 in the low field region and from 2.7×10^3 to 1.6×10^3 in high field regime [26].

Summary and conclusions including future plans of entire thesis work are presented in chapter 8.

References

[1] X S Fang, Y Bando, U K Gautam, C H Ye and D Golberg, *J. Mater. Chem.* 2008, *18*, 509.

[2] C N R Rao, P J Thomas and G U Kulkarni, Nanocrystals: Synthesis, Properties and Applications (Springer, 2007, ISBN: 978-3-540-68751-1).

[3] P Alvisato, *Science* 1996, *271*, 933.

[4] S. Balendhran, S. Walia, H. Nili, J. Z. Ou, S. Zhuiykov, R. B. Kaner, S. Sriram, M. Bhaskaran, and K. Kalantar-zadeh, *Adv. Funct. Mater.* 2013, 23, 3952.

[5] S. Cong, T. Sugahara, T. Wei, J. Jiu, Y. Hirose, S. Nagao, and K. Suganuma, *Cryst. Growth Des.* Doi: 10.1021/acs.cgd.5b00790.

[6] Z. Su, L. Wang, Y. Li, G. Zhang, H. Zhao, H. Yang, Y. Ma, B. Chu, and W. Li, *ACS Appl. Mater. Interfaces* 2013, 5, 12847.

[7] N. Illyaskutty, S. Sreedhar, G. S. Kumar, H. Kohler, M. Schwotzer, C. Natzeckd, and V. P. M. Pillai, *Nanoscale* 2014, 6, 13882.

[8] B.Y. Zhang, A. Zavabeti, A.F. Chrimes, F. Haque, L. A. O’Dell, H. Khan, N. Syed, R. Datta, Y. Wang, A. S. R. Chesman, T. Daeneke, K. K-zadeh and J. Z. Ou, *Adv. Funct. Mater.* 2018, 28, 1706006.

[9] J. K. Shon, H. S. Lee, G. O. Park, J. Yoon, E. Park, G. S.Park, S. S. Kong, M. Jin, J. M Choi, H. Chang, S. Doo, J. M. Kim, W.-Sub Yoon, C. Pak, H. Kim and and G. D. Stucky, *Nat. Commun.*|7:11049, DOI: 10.1038/ncomms11049.

[10] R. Sivakumar, M. Jayachandran and C. Sanjeeviraja. *Surf. Eng.* 2004, 20, 385.

[11] J. N. Yao, K. Hashimoto and A. Fujishima, *Nature* 1992, 355, 624.

[12] Z. Yin, X. Zhang, Y. Cai, J. Chen, J. I. Wong, Y.-Y. Tay, J. Chai, J. Wu, Z. Zeng, B. Zheng, H. Y. Yang and H. Zhang, *Angew. Chem. Int. Ed.* 2014, 52, 1.

[13] P. Guha, A. Ghosh, R. Thapa, E. M. Kumar, S. Kirishwaran, R. Singh and P. V. Satyam, *Nanotechnology* 2017, 28, 415602.

[14] R. S. Datta, F. Haque, M. Mohiuddin, B. J. Carey, N. Syed, A. Zavabeti, B. Zhang, H. Khan, K. J. Berean, J. Z. Ou, N. Mahmood, T. Daeneke and K. Kalantar-zadeh, *J. Mater. Chem. A* 2018, 5, 24223.

[15] D. Lee, D. J. Seong, I. Jo, F. Xiang, R. Dong, S. Oh and H. Hwang, *Appl. Phys. Lett.* 2007, 90, 122104.

[16] Q. H. Wang, K. Kalantar-zadeh, A. Kis, J. N. Coleman and M. S. Strano, *Nat. Nanotechnol.* 2012, 7, 699.

[17] K. Inzani, M. Nematollahi, F. Vullum-Bruer, T. Grande, T. W. Reenaas, and S. M. Selbach, *Phys. Chem. Chem. Phys.* 2017**,** DOI: 10.1039/C7CP00644F.

[18] I. A. Castro, R. S. Datta, J. Z. Ou, A. C. Gomez, S. Sriram, T. Daeneke, and K. Kalantar-zadeh, *Adv. Mater.* 2017, 1701619.

[19] N. Dukstiene, D. Sinkeviciute, and A. Guobiene, *Cent. Eur. J. Chem.* 2012, 10(4), 1106.

[20] P. Maiti, B. Sundaravel, P. Guha, and P. V. Satyam, (ready to be submitted).

[21] https://home.mpcdf.mpg.de/~mam/

[22] P. Maiti, P. Guha, H. Hussain, R. Singh, C. Nicklin, and P. V. Satyam, *Surf. Sci.* 2019, 682, 64.

[23] P. Maiti, P. Guha, R. Singh, J. K. Dash and P. V. Satyam, Appl. Surf. Sci. 2019, 476, 691.

[24] A. Rath, J. K. Dash, R. R. Juluri, A. Rosenauer, M. Schoewalter, and P. V. Satyam, *J. Appl. Phys.* 2012, 111, 064322.

[25] P. Maiti, A. Mitra, R. R. Juluri, A. Rath and P. V. Satyam, *Microscopy and Microanalysis*, (under review).

[26] P. Maiti, R. Singh, P. Nandy and P. V. Satyam, (under preparation).

List of Figures

List of Tables

Chapter 1

Introduction

In recent days, nanoscience and nanotechnology are the most widely used terms as the field is growing very rapidly and its impact is being felt strongly on the multidisciplinary fields due to its diversified field of applications. Nanoscience is the fundamental study of physical and chemical phenomena of materials at atomic and molecular scales whereas nanotechnology is the design, characterization, production and application of those materials in nanometer scale [1]. Usually nanoscale materials are defined as any materials whose characteristic length is less than 100 nm, at least in one direction [2-4]. The properties of nano materials differ significantly from the bulk or macro scale due to larger surface to volume ratio that make materials more chemically active at nano-scale and affect their electrical, magnetic, optical properties [5-11]. The structural arrangement of atoms and the length scales of the material are the two important parameters, which when tuned properly at the nanometer scale, could lead to variation in the properties of the material, as compared to its bulk counterpart. It is also expected that quantum size effects begin to dominate at the nanoscale and these effects have proven to significantly vary the optical, electrical, and magnetic properties of materials. In case of nanomaterials, size, shape, surface composition, inter particle interactions, temperature, thickness can modulate the above properties [12-18]. Nanoribbons and nanoparticles constitute a major class of nanomaterials. The diameter of nanoparticles and width of nanoribbons can vary anywhere between one and a few hundreds of nanometers.

Nanostructures of transition metal oxides (for example, WO_3, MnO_2, SnO_2, TiO_2, MoO_3, etc.) [19] have been studied with great zeal due to their long-term stability under mechanical, electrical, and environmental stress, largely tunable stable physical, chemical and mechanical properties along with easy large scale synthesis viability [9,11,20]. Among many oxide materials, molybdenum oxide is one of the most fascinating and versatile due to its unique physical and chemical properties [21]. It can exist in many different phases (e,g, MoO_3, Mo_8O_{23}, Mo_9O_{26}, Mo_4O_{11}, and MoO_2) depending on the oxidation state of Mo (+6, +5, +4, +3 and +2). This allows the band gap engineering of these materials; from the wide band gap of MoO_3 (≈ 3.2 eV) [22] to the more conducting MoO_{3-x} [23] and then to semi-metallic MoO_2 (≈ 2.6 eV) [21] and finally to the metallic system (in the form of metal – Mo).

There are predominantly two different polymorphs of MoO_3 based on MoO_6 octahedron building block; one has a thermodynamically stable orthorhombic (α-MoO_3) structure and the other a metastable monoclinic (β-MoO_3) structure. There are some reports about the existence of other phases, such as, ε-MoO_3 (also known as metastable high pressure MoO_3–II phase) and relatively stable hexagonal phase h-MoO_3 [24]. α-MoO_3 has unit cell parameters a = 3.96 Å, b= 13.85 Å and c = 3.71 Å in a Pbnm space group (JCPDS: 35-0906) [25] exhibiting a layered like structure. It is a *n-type* semiconductor with an electron affinity above 6 eV and ionization energy greater than 9 eV. So, there is a possibility to produce a 2D layer, composed of bi-layer distorted MoO_6 octahedra which are connected by van der Waals interactions in the [010] direction. Within the bi-layer, MoO_6 units are connected by ionic and covalent bonds [23,26]. One of the reported value of work function ~6.17 ± 0.05 eV and band gap 3.04 eV for α–MoO_3 [26]

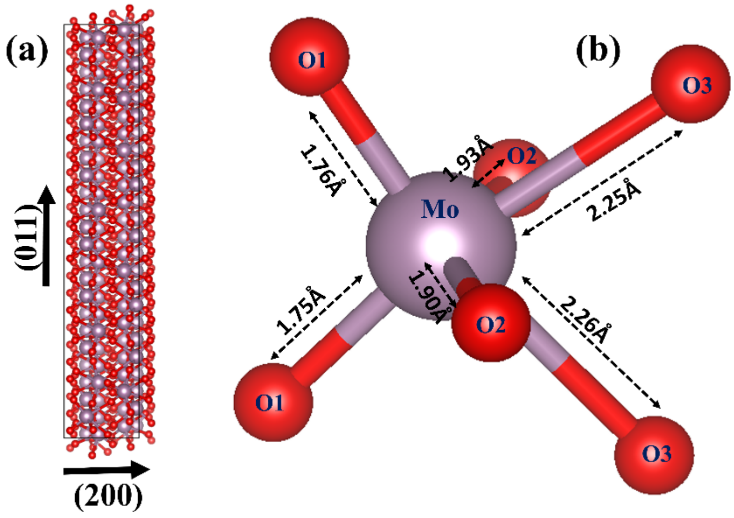

Figure 1.1: *(a) β-MoO_3 structure oriented along (011) and (200) direction, (b) single β-MoO_3 unit cell with different Mo-O bond lengths. Where ● → Mo atom and ● → O atom.*

The structure of β-MoO_3 (unit cell parameters: a = 7.12 Å, b= 5.37 Å, c = 5.57 Å and β = 92.01° in $P2_1/c$ space group) is quite different from α-MoO_3 structure. It can be related to 3D ReO_3 structure like WO_3. It is formed only by the corner sharing MoO_6 octahedron. External conditions like temperature, pressure, and impurities influence the arrangement of the MoO_6 octahedra. β-MoO_3 can be transformed to α-MoO_3 by thermal treatment at temperatures above 350 °C [23]. Crystal structure and Mo-O bond lengths of β-MoO_3 oriented along [011] direction have been depicted in Figure 1.1 (a) and (b) respectively. In this thesis we have reported work function, band gap and field emission properties of β-MoO_3 for the first time [18].

Monoclinic MoO_2 phase (unit cell parameters: a = 5.537 Å, b= 4.859 Å, c = 5.607 Å and β = 120.912 (JCPDS: 86-0135) [27]) also displays a deformed rutile structure. Along the rutile c-axis, two distinct metal to metal bond lengths of 2.51 Å and 3.02 Å arise due to the alternation of Mo-Mo distance. This leads to two distinct oxygen coordination sites [28]. The theoretical band structure calculations of MoO_2 show four Mo 4d bands below the Fermi energy that indicate the material should be semi-metallic in nature. Experimentally, however, it has been observed that the MoO_2 structures are semiconducting in nature with a reduced band gap as compared to MoO_3 [23].

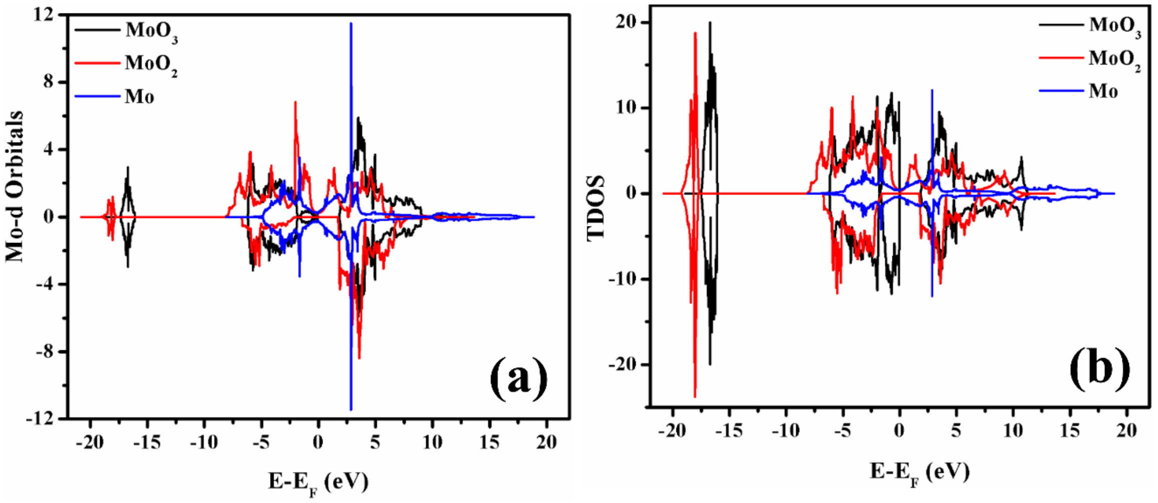

Figure 1.2: *(a) Mo d orbital and (b) total density of states of β-MoO_3, β-MoO_2 and Mo by density functional theory (DFT) calculations.*

Due to the excellent material properties (e.g. low thermal expansion coefficient (5.1 × 10^{-6} m/°C) [29] which is less than steel, good thermal and electrical conductivity and high melting point (2615 °C) [30]) metallic molybdenum is a suitable candidate for a wide range of applications such as an alloying agent, electrodes for electrically heated glass furnace, nuclear energy applications like missile and aircraft parts, filament material for electrical application and thermocouple sheaths. Calculated Mo-d orbital and total density of states of β-MoO_3, β-MoO_2 and Mo by density functional theory (DFT) are shown in Figure 1.2 (a) and (b), respectively. During the reduction process (from MoO_3 to Mo) by releasing the oxygen, Mo 4d states are filled and lowered in energy, as a result, the band gap decreases [22]. Supercell structures of the three phases (β-MoO_3, β-MoO_2 and Mo) have been represented in Figure 1.3.

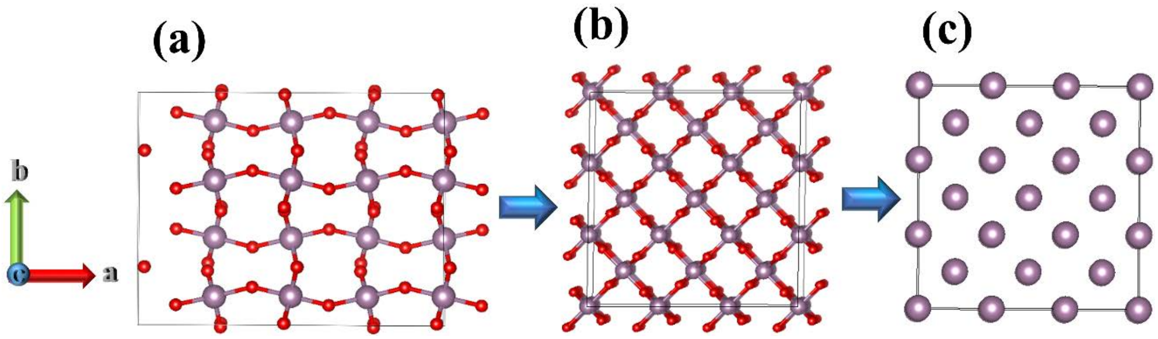

Figure 1.3: *Supercell structures of MoO_3, MoO_2 and Mo. (a) shows 2x2x2 supercell of MoO_3 monoclinic structure, (b) shows 2x2x2 supercell of MoO_2 monoclinic structure and (c) shows Mo cubic structure. Where ● → Mo atom and ● → O atom.*

Different morphologies of MoO_3 nanostructures (NSs) such as nanowires, nanotubes, nanorods, nanobelts, nanoflakes, nanoribbons, whiskers, fibers, nanoplatelets, hollow nanospheres, nanoparticles, nanosheets, nanostructures have been prepared via various physical and chemical methods [17,18,24,26,31-56].Until now, diversified techniques have been adapted for synthesizing MoO_3 NSs such as thermal evaporation, chemical vapor deposition, pulsed laser deposition, hydrothermal growth, flame synthesis, sputtering, electrochemical technique, infrared irradiation, sol-gel, microwave method, sonochemical approach etc. Molybdenum oxide has been extensively probed in various advanced applications and shows promising performances in photochromic devices, electrochromic devices, gas sensing, photocatalysis, resistive switching, lithium-ion batteries, catalysis, field emission, photovoltaic, transistors, inorganic light emitting diode, capacitors, panel displays, smart windows and many more [17,18,24,26,31-56]. It is reported that β-MoO_3 is more superior to α-MoO_3 in electrochemical and catalysis application [57,58]. In this thesis, we have shown that the self-assembled grown β-MoO_3 NRs can offer higher field emission characteristics as compared to α-MoO_3 nanostructures; so far no report has been made related to this material

Several experimental techniques were used to grow β-MoO_3: however, many of these processes are found to be unsuccessful because of the proper molybdic source, metastable state of β-MoO_3 and the final product detected as stable α-MoO_3 [55, 59-62]. In the present thesis work, use of environment processing, such as, molecular beam epitaxy (MBE) process under ultra-high vacuum (UHV) conditions would be reported for the growth of oxide nanostructures. In UHV-MBE system, one can control the growth rate, oxygen concentration very precisely. It is one of the most powerful techniques to grow metastable state of MoO_3 (β-MoO_3) and other oxidation states of Mo. Very few reports are available on MoO_3 nanostructures grown by MBE technique. In most of reports, researchers used either RF plasma cell for oxygen radicals to terminate the surface by oxygen atoms or oxygen plasma assisted MBE to maintain the stoichiometry of the nanostructures [19,63]. *Carcia et al* [64] reported in their study that growth of molybdenum oxide in high (50%) and low (5% - 10%) oxygen atmospheres produce α-MoO_3 strongly oriented in [0k0] direction and β-MoO_3 with strong [0kk] preferred orientation, respectively. Since we have grown the samples in UHV, the as-grown sample is expected to be MoO_3 in the monoclinic phase because of the negligible oxygen content in the chamber.

Recently hybrid semiconductor-metal nanostructures have attracted great research attention because of their tunable physical and chemical properties which are superior to their individual properties [65,66]. Metal nanostructures, in particular, noble metals, such as Au and Ag nanoparticles had been main focus for several years [67-74]. For example, it is very well known that Au nanoparticles enhance visible light absorption and populate conduction band of oxide semiconductor by transferring electron utilizing their surface plasmon resonance (SPR) properties. Similarly, Ag nanostructures have been shown potential for detecting organic dye-molecules, biomolecules via surface enhanced Raman spectroscopy (SERS) technique [67,68]. Embedded Ag nanostructures are known to be efficient for detecting the dye-molecules via SERS technique [69,70]. Besides, Au, Ag have a great scientific significance and technological applications in optical, electrical and biological applications due to their low resistance, high transmittance, electrical conductivity; plasmonic and catalytic properties [71-74].

In this thesis, highly crystalline, defect free, mixed phase free, metastable β-MoO_3 nanoribbons (NRs) were grown in an UHV chamber using commercially available α-MoO_3 powder as source material without passing any oxygen gas to maintain the stoichiometry by MBE technique. The thesis reports on detailed growth, characterizations and application of β-

MoO_3 NRs under MBE conditions. Interesting results on structural phase transformation from MoO_3 to Mo and vacuum annealing effects on the MoO_3 thin films have also be studied in detail. A part of the work is based on the use of Au and Ag nanostructures as catalysts for the growth of molybdenum oxide nanostructures. Experimental methods, such as, resonant Rutherford backscattering spectrometry (RBS) have been used to determine the composition analysis of oxide nanostructures.

This thesis is organized in the following manner. In chapter 2, all the experimental techniques with their basic working principles (that are employed for the preparation of samples, characterizations and multifaceted applications) have been outlined in brief. Chapter 3 deals with Rutherford backscattering spectrometry (RBS) study under resonance condition of different molybdenum oxide NSs and thin films grown by MBE and physical vapor deposition (PVD) techniques. The main focus of this chapter is to determine the oxygen, molybdenum concentration, O/Mo atomic ratio, depth information from ion energy loss, growth mode, surface roughness and phase of the oxide materials. Different NSs are formed by varying the substrate temperature, thickness of the film and vacuum level of the growth chamber. The results obtained by ion scattering method have been complemented by using electron microscopy (SEM or/and TEM) methods and X-ray methods (XRD and XPS). A simple reduction of molybdenum oxide (β-MoO_3) grown on reconstructed Si(100) substrate by thermal annealing in UHV using MBE technique has been addressed in chapter 4. The change in morphologies has been associated with a structural transition from β-MoO_3 to MoO_2 at 400 °C and MoO_2 to Mo at 750 °C. Correlation between ex-situ studies of phase transitions with in-situ XPS analysis has also been described. Local work function and band gap of all the three phases have been measured using Kelvin probe force microscopy (KPFM) and UV-Vis spectroscopy, respectively. The dependence of substrate conditions and the effective thickness of MoO_3 films on the morphology of nanostructures and their structural aspects are studied in chapter 5. In this chapter, observation of enhanced field emission for β-MoO_3 NRs, other associated properties and plausible reason related to the work function have been discussed. The role of metallic nanostructures (such as Au and Ag nanostructures) as nucleation sites in the growth of self-assembled β-MoO_3 has been demonstrated in detail in the chapter 6. Vacuum dependent annealing of molybdenum oxide thin films and their morphological, optical and field emission (FE) studies have been covered in chapter 7. The summary and conclusion of the works presented in the thesis including future research scope are presented in chapter 8.

References

[1] A. Dowling, Nanoscience and nanotechnologies: opportunities and uncertainties (A Report by The Royal Society and The Royal Academy of Engineering, London, July 2004).

[2] D. R. Boverhof, C. M. Bramante, J. H. Butala, S. F. Clanc, M. Lafranconi, J. West, S. C. Gordon, *Regul. Toxicol. Pharmacol.* 2015, 73, 137.

[3] I. Khan, K. Saeed, I. Khan, *Arab. J. Chem.* 2017, doi: 10.1016/j.arabjc.2017.05.011

[4] W. G. Kreylinga, M. S-Behnke, Q. Chaudhry, *Nano Today* 2010, 5, 165.

[5] C. N. R. Rao, P. J. Thomas and G. U. Kulkarni, Nanocrystals: Synthesis, Properties and Applications (Springer, 2007, ISBN: 978-3-540-68751-1).

[6] P. Moriarty, *Rep. Prog. Phys.* 2001, 64, 297.

[7] P. Alvisatos, *Science* 1996, 271, 933.

[8] C. Burda, X. Chen, R. Narayanan and M. A. El-Sayed, *Chem. Rev.* 2005, 105, 1025.

[9] S. Zhuiykov, Nanostructured Semiconductor Oxides for the Next Generation of Electronics and Functional Devices: Properties and Applications (Elsevier, 2013, ISBN: 978- 1-78242-220-4).

[10] Y. Xia, P. Yang, Y. Sun, Y. Wu, B. Mayers, B. Gates, Y. Yin, F. Kim and H. Yan, *Adv. Mater.* 2003, 15, 353.

[11] R. K. Joshi and J. J. Schneider, *Chem. Soc. Rev.* 2012, 41, 5285.

[12] J. P. Borel, *Surf. Sci.* 1981, 106, 1.

[13] Y. D. Glinka, S. H. Lin, L. P. Hwang, Y. T. Chen, N. H. Tolk, *Phys. Rev. B* 2001, 64, 085421.

[14] S. Chen, R. S. Ingram, M. J Hostetler, J. J. Pietron, R.WMurray,T. G. Schaaff, J. T. Khoury, M. M. Alvarez, R. L. Whetten, *Science* 1998, 280,2098.

[15] N. L. Swanson and B. D. Billard, *Nanotechnology* 2003, 14, 353.

[16] H. Xu, E. J. Bjerneld, M. Kall and L. Borjesson, *Phys. Rev.Lett.* 1999, 83, 4357.

[17] P. Maiti, P. Guha, H. Hussain, R. Singh, C. Nicklin and P. V. Satyam, *Surf. Sci.* 2019, 682, 64.

[18] P. Maiti, P. Guha, R. Singh, J. K. Dash and P. V. Satyam, *Appl. Surf. Sci.* 2019, 476, 691.

[19] K. Koike, R. Wada, S. Yagi, Y. Harada, S. Sasa, and M. Yano, Jpn. *J. Appl. Phys.* 2014, 53, 05FJ02.

[20] K. J. Yu, Z. Yan, M. Han and J. A. Rogers, *npj Flexible Electronics* 2017, 4, 1.

[21] N. Dukstiene, D. Sinkeviciute, and A. Guobiene, *Cent. Eur. J. Chem.* 2012, 10(4), 1106.

[22] K. Inzani, M. Nematollahi, F. Vullum-Bruer, T. Grande, T. W. Reenaas, and S. M. Selbach, *Phys. Chem. Chem. Phys.* 2017, DOI: 10.1039/C7CP00644F.

[23] I. A. Castro, R. S. Datta, J. Z. Ou, A. C. Gomez, S. Sriram, T. Daeneke, and K. Kalantar-zadeh, *Adv. Mater.* 2017, 1701619.

[24] L. Zheng, Y. Xu, D. Jin and Y. Xie, *Chem. Mater.* 2009, 21, 5681.

[25] L. Kihlborg, *Arkiv. Kemi.* 1964, 21, 357.

[26] P. Guha, A. Ghosh, R. Thapa, E. M. Kumar, S. Kirishwaran, R. Singh and P. V. Satyam, *Nanotechnology* 2017, 28, 415602.

[27] A. A. Bolzan, B. J. Kennedy, and C. J. Howard, Aust. J. Chem. 1995, 48 , 1473.

[28] T. Ressler, R. E. Jentoft, J. Wienold, M. M. Gunter and O. Timpe, *J. Phys. Chem. B* 2000, 104, 6360.

[29] F. C. Nix, and D. MacNair, *Phys. Rev.* 1942, 61, 74.

[30] J. Dang, G-H. Zhang, and K-C. Chou, *Int. J. Refract. Metals Hard Mater* 2013, 41, 356.

[31] D. Mariotti, H. Lindstrom, A. C. Bose and K. Ostrikov, *Nanotechnology* 2008, 19, 495302.

[32] M. Chen, U. V. Waghmare, C. M. Frienda and E. A. Kaxiras, *J. Chem. Phys.* 1998, 109, 6854.

[33] A. Michalak, K. Hermann and M. Witko, *Surf. Sci.* 1996, 366, 323.

[34] J. N. Yao, K. Hashimoto and A. Fujishima, *Nature* 1992, 355, 624.

[35] C. Bechinger, S. Ferrere, A. Zaban, J. Sprague and B. A. Gregg, *Nature* 1996, 383, 608.

[36] E. Comini, L. Yubao, Y. Brando and G. Sberveglieri, *Chem. Phys. Lett.* 2005, 407, 368.

[37] Y. Chen, C. Lu, L. Xu, Y. Ma, W. Hou and J. J. Zhu, *Cryst. Eng. Comm.* 2010, 12, 3740.

[38] L. Cheng, M. Shao, X. Wang and H. Hu, *Chem. Eur. J.* 2009, 15, 2310.

[39] D. Lee, D. J. Seong, I. Jo, F. Xiang, R. Dong, S. Oh and H. Hwang, *Appl. Phys. Lett.* 2007, 90, 122104.

[40] L. Q. Mai, B. Hu, W. Chen, Y. Y. Qi, C. S. Lao, R. S. Yang, Y. Dai and Z. L. Wang, *Adv. Mater.* 2007, 19, 3712.

[41] J. Zhou, S. Z. Deng, N. S. Xu, J. Chen and J. C. She, *Appl. Phys. Lett.* 2003, 83, 2653.

[42] B. Yan, Z. Zheng, J. Zhang, H. Gong, Z. Shen, W. Huang and T. Yu, *J. Phys. Chem. C* 2009, 113, 20259.

[43] Y. B. Li, Y. Bando, D. Golberg and K. Kurashima, *Appl. Phys. Lett.* 2002, 81, 5048.

[44] S. Balendhran, J. Deng, J. Z. Ou, S. Walia, J. Scott, J. Tang, K. L. Wang, M. R. Field, S. Russo, S. Zhuiykov, M. S. Strano, N. Medhekar, S. Sriram, M. Bhaskaran and K. Kalantar-zadeh, *Adv. Mater.* 2013, 25, 109.

[45] P. S. Wang, I. W. Wu, W. H. Tseng, M. H. Chen and C. I. Wu, *Appl. Phys. Lett.* 2011, 98, 173302.

[46] R. Linag, H. Cao and Q. Qian, *Chem. Commun.* 2011, 47, 10305.

[47] S. Hu and X. Wang, *J. Am. Chem. Soc.* 2008, 130, 8126.

[48] L. Cai, P. M. Rao and X. Zheng, *Nano Lett.* 2011, 11, 872.

[49] S. Wang, Y. Zhang, X. Ma, W. Wang, X. Li, Z. Zhang and Y. Qian, *Solid State Commun.* 2005, 136, 283.

[50] C. V. Krishnan, J. Chen, C. Burger and B. Chu, *J. Phys. Chem. B* 2006, 110, 20182.

[51] K. Kalantar-zadeh, J. Tang, M. Wang, K. L. Wang, A. Shailos, K. Galatsis, R. Kojima, V. Strong, A. Lech, W. Wlodarski and R. B. Kaner, *Nanoscale* 2010, 3, 429.

[52] X. W. Lou and H. C. Zeng, *J. Am. Chem. Soc.* 2003, 125, 2697.

[53] W. Li, F. Cheng, Z. Tao and J. Chen, *J. Phys. Chem. B* 2006, 110, 119.

[54] I. Navas, R. Vinodkumar, K. J. Lethy, A. P. Detty, V. Ganesan, V. Sathe and V. P. M. Pillai, *J. Phys. D: Appl. Phys.* 2009, 42, 175305.

[55] D. D. Yao, J. Z. Ou, K. Latham, S. Zhuiykov, A. P. O’Mullane, K. Kalantar-zadeh, *Cryst. Growth Des.* 2012, 12, 1865.

[56] Y. Li and Y. Bando, *Chem. Phys. Lett.* 2002, 364, 484.

[57] T. T. P. Pham, P. H. D. Nguyen, T. T. Vo, H. H. P. Nguyen and C. L. Luu. *Adv. Nat. Sci.: Nanosci. Nanotechnol.* 2015, 6, 045010.

[58] T. Mizushima, K. Fukushima, H. Ohkita and N. Kakuta, *Appl. Catal. A: Gen.* 2007, 326 106.

[59] I. Juárez Ramírez and A. Martínez-de la Cruz, *J Solid State Electrochem* 2003, 7, 259.

[60] T. M. McEvoy and K. J. Stevenson, *Langmuir* 2003, 19, 4316.

[61] T. Mizushima, Y. Moriya, N. H. H. Phuc, H. Ohkita, and N. Kakuta, *Catal. Commun.* 2011, 13, 10.

[62] Mc Carron, E. M, *J. Chem. Soc., Chem. Commun.* 1986, 336.

[63] E. I. Altman, T. Droubay, S. A. Chambers, *Thin Solid Films* 2002, 414, 205.

[64] P.F. Carcia, E.M. McCarron III, *Thin Solid Films* 1987, 155, 53.

[65] M. D. L. R. Peralta, U. Pal and R. S. Zeferino, *ACS Appl. Mater. Interfaces* 2012, 4, 4807.

[66] W. He, H-K Kim, W. G. Wamer, D. Melka, J. H. Callahan and J-J. Yin, *J. Am. Chem. Soc.* 2014, 136, 750.

[67] K. G. Stamplecoskie, J. C. Scaiano, V. S. Tiwari and H. Anis, *J. Phys. Chem. C* 2011, 115, 1403.

[68] B. Sharma, R. R. Frontiera, A. I. Henry, E. Ringe and R. P. V. Duyne, *Mater. Today* 2012, 15, 16.

[69] R. R. Juluri, A. Rath, A. Ghosh, A. Bhukta, R. Sathyavathi, D. Narayana Rao, K. Muller, M. Schowalter, K. Frank, T. Grieb, F. Krause, A. Rosenauer and P. V. Satyam, *Sci. Rep.* 2014, 4, 4633.

[70] R. R. Juluri, A. Ghosh, A. Bhukta, R. Sathyavathi and P. V. Satyam, *Thin Solid Films* 2015, 586, 88.

[71] Y. C. Yeh, B. Creran and V. M. Rotello, *Nanoscale* 2012, 4, 1871.

[72] C. J. Murphy, T. K. Sau, A. M. Gole, C. J. Orendorff, J. Gao, L. Gou, S. E. Hunyadi and T. Li, *J. Phys. Chem. B* 2005, 109, 13857.

[73] N. V. Long, N. D. Chien, T. Hayakawa, H. Hirata, G. Lakshminarayana and M. Nogami, *Nanotechnology* 2010, 21, 035605.

[74] D. L. Fedlheim and C. A. Foss, Metal Nanoparticles: Synthesis, Characterization, and Applications (CRC Press, 2001, ISBN: 978-0-58540-439-4).

Chapter 2

Growth of nanostructures and different characterization Techniques

2.1 Introduction

This chapter describes a brief overview of thin film growth and different experimental techniques with their basic operational principles. This is a prelude to the subsequent chapters on growth, characterizations and applications of the materials related to the thesis work.

Nanoscience and nanotechnology constitute an active research area in modern device fabrications. It requires one, two or three dimensional confinement (nanoribbons, nanowires and nanodots). The nanostructures with multidimensional confinement will alter significantly in transport and optical properties, compared to bulk heterostructures. But it requires a very precise control over the growth rate, uniformity and thickness of the films. To achieve high purity, excellent material homogeneity, sharp interfaces between the layers or nanostructures with the substrate, epitaxial growth techniques such as molecular beam epitaxy (MBE) is the most promising among all the other techniques. Different other techniques such as physical evaporation method, chemical processes also exist to grow nanostructures as well as thin films.

2.2 Self-assembled growth

Self-assembled growth is a spontaneous formation of nanostructures with well-defined shape and size determined by growth kinetics and/or thermodynamic stability of the nanostructures. In the case of epitaxial nanostructures, free energy minimization leads to the pseudomorphic growth of lattice mismatched overlayer-substrate system to self-assembled structures. They are remarkably influenced by the presence of catalyst, seed etc.

There exist two different types of methodology depending upon the growth strategy, (i) top-down and (ii) bottom-up. In the top-down approach, different lithography techniques such as photolithography, e-beam lithography have been used where the materials are gradually removed from its bulk sizes to achieve well-ordered nanostructures. This technique is widely used in micro fabrication processes but the major drawbacks such as surface defect, structural damage, and internal stress in the fabricated nanostructures limit its applicability. In different growth techniques such as physical vapor deposition (PVD), chemical vapor deposition (CVD), molecular beam epitaxy (MBE), bottom-up approach has been used. In this process atoms, molecules or atomic clusters are added to achieve large size of nanostructures.

2.3 Different growth modes

Depending upon the substrate, substrate temperature, film material and deposition method, a film can grow single crystalline, polycrystalline or amorphous in nature. The film may be epitaxial in single crystalline case where a crystalline film grows on the pre-existing crystalline substrate. “Epitaxy” comes from a Greek root where “epi” means above and “taxis” means in ordered manner. The differences between the crystal growth and epitaxial growth are (i) the nature and strength of the chemical bonds, (ii) crystal lattice parameters. In epitaxial growth, both crystals differ energetically and geometrically but in crystal growth, they do not differ simultaneously which means they are identical [1]. Epitaxial growth can be classified as (i) homoepitaxy and (ii) heteroepitaxy depending upon the film and substrate material. In homoepitaxy, the film and substrate material are same (Si in Si(100)) whereas they are different in heteroepitaxy case like MoO_3 growth on Si (or Ag growth on Si). Figure 2.1 illustrated three principal epitaxial growth modes [2,3] which are named from their original investigators.

Layer-by-Layer or Frank-van der Merwe (FM): Figure 2.1(a) depicts FM growth mode where thin films grow layer-by-layer. The thin film atoms are more strongly bound to the substrate than to each other. As a result, after the completion of one full layer, the next layer starts to grow. This is strictly two-dimensional growth [4].

Island or Volmer-Weber (VW): Figure 2.1(c) corresponds VW growth mode where thin film atoms are more strongly bound to each other than to the substrate. As a result three-dimensional islands nucleate and grow directly on the substrate surface [5].

Layer-plus-island or Stranski-Krastanov (SK): Figure 2.1(b) represents SK growth mode which is the intermediate case of FM and VW growth modes. After the formation of a complete two dimensional layer, growth of three dimensional islands take place. The nature and thickness of the intermediate layer (called as SK layer) depend on the particular case [6].

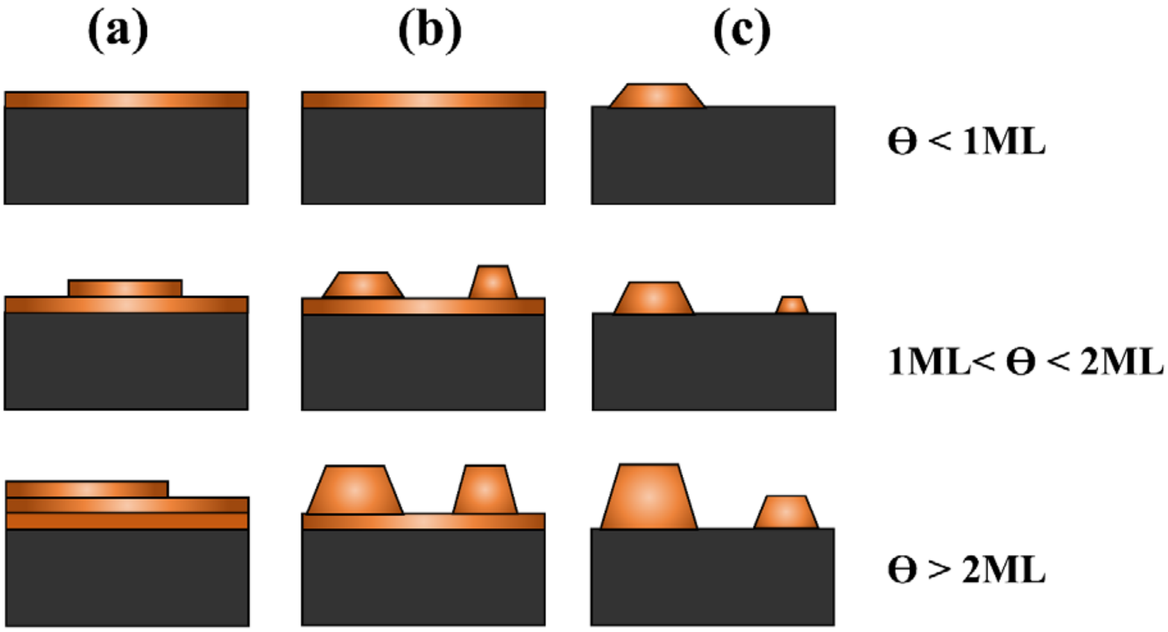

Figure 2.1: *Schematic representation of the three main growth modes: (a) layer-by-layer (Frank-van der Merwe, FM) growth mode (b) layer-plus-island (Stranski-Krastanov, SK) growth mode (c) Island (Volmer-Weber, VW) growth mode [8].*

Different types of growth modes can be explained in terms of thermodynamically equilibrium condition of the surface or interface free energies. It is defined as the work that is needed to build unit area surface of interface. Figure 2.2 depicts the schematic of a film island on the substrate which makes a contact angle of ϕ. Here σ can be described as force per unit length of boundary. So the force equilibrium can be written as

$$\sigma_s = \sigma_i + \sigma_f \cos\phi \qquad (2.1)$$

where, σ_s, σ_f are the surface free energies of the substrate surface and film surface respectively. Interfacial energy [7] σ_i is the surface free energy for film-substrate interface. To follow layer-by-layer or FM growth mode it must be $\Delta\sigma = \sigma_s - \sigma_i - \sigma_f \geq 0$. The strain energy of the film has been included in σi. So we can write from Equation 2.1 in more general way for FM growth mode as

$$\Delta\sigma(n) = \sigma_s - \sigma_i(n) - \sigma_f(n) \geq 0 \tag{2.2}$$

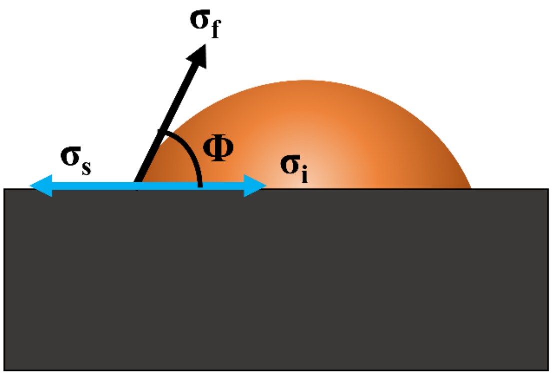

Figure 2.2: *Schematic of an island film on a substrate.* σ_s *is the surface free energy of substrate,* σ_f *is the surface free energy of film surface and* σ_i *is that for film/substrate interface. The balance of forces acting along the substrate surface yields equation 2.1.*

where, “n” correspond to the number of monolayers in the film. There is a deviation between $\sigma_f(n)$ and σ_f because $\sigma_f(n)$ absorbes n dependent surface strain. Layer-by-layer growth can only be possible for homoepitaxial and heteroepitaxial with no lattice mismatch cases. In homoepitaxy case, there is a zero misfit between thin film and the substrate because they are same material. So $\sigma_i(n) = 0$ and $\sigma_s = \sigma_f$ has been satisfied for FM growth mode. In other growth mode cases, with increasing n, strain energy increases leads to the increase of $\sigma_i(n)$. When $n = n^*$ the FM condition is not fulfilled and as a result layer-plus-island (SK) growth mode occurs. In the island (VW) growth mode case, FM condition is not fulfilled from n = 1. These three types of growth modes (FM, SK, VW) have been studied in the theory of wetting and layering transitions as wetting, incomplete wetting and nonwetting cases [8,9,10].

Lattice misfit between the film and the substrate leads to the strain energy which serves as the driving force for island formation. Figure 2.3 shows schematically the strain in epitaxial layer. We have plotted equilibrium growth mode as a function of strength of film-substrate interaction (W) with lattice misfit (η) in Figure 2.4 [11]. W can be defined as the ratio of σ_i with σ_f,

$$W = \sigma_i / \sigma_f \tag{2.3}$$

and lattice misfit is defined as the ratio of the difference in film lattice constant (a_f) and substrate lattice constant (a_s) with substrate lattice constant (a_s),

$$\eta = (a_f - a_s) / (a_f) \tag{2.4}$$

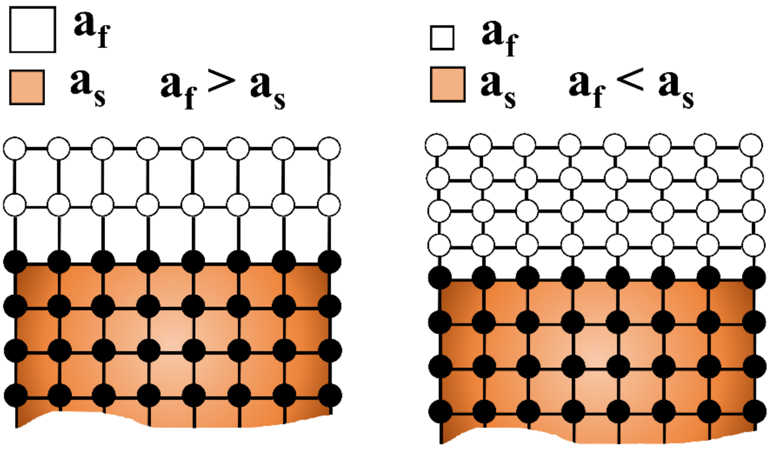

Figure 2.3: *Illustration of strain of the overlayer due to the lattice mismatch of substrate and film material.*

W >> 1, when film-substrate interactions are very large. It has been observed from Figure 2.4 that layer-by-layer (FM) growth mode occurs when there is zero misfit and strong interaction between film and substrate i.e. $\eta = 0$ and $W > 1$. For zero misfit, island (VW) growth mode occurs only when $W < 1$ that means interaction between the film atoms is larger than the film-substrate interaction. In the non-zero misfit case, VW growth mode arises when $W \geq 1$. Layer-plus-island (SK) growth mode happens for smaller misfit and $W > 1$.

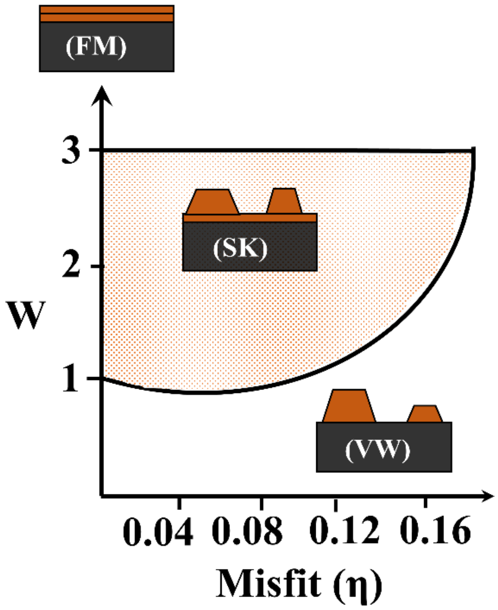

Figure 2.4: *Equilibrium growth modes, as a function of misfit (η) and strength of film-substrate interaction (W). The solid line separates the regions of VM mode and SK mode. FM mode is confined to the region $\eta = 0$ with $W > 1$.*

2.4 Different growth techniques

Thin films can be deposited by various techniques such as molecular beam epitaxy (MBE), metal organic vapor phase epitaxy (MOVPE), solid phase epitaxy (SPE), chemical beam epitaxy, liquid phase epitaxy etc. In this section we have presented experimental methods of MBE, physical vapor deposition (PVD) and chemical vapor deposition (CVD) techniques which have been used for the growth and annealing of molybdenum oxide nanostructures.

2.4.1 Molecular beam epitaxy (MBE)

Thin films and nanostructures were grown using a custom-built MBE system (M/S Omicron GmbH) installed @ IOP, BBSR (shown in Figure 2.5) [12]. For initial sample mounting, a small load lock chamber is attached with MBE growth chamber. Load lock chamber is pumped down by turbo molecular pump (TMP) which is backed by a diaphragm pump. Then the sample of 3 × 9 mm^2 has been mounted on the manipulator using a magnetically coupled sample transfer rod. This manipulator comprises Z-translation (vertical) and X-, Y- translation facilities (horizontal). Along these, it can be rotated 0-360° azimuthally about the vertical direction (Z axis). Manipulator is also comprised of direct heating (DH) and resistive heating (RH) facilities. Using DH and RH the substrate temperature can be raised up to ~ 1200 °C, ~ 700 °C respectively. Substrate temperature has been measured by type K thermocouple attached at the backside of the substrate holder and optical pyrometer. To evaporate the source material, effusion cells (K cells) and e-beam evaporator have been used. Out of four K cells, SEZ-40 has the facility to reach temperature up to ~ 1400 °C which is used to evaporate of Ag. Another two K cells (MTEZ) are used for evaporation of Au and Ge which have the facility to achieve temperature at ~ 1700 °C. Using other K cell (HTEZ), we can raise the temperature of source up to 1900 °C, which is employed for growth of MoO_3. E-beam evaporator (EVC 300) has been used for Si growth. Source temperature is measured by type C thermocouple placed ~ 1 cm below the crucible. Flux rate is maintained by controlling the source temperature using PID controller. Thickness of the grown film is determined by quartz crystal microbalance which has been calibrated by Rutherford backscattering spectrometry (RBS) and cross sectional transmission electron microscopy (XTEM). In-situ reflection high energy electron diffraction (RHEED) and variable temperature scanning tunneling microscope (VTSTM) are also attached with the MBE growth chamber. For in-situ STM study sample has been transferred from growth chamber to STM chamber with the help of magnetically coupled sample transfer rod.

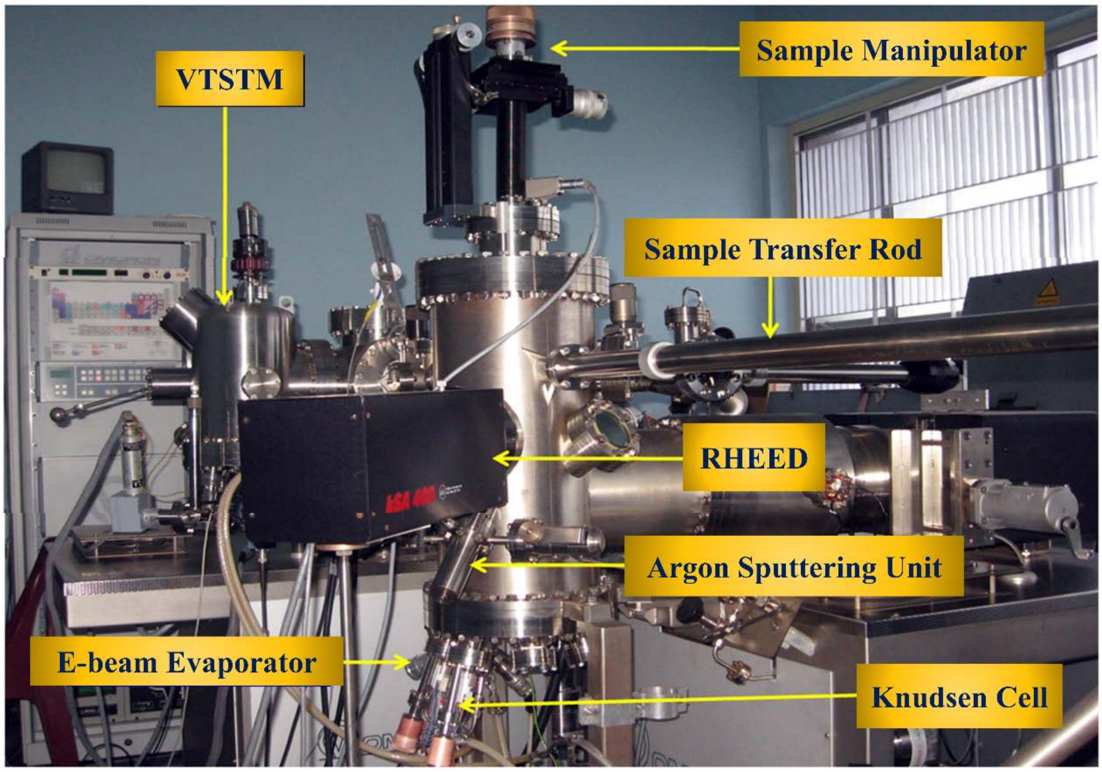

Figure 2.5: *A custom-designed compact MBE system (MBE chamber diameter: 250 mm) and a UHV variable temperature scanning tunneling microscope (VTSTM) attached to it.*

The base pressure ≈ 2.3×10^{-10} mbar maintained routinely and it rises to ≈ 1.1×10^{-8} mbar during molybdenum oxide deposition. To achieve this ultra-high vacuum (UHV) condition, we need to follow few steps. First the system has to bake for 24-32 hours at 130 °C which is much larger than water vaporization temperature and many organic impurities. During baking, the system is connected with turbo molecular pump (TMP) which is backed by a diapharm pump so that the impurity particles from the chamber wall, manipulator and the interior region of the chamber are pumped out to the atmosphere. A typical vacuum level of ≈ 1.3×10^{-8} mbar reached at the end of baking. After that ion pump of very high voltage (typically Kilovolt) has been employed. All the impurities with ionic bond have been ionized and attracted towards the electrode of opposite bias. In this way UHV of ≈ 2.3×10^{-10} mbar could be reached. To maintain better vacuum level in the chamber, Titanium sublimation pump (TSP) is also used. TSP consists of filaments made of Ti-Mo alloy. When a very high current of ~ 50 amp passes through the filaments, titanium particles come out and form a layer inside the chamber wall. Such Ti atoms are very reactive and they form very stable, nonvolatile compound of Ti after reacting with the residual molecules. Utilization of TSP, H_2, O_2 and N_2 can be pumped out from the MBE chamber but not inert gases and methane.

Impurity level significantly influences the surface atomic arrangement of the reconstructed surface. Variation of different vacuum parameters with the base pressure have been summarized in Table 2.1 where P, n, λ, τ defined as base pressure, particle density, mean free path and time for formation of one atomic layer of residual gas respectively.

Table 2.1: Evolution of various vacuum parameters, in accordance with variation of base pressure of the chamber.

P (mbar)	**n (molecules/m^3)**	**λ (m)**	**τ (sec)**
1013	2.7×10^{25}	6.7×10^{-8}	2.9×10^{-9}
1	3.2×10^{22}	5.1×10^{-5}	2.2×10^{-6}
10^{-3}	3.2×10^{19}	5.1×10^{-2}	2.2×10^{-3}
10^{-6}	3.2×10^{16}	51	2.2
10^{-9}	**3.2×10^{13}**	**5.1×10^{4}**	**2.2×10^{3}**
10^{-12}	3.2×10^{10}	5.1×10^{7}	2.2×10^{6}
10^{-15}	3.2×10^{7}	5.1×10^{10}	2.2×10^{9}

At the base pressure of 10^{-9} mbar, particle density reduced and mean free path increased significantly compared to the atmospheric condition which means there is an appreciable reduction of collision probability between the residual gas molecules. In this UHV condition, time for formation of one atomic layer of residual gas after removal of top native oxide layer is very large (~ 12 hours). This is very helpful to carry out different in-situ characterizations such as reflection high energy electron diffraction (RHEED), scanning tunneling microscope (STM) study on the reconstructed surface.

To get highly crystalline, defect free, contamination free thin film, MBE is one of the most delegate and refined technique [13] as interfacial defects drastically degrade the device quality. Amorphous or polycrystalline thin film with interfacial defect causes unavoidable dissipation of heat. Schematic sketch of the main facilities used in MBE growth has been presented in Figure 2.6. In this method, incoming flux rate is very low and controlled very precisely such that evaporate atoms can reach to the substrate without any disruption. After reaching the substrate, evaporate atoms gain enough energy due to keeping the substrate temperature high to migrate on the surface and follow the substrate ordering. In the room temperature (RT) deposition, evaporate atoms agglomerate on the surface due to the lag of enough kinetic energy. As a result, crystalline quality of the thin films degraded and there is a formation of polycrystalline or amorphous films.

In the present thesis work, MoO_3 and Ag have been deposited on varied substrates such as Si(hkl) with and without native oxide layer and FTO. 99.995% pure MoO_3 powder and Ag wire were used as source materials and put in pyrolytic graphite (PG) crucibles. The deposition rates of MoO_3 and Ag were ≈ 0.1nm/min, ≈ 0.2nm/min and the chamber base pressure went to ~ 6.9×10^{-9} mbar, ~7.5×10^{-10} mbar during deposition respectively.

Commercially available Si wafer consists of ~ 2-5 nm amorphous oxide layer at the top of the surface and it contains Si compounds like SiH_4, SiH_2. This native oxide layer acts as a barrier in epitaxial thin film growth. In our system, this native oxide layer has been removed by thermal hating processes. First the sample is ultrasonicated in methanol solution for ~ 5 minutes to remove different organic contamination and dust due to keeping in air. After that it is brought inside the UHV chamber and degassed at 600 °C by DH mode for 12-15 hours. Next it is repeatedly flashed at ~ 1200 °C for 5 minutes.

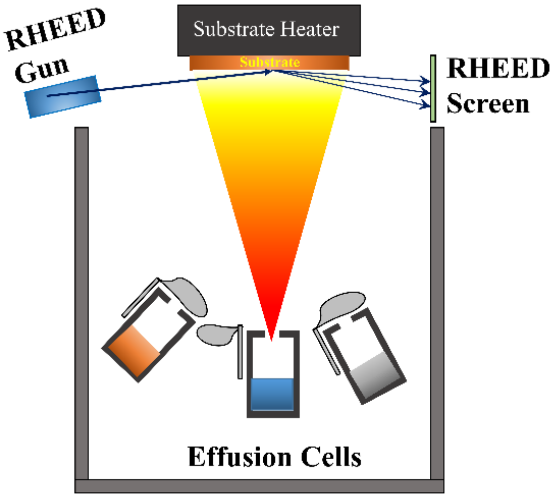

Figure 2.6: *Schematic sketch of MBE set up depicting its main facilities effusion cell, substrate heater, LN_2 cooling and RHEED system (including electron gun, phosphor screen) installed in a UHV chamber.*

Surface atoms comprise unsaturated dangling bonds after removal of the native oxide layer. Depending upon the (hkl) orientation of the single crystal substrate, no of unsaturated dangling bonds per surface atoms varied. To minimize the total energy of the system, the dangling bonds form dimer and surface also absorbs some adatoms which are formed during removal of oxide layer and they rearrange themselves. Rearrangement of the surface atoms is totally different from the bulk. This phenomena is called "reconstruction". Reconstructed surface depends on (hkl) orientation of the substrate, cleaning procedure, contamination and many more. For example reconstructed Si(111) surface shows '7 × 7' unit cell [14].

2.4.2 Physical vapor deposition (PVD) technique

Various sources such as thermal evaporation, e-beam evaporation, sputtering, and plasma spray deposition have been used for producing vapor in physical vapor deposition (PVD) technique [15]. To grow thin films by thermal evaporation in the PVD system (M/s Vacuum Techniques Pvt. Ltd) installed @ IOP, BBSR (shown in Figure 2.7) has been employed.

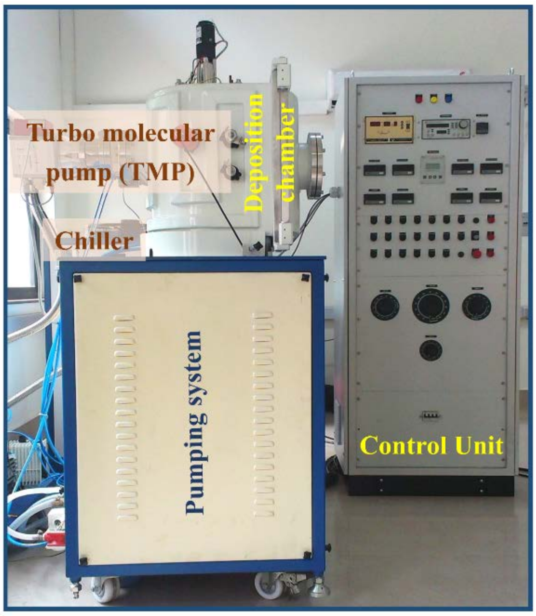

Figure 2.7: *High vacuum coating unit (M/s Vacuum Techniques Pvt. Ltd), Institute of Physics, Bhubaneswar.*

The system consists of a cylindrical, stainless steel vacuum chamber, approximately ≈ 55 cm height and ≈ 40 cm in diameter, where three different materials can be co-deposited simultaneously. A heater is attached to the substrate plate, which can go up to 500 °C from room temperature. Substrate temperature is measured by a thermocouple, placed close to substrate plate. In this technique, heat is provided close to the melting point of the source material in high vacuum (HV) (≈ 10^{-6} mbar) such that source atoms/molecules come out from the surface and the vapor pressure becomes appreciable [16]. HV is obtained by using rotary oil pump, dry pump and turbo molecular pump (TMP). To monitor the vacuum inside the chamber, pirani and penning gauges are used. Quartz crystal microbalance has been used to monitor the deposited film thickness by measuring the variations in the resonant frequencies [17].

Three main basic steps have been involved in thermal evaporation technique, (i) hot source material evaporation, (ii) transportation of vapor from source to the substrate and (iii) deposition of the heated source material on the substrate by condensation of vapor. These three steps have been schematically represented in Figure 2.8.

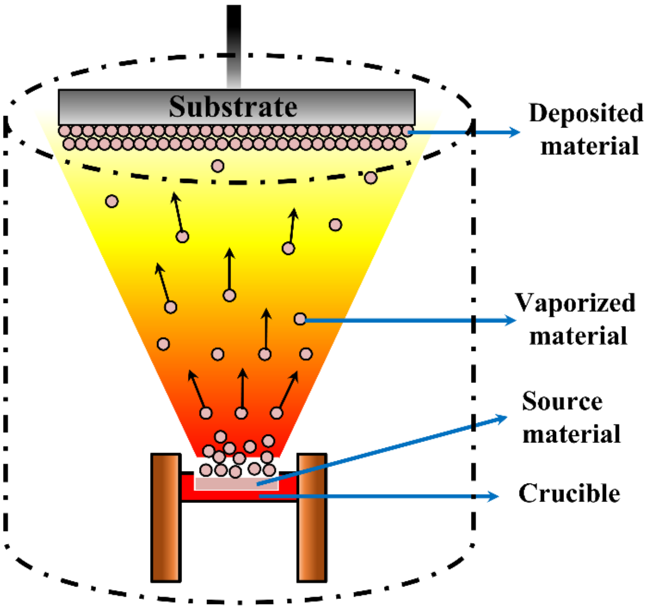

Figure 2.8: *Schematic diagram of thermal evaporation process.*

Source material is kept normally in a molybdenum or tungsten boat and heated by resistive heating (RH). Boat has been chosen in such a way that melting point is higher than the source so that boat will not react with source material. A chiller is attached to the system to maintain temperature at 20 °C during deposition process. Power unit, pumping system, deposition rate are controlled by the control unit as shown in Figure 2.7.

In this thesis work, molybdenum trioxide (MoO_3) and Au thin films of 250 nm and 50 nm respectively have been deposited. Commercially available molybdenum trioxide (α-MoO_3) powder (99.995% purity from Alfa-aeser) and Au wire have been employed as source materials and Si(100) (*n-type*, phosphorus doped, resistivity ≈ 1-20 Ω–cm) with ≈ 2-3 nm thick native oxide on top has been used as substrate. Source to substrate and source to thickness monitor distances were kept at 13.0 cm and 10.0 cm respectively in HV condition ($\approx 1.8 \times 10^{-6}$ mbar). To get high quality uniform thin films, the deposition rate was maintained at ≈ 1 Å/sec.

2.4.3 Chemical vapor deposition (CVD) technique

Thin solid films and nanostructures will be formed by the chemical reaction among the vapor phase precursors in chemical vapor deposition (CVD) technique [18]. The chemical reactions can be stimulated by different processes such as heat in thermal CVD, ultra violet (UV) light in photo assisted CVD and high frequency plasma radiations in plasma enhanced CVD. The schematic diagram of the experimental apparatus used in the present thesis work has been depicted in Figure 2.9.

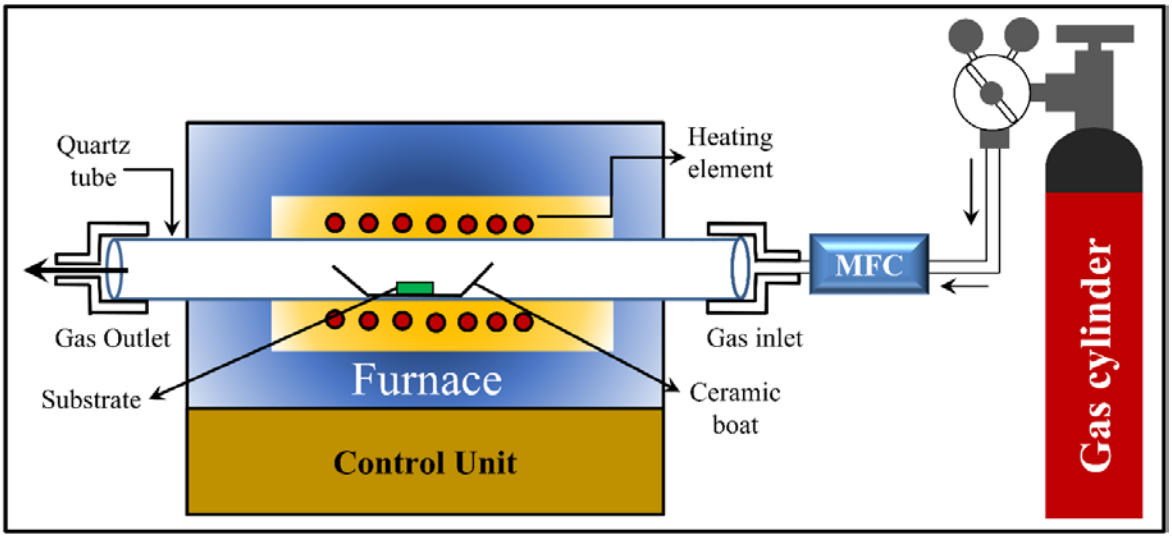

Figure 2.9: *Schematic illustration of the single zone horizontal quartz tube furnace that is used for annealing the samples at different ambience related to this thesis.*

The furnace consists of a ≈ 100 cm long horizontal quartz tube with inner and outer diameter ≈ 4.5 cm, ≈ 5.0 cm respectively where one side is connected to gas cylinder (inlet) controlled by a Sevenstar D07-19B mass flow controller (MFC) and the other side has a gas outlet. Both ends of the tube are covered by stainless steel flanges with water cooling shroud and sealed with rubber O-ring. This tube furnace can also be evacuated in low vacuum order ($\approx 10^{-2}$ mbar) by rotary pump connected with this. The maximum reaction temperature of the chamber can be reached up to 1400 °C with heating rate 1°C to 10 °C and Silicon carbide (SiC) rods are used as heating elements. The temperature is controlled by the Honeywell DC-1040 temperature controller with 10 steps programmable and automatic control. In this thesis work, we used this CVD facility to anneal the MoO_3 thin films grown by PVD technique at different temperatures in low vacuum, argon and atmospheric conditions.

2.5 Characterization techniques

Different characterization techniques have been discussed in this section. To study the morphology, shape, size, crystal structure of the samples, field emission gun based scanning electron microscope (FEGSEM) and transmission electron microscope (TEM) and scanning tunneling microscope (STM) have been utilized. Grazing incidence X-ray diffraction (GIXRD) and reflection high energy electron diffraction (RHEED) have been used to know the large scale crystallinity of the samples. We have also used X-ray photoelectron spectroscope (XPS) for chemical analysis, UV-Vis reflectance for optical properties study, Kelvin probe force microscope (KPFM) for measuring local work function of the samples.

2.5.1 Reflection high energy electron diffraction (RHEED)

After the discovery of electron diffraction by Davison and Germer (1927), Nishikawa and Kikuchi first performed reflection high energy electron diffraction (RHEED) at nearly the same time. This is a very surface sensitive technique to investigate the arrangements of surface atoms on crystalline substrate at the time of epitaxial thin film deposition. This technique is routinely used in MBE method to understand the surface defects (like steps and terrace) of the growth template. With in-situ facility, RHEED is also used to monitor different growth mode (FM, SK or VW) and thickness measurement. This technique enumerate the crystalline quality of the thin film and the crystallographic relationship (epitaxial or non-epitaxial) with the underneath substrate.

In this technique, when an incident coherent beam directed at a very low angle to the surface having ordered array of surface atoms, is reflected and the emergent electron beam comprises well defined phase relationship among the electrons.

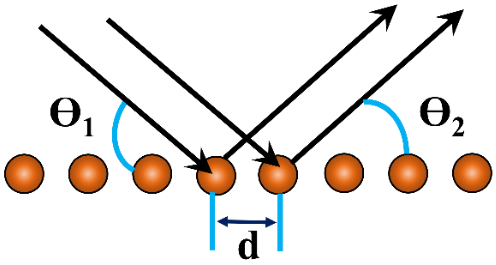

Figure 2.10: *Schematic diagram of the reflected electron beams from two consecutive atoms in a one-dimensional chain to show path difference.*

Figure 2.10 describes the schematic diagram of this process where the in-plane distance between two successive scatters is d. Incident and reflected electron beams make angle Θ_1 and Θ_2 respectively with the surface. Path difference (Δ) between two consecutive reflected electron beams will be

$$\Delta = d\,(\mathrm{Cos}\ \Theta_1 - \mathrm{Cos}\ \Theta_2) \qquad (2.5)$$

Interference takes place only when the path difference becomes an integral multiple of the de Broglie wavelength (λ) of electron such that

$$\Delta = n\lambda \qquad \text{where } n = 1,2,3,\ldots \qquad (2.6)$$

In the fluorescent screen as shown in Figure 2.11, diffraction spots are generated for different n values. For n = 0, an intense bright spot is observed on the screen which indicates the specular reflection of the incident electron beam. Distance of the diffraction spots from direct beam, changes with the inter-scattering element distance (d). When an electron beam is incident on the surface by RHEED method, Ewald sphere has been formed (shown in Figure 2.11). For example, if the inter-scattering element distance (d) ~ 3Å, the radius of the Ewald sphere becomes very large due to the high energy (~ 20 KeV) electron beam. Due to incidence of electron beam in grazing condition with angle of incidence 1-3°, the vertical component of the electron beam becomes very small in comparison with the horizontal component. As a result, only few top atomic layers of the substrate participate in the interaction process with the electron beam. Comparing this distance from the top of the surface (Δz), in other two directions, length for electronic interaction process (Δx and Δy) becomes infinitely large. Then the reciprocal space of the substrate comprises of reciprocal rods only. Such reciprocal rods are infinite along the vertical direction of the substrate and finite in the other two directions (X and

Y) along the substrate plane [19]. When Ewald sphere intersects with these reciprocal rods, diffraction spots are formed. Due to the infinite dimension of the reciprocal rods in z direction, compared to other two directions, constructive diffraction results in streaky nature on the screen.

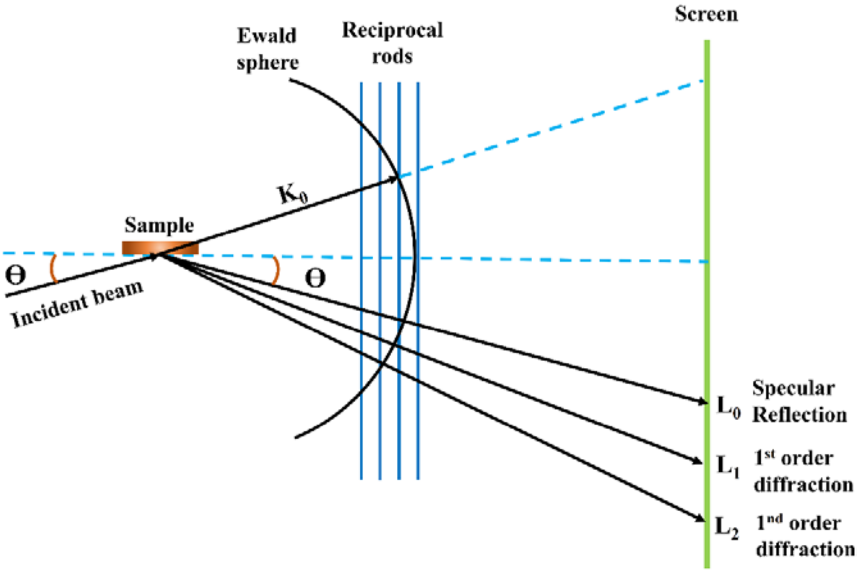

Figure 2.11: *Ewald sphere construction during electron diffraction in RHEED method.*

In 3D island case, electron beam transmits through the nanostructures and the diffraction takes place among the different planes of the nanostructures. Then the dimensions Δx, Δy and Δz along three orthogonal directions become finite. So in the reciprocal space, instead of formation of infinite reciprocal rods, a set of spots is generated. Hence the streaky pattern of the RHEED, becomes spotty in nature after formation of the 3D nanostructures. This phenomenon becomes similar as the transmission electron diffraction (TED) in the TEM method [20]. We have shown schematically such diffraction process in Figure 2.12. However, inappropriate sample preparation method and presence of appreciable amount of contamination also gives rise to transmitted electron diffraction.

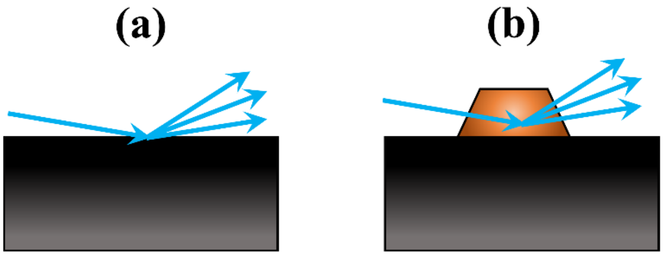

Figure 2.12: *Schematic of electron diffraction in RHEED method due to a) reflection from the surface and b) transmission through the crystalline three dimensional islands.*

2.5.2 Scanning tunneling microscope (STM)

Scanning tunneling microscope (STM) has the capability of atomic resolution directly in real space for the surfaces of conducting materials. It was developed in the early 1980s by Gerhard Bining and Heinrich Rohrer, who were awarded the Noble Prize in Physics in 1986.

The capability of monitoring surface structures with atomic resolution combined with the ability to position the tip with atomic accuracy leads to perform direct and controlled manipulation at the atomic level, offering the opportunity to create atomic-scale devices. Based on the atomic resolution capability, the tip can be positioned with atomic accuracy above a pre-selected atomic site and a local experiment can be performed. In this regard, electronic local density of states (LDOS) can be determined through I-V measurements using scanning tunneling spectroscopy (STS).

A block diagram of the main components of STM has been depicted in Figure 2.13.STM tips are generally fabricated for the metal wires such as W, Pt-Ir, Au. The preparation procedure of the atomically sharp tip follows some steps, (i) first ex-situ treatments like mechanical grinding, cleavage or electrochemical etching; (ii) then in-situ treatments like annealing, field emission. Sometimes "soft crash" of the tip on the surface also results in formation of good quality tip. To raster the tip over the area of the sample to be studied, a scanner is attached with the tip. Piezoelectric ceramics are used in scanners as electromechanical transducers, as they can convert electric signals of 1 mV to 1 kV into mechanical motion in the range from fraction of an Å to a few µm. A feedback electronics control the tip-sample gap.

When the tip is brought very close to the surface with a typical gap less than 1.0 nm, wave functions of the tip atom and surface start to overlap. In this condition, if an electrostatic bias voltage is applied between the tip and the surface, quantum mechanical tunneling of the electrons takes place (Figure 2.14) [7]. Depending on the polarity of bias voltage, electrons tunnel from the tip to the surface or vice versa. The magnitude of the tunneling current depends on the various factors such as (i) tip to surface distance, (ii) magnitude of the bias voltage, (iii) local density of states of the tip and sample atoms which can be represented as

$$j = [D(V)V/d] \exp(-A\Phi^{1/2}d) \tag{2.7}$$

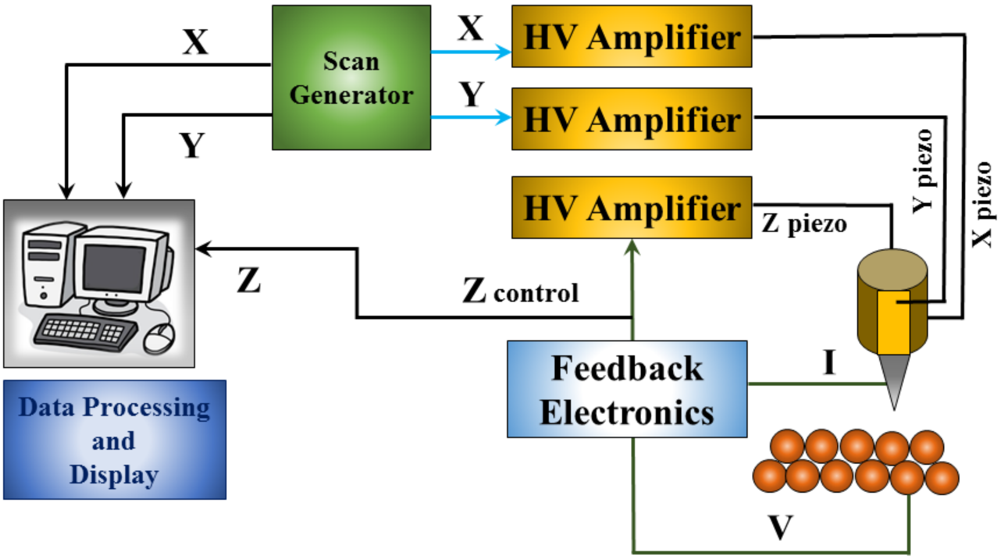

Figure 2.13: *Schematic diagram of the main components of STM set-up.*

where, d, D(V),V, A, Φ represent the effective tunneling gap, electron density of states, applied bias voltage, constant and effective barrier height at the tip sample junction respectively [7]. There is a sharp dependence between tunneling current and the gap. A change of the gap by Δd = 1Å results by an order of magnitude in tunneling current or if the current is kept constant to within 2%, the gap width remains constant to within 0.01Å. Surface atoms with an atomic separation of ~ 2Å can be resolved.

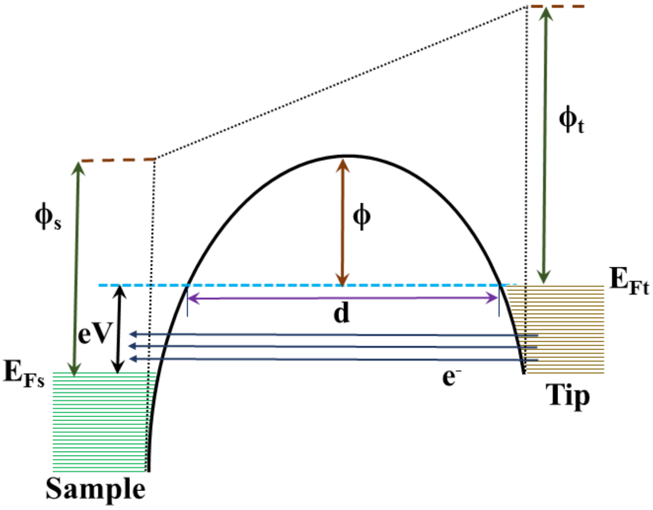

Figure 2.14: *Energy diagram of the tunneling contact between STM tip and the metallic sample.* E_{Fs} *and* E_{Ft} *are the Fermi levels of the surface and the tip, Φs and Φt are the work functions of the surface and the tip, Φ is the effective barrier height, d is the effective tunneling gap and V is the bias voltage. The diagram illustrates the situation when STM probes the empty substrates of the surface.*

2.5.2.1 Different modes of operation

STM topography is very sensitive to local density of states (LDOS). When the tip bias voltage is positive with respect to the sample, the STM image corresponds to the surface map of the filled electronic states. With a negative tip bias voltage, the empty-state STM image of the surface is obtained. The basic parameters for STM operation are the lateral coordinates, x and y, height h, the bias voltage V and tunneling current I. There are different modes of operation of STM depending on the manner in which these parameters are varied. In this section we shall discuss about the constant current mode and constant height mode of operations of STM. Apart from these two modes there is scanning tunneling spectroscopy (STS) which is a series of various modes in which V is varied.

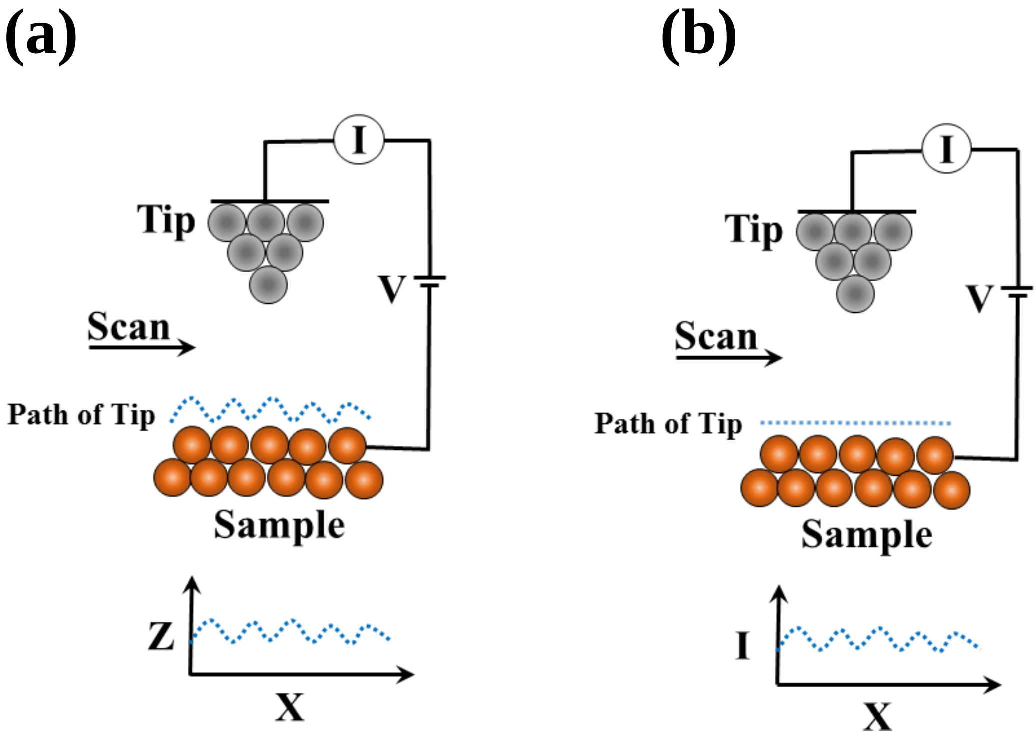

Figure 2.15: *Schematic diagram of (a) constant current mode and (b) constant height mode of STM operation.*

Constant current mode: Figure 2.15(a) shows the schematic representation of constant current mode [21]. In this mode tip is scanned over the surface at constant current and voltage. To maintain the tunneling current at the preset value, a feedback system continuously adjusts the vertical position of the tip by variation of the feedback voltage Vz on the Z-piezoelectric driver. This method is very helpful for probing the surfaces which are not atomically flat but the main disadvantage is the slow scan speed due to finite response time of the feedback system.

Constant height mode: In this mode tip is scanned over the surface at constant Vz and the current variation is recorded as a function of tip position which has been illustrated in Figure 2.15(b) [21]. This method is not influenced by the finite response time of the feedback signal due to switch off the feedback circuit. This mode is very much useful to investigate the dynamical process such as surface diffusion by fast imaging. But smooth surface is required to image in this method otherwise the tip will crash.

2.5.3 Focused ion beam (FIB) - scanning electron microscope (SEM) cross beam system

The scanning electron microscope (SEM) is a leading technique in modern science and nanotechnology. It provides the informations about surface topography and composition of the sample. Charles Oatley and co-workers at Cambridge University developed SEM in the late 1940s. In SEM technique, when sample is irradiated with a fine electron beam, secondary electrons (SEs) are emitted. Topography of the sample surface is visualized as an image constructed by SEs. In this thesis work, we have carried out SEM analysis by a cross-beam scanning electron microscope (Carl Zeiss, Neon 40) with Gemini column and Canion 31 focused ion beam (FIB, Orsay Physics), equipped with gas injection system (GIS, Orsay Physics), SE detector, in-lens detector, STEM detector, back scattered electron detector and X-ray energy-dispersive spectrometry (EDS) detector (INCA, Oxford) (Figure 2.16). These two columns are situated at 54° angle; to see same spot with SEM and FIB, tilt angle will be 54° with 5 mm working distance (WD). WD is defined as the distance between sample and pole piece. The sample can be tilted between 0° and 54° to face the ion beam or the electron beam perpendicularly. When tilt angle is 0°, which means electron beam is falling on sample at normal incidence whereas ion beam is irradiating at 54°. The system is fitted with a computer controlled gas injection system (GIS) in which five different gases for metal and insulator deposition or enhanced and selective etching could be possible. The system is attached with a turbo molecular pump (TMP) which ensures a dynamic pumping and the chamber base pressure is $\leq 10^{-6}$ mbar.

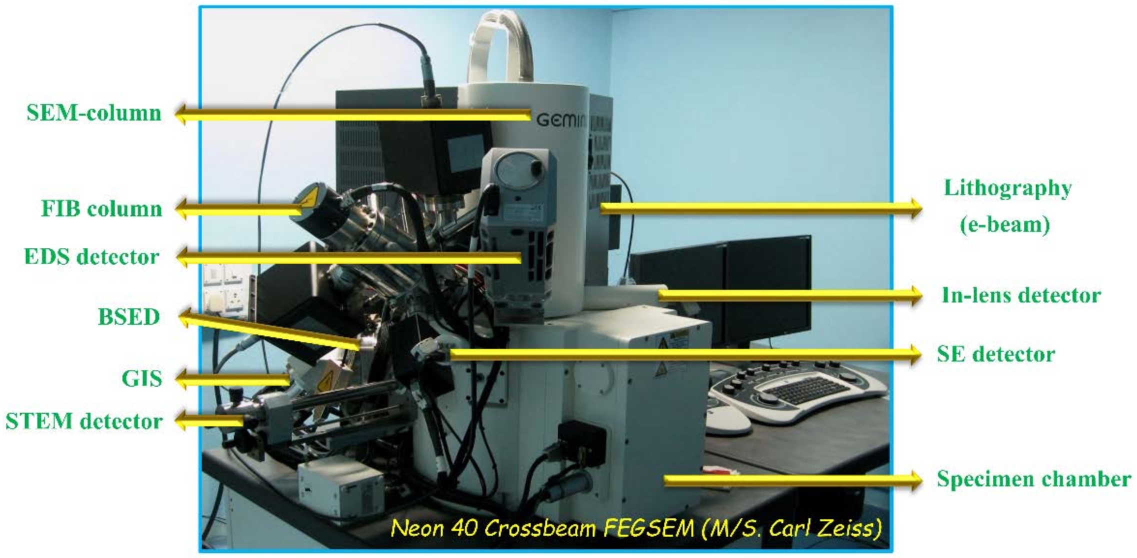

Figure 2.16: *FIB-SEM cross-beam system (M/S. Carl Zeiss, Neon 40), Institute of Physics, Bhubaneswar.*

2.5.3.1 Scanning electron microscope (SEM)

SEM consists of electron beam, optics, detectors, vacuum pumps and control system. Generally two kinds of electron sources are used; thermionic and field emission. In the case of thermionic emission, metal sources are heated up enough such that electrons can overcome the work function barrier and are emitted. Tungsten, Lanthanum hexaborate (LaB_6) are used in thermionic emission due to high melting point and low vapor pressure. Field emission sources are more useful than thermionic emission because of smaller sized coherent beam spot, higher current density and better signal to noise ratio. In this process, metal cathode with sharp tip is negatively biased with several kilovolt voltage difference with respect to corresponding anode. Then at the apex of the tip, electron are pulled out overcoming the barrier due to the generation of very high electric field. In our SEM system, field emission based electron gun is used as electron source. After emergence of the electron beam from the source, it is accelerated down the column, then pass through a series of condenser, objective lenses, apertures and interact with the sample and produce different types of signals. Condenser and objective lenses act to control the diameter of the beam and to focus the beam on the sample. The main characteristic of GEMINI optics is the use of a beam booster and an objective lens which acts as a combined electrostatic/ electromagnetic lens. In SEM, magnification is determined by the ratio of display device dimension (A_1) with the dimension of 'raster area' on the sample (A_2) [22]. As A_1 can be considered as unchanged, smaller A_2 implies larger the magnification and vice versa.

Image formation:

In SEM, when electron beam is incident on the sample, interacts with the sample material via repeated random scattering and absorption within a teardrop shaped region (Figure 2.17) in the material. The image formation of an object depends on the collection of beam-sample interacted signals. There are two types of beam-sample interactions; elastic (by electrostatic interaction with atomic nuclei) and inelastic (by interaction with atomic electrons). In the electron – sample inelastic interaction, the sample electrons are excited individually or collectively on which the amount of energy loss completely depends on the binding energy of the electron to the atom. In this process secondary electron (SEs) are generated. Backscattered electrons (BSEs) are generated in the beam-sample elastic interaction and SEs have lower energy compared to BSEs. SEs and BSEs are mainly used for imaging. Other than these two signals, a number of other signals such as characteristic X-rays, Auger electrons and cathodoluminescence are produced upon the beam impingement on the sample (Figure 2.17). According to Reimer formula, the range (R) of electron having incident energy E is given by

$$R \approx aE^{r} / \rho \qquad (2.8)$$

where, ρ is the sample density. With increasing atomic number (Z), density of solids tend to increase. As a result, R decreases with increasing Z and decreasing the incident electron energy. SEs are generated within very small depth (may be < 2 nm) below the sample surface. So SEs image is the property of the surface structures of the sample and the corresponding image is called topographical image. The Everhart-Thornley detector (E-T detector), named after the scientists who first applied this design to the SEM, is used to detect the electron signals. BSEs are basically primary electrons which have been reflected back from a specimen via elastic interactions in one of two ways: (i) under the strong Coulomb field of an atomic nucleus (i.e. Rutherford scattering) and (ii) incident beam of electrons can undergo multiple low-angle deflections/scattering which together comprise a deflection of > 90°. Strong atomic number (Z) contrast image has been expected in the first case because of the Z^2 proportionate of the cross section in high-angle elastic scattering whereas SE emission is almost Z independent. In the case of different atomic number Z contained sample, BSEs image will give different intensities and contrasts. Higher Z area will appear as brighter than smaller Z area unlike to SE image.

Since BSEs are coming from the deep, it contains little topographic contrast but shows material (atomic number, Z) contrast [22].

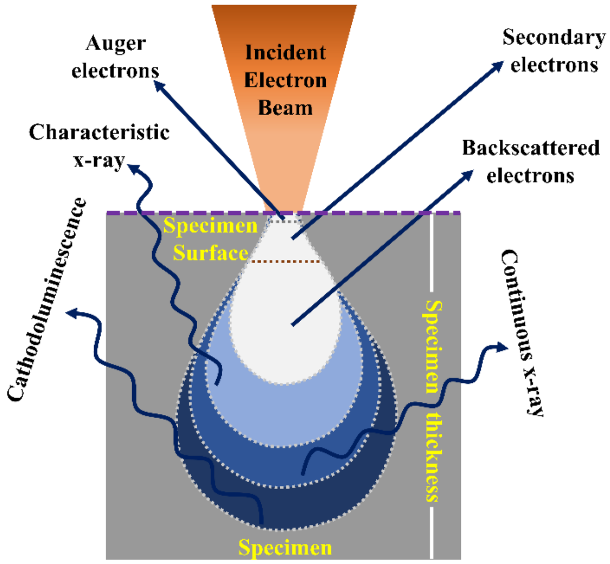

Figure 2.17: *Schematic representation of the generated various signals due to electron-sample interaction in SEM.*

Energy-dispersive X-ray spectrometry (EDS)

When an incident electron is scattered inelastically, it knocks out a core level electron. Then an electron from higher orbital fills the empty state in the lower energy core level orbital. The energy difference between these two orbitals is released in the form of photons and the photon energy used to be in the X-ray regime which follows Mosley’s law. This technique is very useful for the elemental or compositional analysis of the sample. The EDS detector (Si(Li)) is the only X-ray spectrometer currently used to detect X-ray. An EDS spectrum displays peaks across the energy range that contains all the characteristic peaks for which the most X-rays are received. The higher intensity peak in a spectrum corresponding to an element, confirms its more presence in the sample [22,23].

2.5.4 Transmission electron microscope (TEM)

Transmission electron microscopy (TEM) is a very important technique in the field of materials science and is routinely used for studying the crystal structure and microstructure of materials [23−25]. Microscopy can be carried out with various probes, such as visible light, X-rays, electrons besides various scanning probe methods as atomic force microscopy, scanning tunneling microscopy etc. Historically, TEMs were developed as the light microscope is limited by wavelength dependent diffraction limit. In 1932, Knoll and Ruska established the idea of electron lenses and illustrated by taking electron images in the instrument built by them [26]. This was the most important achievement, for which Ruska received the Nobel Prize in 1986. There are various types of TEM machines, in which both the particle and wave nature of electrons are utilized. In a TEM, a huge number of signals are generated due to the interaction of a highly energetic beam of electrons with the specimen, which can be utilized to get more information about that specimen (from a very small area). During transmission, the electrons interact with the specimen, giving rise to signals containing information about the internal structure and chemistry of the material. DPs and lattice images are two forms of data obtained in TEM. In TEM, DPs are the basis of all image formation as well as all crystallographic investigations and defect studies; DPs are interpreted in terms of Bragg reflection from planes of atoms of sample. In any TEM image, contrast basically comes from the scattering of the incident electron beam from the specimen. Lattice images are understood as interference patterns formed between the direct beam and diffracted beam, which are made use to form high resolution TEM (HRTEM) imaging. Usually the lattice spacing is obtained from the fringe width of HRTEM micrograph [23].

2.5.4.1 Instrumentation

A typical microscope consists of three parts: i) illumination system, ii) objective lens/stage and iii) imaging system. In a TEM, the illumination system consists of an electron gun and the condenser lens assembly and is used to generate and to guide energetic electrons towards the specimen. The illumination system can be operated into two prime modes: parallel beam and convergent beam. The first mode is used primarily for conventional TEM imaging and selected area electron diffraction (SAED). The core part of any TEM is the objective lens (OL) and the specimen holder/stage system. The imaging system comprises of a few lenses to magnify the image or the DP formed by the OL and to focus these patterns on the viewing screen or onto the detector (like charged coupled device (CCD)).

Illumination section consists of electron source, acceleration column and condenser lenses. One of the most important parts in TEM is an electron source that illuminates the specimen and determines the image quality partially. There are two types of electron sources:

thermionic emission (tungsten filaments or lanthanum hexaboride (LaB_6) crystals) and field emission (fine tungsten needles). An electrostatic lens in the form of Wehnelt cup is used after the filament to converge the maximum number of emitted electrons (Figure 2.18(a)). A high voltage is generated in a separated power supply unit using Cockcroft-Walton technique and is coupled to the acceleration column followed by condenser lens system assembly. After generation of electrons from the gun, they are accelerated towards the anode and enter into the acceleration column. As the velocity of the electrons close to the speed of light, the wavelength of the electrons having energy V (with relativistic correction)

$$\lambda = h/[2m_0eV(1 + eV/2m_0c^2)]^{0.5} \tag{2.9}$$

where, all the notations denote standard parameters.

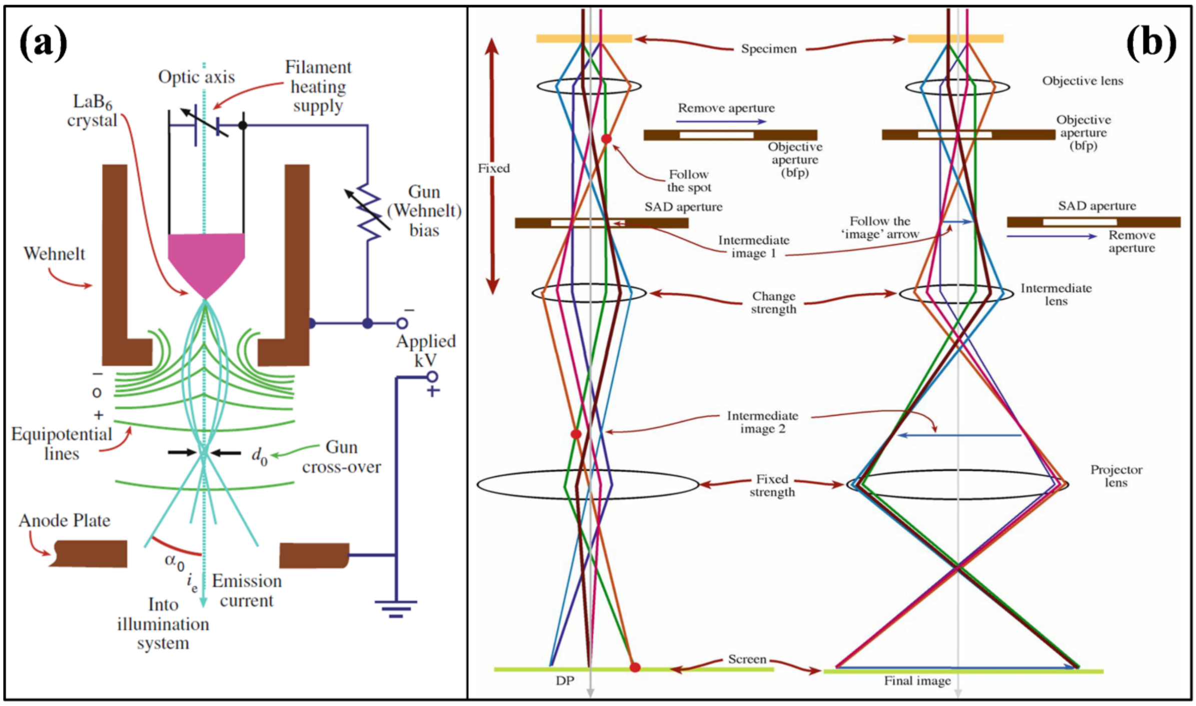

Figure 2.18: *A schematic diagram of (a) filament and illumination part, (b) diffraction pattern formation and image formation [23].*

The function of the condenser lens system is to provide a parallel or convergent beam of electrons at sample surface (Figure 2.19). Gun crossover appears as the object for the first lens in the illumination system, having different condenser lenses. After this stage, specimen is used insert either from the side (our case) or from the top. Just below the sample (2-5 mm), objective lens (OL) is situated. The objective lens (OL) is the most crucial part of the TEM. OL is very important component of a TEM, as its quality determines the quality of all the information about the specimen that we observe. In diffraction mode, one has to adjust the imaging system lenses such that the back focal plane of the objective lens behaves as the object plane for the intermediate lens.

Then the DP is projected onto the viewing screen/CCD (Figure 2.18(b)).

The imaging system consists of several magnifying lenses (termed as intermediate lenses), which magnify the image or SAD formed by the objective lens. Finally these will be projected onto the viewing screen/CCD detector. The combination of intermediate and projector lenses do the image magnification. Projector lens system projects the image onto electron detector (CCD/TV Camera), which is coupled to a computer to grab such images. Here, the quality of the image is taken care by the objective lens which eventually decides the resolution of the microscope. SAED aperture will select a specific area of the sample, which is in the image plane conjugate with the sample [23].

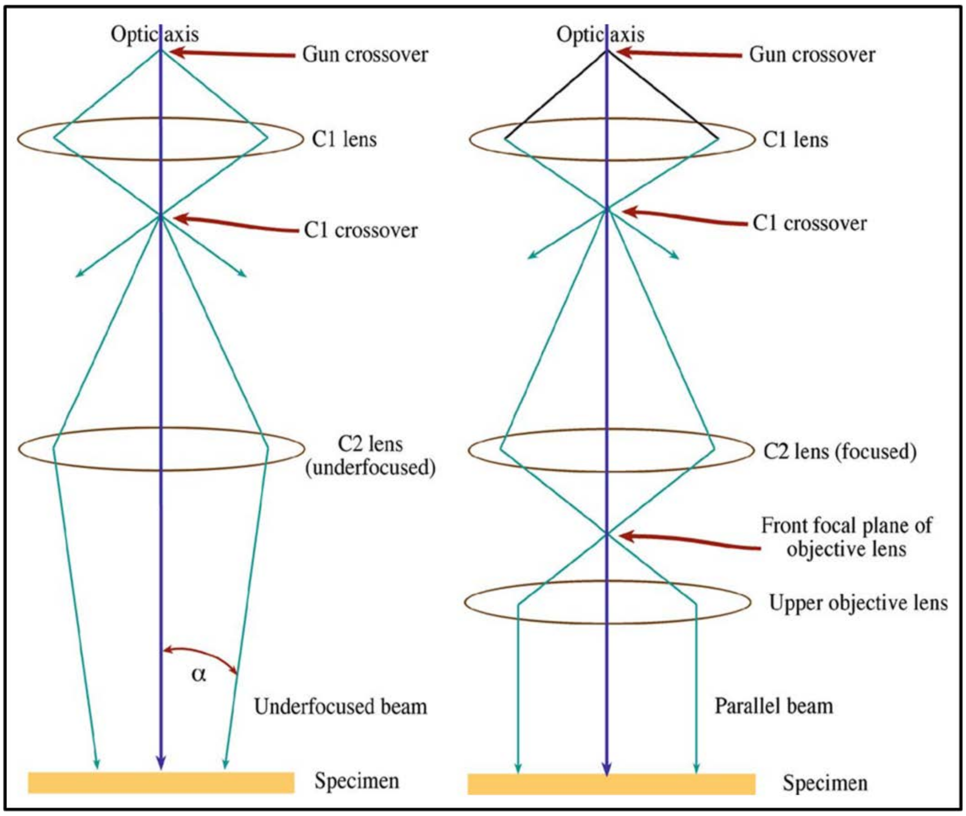

Figure 2.19: *Parallel-beam operation in the TEM: the basic principle illustrated (left) and the practical situation in most TEMs (right) [23].*

Electrons being charged particles, TEM column is always kept at high vacuum (~ 10^{-8} mbar) in order to get a collimated beam of electrons. In this thesis, all the TEM measurements have been carried out using JEOL JEM-2010 machine (Figure 2.20) with LaB_6 thermionic emission type gun operating at 200 keV (corresponding $\lambda \approx 0.0025$ nm). The pole piece of OL is an ultra-high resolution pole piece (UHR-URP22) with a spherical aberration coefficient (C_s) of 0.5 mm, which allows us to obtain point-to-point resolution of ≈ 0.19 nm. The images were recorded in a charge-coupled device (CCD) based detector with 40 ms time resolution and with 4008 × 2672 pixels (Model 832, Gatan Inc.).

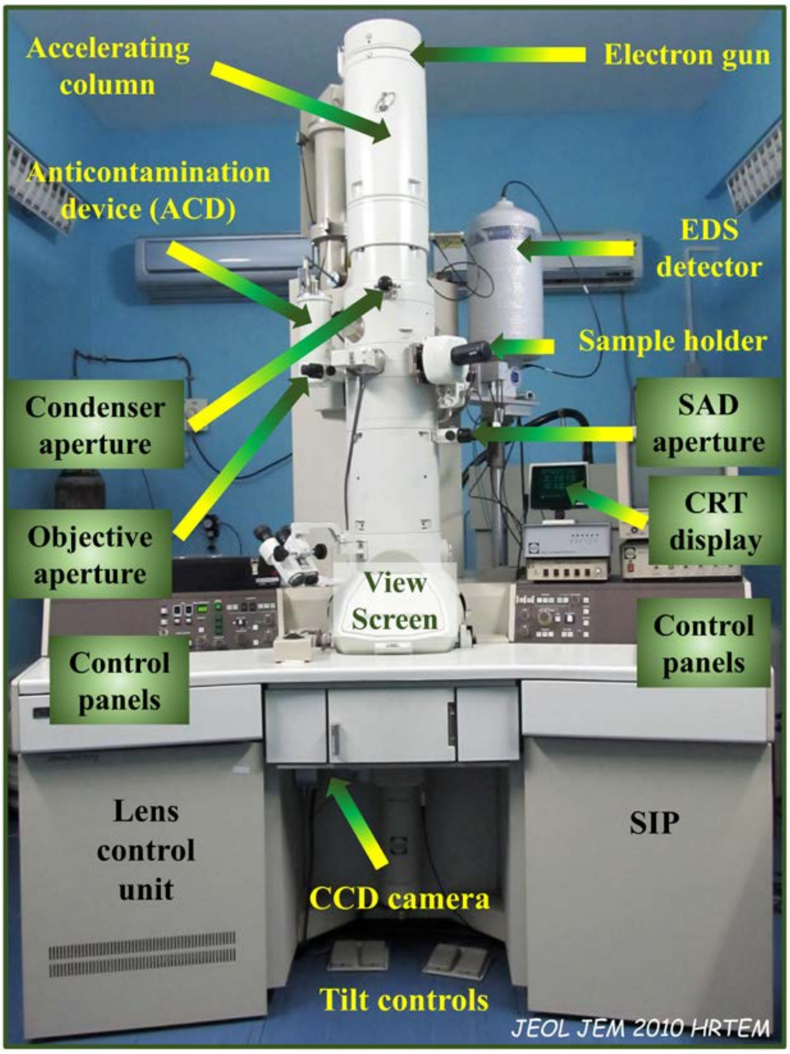

Figure 2.20: *200 keV JEOL JEM-2010 TEM, Institute of Physics, Bhubaneswar.*

2.5.4.2 Diffraction and imaging

TEM image contrast is coming due to the scattering of the incident electron beam by the specimen. When the electron wave is transmitting through a specimen, its amplitude and phase will be changed which will contribute to contrast of an image. Amplitude contrast has two forms: mass-thickness contrast and diffraction contrast. Amplitude contrast culminates from variations in mass or thickness or a combination of the two. From greater atomic number (Z) and/or higher thick specimen, electrons will be scattered more strongly, and therefore that area will appear as darker in bright field (BF) images (select direct beam to produce image) and brighter in dark field (DF) images (select diffracted/scattered beam to produce image). Diffraction contrast is simply a special form of amplitude contrast, where the scattering happens at special (Bragg) angles. Coherent elastic scattering produces diffraction contrast in TEM. In diffraction contrast, contrast depends up on the crystallinity of the specimen. However, for thin specimen at high resolution, this description fails because the wave nature of the electrons is then needs to be invoked. If the specimen is thin enough and crystalline, then elastic scattering is usually coherent and these scattered/transmitted electrons contribute to the image formation. After the exit of electrons (elastically transmitted coherent electron beams), the diffraction spots and image are used to form at back-focal plane and image plane of OL respectively. The diffraction pattern can be understood by taking the fast Fourier transform (FFT) of the wave function of electron at the back focal plane of OL. The lattice image will form due to interference between the direct and diffracted beams depending on the phase difference between these two. So the highly diffracted beams are used to cut down by the objective aperture. The resolution and the details of image formation are governed by the contrast transfer function (CTF). The CTF depends on microscope parameters such as λ, spherical aberration coefficient (C_s), chromatic aberration coefficient (C_c), defocus, width of defocus, stabilities in high voltage, OL current etc. To obtain the structural information about the sample from the images, the trajectory of the electron wave through the specimen needs to be calculated. In order to understand the geometry of electron diffraction, we can ignore the lens system, which merely magnifies the DP.

Normally we interpret the DPs in terms of Bragg reflection due to the planes of atoms in specimen and one can introduce diffraction vector $\vec{g}$ associated with each Bragg reflection and link each g with a crystal plane (hkl). The reciprocal lattice provides a very simple way of understanding the diffraction, when combined with the Ewald-sphere construction. Bragg's law or the Laue equations are satisfied exactly, when the sphere exactly cuts through a point. The Ewald sphere has a radius of 1/λ. Most importantly, since λ is small in TEM, the radius of the Ewald sphere is large and hence the Ewald sphere is quite flat. This results the formation of many spots in the DP. A schematic diagram showing the geometry of diffraction pattern formation and may consider the much simpler ray diagram shown in Figure 2.21. When a beam of electrons falls on a crystalline specimen, some of them will transmit through the specimen without any interaction (direct beam) and impinge on the CCD. Other electrons are diffracted through an angle 2θ by the crystal planes of spacing d and impinge on CCD detector at a distance R from the direct beam. According to Bragg's law, the diffracted beam follows the relation $2d\sin\theta = \lambda$, which can be simplified for the small angles as $\lambda/d = 2\theta$. From the trigonometric relation using small angle approximation, one can write $R/L = 2\theta$. Combining these two,

$$d = \lambda L/R \tag{2.10}$$

where, R is the distance between the direct and diffracted beams as measured on the screen.

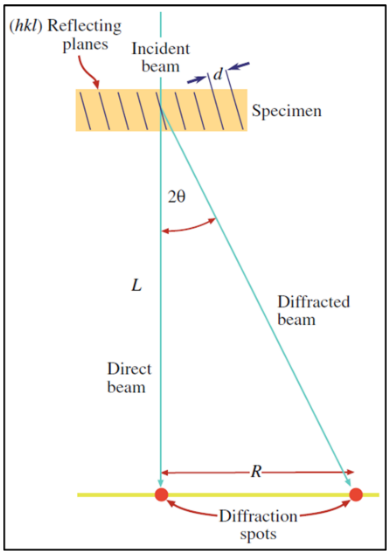

Figure 2.21: *A schematic diagram showing the geometry of diffraction pattern formation [23]*.

As the λ and L (camera length) are constant for the instrument, the quantity λL is called camera constant. So, d can be determined easily. Note that, L is not a physical distance between the specimen and screen, but is a notional distance which can be changed while operating [23].

2.5.4.3 Beam (electrons)-specimen interaction

Electron, being a low-mass, negatively charged particle, can easily be deflected while travelling close to other electrons or the positively charged nucleus of an atom. These Coulomb (electrostatic) interactions cause electron scattering, which can be broadly divided in two groups: elastic (no loss of energy) and inelastic (some measurable loss of energy) scattering. The all possible interactions of electrons with solid have schematically shown in Figure 2.22.

One can also split the scattered electrons into coherent and incoherent. Elastic scattering is usually coherent (if the specimen is thin and crystalline) and usually occurs at relatively low angles (1–10°). At higher angles (> 10°) elastic scattering becomes more incoherent. After entering into the specimen, most of the electrons are scattered elastically by the nuclei of the atoms in the specimen. Some electrons are also scattered inelastically by the electrons in the specimen. Compared to X-ray or neutron diffraction, the interaction of electrons with the specimen is quite large and they go through multiple scatterings.

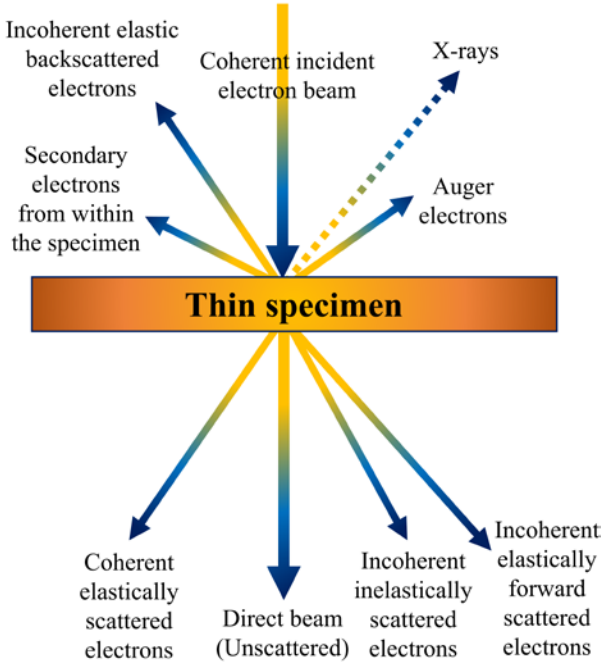

Figure 2.22: *Schematic presentation of various signals generated when a high-energy beam of electrons interacts with a thin specimen.*

The prime origin of contrast in TEM images are the elastically scattered electrons. When the specimen is thick, the interaction between the electrons and the specimen can be described by an incoherent particle model. However, considering thin specimen, the wave character of the electrons will dominate and the particle model can be discarded. The electrons, while transmitting through the specimen near the nuclei, are accelerated towards the nuclei and will experience a small change of phase of them. This minimal change in phase also contains structural information. For high resolution images, only the elastically scattered electrons are of importance. Inelastic scattering transfers energy to the specimen and generates a lot of useful signals, from which one can produce different images or gain spectroscopic knowledge regarding the chemistry and electronic structure of the specimen. Electron energy loss spectrum (EELS) of the inelastically scattered electrons provides the information about chemical composition of the sample at a very spatial high resolution. These inelastic scattered electrons also contribute to the formation of Kikuchi lines in the electron diffraction pattern that is needed for attaining the crystallographic alignment of the crystals in specimen [23].

2.5.4.4 Sample preparation (mechanical process)

Sample preparation is the most important aspect of all of TEM works. Since the electrons have to transmit through the specimen, the specimen has to be thin enough for the electron transparency. Generally, for 200 keV electron beam, sample thickness should be ≤ 100 nm (even thinner (<10 nm) for HRTEM) to transmit energetic electrons. There are two types of samples to be prepared depending on the interest of study. Cross-sectional TEM (XTEM) sample is required to study the interface and/or bulk solid while planar TEM specimen preparation is required for in-plane study. Figure 2.23 and Figure 2.24 display the schematic illustrations of conventional methods (mechanical process) to prepare both planar and cross-sectional TEM samples respectively.

Planar specimen preparation:

For Planar TEM sample preparation, we cut the sample into 3 mm disc using ultrasonic disc cutter and thin down to ≈ 80-100 μm from rare side (substrate side) by using lapping and polishing system (South Bay Technology (SBT) Model 910). Here, the mechanical thinning is performed by grit paper with larger size initially, and then finer grit size and finally polished with finer polishing paper. The specimen is then loaded on dimple grinder stage (Gatan, Model 656). The aim of this process is to thin the center of the disk while minimizing damage to the surface of the sample and typically dimpling is carried out up to ≈ 20 μm thick using diamond paste and then polished by using alumina suspension. Final electron transparency is achieved by ≈ 3 keV Ar ion (Ar^+) milling at grazing incidence (5°-7°) in the Gatan made precision ion polishing system (PIPS, Model 691) (Figure 2.23).

Cross-sectional specimen preparation:

For cross-sectional TEM sample preparation, we cut two rectangular pieces of dimensions (≈ 2.5 mm × 5 mm) from the main sample using SBT made abrasive slurry saw

(Model 850). Then the pieces were glued face to face using Gatan G1 epoxy. Following this, the above assembly is glued with two dummy pieces having similar sizes. After that the whole assembly is packed into a stainless steel tube having inner and outer diameter ≈ 2.9 mm and ≈ 3.1 mm respectively using the same epoxy glue. Next, we cut ≤ 500 μm thick slices from the tube using SBT made Low speed diamond wheel saw (Model 650). Mechanical thinning and polishing are performed from both sides (using LPS) as like planar sample preparation case, and similarly one side is dimpled using DG. Finally, electron transparency is achieved by ≈ 3 keV Argon ion milling using PIPS in similar way mentioned above (Figure 2.24).

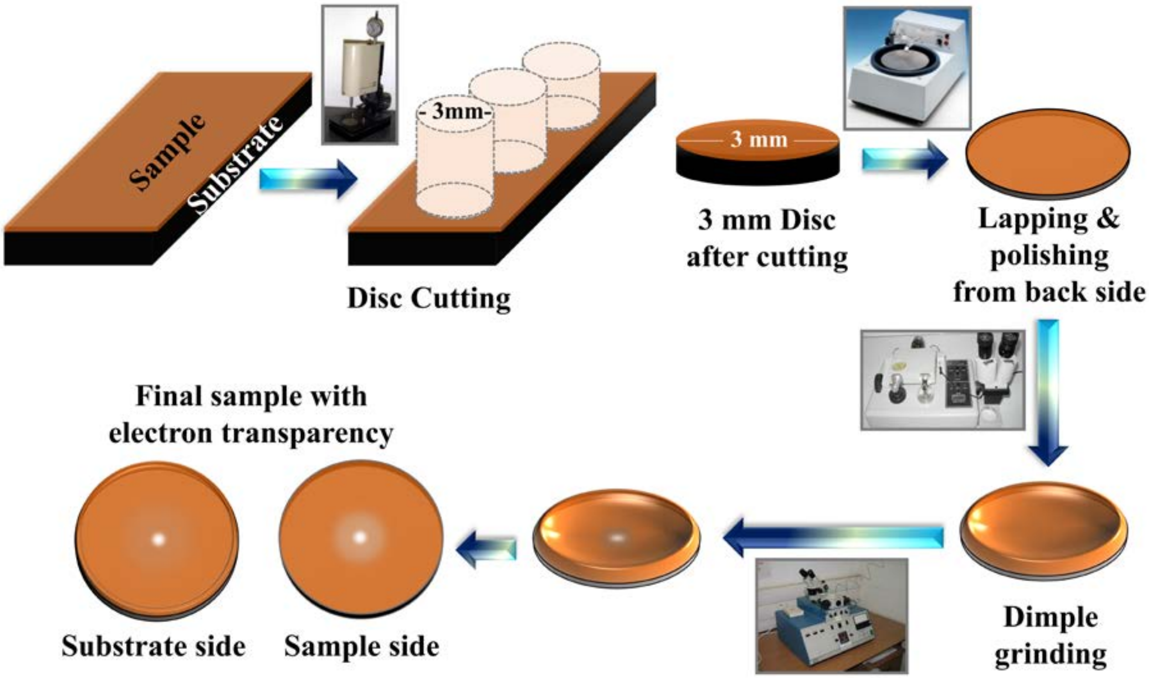

Figure 2.23: *Schematic diagram of a typical planar TEM specimen preparation procedure.*

2.5.5 X-ray diffraction (XRD)

To know the large scale crystalline quality, crystal structure, lattice parameters, strain of the system, X-ray diffraction (XRD) technique is very essential. When system interacts with X-ray, scattering and absorption take place. But due to weakly interaction, multiple reflections are neglected. X-ray penetration depth depends on its energy, angle of incidence and the material. When a beam of monochromatic x-rays impinges on a sample, most of the radiation gets scattered from the atoms and interferes destructively with radiation scattered from other atoms. Hence, no signal is detected. However, when there is a long range order in the atomic arrangement of a material, scattered X-rays interfere constructively. The condition of interference is defined by Bragg's law (Equation 2.11). These interfered beam is collected by the scintillation detector. The detector converts it into voltage pulse which will be fed to a computer to display the spectrum of intensity vs. angle of incidence.

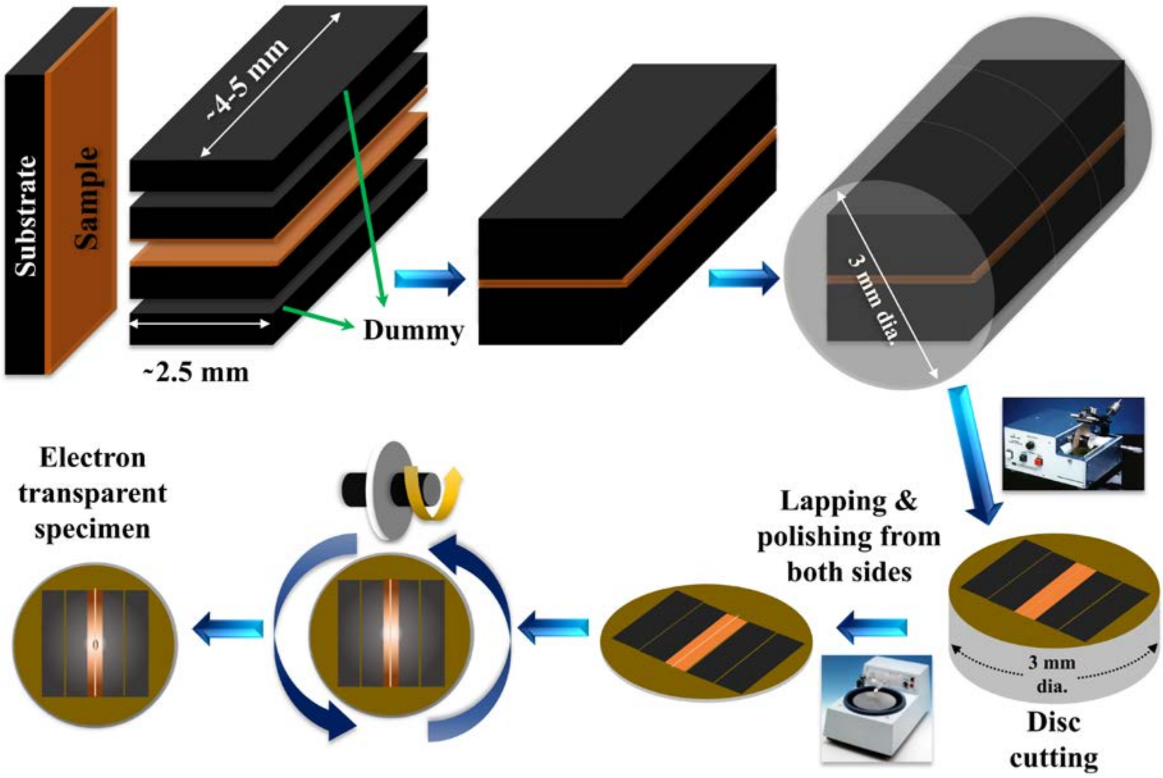

Figure 2.24: *Schematic diagram of a typical cross-sectional TEM specimen preparation procedure.*

$$2d\sin\theta = n\lambda \tag{2.11}$$

where, d is the inter-planer spacing of the different planes, θ is the incident angle, λ is the incident X-ray wavelength and n is an integer (see Figure 2.25). The crystallite size is given by Scherrer's formula (Equation 2.12) [27]:

$$D = \frac{K\lambda}{\Delta\cos\theta} \tag{2.12}$$

where, D is the average crystallite size, K is a dimensionless shape factor, with a value close to unity (typical value 0.9 according to [27]), Δ is the FWHM of the diffraction peak.

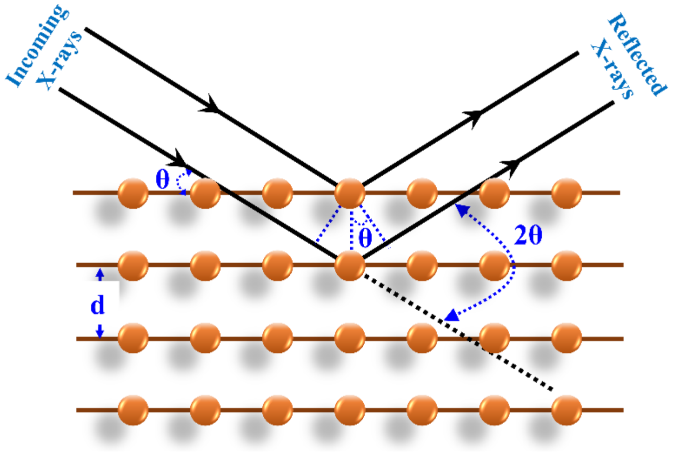

Figure 2.25: *Schematic representation of X-ray diffraction occurring in a crystal with inter-planar spacing d.*

XRD system can be broadly divided into three parts: (i) X-ray source, (ii) goniometer for mounting the sample and (iii) the detector in the reflection geometry. When the sample stage moves in θ, the detector is moved to a value of 2θ to collect the data (this is called θ–2θ geometry) [28]. In this thesis work, we have used grazing incident XRD (GIXRD) with Cu K_α source (λ= 1.54 Å).

2.5.6 Rutherford backscattering spectrometry (RBS)

To investigate structural and compositional details of a material, Rutherford backscattering spectrometry (RBS) is an important analytical technique which deals with the analysis of high energy backscattered ions. It is based on classical scattering in a central-force field. In 1911, Ernst Rutherford first found that when a beam of energetic α particles was incident on the thin gold foil, fraction of them were backscattered. Then he concluded that an atom comprises of heavy positive mass called nucleus [29]. This principle was developed into a popular spectroscopic technique and various aspects of this technique have been described in Ref. [30].

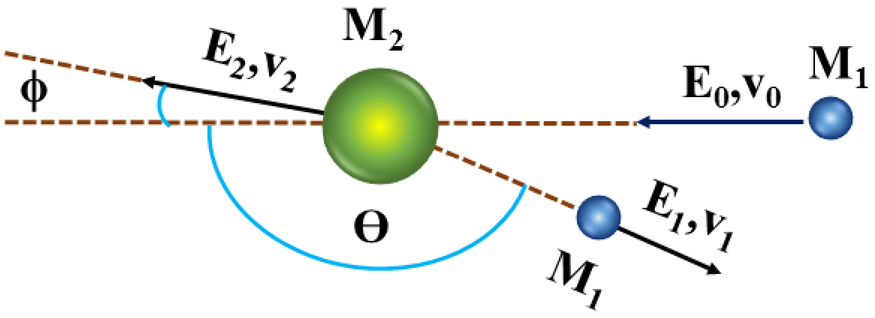

Figure 2.26: *A schematic diagram of the interaction of two particles [30].*

When a projectile of mass M_1, velocity v_0 and energy E_0 (= ½ $M_1v_0^2$) collides elastically with stationary target atom of mass M_2 where $M_2>>M_1$, energy will be transferred from projectile to target atom. After the collision v_1 and v_2 be the velocities and E_1= ½ $M_1v_1^2$, $E_2=1/2\ M_2v_2^2$ be the energies of the projectile and target atom respectively. Schematic diagram of this two particle system has been represented in Figure 2.26. E_0 is much larger than the target atom binding energy (chemical bonds are of the order of 10 eV) [30] but less than nuclear reaction and resonance energy. Kinematic factor is defined as the ratio of the projectile energy after the collision to the energy before collision and can be expressed as

$$K_{M2} = E_1/E_0 = [\{M_1\mathrm{Cos}\theta + (M_2^2 - M_1^2\mathrm{Sin}^2\theta)^{1/2}\} / \{M_1+M_2\}]^2 \qquad (2.13)$$

where, E_1 is the projectile energy after collision, θ is the backscattered angle.

Thickness analysis

A beam of light positive ions such as He ions or protons incident upon a target material in the real time experiment. Differential scattering cross section is defined as the number of backscattered ions from the target that are directed towards a certain solid angle dΩ and is given by the following equation

$$\frac{d\sigma}{d\Omega} = \left(\frac{1}{Nt}\right)\frac{dQ/d\Omega}{Q} \qquad (2.14)$$

where, N is the volume density of atoms in the target, t is the thickness and Nt is the number of target atoms per unit area (areal density). σ is the *average differential scattering cross section* which can be defined as

$$\sigma = \frac{1}{\Omega}\int_{\Omega}\frac{d\sigma}{d\Omega}d\Omega \tag{2.15}$$

Total number of detected particles A can be written as

$$A = \sigma\Omega.\ Q.\ Nt \tag{2.16}$$

(number of detected particles) = σΩ. (total no of incident particles) . (areal density)

From the above equation, areal density (Nt) can be determined. Differential scattering cross section for an elastic collision between two atoms is given by

$$\frac{d\sigma}{d\Omega} = \left[\frac{Z_1Z_2e^2}{4E_0}\right]\frac{4}{Sin^4\theta}\frac{\left[\left[1-\left(\frac{M_1}{M_2}Sin\theta\right)^2\right]^{1/2}+Cos\theta\right]^2}{\left[1-\left(\frac{M_1}{M_2}Sin\theta\right)^2\right]^{1/2}} \tag{2.17}$$

where, Z_1 and Z_2 are the atomic number of the projectile and target atom respectively, e is the electronic charge. Equation 2.17 is valid only when $M_1 << M_2$.

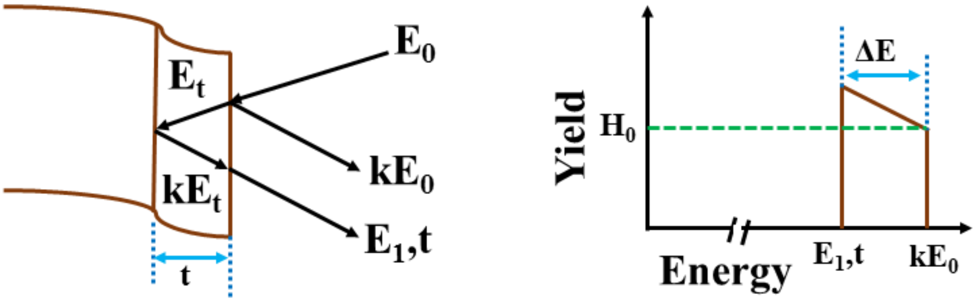

Figure 2.27: *A schematic diagram of the RBS spectrum for a thin film [30].*

Figure 2.27 describes the schematic representation of the formation of RBS spectrum from thin film. So one can find the thickness (t) in terms of E_0 and E_1 by assuming constant value of dE/dx along the inward and outward paths. When a beam of charged particles is incident on the target normally, the number of counts H_i in channel i depends on two factors; (i) the thickness of the slab and (ii) the number of scattering centers in that slab which ca be written as

$$H_i = \sigma(E_i)\Omega QNdt \tag{2.18}$$

So, the total number of detected backscattered particle is denoted by adding up all H_i values and total thickness of the thin film is given by $t = i \times dt$. In Figure 2.26, 'E_0', 'kE_0' indicate the incident kinetic energy and backscattered energy of the probe from the top surface of the film. 'Et', 'kEt' denote the incident energy and backscattered energy of the probe atom at a layer which is situated inside of the thin film at a distance t from the top surface. '$E_{1,t}$' is the energy of the probe atom during exit from the thin film followed by the backscattering from a layer which is at a distance t inside from the top surface.

Instrumentation

RBS instrumentation can be broadly divided into three parts; (i) accelerator, (ii) target chamber and (iii) energy analyzer. In accelerator, first H or He ions are generated through ionization process. Then, these ions are accelerated up to an energy of 1-3 MeV. When the ion beam passes through the mass analyzer, required isotope is selected. Then the collimated beam with selected isotope falls on the sample (target chamber). In the target chamber, a surface barrier detector (SBD) is used to detect backscattered projectiles kept at a very high angle (≥160°). The sample is connected with the current integrator to get the total number of incident ions (total charge accumulated on the target). The energy related output from SBD goes through the energy analyzer. It consists of preamplifier, amplifier, analog to digital converter and multi-channel analyzer (MCA). Finally, the output of MCA can be fed to the computer, where the resulting RBS spectrum can be stored for further analysis. For this thesis work, RBS measurements and resonance RBS (RRBS) for MoO_x systems were carried out using 3.045 MeV He particles from 1.7 MV Tandetron Accelerator (HVEE, The Netherlands) at Indira Gandhi Centre for Atomic Research, Kalpakkam, India. All the experiments of MoO_3 on Si substrates were done using the beam of helium (He^+) ion having energy 3.045 MeV. Based on the experimental observations, compositional depth profile analysis and the thickness of NSs and thin films were investigated using SIMNRA software package [31,32].

2.5.7 X-ray photoelectron spectroscopy (XPS)

X-ray photoelectron spectroscopy (XPS), a surface sensitive technique is based on photoelectric effect, where electrons are emitted from the sample via interaction with electromagnetic radiation [33]. In 1905, photoelectric effect was explained by Albert Einstein through a hypothesis that light energy is carried in discrete quantized energy packets [34]. XPS is used to measure the elemental composition of the surface, empirical formula, chemical or electronic state of each element on the surface, uniformity of elemental composition as a function of ion beam etching (depth profiling) and elements that contaminate a surface. In 1981 Siegbahn won the Nobel Prize for his contribution to the field of XPS [35]. In this thesis work we have used XPS to obtain the oxidation states and atomic composition of Molybdenum oxide at different substrate temperatures.

In XPS, when X-ray photons strike a surface, in vacuum, electrons in core level get excited and produce photoelectrons. A photoelectron will be emitted only when the photon energy is larger than the binding energy of the electron. These photoelectrons are energy analyzed and provide information on density of state (DOS) of the sample. The binding energy (E_B) of the emitted electrons can be evaluated by following equation which is coming from energy conservation

$$E_B = E_{photon} - (E_{kinetic} + \Phi) \qquad (2.19)$$

where, E_{photon} is the X-ray photon energy; $E_{kinetic}$, the kinetic energy of the emitted electron is measured by an electron analyzer; Φ the work function is dependent on both the material and spectrometer. XPS spectrum is recorded by counting ejected photo electrons as a function of binding energy. E_B can be obtained by measuring $E_{kinetic}$, as E_{photon} and work function of the spectrometer are known quantities. Figure 2.28 shows the schematic representation of core level photoelectron emission process.

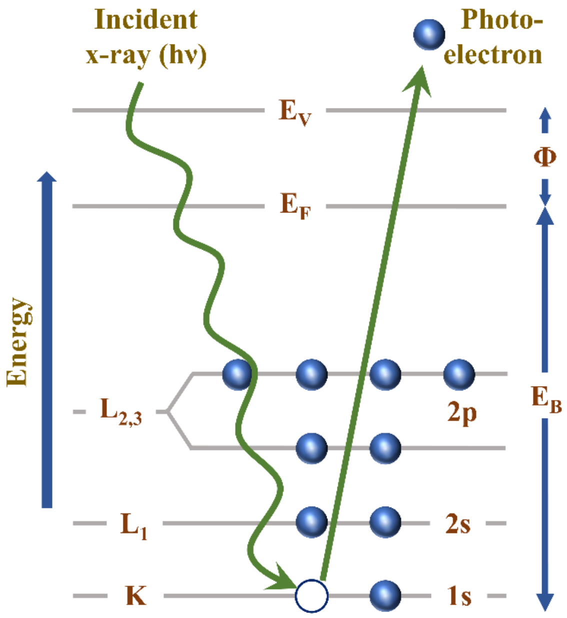

Figure 2.28: *Schematic illustration of core energy level during photoelectron emission process.*

XPS instrumentation consists of an X-ray source, a sample holder, an electrostatic lens system, an electron energy analyzer, an electron detector and a computer system for data collection and processing [36,37]. The X-rays are generated by bombarding a metallic anode with high energy electrons (10-15 KeV) and are then focused onto the sample by using of a monochromator. An electrostatic lens system collects a portion of these emitted electrons and focuses them into an electron energy analyzer called a concentric hemispherical analyzer (CHA). Only electrons in a narrow energy region, referred to as the pass energy, are able to travel the distance of the analyzer and reach the detector.

In this thesis work, i*n-situ* XPS measurements were performed on an Omicron XPS instrument with monochromatic Al Kα X-ray source (hν = 1486.6 eV) (including an Omicron SPHERA energy analyzer with 7 Channeltron electron multipliers detection) at Diamond Light Source (DLS), Didcot, UK. A dual tungsten filament e-beam heater beneath the substrate holder has been used to anneal the specimen and the temperature was monitored via an infrared pyrometer [38]. During the XPS measurements, the chamber base pressure was 8.1×10^{-10} mbar and raised to a maximum of 5.7×10^{-9} mbar during *in-situ* heating experiment.

2.5.8 UV-Vis-NIR spectrophotometer

Reflectance is the amount of incident light that is reflected by the surface. In this thesis work optical reflectance measurements of the as grown samples have been performed using a Shimadzu UV 3101PC ultra-violet-visible-near infrared (UV-Vis-NIR) spectrophotometer equipped with a specular reflectance measurement accessory. The spectral range that can be studied with this instrument is 200 to 3200 nm. However, in the present thesis work, most of the spectra (in reflectance mode) were collected over a wavelength range of 250–850 nm at room temperature. The reflectance mode works in a specular reflection geometry arrangement with 45^0 incidence angle of light.

2.5.9 Kelvin probe force microscopy (KPFM)

Kelvin probe force microscopy (KPFM) is a technique which enables nanometer scale imaging and the potential difference between the tip and the sample [39]. This technique is based on atomic force microscope (AFM) technique in non-contact mode. When an AFM tip is brought close to the sample surface, due to the difference in their Fermi energy levels, an electric force will be acted between tip and the sample surface. To generate oscillating electrostatic force between tip and sample surface when an AC voltage is applied to the tip, an apparent contact potential difference V_{CPD} will form. To nullify the generated electrostatic force, an external DC voltage V_{DC} with the same value of V_{CPD} but in opposite direction is required. So the mapping of this nullifying V_{DC} with the lateral position coordinate composes work function mapping image of the sample surface called KPFM image. So the work function of the sample surface can be calculated by the following equation [38,40]

$$V_{DC} = V_{CPD} = (\Phi_{tip} - \Phi_{sample})/q \tag{2.20}$$

Where, Φ_{tip} and Φ_{sample} are work function of the tip and sample respectively. The work function of the tip has been calibrated with respect to standard HOPG sample and comes out to be $\Phi_{tip} = 5.2$ eV. So Φ_{sample} will be

$$\Phi_{sample} = \Phi_{tip} - qV_{CPD} = 5.2 \text{ eV} - qV_{CPD} \tag{2.21}$$

So, higher the value of V_{CPD}, lower the work function of the sample.

In this thesis work, KPFM of the samples was examined by *ex-situ* atomic force microscopy (AFM) (MFP-3D, Asylum Research USA) in lift mode, with a lift height of 60 nm, using a conductive Ir/Pt tip (AC240TM, Electric-Lever, Olympus) having ≈ 30 nm radius of curvature, ≈ 2 $N\text{-}m^{-1}$ stiffness, and a resonance frequency of ≈ 70 kHz. In the two pass MFP-3D technique, first pass is used to determine the topography of the surface which is exactly like a standard tapping mode scan line, whereas the second one is used to find the surface potential.

2.6 Applications

Molybdenum oxide is found to be a potential candidate towards field emission (FE). In this section, the working principle and instrumentation of the technique utilized for the above purpose will be discussed.

2.6.1 Field emission (FE)

Field emission is the emission of electrons from the surface of a material induced by external energy/field to the electrons in the material. Depending upon the type of external energy source, the process can be categorized as photoemission, thermionic emission, secondary electron emission and field emission (FE) etc. where light, heat (therm), energetic electrons and electric field are applying as external energy sources respectively. It is much known to all that the minimum energy, required to remove an electron from the Fermi level to a point an infinite distance away from the surface is known as the work function (Φ) of that surface [41]. In this thesis, we have focused on the FE of different molybdenum oxide nanostructures (NSs). A relevant electron emission mechanism theory will be discussed in brief, where emission is taking place solely under the influence of an electric field.

Fowler-Nordheim Theory:

In 1897, Wood [42] first observed that, electron field emission (EFE) is based on the quantum mechanical tunneling mechanism. But this was first explained correctly by R. Fowler and L. Nordheim in 1928 [43]. In Fowler-Nordheim (FN) Model [44], they described the electron emission from metals in vacuum under high electric field on the basis of the following assumptions:

(i) The metal is at 0 K.
(ii) The free electron approximation applies inside the metal.
(iii) The surface is treated to be smooth (compared to width of the potential barrier, small roughness was neglected) and
(iv) The effective potential barrier close to the surface in the vacuum region is a combination of image charge potential and potential due to external electric field.

In the case of metal, electrons are assumed to have a constant effective potential energy $-W_a$. After the application of electric field (E), the potential barrier is described by [45]:

$$V(x) = -W_a \qquad \text{where } x < 0 \tag{2.22}$$

$$= -e^2/4x - eFx \qquad \text{where } x > 0 \tag{2.23}$$

Generally the FE behavior (J-E plot) can be analyzed theoretically by FN equation [43]

$$J = (aB^2E^2/\Phi)\exp(-b\Phi^{3/2}/BE) \tag{2.24}$$

or,

$$\ln(J/E^2) = \ln(aB^2/\Phi) - (b\Phi^{3/2}/B) \times (1/E) \tag{2.25}$$

where, a and b are constants with $a = 1.54 \times 10^{-6}$ A-eV/V^2 and $b = 6.83 \times 10^3$ eV$^{-3/2}$ –V μm^{-1}, B is the field enhancement factor (FEF), Φ is the work function of the emitter, J is the FE current density (μA/cm^2), E is the applied electric field (V/μ) [46]. FEF (B) defined as the ratio of local to applied electric field and it also depends on geometry of the emitter (such as dimension and shape, aspect ratio etc.), emitter's surroundings and also distance of the counter electrode. By plotting ln (J/E^2) versus $(1/E)$ (called F-N plot), from the slope $(b\Phi^{3/2}/B)$, we can calculate B, i.e. field enhancement factor by knowing the constant b and work function value.

$$B = - b\Phi^{3/2}/ \text{slope} \tag{2.26}$$

So, smaller slope value corresponds to higher FEF (B) value [46].

In this thesis, field emission (FE) performances of the as-grown molybdenum oxide samples (called as emitters) were performed in a simple diode configuration in a custom made high vacuum ($\approx 2.3 \times 10^{-7}$ mbar) chamber by Excel Instruments, FE System-150 and current vs. voltage (I-V) data was recorded using Keithley, 2410 as voltage source meter. The as-grown samples, fixed to the bottom plate with a copper tape were used as the cathodes and a copper plate having ≈ 2.5 mm tip diameter was served as the anode. For the FE measurements, electrodes separation was kept at ≈ 40 µm/ ≈ 50 µm [46].

2.7 References

[1] I. V. Markov, Crystal Growth for Beginners - Fundamentals of Nucleation, Crystal Growth and Epitaxy (World Scienti¯c, Singapore, 1995), doi.org: 10.1142/2145.

[2] E. Bauer, Z. Kristallogr. 1958, 110, 372.

[3] E. Bauer and J. H. van der Merwe, Phys. Rev., B 1986, 33, 3657.

[4] F. C. Frank and J. H. van der Merwe, Proc. Roy. Soc. London, 1949, A198, 205.

[5] M. Volmer and A. Weber, Z. Phys. Chem. 1926, 119, 277.

[6] I. N. Stranski and Von L. Krastanov, Akad. Wiss. Lit. Mainz Math -Natur. Kl. IIb 1939, 146, 797.

[7] K. Oura, V. G. Lifshits, A. A. Saranin, A. V. Zotov and M. Katayama, Surface Science - An Introduction, Springer-Verlag, (2003).

[8] R. Pandit, M. Schick and M. Wortis, Phys. Rev. B 1982, 26, 5112.

[9] C. Ebner, C. Rottman and M. Wortis, Phys. Rev. B 1983, 28, 4186.

[10] S. J. Kennedy and J. S. Walker, Phys. Rev. B 1984, 30, 1498.

[11] M. H. Grabow and G. H. Gilmer, Surf. Sci. 1988, 194, 333.

[12] D. K. Goswami, B. Satpati, P. V. Satyam, and B. N. Dev, Curr. Sci. 2003, 84, 902.

[13] J. R. Arthur, Surf. Sci. 2002, 500, 189.

[14] G. Binnig, H. Rohrer, Ch. Gerber, E. Weibel. Phys. Rev. Lett. 1983, 50, 120.

[15] G S May and C J Spanos, Fundamentals of Semiconductor Manufacturing and Process Control (John Wiley & Sons, Inc., 2006, ISBN: 10.1002/0471790281).

[16] I L Maissel and R Glang, Handbook of Thin Film Technology (McGraw-Hill Book Co., 1970, ISBN: 007-0-39742-2).

[17] M Ohring, Materials Science of Thin Films. Deposition and Structure (Elsevier, Academic Press, 2002, ISBN: 978-0-12-524975-1).

[18] H O Pierson, Handbook of Chemical Vapor Deposition Principles, Technology and Applications (Elsevier, William Andrew, 1999, ISBN: 978-0-8155-1300-1)

[19] J. E. Mahan, K. M. Geib, G. Y. Robinson and Robert G. Long, J. Vac. Sci. Technol. A 1990, 8, 3692.

[20] A. Bhukta, P. Guha, A. Ghosh, P. Maiti, P. V. Satyam Appl. Phys. A 2016, 122, 356.

[21] R. Wiesendanger, Scanning Probe Microscopy and Spectroscopy: Methods and applications, (Cambridge University Press, 1994).

[22] R F Egerton, Physical Principles of Electron Microscopy, An Introduction to TEM, SEM, and AEM (Springer, 2005, ISBN-13: 978-0387-25800-0).

[23] D B Williams and C B Carter, Transmission Electron Microscopy: A Textbook for Materials Science (Springer, 2009, ISBN: 978-0-387-76500-6).

[24] J C H Spence, High-resolution Electron Microscopy (Oxford Science Publications, 2013, ISBN: 978-0-199-66863-2).

[25] B Fultz and J Howe, Transmission Electron Microscopy and Diffractometry of Materials (Springer, 2005, ISBN: 978-3-642-29761-8).

[26] M. Knoll and E Ruska, Z. Physik. 1932, 78, 318.

[27] A. L. Patterson, Phys. Rev. 1939,56, 978.

[28] C Suryanarayana and M G Norton, X-Ray Diffraction: A Practical Approach (Springer, 1998, ISBN: 978-1-4899-0148-4).

[29] E. Rutherford, Phil. Mag. 1911, 21, 669.

[30] W. K. Chu, J. W. Mayer, M. A. Nicolet, Backscattering spectrometry, Academic Press, New York, (1978).

[31] W. K. Chu, J. W. Mayer, M. A. Nicolet, T. M. Buck, G. Amesel and F. Eisen Thin Solid Films 1973, 17,1.

[32] M. Mayer, Nucl. Instr. Meth. Phys. Res. B 2002, 194, 177.

[33]] J F Watts and J Wolstenholme, An Introduction to Surface Analysis by XPS and AES (Wiley & Sons, 2005, ISBN: 978-0-470-86793-8).

[34] A Einstein, Ann. Physik 1905, 322, 132.

[35] K. Siegbahn, “Electron Spectroscopy for Atoms, Molecules and Con-densed Matter”, Nobel Lecture, December 8, 1981.

[36] J. C. Riviere, Practical Surface Analysis: Auger and X-ray Photoelec- tron Spectroscopy, 2nd edn (New York: Wiley (1990).

[37] J. C. Riviere, S. Myhra, Handbook of Surface and Interface Analysis: Methods for Problem-Solving (New York: Marcel Dekker (1998)).

[38] P. Maiti, P. Guha, H. Hussain, R. Singh, C. Nicklin and P. V. Satyam, *Surf. Sci.* 2019, 682, 64.

[39] L. Nony. Principles of Kelvin Probe Force Microscopy and applications. DEA. Laurent NONY, 1st German-French Summer School on noncontact -AFM Porquerolles. 2013: France.

[40] P. Guha, A. Ghosh, R. Thapa, E. M. Kumar, S. Kirishwaran, R. Singh, and P. V. Satyam, *Nanotechnology* 2017, 28, 415602.

[41] J I Gersten and F W Smith, The Physics and Chemistry of Materials (Wiley, 2001, ISBN: 978-0-471-05794-9).

[42] R W Wood, *Phys. Rev. (Series I)* 1897, 5, 1.

[43] R H Fowler and L Nordheim, *Proc. R. Soc. London, Ser A* 1928, 119, 173.

[44] A G J V Oostrom, Validity of the Fowler-Nordheim Model for Field Electron Emission (Netherland Philips Research Laboratories, 1966).

[45] E L Murphy and R H Good, *Phys. Rev.* 1956, 102, 1464.

[46] P. Maiti, P. Guha, R. Singh, J. K .Dash and P. V. Satyam, *Appl. Surf. Sci.* 2019, 476, 691.

Chapter 3

Growth and Compositional Analysis of Molybdenum oxide nanostructures

3.1 Introduction

The molybdenum oxide nanostructures (NSs) and thin films were grown by molecular beam epitaxy (MBE) and physical vapor deposition (PVD) techniques. In this chapter, we briefly discuss on the growth of the NSs and then report on the composition and crystal structure of molybdenum oxide NSs. The emphasis in the present chapter is to determine oxygen & molybdenum concentration, O/Mo atomic ratio, depth profiling using Rutherford backscattering spectrometry (RBS) both in resonant (for Oxygen concentration) and non-resonant RBS. The MoO_x NSs were grown by varying the substrate temperature, thickness of the film and vacuum level of the growth chamber. With increasing the substrate temperature from 350 °C to 550 °C, nanoribbons (NRs) of β-MoO_3 transform to MoO_2 nanoparticles (NPs). Phase changes from MoO_3 to MoO_{3-x} to MoO_2 when we annealed the thin film deposited sample at ≈600 °C for 30 minutes in air, low vacuum (LV) and ultra-high vacuum (UHV) conditions. The results obtained by ion scattering method have been complemented by using electron microscopy (SEM or/and TEM) methods and X-ray methods (XRD and XPS) [1].

For more than two decades, nanostructures of transition metal oxides (for example, WO_3, MnO_2, SnO_2, TiO_2, MoO_3, etc.) [2] have been studied with great zeal due to their interesting properties relating to gas sensors [3-6], field emission [7], solar cell [8],

---

The work presented in this chapter will be published as P Maiti et al. (*To be submitted*, 2019) photochromic electrochromic devices [9,10], Li-ion batteries [11,12], 2D field effect transistors [13], organic light emitting diodes [14], hole transport material [15,16] and many others due to its special crystalline structure and polyvalency. However, to synthesize well-ordered and oriented 1-D or 2-D oxide nanostructures (e.g. nanorods, nanobelts, nanotubes, nanoribbons and nanoplates) by simple growth methods has proven to be a great challenge [13,17]. Among the many oxide materials, molybdenum oxide is arguably the most fascinating and versatile due to its unique physical and chemical properties [18]. It can exist in many different phases (e,g, MoO_3, Mo_8O_{23}, Mo_9O_{26}, Mo_4O_{11}, and MoO_2) depending on the oxidation state of Mo (+6, +5, +4, +3 and +2). This allows for band gap engineering of these materials: from the wide band gap of MoO_3 (≈ 3.2 eV) [19] to the more conducting MoO_{3-x} [20] and then to semi-metallic MoO_2 (≈ 2.6 eV) [18] and finally to the metallic system (in the form of metal – Mo). The most studied phase in MoO_3 is α-MoO_3. The main aim of this chapter is to grow and characteristics study of defect free, mixed phase free metastable molybdenum trioxide (β-MoO_3), MoO_{3-x} and MoO_2 and then the phase transition from β-MoO_3 to MoO_2 by simple thermal reduction process in UHV condition by MBE technique.

In MeV ion scattering method, energetic He ions (either He^+ or He^{++}) of typically 1.0 – 4.0 MeV energy that are generated from an ion accelerator are used to determine elemental compositions. The ion scattering experiments use various energy regimes of projectile: keV – MeV ions [21–25]. The low energy regime, in which a maximum of 20 keV energetic ions are used, is extremely surface sensitive and suitable to study top one monolayer ($\cong 10^{15}$ atoms cm^{-2}) [26,27]. Medium energy ion scattering is usually from 20 – 250 keV and is used to carry out structural investigation of top few nanometers of thin film nanostructures [28]. For these energy regimes, usually one needs UHV condition in the scattering chamber and hence a general non-destructive testing becomes rather difficult. However, using higher energies, typically 1.0 – 4.0 MeV ions, the scattering chamber afford to have high vacuum conditions instead of UHV condition. MeV ion scattering methods have been in use for many decades and several review articles have been devoted for this purposes [21–25]. Chu et al., had reviewed the principles and applications of various energetic ion beam methods to determine the atomic mass distributions with depth resolution of less than a *nm* of bulk materials and thin film structures in a non-destructive manner using MeV ion scattering method, namely RBS both in random and channeling conditions [21,22]. In the book of Terry L. Alford, Leonard C. Feldman, and James W. Mayer, various experimental methods for surface and interface have been presented with emphasis on ion scattering methods [23]. Though the RBS experiments are very useful for determining the atomic masses (or composition) at nanometer (*nm*) depth resolution, its sensitivity is poor for low atomic number target atoms, in particular when these are surrounded by high atomic number matrix. However, specific resonant reactions are available to detect low Z elements as well. Further details on the use of 3.045 MeV alpha particle for detection of oxygen would be discussed in this article [29].

The cross-section for RBS yield is directly proportional to $(Z_1Z_2)^2$ implying that for a fixed Z_1, the sensitivity is higher for higher Z_2 (target atom). This make it difficult to detect the low Z target atoms, in particular when the matrix atomic mass (or number) is large compared to the one that is being studied. A careful study on the value of cross-sections for alpha particles as projectiles yielded that there are some specific energies of alpha particles for which the cross-sections found to be quite large [30]. Blanpain et al. reported in detail on the use of the 3.045 MeV oxygen resonance for ^{4}He backscattering near surface analysis of oxygen-containing high atomic number target compounds in which the authors found that backscattering cross-section near the resonance energy (3.045 MeV alpha particles following nuclear reaction, $^{16}O\ (\alpha\ ,\alpha)\ ^{16}O$) is as much as 25 times greater than the Rutherford cross-section [29]. The resonance width found to be about 11.0 keV. This combination of higher cross-section and lower energy width found to be very useful in determining the oxygen concentration in many important thin film and bulk structures. As an example the authors determined the composition of thermally grown SiO_x layer on silicon [29]. Li et al [31] studied the kinetics of nucleation and growth of the Cu_2O phase in CuO matrix with the help of oxygen diffusion induced phenomena in copper oxide thin films by a combination of oxygen resonance technique (using MeV alpha particles) and TEM. Zoller et al., reported systematic study of composition analysis of nanometer oxide films by ion-beam channeling and elastic scattering using nuclear resonances using MeV ions for technologically relevant high-k dielectric materials, such as, HfO_2 and HfAlO [32]. Recently Udaya Bhanu et al., reported resonant scattering measurements on the elctron beam evaporated Mg doped ZrO_2 (Mg:ZrO_2) high-k thin films on p-type Si(100) substrate and their metal oxide semiconductor (MOS) capacitors [33] They have shown the oxygen variation monitored at 3.05 MeV near the surface of the CuO sample as a function of time at 550 °C. Significant oxygen loss from CuO starts in the presence of carbon at 250 °C in the samples with C/CuO/Si and CuO/C/Si structures. CO_2 is the reaction product. The combination of carbon and oxygen atoms to form CO_2 at the carbon/ copper oxide interface enhances the oxygen loss rate from CuO thin films. Cole et al determined the thickness of ultrathin SiO_2 layer by many analytical techniques like XPS, secondary ion mass spectrometry (SIMS), RBS, TEM and ellipsometry [34]. They reported that high resolution cross section TEM is one of the most effective technique to measure the thickness because there is no need of density assumption. XPS offers precise measurement for < 3 nm films due to exponential decay function that describes the sampling depth. SIMS has been used for thick films > 10 nm but not for thin films because of atomic mixing effect. RBS is used to measure oxide thickness over a wide thickness range [34]. Structure and composition of passive titanium oxide film composed of an amorphous TiO_2 outer layer (10-20 nm), an intermediate TiOx layer and the metallic substrate analyzed by RBS, XPS and x-ray diffraction technique was studied by Pouilleau et al [35]. In RBS from the ion energy loss, one can get the depth information. Film thickness can be calculated if material density is known. In the case of the crystalline layers it is possible to detect interstitials and other kind of lattice disorder with the ion channeling technique [36]. There was also report on the RBS study of molybdenum oxide film. Mohamed et al has shown in their paper, RBS spectra for films deposited at different oxygen partial pressures and reported O/Mo atomic ratio increases almost linearly with increasing oxygen partial pressure. Higher than 0.16 Pa oxygen partial pressure there is slightly more oxygen than expected for MoO_3 and this is due to both chemically bonded and physically trapped oxygen [37].

In the present work we employed the resonant RBS technique for evaluation of the properties of molybdenum oxide nanostructures using 3.045 MeV alpha particles. The average thickness, depth information from the ion energy loss, oxygen, molybdenum concentration, and O/Mo atomic ratio from the RBS experiments and then using the simulation by SIMNRA package [38] have been studied. Composition of the nanostructures has also been confirmed by XPS, XRD and TEM techniques.

3.2 Experimental Details

MoO_3 NSs were grown by MBE (M/S Omicron GmbH) system consisting of high temperature effusion cell with cooling shroud, and rotary shutter. Pyrolythic graphite (PG) crucible was used to evaporate the MoO_3 powder. For the source material a commercially available molybdenum trioxide powder (α-MoO_3) (99.995% purity from Alfa-aeser) and cleaned Si(100) (*n-type*, phosphorus doped, resistivity ≈ 1-20 Ω–cm) were used as substrate material in a two-step process of cleaning the silicon substrate (so as to have a reconstructed surface and that inhibits the further growth of native oxide layer on the Si substrate) under UHV conditions. First, the Si substrates were degassed at 600 °C by direct heating (DH) for 12

– 15 hours, second to remove the native oxide layer, they were repeatedly flashed at 1200 °C for few minutes in DH mode. Reconstruction of the surface is confirmed by in-situ reflection high energy electron diffraction (RHEED) prior to MoO_3 deposition. The MBE chamber base pressure was $\approx 2.3 \times 10^{-10}$ mbar before the deposition and it rose to $\approx 1.8 \times 10^{-9}$ mbar during degassing and flashing. MoO_3 source temperature was kept at 670 °C to have deposition rate of $\approx$ 1 Å/min and a 10 nm MoO_3 was deposited on atomically cleaned Si(100) substrate at different substrate temperatures. During deposition chamber base pressure raised to $\approx 1.1 \times 10^{-8}$ mbar from $\approx 2.3 \times 10^{-10}$ mbar. Type K thermocouple, optical pyrometer were used to measure the substrate temperatures. To observe the thickness dependent effect, we kept the substrate temperature at 350 °C and deposited different thickness (15nm, 20nm and 30nm) of MoO_3 films on Si substrates. For vacuum dependent study, 250 nm MoO_3 thin films were grown at room temperature (RT) with a deposition rate $\approx$ 1 Å/sec by PVD system with base pressure of 1.8×10^{-6} mbar. For that Si(100) substrate with $\approx$ 2-3 nm thick native oxide on top and same MoO_3 powder were used as substrate and source material. After deposition, the samples were annealed at 600 °C in atmosphere, LV and UHV conditions to notice the vacuum dependency on molybdenum oxide thin films.

The post growth characterizations, such as, elemental composition, structure, surface morphology, shape, and size of as grown nanostructures were performed by Field Emission Gun based Scanning Electron Microscopy (FEGSEM) with 20 keV electrons using Neon 40 cross-beam system (M/S Carl Zeiss GmbH) and Transmission Electron Microscopy (TEM) (JEOL JEM-2010) with 200 keV electrons at Institute of Physics, Bhubaneswar, Odisha, India. The TEM machine has ultra-high-resolution pole piece with a point to point resolution of 0.19 nm. Preparing for planer TEM, a 3 mm diameter disc was cut from the as-grown sample by ultrasonic disc cutter. Then such a disc was lapped (SBT, LPS model 900) using different sizes of emery papers to get a final thickness of 100 µm. Using a dimple grinder (DG, GATAN, model 656) a dimple was created at the center of the sample while maintaining 100 µm thickness at the periphery for handling purpose. Now electron transparency was achieved through 3.0 KV Ar ion milling (PIPS, model 691). RBS measurements and Resonance RBS (RRBS) for MoO_x systems were carried out using 3.045 MeV He particles from 1.7 MV Tandetron Accelerator (HVEE, The Netherlands) at Indira Gandhi Centre for Atomic Research, Kalpakkam, India. Based on the experimental observations, compositional depth profile analysis and the thickness of NSs and thin films were investigated using SIMNRA software package [21,38,39] developed by Mayer [40]. This program can incorporate the resonance cross-sections (NRA or RRBS) as well. XPS measurements were carried out to determine the oxidation state in MoO_x system to complement the Resonant RBS measurements

3.3 Results and discussion

3.3.1 Temperature dependent effect on molybdenum oxide NSs

After deposition of 10 nm MoO_3 on cleaned Si(100) substrate at 350 °C substrate temperature, we have seen from FEGSEM image as shown in Figure 3.1 (a) that randomly oriented nanoribbons (NRs) structures are grown on the substrate. The average value of length, width and aspect ratio (length/width) of the NRs are calculated from different frames of FEGSEM images followed by and fitting with lognormal curve which come out to be 86±2 nm, 17.1±0.9 nm and 5.2±0.1 respectively. To know the growth direction of NRs, planer TEM and selected area electron diffraction (SAED) were performed (shown in Figure 3.1(c)). In SAED pattern all the circular rings correspond to the monoclinic β-phase of MoO_3.

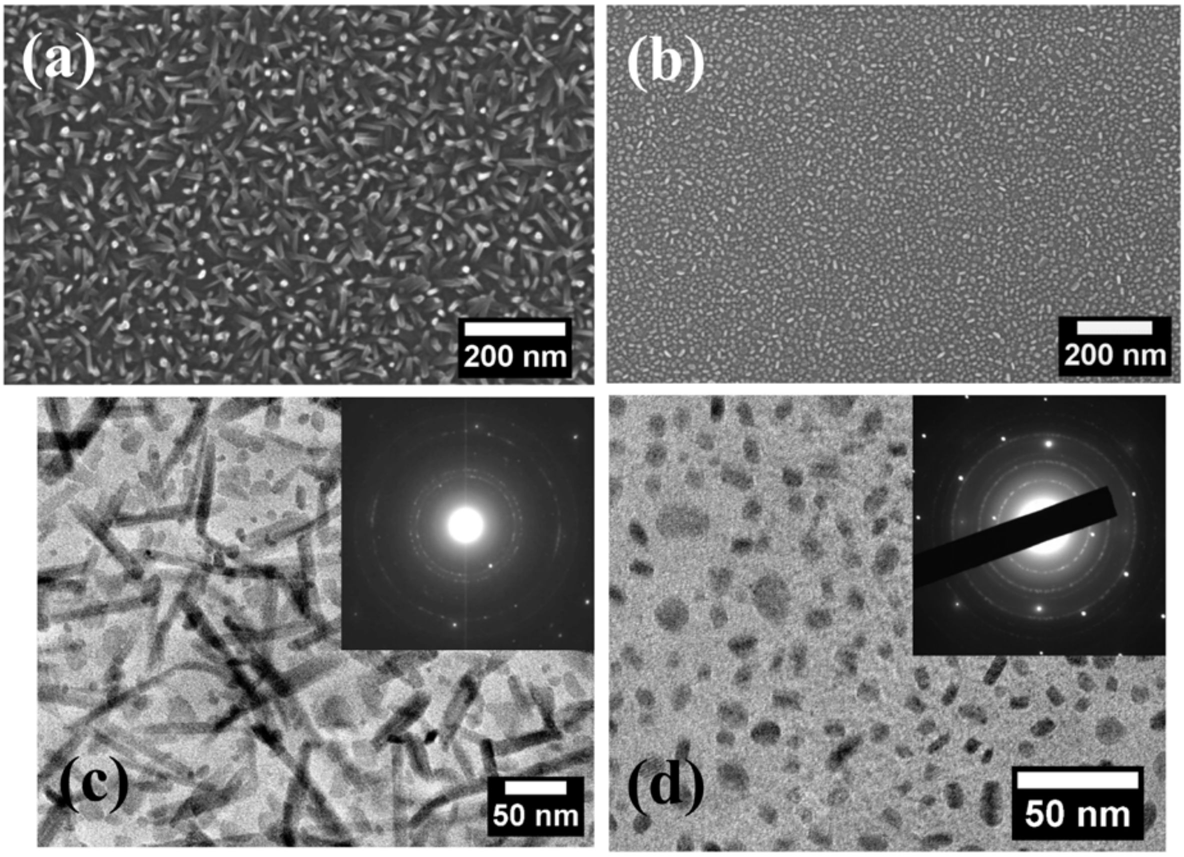

Figure 3.1: *High magnification SEM image for 10 nm* MoO_3 *deposited on cleaned Si(100) substrate at substrate temperature of (a)350 °C and (b)550 °C and their corresponding planer TEM images have been shown in (c) and (d) respectively. Insets in (c) and (d) represent the SAED pattern of the TEM images.*

When the substrate temperature is increased from 350 °C to 400 °C the morphology changes from NRs to nanoparticles (NPs). From SEM image we have measured the size of the NPs which has come out to be ≈ 14.8 ± 0.3 nm. All the samples having substrate temperature ranging from 400 °C to 600 °C show same morphology. In Figure 3.1(b) we have depicted the SEM image of 10 nm MoO_3 deposited on cleaned Si(100) substrate at 550 °C substrate temperature and their corresponding planer TEM image and SAED pattern have been shown in Figure 3.1(d). The circular rings in the SAED pattern represent monoclinic MoO_2 structure [41].

To gain knowledge about the chemical composition of nanostructures, in-situ X-ray photoelectron spectroscopy (XPS) was performed [detailed analysis using microscopy and spectroscopy has been dealt in Chapter 4]. In this chapter, emphasis is on the resonant RBS analysis and to freeze certain parameters to make RBS more effective, results from XRD, SEM/TEM and XPS are used. In XPS experiment, we took the NRs sample i.e 10 nm MoO_3 deposited at 350 °C on cleaned Si(100) substrate, done XPS measurements were carried out on an Omicron XPS instrument with monochromatic Al Kα X-ray source (hν = 1486.6 eV) (including an Omicron SPHERA energy analyzer with 7 Channeltron electron multipliers detection) at room temperature followed by heating to 550 °C for 30 mins. After cooling down to room temperature we performed the XPS measurements again. The Mo 3d core level spectrum at 350 °C corresponds to Mo^{6+} $3d_{5/2}$, Mo^{6+} $3d_{3/2}$, Mo^{5+} $3d_{5/2}$, Mo^{5+} $3d_{3/2}$ but the major contribution (92%) came from Mo^{6+}. O 1s core level spectrum corresponds to the lattice oxygen (O_L) of MoO_3 and Oxygen deficiency (O_V) in MoO_3 matrix which is due to Mo^{5+}. So the NRs maintain the stoichiometry of MoO_3. After heating that sample at 550 °C for 30 minutes and cooling down to room temperature, Mo 3d core level spectrum corresponds to Mo^0, Mo^{4+}, Mo^{5+} and Mo^{6+} with larger contribution (59.5%) of Mo^{4+}. O 1s spectrum corresponds to lattice oxygen (O_L) of MoO_2, O_V and the oxidation state of Si. So the composition of NPs is MoO_2 and a small amount of Mo^{5+} and Mo^{6+} signal is obtained because all NRs structures do not totally converted to MoO_2. With increasing substrate temperature some materials are evaporated, so the Si substrate get exposed and oxidized and we get the corresponding peak in O 1s core level spectrum [41 and chapter 4 in this thesis].

For investigating structural and compositional aspects, resonant RBS (RRBS or NRA) is an important method which deals with the analysis of high energy backscattered particles like proton or alpha. After the morphological, crystal structure, growth direction, chemical composition analyses using FEGSEM, TEM, XPS, the samples were characterized by RBS method at RT to know about the thickness, composition, and the growth mode. Figure 3.2(a) depicts RBS spectrum for 10 nm MoO_3 deposited on cleaned Si(100) substrate at substrate temperature of 350 °C and 550 °C. If we observe the Mo peak for different temperature shown in the right inset of Figure 3.2(a), there is a tail of Mo peak towards lower backscattered energy and the tail decreases with increasing substrate temperature. This type of tail can be originated for two reasons (i) for diffusion and (ii) surface roughness. There is no shifting of Si edge, no hump is observed near Si edge and no reduction of Si spectrum height is seen. These all indicate that there is no Si out-diffusion. Therefore, the possibility of Mo diffusion into Si matrix has been ruled out. We have already seen from SEM images that the as grown sample is NRs in structures and randomly oriented. But when the substrate temperature increases NRs transform to NPs. The roughness of the NRs is much higher than that of the NPs. So the tailing of the Mo peak decreases for NPs cases.

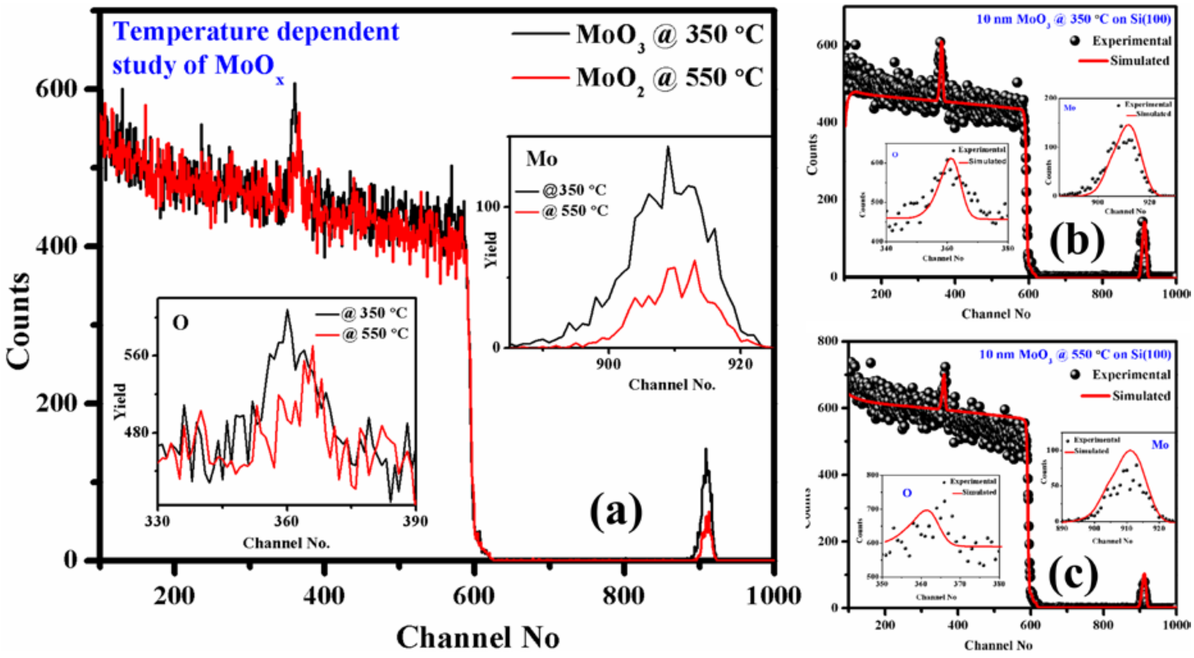

Figure 3.2: *RBS study (random) to understand substrate temperature dependence of MoO_3 on Si matrix. (a) experimental spectrum for 10 nm MoO_3 deposited on cleaned Si(100) substrate at substrate temperature of 350 °C and 550 °C. Experimental along with simulated spectrum for (b) 350 °C, (c) 550 °C substrate temperature. In Figure 3.2(a), (b), (c) insets show enlarged portion of Mo (right) and O (bottom left) peaks.*

Though we deposited 10 nm in both the cases, but from the Figure 3.2(a) we can recognize that at higher substrate temperature the Mo counts are less than the lower substrate temperature. This is because of some material evaporation which was also confirmed by in-situ XPS study where we get an extra peak for Si oxidation in O 1s core level spectrum. The lower counts in oxygen peak (see the bottom left inset of Figure 3.2(a)) at 550 °C substrate temperature are due to the phase change from MoO_3 to MoO_2 which was confirmed by TEM and in-situ XPS study (discussed at later chapter in detail). The experimental RBS spectrum with simulated curve have been presented in Figure 3.2(b) (for 350 °C substrate temperature), Figure 3.2(c) (for 550 °C substrate temperature) and fitted parameters using SIMNRA software package in Table 3.1.

Table 3.1: Obtained parameters after fitting RBS spectrums (random) to understand temperature dependent effect on MoO_3 using SIMNRA code.

Temp (°C)	**Elemental Concentration (%)**				**Composition**	**Thickness calculated by fitting (atoms/cm^2)**	**Thickness calculated by fitting (nm)**	**Total thickness (nm)**
		Mo	**O**	**Si**				
350	Layer 1	25	75	0	MoO_3	70×10^{15}	8.89	8.89
	Layer 2	0	0	100	Si	Bulk	Bulk	
550	Layer 1	30	60	10	MoO_2	20×10^{15}	2.2	4.6
	Layer 2	25	60	15	$MoO_{2.4}$	10×10^{15}	1.1	
	Layer 3	20	56	24	$MoO_{2.8}$	10×10^{15}	1.3	
	Layer 4	0	0	100	Si	Bulk	Bulk	

3.3.2 Thickness dependent effect on molybdenum oxide NSs

To understand the thickness dependence of MoO_3 NSs on cleaned Si matrix, we fixed the substrate temperature at 350 °C and kept other experimental conditions same as 10 nm MoO_3 deposited on cleaned Si(100) substrate at 350 °C substrate temperature (NRs sample), only varying the thickness 15 nm, 20 nm, and 30 nm. With the increasing thickness from 5 nm to 30 nm, length of the NRs gradually increase from 57.9±0.3 nm to 195.0±3.0 nm, (obtained from FEGSEM data) whereas the width does not change much. As the width remains constant; aspect ratio follows the length and is gradually increased from 3.9±0.1 to 14.1±0.5 nm with increasing thickness from 5 nm to 30 nm [42]. Figure 3.3(a) represents RBS spectrum for four different thicknesses of MoO_3 NRs samples. Random RBS spectrum with simulated curve using SIMNRA software package have been depicted in Figure 3.3(b) 15 nm, 3.3(c) 20 nm and 3.3(d) 30 nm, respectively and the fitted parameters are tabulated in Table 3.2. Here, it should be noted that the "thickness" is an effective thickness in terms of atoms/cm^2, Nt, where N is the atomic density and t is the thickness assuming uniform film thickness). For each of the thicknesses, NRs maintain perfect MoO_3 stoichiometry. Only roughness increases with increasing film thicknesses which supports the SEM measurements.

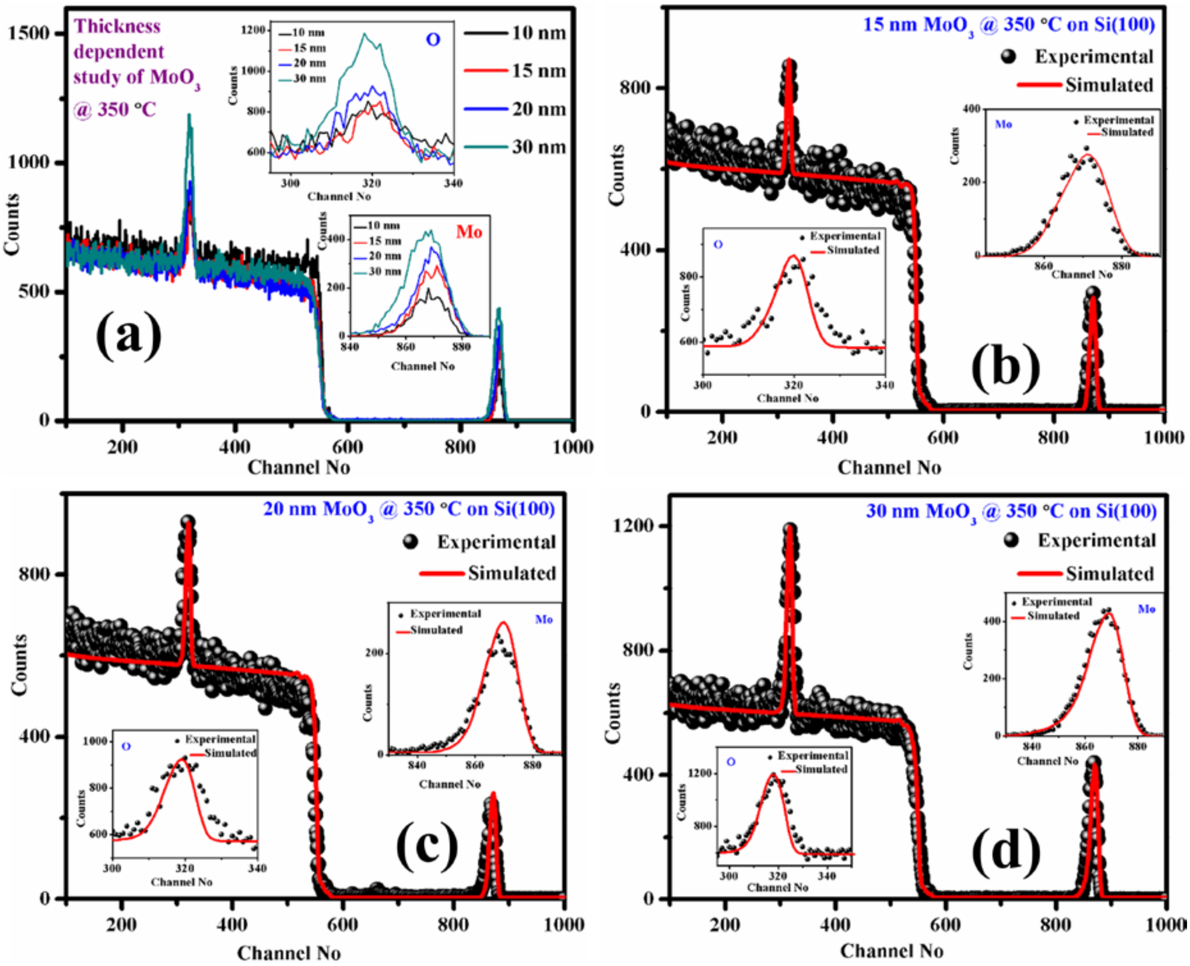

Figure 3.3: *RBS study (random) to understand thickness dependence of MoO_3 on Si matrix. (a) Experimental spectrum for (effective thickness of) 10 nm, 15 nm, 20 nm, 30 nm MoO_3 deposited on cleaned Si(100) substrate at substrate temperature of 350 °C. In Figure 3(a), insets show enlarged portion of Mo (bottom right) and O (upper right) for different thicknesses. Experimental along with simulated spectrum for different thicknesses of (b) 15 nm, (c) 20 nm, (d) 30 nm of MoO_3 at 350 °C substrate temperature and insets of (b), (c), (d) show enlarged portion of Mo (right) and O peak (left) for random with simulated data.*

Table 3.2: Obtained parameters after fitting RBS spectrums (random spectra) to understand thickness dependent effect of MoO_3 using SIMNRA code.

Thickness Measured by QCM (nm)	Elemental Concentration (%)		Composition	Thickness calculated by fitting (atoms/cm^2)	Thickness calculated by fitting (nm)
	Mo	O			
10	25	75	MoO_3	70×10^{15}	8.89
15	25	75	MoO_3	100×10^{15}	12.7
20	25	75	MoO_3	120×10^{15}	15.2
30	25	75	MoO_3	200×10^{15}	25.4

From Table 3.2 we can conclude that in each of the cases the stoichiometry is very close to the expected values, viz., MoO_3. If we observe the Mo peak for different thickness shown in the bottom right inset of Figure 3.3(a), there is a tail of Mo peak towards lower backscattered energy similar to temperature dependent study and the tail increases with increasing MoO_3 thickness. We have already discussed that this type of tailing comes from the surface roughness. We have also calculated thickness from the fitted curve and it comes out to be 8.89 nm, 12.7 nm, 15.2 nm, and 25.4 nm for MoO_3 effective film thicknesses of 10 nm, 15 nm, 20 nm and 30 nm respectively.

3.3.3 Vacuum dependent effect on molybdenum oxide NSs

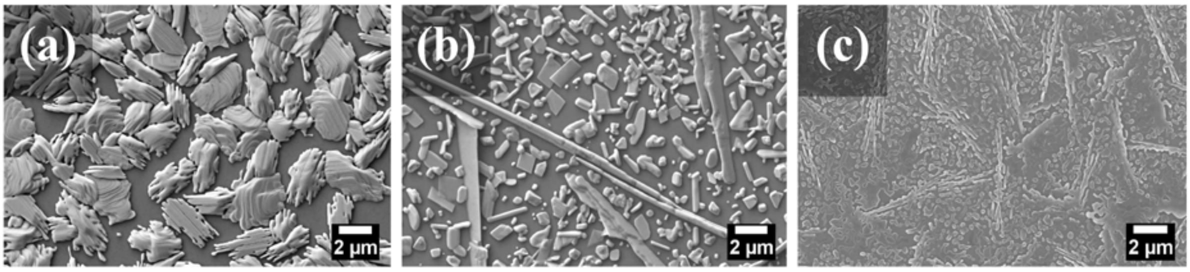

Figure 3.4: *250 nm MoO_3 deposited on Si(100) substrate with a native oxide layer by PVD followed by post anneal at 600 °C for 30 min in (a) air by CVD, (b) low vacuum by CVD and (c) ultra-high vacuum (UHV) using MBE.*

SEM images shown in Figure 3.4(a) depicts layered like structures after annealing in air at 600 °C whereas plate like microstructures are formed when we annealed 250 nm thick MoO_3 thin films in LV (see Figure 3.4(b)). After annealing at 600 °C in UHV, granular structures are formed as shown in Figure 3.4(c).

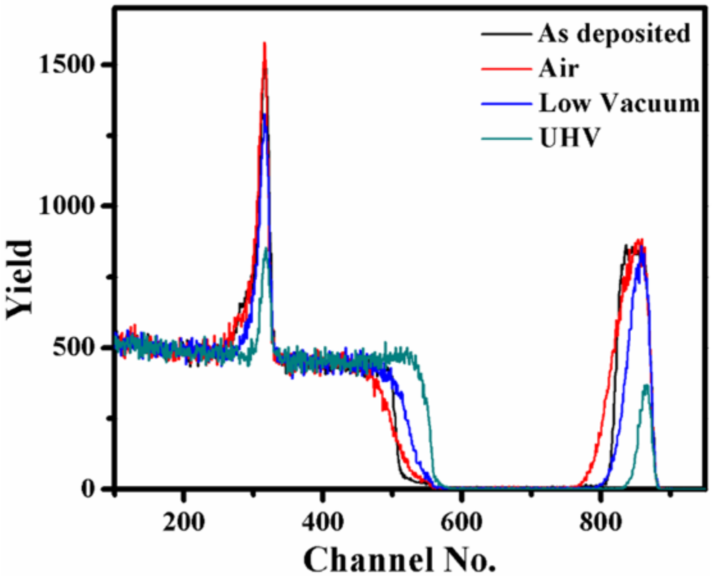

Figure 3.5: *(a) RBS study (random) to understand vacuum dependency of* MoO_3 *on Si matrix. Experimental spectrum from the samples of as deposited and after post anneal at 600 °C for 30 min in air, low vacuum and UHV.*

To know the structural stoichiometry and thickness, we performed RBS study in the resonance mode. Experimental spectrum from the samples of as deposited and after post anneal at 600 °C for 30 min in air, low vacuum and UHV was depicted in Figure 3.5. Random RBS spectrum with simulated curve using SIMNRA software package have been depicted in Figure 3.6(a) – (d) and the fitted parameters are tabulated in Table 3.3.

From Table 3.3, it can be observed that the as deposited sample is MoO_3. Total thickness of 243.5 nm has been come out after fitting the experimental data with simulated curve, which is same as deposited thin film (250 nm). PA in air sample consists of five layers. Mo, O and Si concentration, thickness have been calculated for each layer. In this case total thickness is 242.9 nm. SEM image already presented that they are layered like structures but not totally covered the surface. That’s why a very small concentration of Si (5%) presents at the top layer (Layer 1). Similarly there also exist five layers in the PA in LV sample. As the structures are microplates, the roughness is lower than the previous case. In the case of PA in UHV sample, total four layers exist.

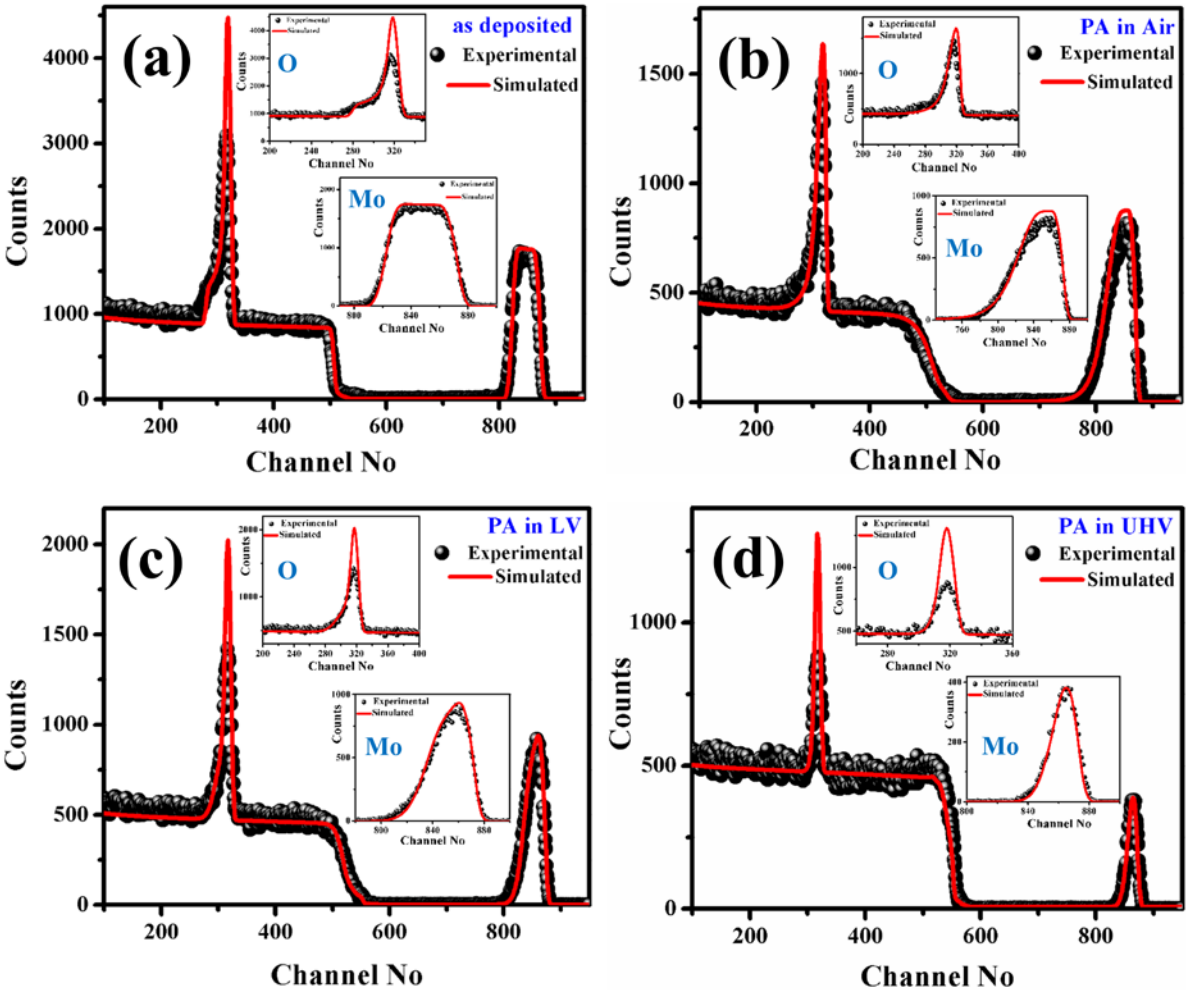

Figure 3.6: *Experimental along with simulated spectrum from the (a) as deposited 250 nm* MoO_3 *films on Si(100) substrate with native oxide layer by PVD followed by post anneal at 600 °C for 30 min in (b) air, (c) low vacuum and (d) ultra-high vacuum (UHV) by MBE. Insets of (a), (b), (c) and (d) show enlarged portion of Mo (bottom) and O peak (top) for random with simulated data.*

The roughness is lowest for UHV annealed sample among the three post annealed samples. After fitting with simulated curve, total thickness of 87.4 nm is calculated which is very less as compared to the deposited thin film. The reason behind the difference in the film thickness is that some of the material evaporated from the surface which is reflected from the Si concentration (52%) in Layer 1. At 700 °C MoO_3 starts to sublimate which is very close to the annealing temperature.

Table 3.3: Obtained parameters after fitting RBS spectrums (random) to understand vacuum dependent effect on MoO_3 using SIMNRA code.

Samples	**Elemental Concentration (%)**				**Composition**	**Thickness calculated by fitting (10^{15} atoms/cm^2)**	**Thickness calculated by fitting (nm)**	**Total thickness (nm)**
		Mo	**O**	**Si**				
As deposited	Layer 1	25	75	0	MoO_3	2000	243.5	243.5
	Layer 2	0	0	100	Si	Bulk	Bulk	
PA in Air	Layer 1	25	70	5	$MoO_{2.8}$	780	108.2	242.9
	Layer 2	25	65	10	$MoO_{2.6}$	500	69.3	
	Layer 3	22	55	23	$MoO_{2.5}$	350	51.3	
	Layer 4	10	24	66	$MoO_{2.4}$	100	14.1	
	Layer 5	0	0	100	Si	Bulk	Bulk	
PA in (LV)	Layer 1	25	65	10	$MoO_{2.6}$	750	104.0	200.7
	Layer 2	20	52	28	$MoO_{2.6}$	400	58.3	
	Layer 3	15	38	47	$MoO_{2.5}$	200	31.2	
	Layer 4	10	23	67	$MoO_{2.3}$	50	7.2	
	Layer 5	0	0	100	Si	Bulk	Bulk	
PA in (UHV)	Layer 1	15	33	52	$MoO_{2.2}$	360	28.3	87.4
	Layer 2	10	21	69	$MoO_{2.1}$	170	25.2	
	Layer 3	5	10	85	MoO_2	200	33.9	
	Layer 4	0	0	100	Si	Bulk	Bulk	

In the temperature dependent study, we have already seen, MoO_2 NPs are formed at 550 °C. Further, MoO_2 granular structures are formed after annealing at 600 °C in UHV. XRD and

AFM measurements were also done (detailed in chapter 7) to know about the large scale crystalline quality, roughness of these samples, which are in good agreement with RBS results.

3.4. Conclusion

In summary, we have described growth mode, oxygen concentration, stoichiometry and effective thickness of temperature, thickness and vacuum dependent molybdenum oxide NSs from the RBS spectrum in resonance mode.

3.5. References

[1] P. Maiti, B. Sundaravel and P. V. Satyam, (to be submitted).

[2] K. Koike, R. Wada, S. Yagi, Y. Harada, S. Sasa, and M. Yano, *Jpn. J. Appl. Phys.* 2014, 53, 05FJ02.

[3] N. Illyaskutty, S. Sreedhar, G. S. Kumar, H. Kohler, M. Schwotzer, C. Natzeck, and V. P. M. Pillai, *Nanoscale* 2014, 6, 13882.

[4] E. Comini, G. Faglia, G. Sberveglieri, C. Cantalini, M. Passacantando, S. Santucci, Y. Li, W. Wlodarski, and W. Qu, *Sens. Actuator B* 2000, 68, 168.

[5] M. Ferroni, V. Guidi, G. Martinelli, P.Nelli, M. Sacerdoti, and G. Sberveglieri, *Thin Solid Films* 1997, 307, 148.

[6] M. Ferroni, V. Guidi, G. Martinelli, M. Sacerdoti, P. Nelli, and G. Sberveglieri, *Sens. Actuator B* 1998, 48, 285.

[7] A. Khademi, R. Azimirad, A. A. Zavarian, and A. Z. Moshfegh, *J. Phys. Chem. C,* 2009, 113, 19298.

[8] Z. Su, L. Wang, Y. Li, G. Zhang, H. Zhao, H. Yang, Y. Ma, B. Chu, and W. Li, *ACS Appl. Mater. Interfaces* 2013, 5, 12847.

[9] Y. A. Yang, Y. W. Cao, B. H. Loo, and J. N. Yao, *J. Phys. Chem. B* 1998, 102, 9392.

[10] R. Sivakumar, M. Jayachandran, and C. Sanjeeviraja, *Surf. Eng.* 2004, 20, 5.

[11] G. Wang, J. Ni, H. Wang, and L. Gao, *J. Mater. Chem. A* 2013,1, 4112.

[12] B. Han, K. -H. Lee, Y. –W. Lee, S. -J. Kim, H. -C. Park, B. -M. Hwang, D. -H. Kwak, and K. –W. Park, *Int. J. Electrochem. Sci.* 2015, 10, 4232.

[13] S. Balendhran, S. Walia, H. Nili, J. Z. Ou, S. Zhuiykov, R. B. Kaner, S. Sriram, M. Bhaskaran, and K. Kalantar-zadeh, *Adv. Funct. Mater.* 2013, 23, 3952.

[14] Z. Yin, X. Zhang, Y. Cai, J. Chen, J. I. Wong, Y. –Y. Tay, J. Chai, J. Wu, Z. Zeng, B. Zheng, H. Y. Yang, and H. Zhang, *Angew. Chem. Int. Ed.* 2014, 53, 1.

[15] S. Hamwi, J. Meyer, T. Winkler, T. Riedl, and W. Kowalsky, *Appl. Phys. Lett.* 2009, 94, 53307.

[16] S. Chen, X. Yu, M. Zhang, J. Cao, Y. Li, L. Ding, and G. Shi, *J. Mater. Chem. A* 2015, DOI: 10.1039/C5TA04823K.

[17] S. Cong, T. Sugahara, T. Wei, J. Jiu, Y. Hirose, S. Nagao, and K. Suganuma, *Cryst. Growth Des.* Doi: 10.1021/acs.cgd.5b00790.

[18] N. Dukstiene, D. Sinkeviciute, and A. Guobiene, *Cent. Eur. J. Chem.* 2012, 10(4), 1106.

[19] K. Inzani, M. Nematollahi, F. Vullum-Bruer, T. Grande, T. W. Reenaas, and S. M. Selbach, *Phys. Chem. Chem. Phys.* 2017, DOI: 10.1039/C7CP00644F.

[20] I. A. Castro, R. S. Datta, J. Z. Ou, A. C. Gomez, S. Sriram, T. Daeneke, and K. Kalantar-zadeh, *Adv. Mater.* 2017, 1701619.

[21] W. K. Chu, J. W. Mayer, M. A. Nicolet, T. M. Buck, G. Amesel and F. Eisen, *Thin Solid Films* 1973, 17, 1.

[22] W. K. Chu and J. W. Mayer, Backscattering Spectrometry, *Academic Press*.

[23] T. L. Alford, L. C. Feldman and J. W. Mayer, *Fundamentals of Nanoscale film analysis* Springer 2007.

[24] L. C. Feldman and J. M. Poate, *Ann. Rev. Mater. Sc.* 1982, 12, 149.

[25] K. Sekar, G. Kuri, P. V. Satyam, B. Sundaravel, D. P. Mahapatra and B. N. Dev, *Indian K. Phys.* 1994, 68A, 1. .

[26] M. Aono, *Nuclear Instrum. Methods B* 1984, 2, 374.

[27] H. Winter, *Phys. Rep.* 2002, 362, 387.

[28] J. F. van der Veen, *Surf. Sci. Rep.* 1985, 5, 199.

[29] B. Blanpain, P. Revesz, L. R. Doolittle, K. H. Purser and J. W. Mayer, *Nucl. Instr. Meth.* 1988, B34, 459.

[30] J. R. Cameron, *Phys. Rev.* 1953, 90, 839.

[31] J. Li and J. W. Mayer, *Mater. Chem. Phys.* 1992, 32, 1.

[32] C. J. Zoller, E. D. Litta and D. Primetzhofer, *Nucl. Instr. Meth. B* 2015, 347, 52.

[33] J. U. Bhanu, A. Amutha, G. R. Babu, B. Sundaravel and P. Thangadurai, *Mater. Sci. Semicond. Process.* 2018, 81, 7.

[34] D. A. Cole, J. R. Shallenberger, S. W. Novak, R. L. Moore, M. J. Edgell, S.P. Smith, C. J. Hitzman, J. F. Kirchhoff, E. Principe, W. Nieveen, F. K. Huang, S. Biswas, R. J. Bleiler and K. Jones, *J. Vac. Sci. Technol. B* 2000, 18(1), 440.

[35] J. Pouilleau, D. Devilliers, F. Garrido, S. Durand-Vidal and E. Mahe, *Mater. Sci. Eng. B* 1997, 47, 235.

[36] R. Ratajczak, A. Stonert, E. Guziewicz, S. Gieraltowska, T. A. Krajewski, G. Luka, L. Wachnicki, B. S. Witkowski and M. Godlewski, *Acta. Phys. Pol. A* 2012, 123, 899.

[37] S. H. Mohamed, O. Kappertz, J. M. Ngaruiya, T. P. L. Pedersen, R. Drese and M. Wuttig, *Thin Solid Films* 2003, 429, 135.

[38] https://home.mpcdf.mpg.de/~mam/

[39] J. L. Duggan and I. L. Morgan, *American Institute of Physics Conference Proceedings* 1999, 475, 541.

[40] M. Mayer, *Proceedings of the 15th International Conference on the Application of Accelerators in Research and Industry.*

[41] P. Maiti, P. Guha, H. Hussain, R. Singh, C. Nicklin and P. V. Satyam, *Surf. Sci.* 2019, 682, 64.

[42] P. Maiti, P. Guha, R. Singh, J. K. Dash and P. V. Satyam, *Appl. Surf. Sci.* 2019, 476, 691.

Chapter 4

Microscopy and Spectroscopy Study of Nanostructural Phase Transformation from β-MoO_3 to Mo under UHV – MBE Conditions

4.1 Introduction

This chapter is devoted on morphological and structural phase transition from Molybdenum trioxide (β-MoO_3) to Molybdenum (Mo) through Molybdenum dioxide (MoO_2) in ultra-high vacuum condition. Though the earlier works on the phase transition from α-MoO_3 to MoO_2 and MoO_2 to Mo were reported, the formidable task of carrying out in-situ measurements were necessary to shed a light on the phase transition in UHV starting from β-MoO_3. Here, we report a simple reduction of molybdenum oxide (β-MoO_3) grown on reconstructed Si(100) by thermal annealing in ultra-high vacuum (UHV) using molecular beam epitaxy (MBE). By increasing the substrate temperature during deposition or the annealing temperature after growth, the morphologies of as-deposited structures were found to vary from nanoribbons (NRs) of β-MoO_3 to nanoparticles (NPs) of Mo. The change in morphologies have been associated with a structural transition from β-MoO_3 to MoO_2 at 400 °C and MoO_2 to Mo at 750 °C. The *in-situ* X-ray photoelectron spectroscopy (XPS) measurements revealed a shift

---

The work presented in this chapter has been published in "P. Maiti, P. Guha, H. Hussain, R. Singh, C. Nicklin and P. V. Satyam, *Surf. Sci.* 2019, 682, 64".

of the Mo 3d peaks towards lower binding energies, representing the reduction in Mo oxidation states until a pure Mo 3d peak at 750°C was observed. The *ex-situ* KPFM measurements showed a decrease in the local work function (Φ) (from ≈ 5.27 ± 0.05 eV to ≈ 4.83 ± 0.05 eV) with increasing substrate temperature. A gradual reduction of the band gap from ≈ 3.32 eV for β-MoO_3 NRs to zero band gap for Mo NPs is also observed during the annealing up to 750 °C [1].

The main aim of this section of the thesis is to report on a detailed in-situ XPS study for understanding the structural phase transition from β-MoO_3 (metastable molybdenum trioxide) to MoO_2 and then to Mo by simple thermal reduction process in UHV condition by MBE technique. By using appropriate experimental tools, we have succeeded in determining the band gap and work function of β-MoO_3 that are not reported earlier. Several experimental techniques (namely, in-situ XPS, field emission gun based scanning electron microscopy (FESEM), high resolution transmission electron microscopy (HRTEM), X-ray diffraction (XRD), Kelvin probe force microscopy (KPFM) and UV-Vis spectroscopy) have been extensively used for this study.

There are predominantly two different polymorphs of MoO_3 based on MoO_6 octahedron building block: one has a thermodynamically stable orthorhombic (α-MoO_3) structure and the other a metastable monoclinic (β-MoO_3) structure. α-MoO_3 has unit cell parameters a = 3.96 Å, b= 13.85 Å and c = 3.71 Å in a Pbnm space group (JCPDS: 35-0906) [2] exhibiting a layered like structure. The structure of β-MoO_3 (unit cell parameters: a = 7.12 Å, b= 5.37 Å, c = 5.57 Å and β = 92.01° in $P2_1/c$ space group) is quite different from α-MoO_3 structure. It can be related to 3D ReO_3 structure like WO_3. It is formed only by the corner sharing MoO_6 octahedron. External conditions like temperature, pressure, and impurities influence the arrangement of the MoO_6 octahedra. β-MoO_3 can be transformed to α-MoO_3 by thermal treatment at temperatures above 350 °C [1,3]. Various types of MoO_3 nanostructures have been prepared by different physical and chemical processes like chemical vapor deposition (CVD) [4], thermal evaporation [5], van der Waals epitaxy [6], e-beam evaporation [7], DC magnetron sputtering [8] and many more.

Monoclinic MoO_2 phase (unit cell parameters: a = 5.537 Å, b= 4.859 Å, c = 5.607 Å and β = 120.912 (JCPDS: 86-0135) [9]) also displays a deformed rutile structure. Along the rutile c-axis, two distinct metal to metal bond lengths of 2.51 Å and 3.02 Å arise due to the alternation of Mo-Mo distance. This leads to two distinct oxygen coordination sites [10]. The theoretical band structure calculations of MoO_2 show four Mo 4d bands below the Fermi energy that indicate the material should be semi-metallic in nature. Experimentally, however, it has been observed that the MoO_2 structures are semiconducting in nature with a reduced band gap compared to MoO_3 [3]. Different types of MoO_2 nanostructures including micro spheres [11,12], nanoparticles [13] or sub-micron scale sheets [32] have been prepared by hydrothermal reaction [28,31], Pechini method [30], CVD technique [14] and electro deposition from solution [15].

Molybdenum (Mo) has a cubic structure with unit cell parameter a = 3.15 Å. Due to its excellent material properties (e.g. low thermal expansion coefficient (5.1×10^{-6} m/°C) [16] which is less than steel, good thermal and electrical conductivity and high melting point (2615 °C) [17]) metallic molybdenum is a suitable candidate for a wide variety of applications including high temperature applications such as an alloying agent, electrodes for electrically heated glass furnace, nuclear energy applications like missile and aircraft parts, filament material for electrical application and thermocouple sheaths. Production of metallic molybdenum from MoO_3 follows a two-step process; (i) reduction of MoO_3 to MoO_2 and (ii) further reduction of MoO_2 to Mo [17]. Step (i) plays a critical role in the production of high purity Mo. There are various reports where MoO_3 has been reduced to MoO_2 by hydrogen gas [18,19] and electron beam [20]. To get crystalline MoO_2 in hydrogen gas reduction process by controlling experimental conditions, precursor and reducing agent is very challenging. For electron beam induced transformation of MoO_3 to MoO_2, we need to care about applied electron current density because in low current density MoO_2 is obtained but at high current density rock-salt like MoO structure formed.

Elucidation of the morphology and structural properties of NRs and NPs have been undertaken using *ex situ* FEGSEM, TEM and grazing incidence (GIXRD). Plausible mechanism for reduction and chemical information of the phase transformation from MoO_3 to MoO_2 and then to Mo, was obtained using *in situ* XPS. In this chapter, we report on the (i) growth of metastable monoclinic molybdenum trioxide (β-MoO_3), (ii) morphological evolution with temperature (iii) phase transformations from β-MoO_3 to MoO_2 and then Mo by thermal treatment in UHV, (iv) correlation between the ex-situ studies of the phase transitions with in-situ XPS analysis and their (v) band gap, work function studies.

4.2 Experimental Details

The β - MoO_3 NRs were grown using a custom-built MBE system (M/S Omicron GmbH, base pressure ≈ 2.3×10^{-10} mbar) and details are given in the previous chapters.

Ex-situ surface structure characterizations (surface morphology, shape and size) of as-grown samples were performed using FEGSEM with 20 keV electrons, TEM with 200 keV electrons and GIXRD with a Cu Kα source. For TEM, samples were prepared by mechanical thinning process and final electron transparency was obtained by low energy argon (Ar^+) ion milling. An ultraviolet-visible-near infrared (UV-Vis-NIR) spectrometer (Shimadzu Corporation, UV-3101PC) was used to study the optical properties of as-grown samples at room temperature. *In-situ* XPS measurements were performed on an Omicron XPS instrument with monochromatic Al Kα X-ray source (hν = 1486.6 eV) (including an Omicron SPHERA energy analyzer with 7 Channeltron electron multipliers detection) at Diamond Light Source (DLS), Didcot, UK [21]. A dual tungsten filament e-beam heater beneath the substrate holder has been used to anneal the specimen and the temperature was monitored via an infrared pyrometer. During the XPS measurements, the chamber base pressure was 8.1×10^{-10} mbar and raised to a maximum of 5.7×10^{-9} mbar during *in-situ* heating experiment. In order to find the local work function of the as-grown samples, Kelvin probe force microscopy (KPFM) was used. KPFM of the samples was examined by *ex-situ* atomic force microscopy (AFM) (MFP-3D, Asylum Research USA) in lift mode, with a lift height of 60 nm, using a conductive Ir/Pt tip (AC240TM, Electric-Lever, Olympus) having ≈ 30 nm radius of curvature, ≈ 2 N-m^{-1} stiffness, and a resonance frequency of ≈ 70 kHz.

4.3 Results and discussion

A ≈ 10 nm MoO_3 film was deposited on atomically cleaned Si(100) substrates at six different substrate temperatures ranging from 350 °C to 600 °C. Figure 4.1(a) shows high magnified SEM image of 10 nm MoO_3 deposited on Si(100) revealing nanoribbon structures on the surface. During deposition substrate temperature (by RH) was 350 °C. For large scale crystalline information of this as-prepared sample, GIXRD analysis was conducted and the result has been shown in Figure 4.1(b). All the peaks can be indexed to the monoclinic phase of MoO_3 (β-MoO_3) (JCPDS card, #89-1554) [22].

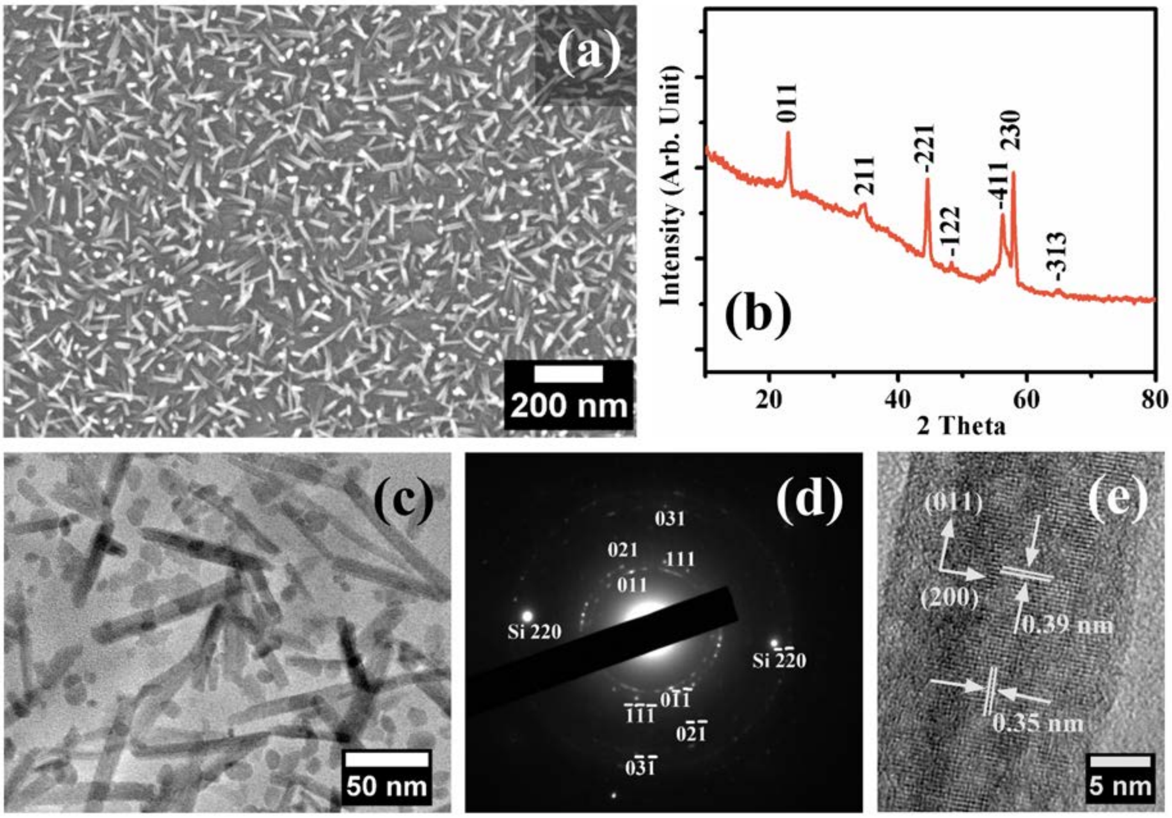

Figure 4.1: *(a) SEM micrograph and (b) GIXRD spectrum of 10 nm MoO_3 grown on cleaned Si(100) substrate at 350 °C substrate temperature. (c) Planar TEM micrograph and (d) corresponding selected area electron diffraction (SAED) pattern of MoO_3 nanoribbons (NRs). (e) High resolution TEM (HRTEM) image, representing preferential growth along <011> [1].*

To gain an understanding of the NRs growth direction, we have used planer TEM and selected area electron diffraction (SAED) and the results are shown in Figure 4.1(c) and Figure 4.1(d) respectively. The circular rings indicated in the SAED pattern correspond to (011), (111), (021) and (031) planes of monoclinic MoO_3. Figure 4.1(e) shows a high resolution TEM (HRTEM) image, revealing that the NRs have lattice planes with d-spacing of $d_{(011)} \approx 0.39$ nm and $d_{(200)} \approx 0.35$ nm for the β-MoO_3 phase, depicting growth along <011> direction. Here, we observe a phase change from α-MoO_3 (source material) to the monoclinic phase of MoO_3 on the substrates/templates. One possible reason for this transformation could be the annealing temperature of the substrate. Mizushima et al [23] have shown this for 573 K substrate temperature case.

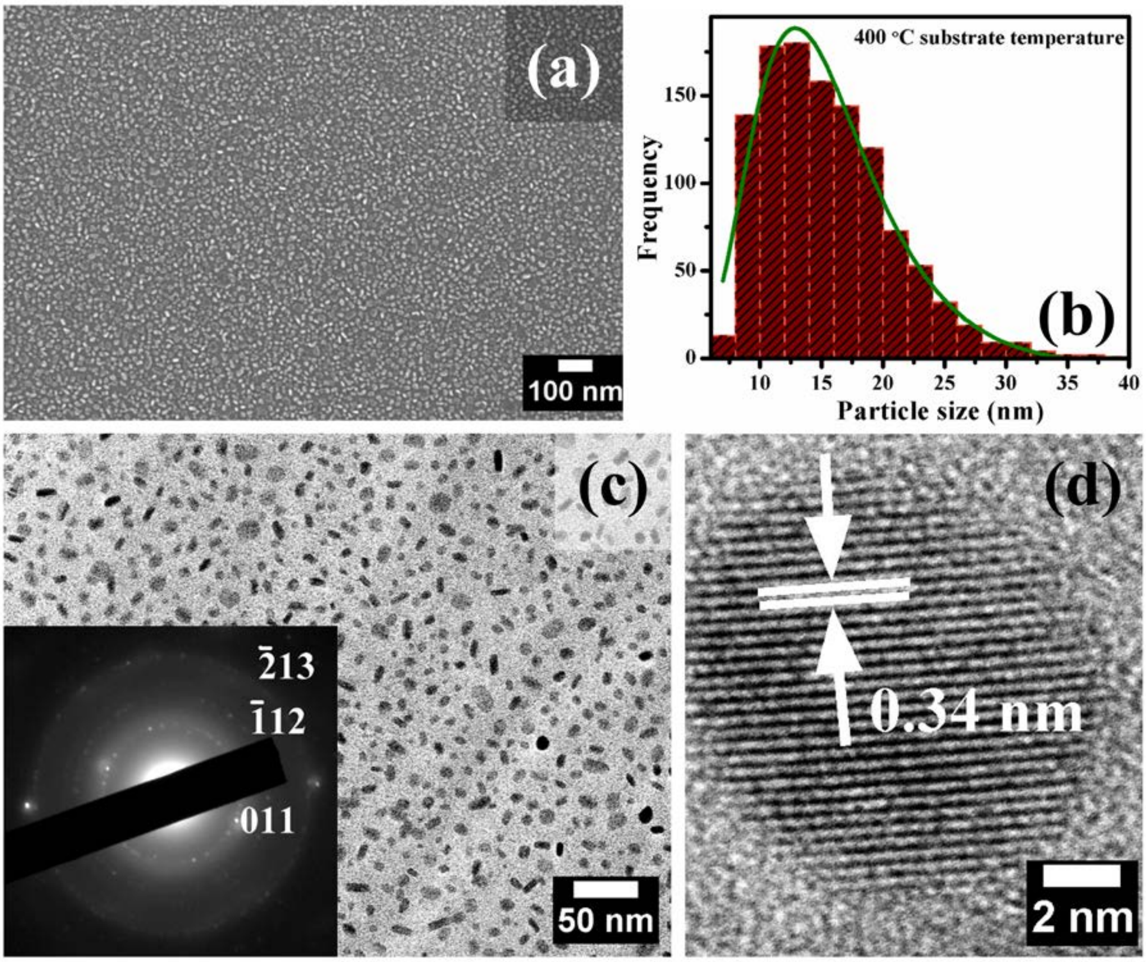

Figure 4.2: *(a) High magnification SEM micrograph of 10 nm* MoO_3 *deposition on cleaned Si (100) substrate at 400 °C, and (b) corresponding particle size distribution. (c) Planar TEM micrograph of the corresponding sample; inset of (c) represents corresponding selected area electron diffraction (SAED) pattern. (d) High resolution TEM (HRTEM) image, representing NPs are* MoO_2*, and the corresponding d-spacing 0.34 nm of <011> has shown [1].*

Another possible reason could be due to the partial pressure of oxygen in the system. *Carcia et al* [24] reported in their study that growth of molybdenum oxide in high (50%) and low (5% - 10%) oxygen atmospheres produce α-MoO_3 strongly oriented in [0k0] direction and β-MoO_3 with strong [0kk] preferred orientation, respectively. Since we have grown the samples in UHV, the as-grown sample is expected to be MoO_3 in the monoclinic phase because of the negligible oxygen content in the chamber.

Interestingly, after raising the substrate temperature to 400 °C with ≈ 10 nm MoO_3 deposition (i.e. MoO_3 deposited at 400 °C), morphology changes from NRs to nanoparticles (NPs), as shown in Figure 4.2(a) SEM image.

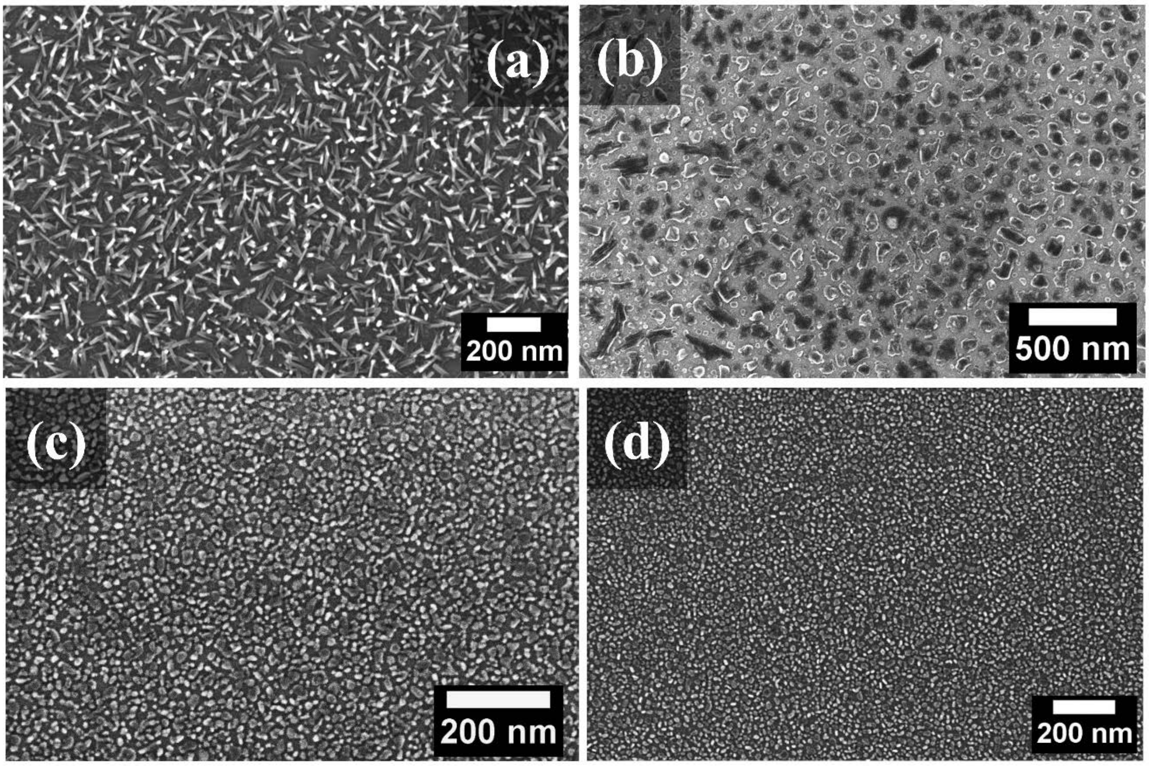

Figure 4.3: *High resolution SEM micrograph of 10 nm* MoO_3 *deposition on cleaned Si (100) substrate at substrate temperature of (a) 350 °C, (b) 365 °C, (c) 375 °C , (d) 400 °C respectively [1].*

The size distribution of these NPs is presented in Figure 4.2(b) and fitting with log-normal distribution gives an average NPs size of ≈ 14.8 ± 0.3 nm. Planer TEM result of the corresponding sample is shown in Figure 4.2(c). The circular rings indicated in the SAED pattern (Figure 4.2(c) inset) correspond to (011), (-112) and (-213) planes of monoclinic MoO_2. The HRTEM image (Figure 4.2(d)) of a single nanoparticle depicts the d-spacing of ≈ 0.34 nm which corresponds to (011) planes of β-MoO_2. It has been reported that reduction from α-MoO_3 to β-MoO_2 can occur at 673K (400 °C) [25]. To understand the morphological evolution from NRs (i.e. 350 °C substrate temperature) to NPs (i.e. 400 °C substrate temperature), we have grown the sample at two different substrate temperatures, 365 °C and 375 °C, purposely in between 350 °C to 400 °C. The corresponding SEM images of the samples are shown in Figure 4.3(b) and 4.3(c), respectively along with 350 °C (Figure 4.3(a)) and 400 °C (Figure 4.3(d)) substrate temperatures. It can be clearly seen that at 365 °C substrate temperature (Figure 4.3(b)) the NRs have started to decompose to NPs.

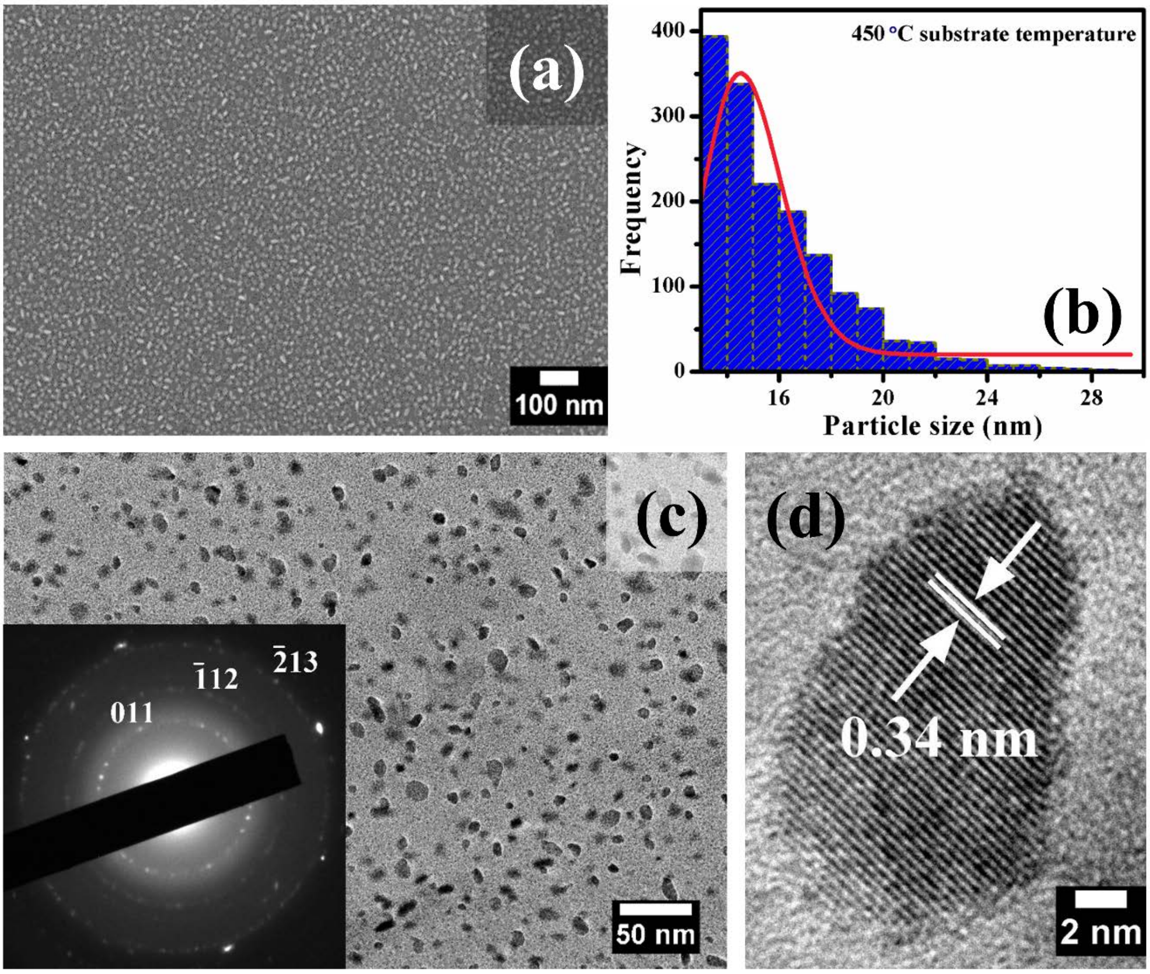

Figure 4.4: *(a) High magnification SEM micrograph of 10 nm MoO_3 deposition on cleaned Si (100) substrate at 450 °C, and (b) corresponding particle size distribution. (c) Planar TEM micrograph of the corresponding sample; inset of (c) represents corresponding selected area electron diffraction (SAED) pattern. (d) High resolution TEM (HRTEM) image representing NPs are MoO_2, and the corresponding d-spacing 0.34 nm of <011> has shown [1].*

Next, we deposited ≈ 10 nm MoO_3 on cleaned Si(100) at 450 °C but observed very little difference in the morphology when compared to deposition at 400 °C (see Figure 4.4(a)). The calculated particles size distribution with log-normal fitting (Figure 4.4(b)) produced average particle size ≈ 14.7 ± 0.2 nm. A planar TEM micrograph of the corresponding sample is shown in Figure 4.4(c) with the SAED pattern in the inset. The circular rings in the SAED pattern correspond to the (011), (-112) and (-213) planes of monoclinic MoO_2. In Figure 4.4(d), HRTEM image of a single nanoparticle is presented, depicting lattice spacing of ≈ 0.34 nm (corresponds to d(011) of β-MoO_2).

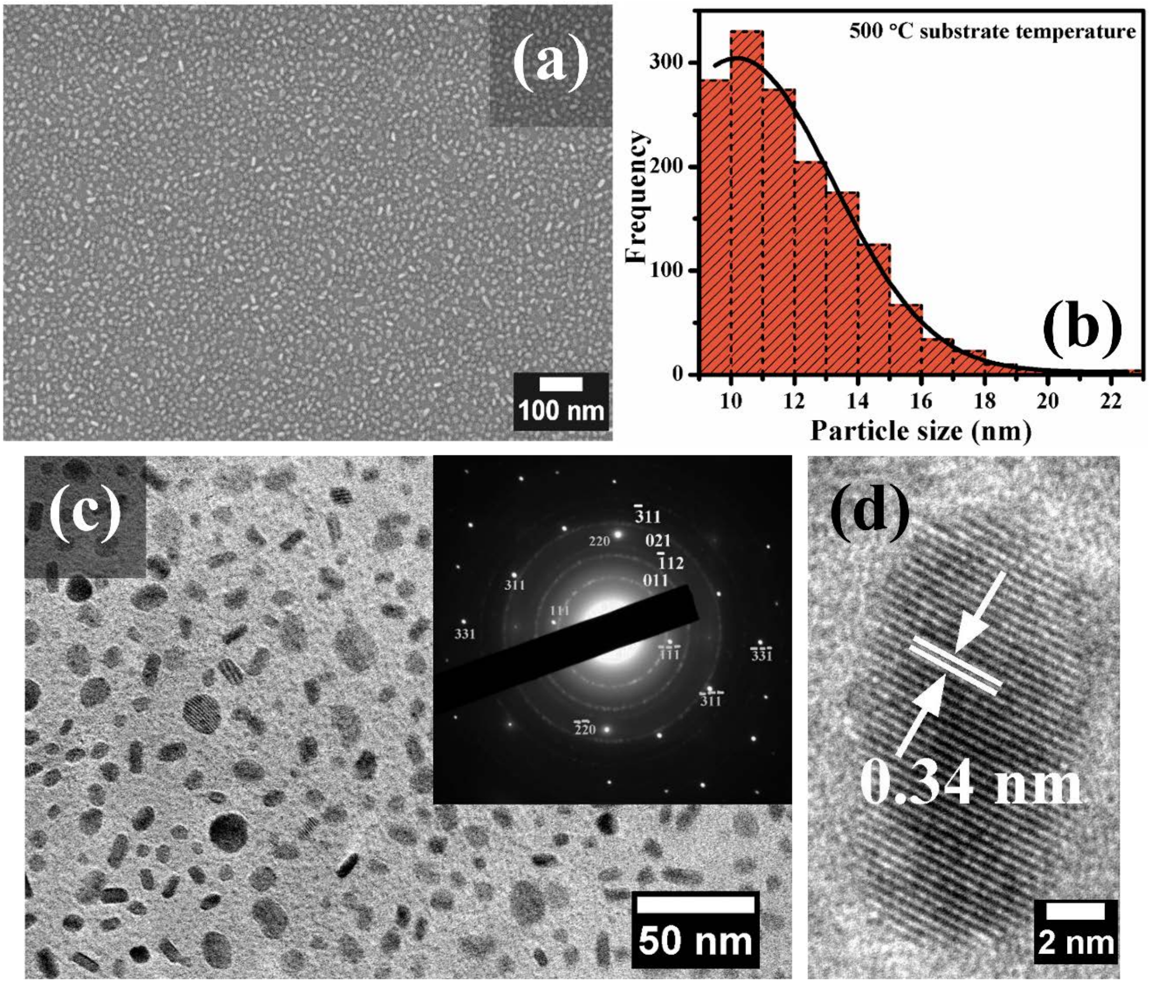

Figure 4.5: *(a) High magnification SEM micrograph of 10 nm MoO3 deposition on cleaned Si(100) substrate at substrate temperature of 500 °C, and (b) corresponding particle size distribution. (c) Planar TEM micrograph of corresponding sample; inset of (c) represents corresponding selected area electron diffraction (SAED) pattern.(d) High resolution TEM (HRTEM) image, representing NPs are* MoO_2*, and the corresponding d-spacing 0.34 nm of <011> has shown [1].*

In a similar fashion, Figure 4.5 displays the results of the as-prepared sample grown at 500 °C. Figure 4.5(a) shows high resolution SEM image of the sample and its particles size distribution fitted with log-normal distribution is presented in Figure 4.5(b) revealing the average size of the nanoparticles to be ≈ 10.6 ± 0.3 nm.The planer TEM image of ≈ 10 nm MoO_3 grown at 500 °C substrate temperature is displayed in Figure 4.5(c) and the SAED pattern taken from Figure 4.5(c) is shown at the inset. The circular rings can readily be indexed to the (011), (-112), (021) and (-311) planes of β-MoO_2. The HRTEM image (Figure 4.5(d)) exhibits lattice planes with spacing of ≈ 0.34 nm corresponding to d spacing (d_{011}) of the (011) planes of β-MoO$_2$, similar to the previous results.

After these measurements, the substrate temperature was further increased to 550 °C while depositing ≈ 10 nm MoO$_3$. Here, again we observe very little change in the morphology as shown in Figure 4.6(a-d); The average size of the nanoparticles are calculated to be ≈ 10.2 ± 0.2 nm, fitted with log-normal distribution (shown in Figure 4.6(b)) and the circular rings of the SAED pattern (Figure 4.6(c)) show polycrystalline rings of (011), (-112) and (-213) of β-MoO$_2$. Analogously, from the HRTEM image, the d-spacing of the particle is determined to be ≈ 0.34 nm, corresponding to d_{011} of monoclinic MoO$_2$ phase.

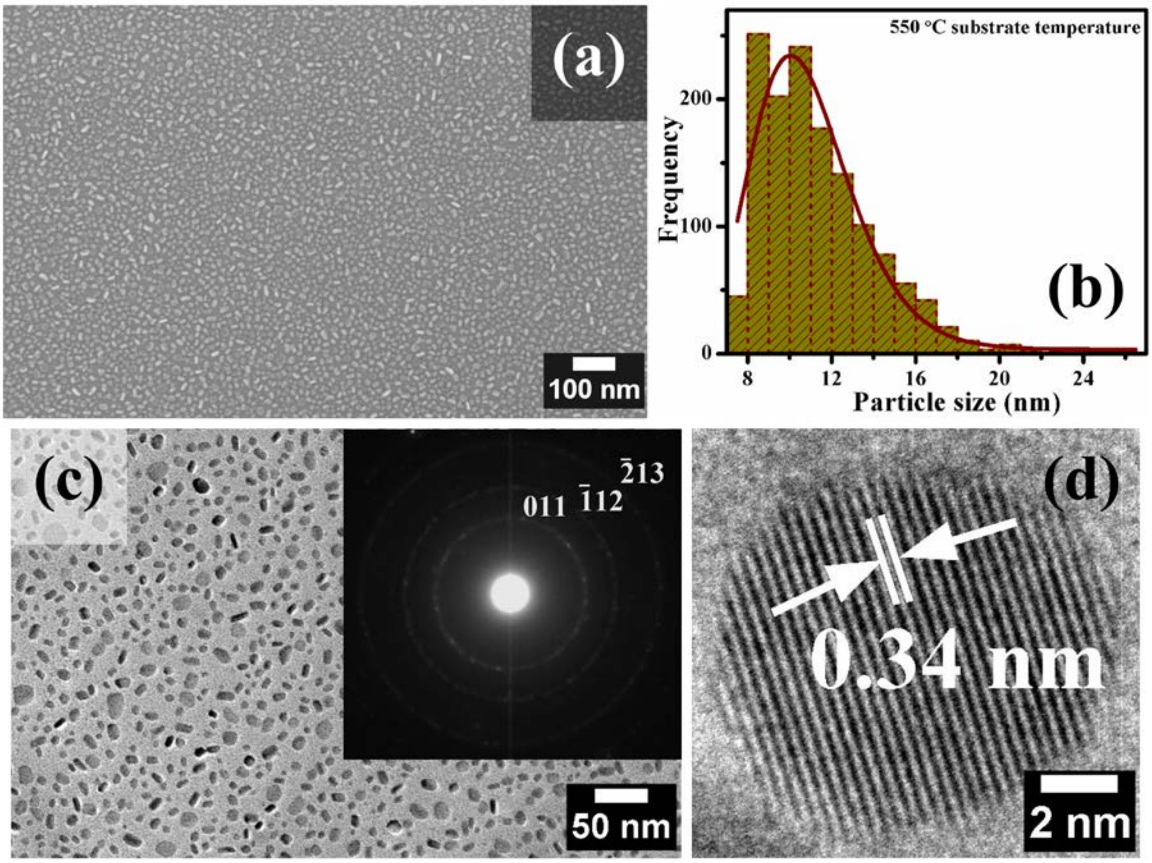

Figure 4.6: *(a) High magnification SEM micrograph of 10 nm* MoO$_3$ *deposition on cleaned Si(100) substrate at 550 °C, and (b) corresponding particle size distribution. (c) Planar TEM image of corresponding sample; inset of (c) represents corresponding selected area electron diffraction (SAED) pattern. (d) High resolution TEM (HRTEM) image, representing NPs are* MoO$_2$*, and the corresponding d-spacing 0.34 nm of <011> has shown [1].*

The substrate temperature was increased yet again to 600 °C, with the results presented in Figure 4.7(a-d). Figure 4.7(a) shows SEM image of as-grown nanoparticles, manifesting the particle size ≈ 9.5 ± 0.1 nm (see Figure 4.7(b)) fitted with log-normal distribution. Planer TEM measurements of the corresponding sample are shown in Figure 4.7(c) and its inset shows SAED pattern taken from it. Circular rings in SAED pattern are referring to (011), (-112) and (-213) planes of monoclinic MoO_2 structures. HRTEM (see Figure 4.7(d)) reveals d-spacing ≈ 0.34 nm, which matches with d011 of β-MoO_2 structure.

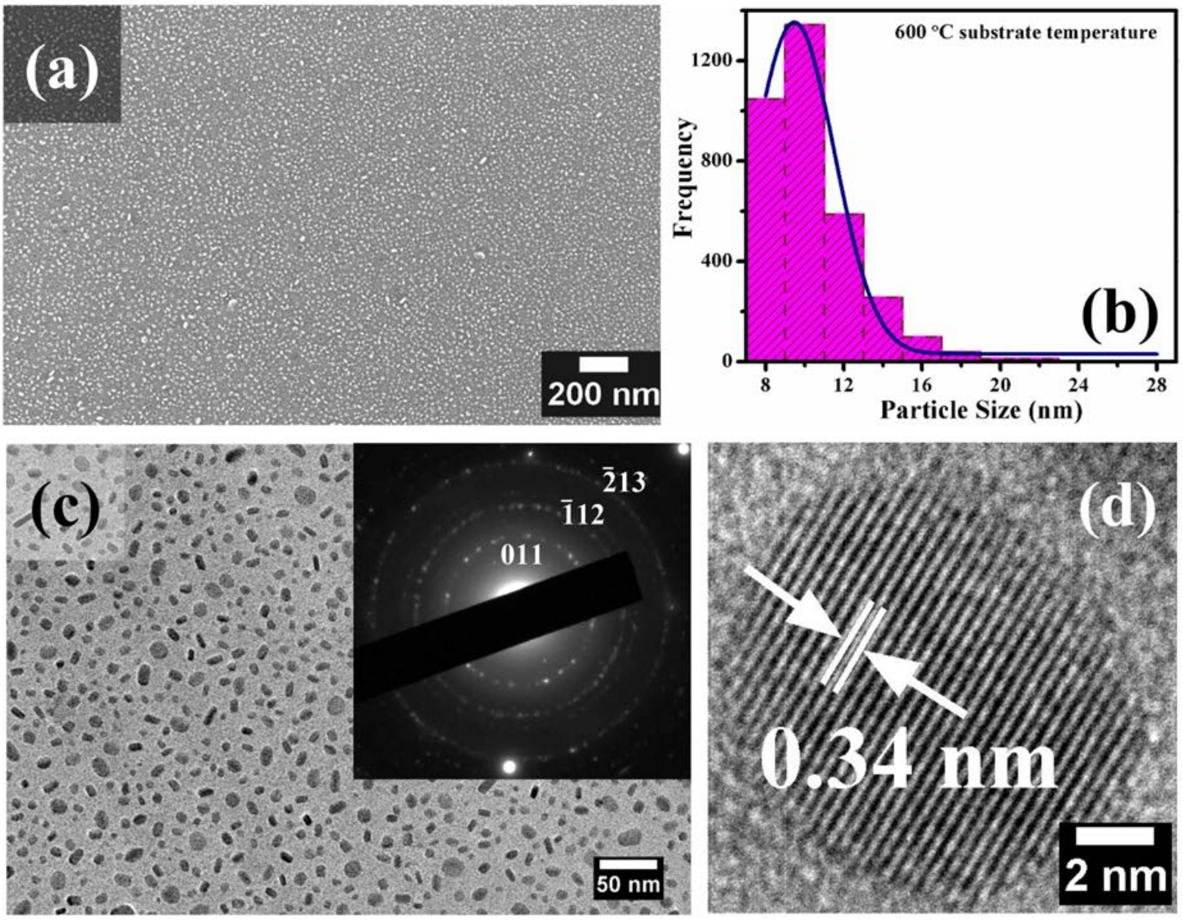

Figure 4.7: *(a) High magnification SEM micrograph of 10 nm MoO_3 deposition on cleaned Si(100) substrate 600 °C and (b) corresponding particle size distribution. (c) Planar TEM micrograph of corresponding sample; inset of (c) represents corresponding selected area electron diffraction (SAED) pattern. (d) High resolution TEM (HRTEM) image, representing NPs are MoO_2, and the corresponding d-spacing 0.34 nm of <011> has shown [1].*

Thus we have observed from microscopy that all the as-grown samples having substrate temperature ranging from 400 °C to 600 °C, exhibit similar morphology (i.e. monoclinic

MoO2) with the average particle size decreasing with increasing temperature. This is summarized in Table 4.1, where the size, coverage area and areal density of the NPs are compared at different temperatures. It can be easily seen that with increasing substrate temperature, the size of the NPs, as well as the coverage area are decreasing most likely due to the evaporation of the material.

Table 4.1: Structural dimensions of NPs in different temperatures [1]

Temperature (°C)	**Size (nm)**	**Coverage Area of NPs (%)**	**Areal Density (per cm^2)**
400	14.8 ± 0.3	49.5	7.18×10^{10}
450	14.7 ± 0.2	48.2	7.19×10^{10}
500	10.6 ± 0.3	45.0	7.42×10^{10}
550	10.2 ± 0.2	39.8	7.44×10^{10}
600	9.5 ± 0.1	33.1	7.49×10^{10}

4.3.1 Elemental Quantification: *In-situ* XPS Study

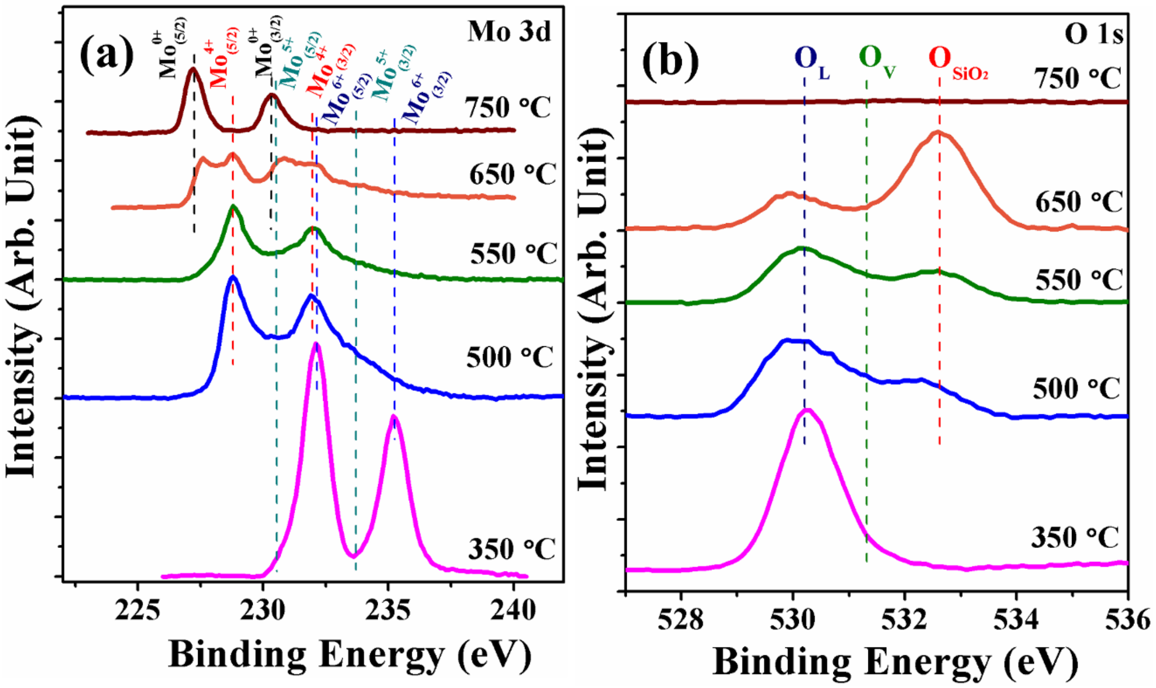

Figure 4.8: Temperature dependent XPS spectra of (a) Mo 3d and (b) O 1s [1].

To gain an understanding of the chemical composition of the grown films, we employed *in-situ* XPS on the sample exhibiting NRs (i.e. ≈ 10 nm MoO_3 at 350 °C substrate temperature on cleaned Si(100)) varying the temperature from 350 °C to 750 °C. Figures 4.8(a) and 4.8(b) show temperature dependent XPS spectra of Mo 3d and O 1s core levels at different substrate temperatures of 350 °C, 500 °C, 550 °C, 650 °C and 750 °C.

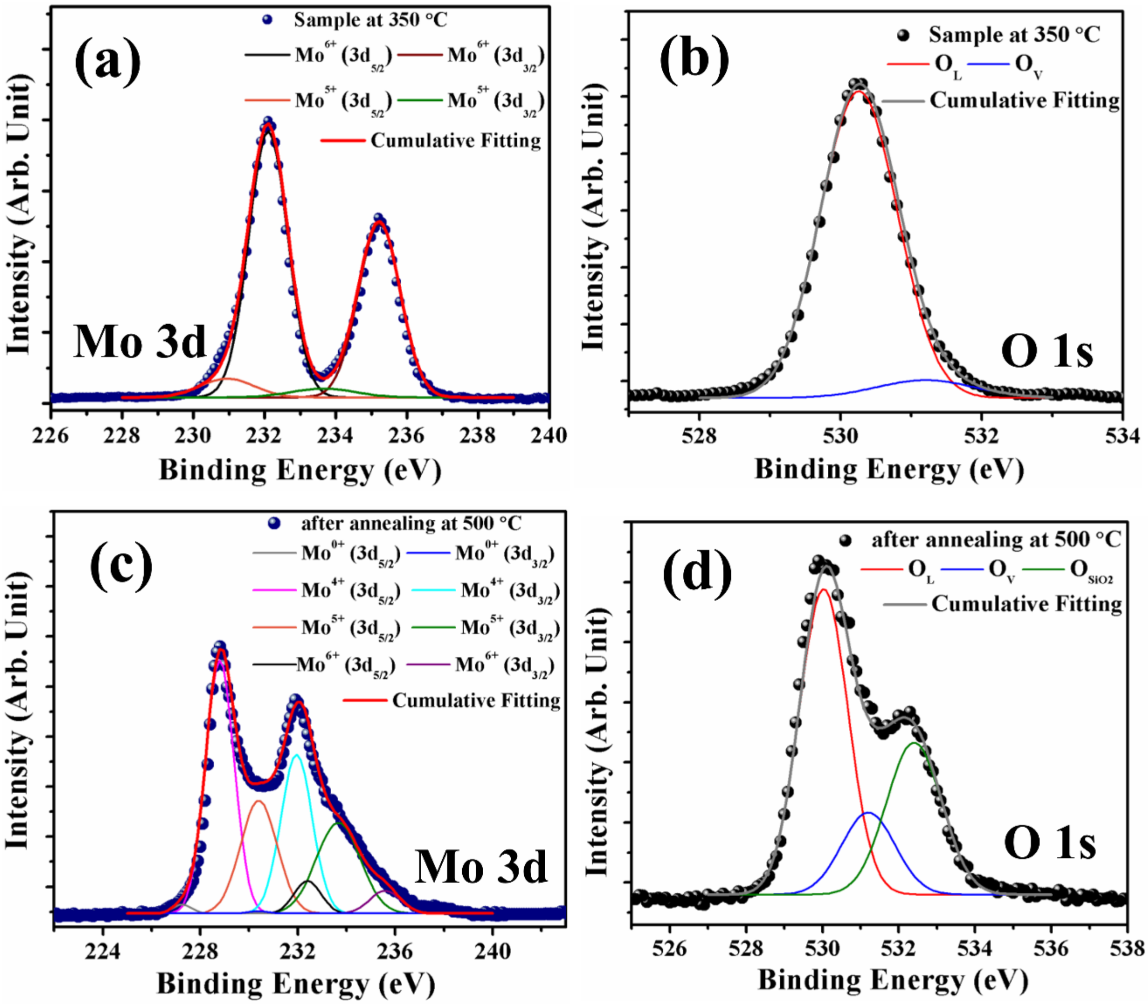

Figure 4.9: *XPS core level spectra of (a) Mo 3d, (b) O 1s from the sample at 350 °C. Core level XPS spectra of (c) Mo 3d and (d) O 1s from the sample after annealing at 500 °C for 30 min [1].*

The Mo 3d core level at 350 °C features four components at 232.35 eV, 235.55 eV, 230.45 eV and 233.65 eV corresponding to Mo^{6+} $3d_{5/2}$, Mo^{6+} $3d_{3/2}$, Mo^{5+} $3d_{5/2}$ and Mo^{5+} $3d_{3/2}$ respectively (as shown in Figure 4.9(a)) [26]. The concentration of Mo^{6+} and Mo^{5+} are 92% and 8%. Figure 4.9(b) displays the O 1s core level spectrum of the same sample and is fitted with two Gaussian peaks at 530.06 eV and 531.20 eV; first peak corresponds to the lattice oxygen (OL) in monoclinic MoO_3 [26] whereas the remaining peak at 531.20 eV originates from the oxygen deficiency (OV) in MoO_3 matrix [4], which is also reflecting from Mo 3d spectrum. As mentioned earlier, the phase of the NPs is monoclinic MoO_2 when growth occurs at a substrate temperature of between 400 °C to 600 °C. XPS measurements were performed on the same sample when heated to 500 °C for 30 min and allowed to cool to room temperature. The results show a clear shift (≈ 3.20 eV) to lower binding energy for the Mo 3d and an extra peak other than lattice oxygen (OL) and OV for O 1s (see Figures 4.9(c) and 4.9(d)). Raising the temperature further to 550 °C (30 min) and allowing to cool, the Mo 3d exhibits an admixture of Mo$^{0+,}$ Mo^{4+} , Mo^{5+} and Mo^{6+} with a larger contribution (59.5%) coming from Mo^{4+} (see Figures 4.10(a) and 4.10(b)).

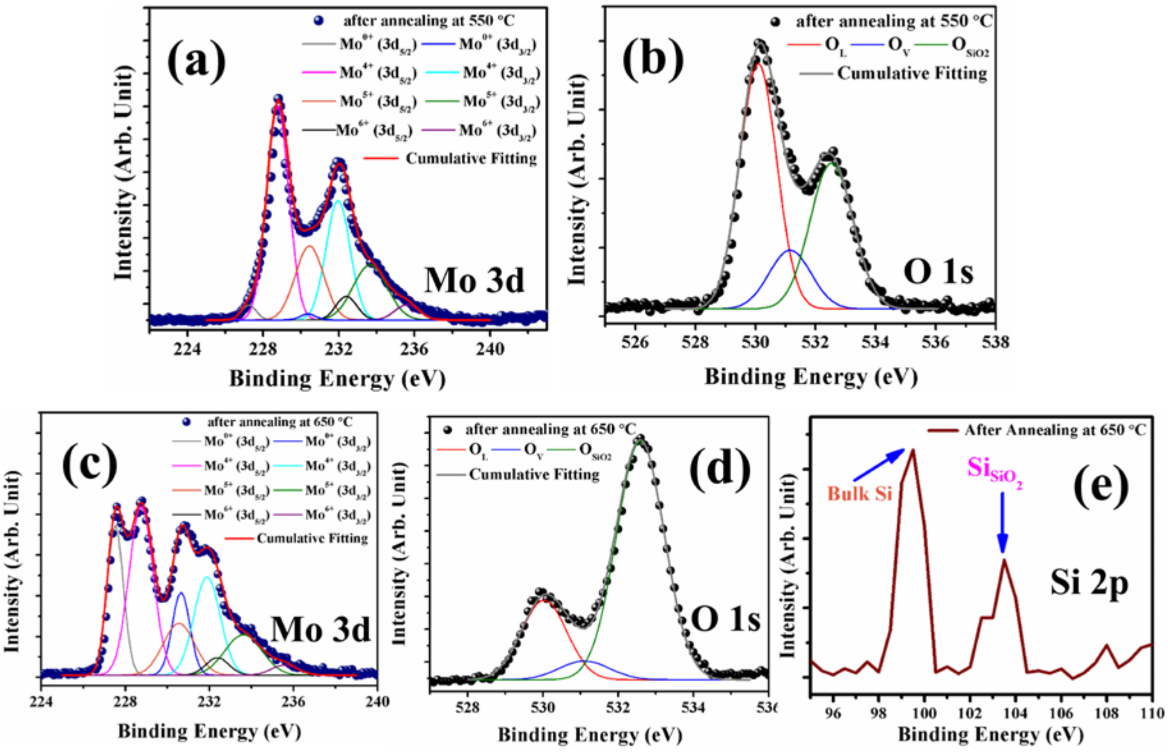

Figure 4.10: *XPS core level spectra of (a) Mo 3d, (b) O 1s from the sample after annealing at 550 °C for 30 min ; (c) Mo 3d and (d) O 1s core level spectra, (e) Si 2p broad level XPS spectra from the same sample after PA at 650 °C for 30 min [1].*

The new components Mo^{0+} attributes to pure metallic molybdenum and Mo^{4+} corresponds to MoO_2. The origin of Mo^{6+} and Mo^{5+} can be associated with all the structures that have not been fully transformed to MoO_2. There were no clear indications of the existence of a sub-oxidized phase of molybdenum from TEM, most likely due to the small amount of Mo^{5+} state as observed in XPS. The Mo 3d core level has been fitted into eight Gaussian components with the peak positions at 227.25 eV, 230.37 eV, 228.77 eV, 231.96 eV, 230.45 eV, 233.65 eV, 232.35 eV and 235.55 eV corresponding to Mo^{0+} $3d_{5/2}$, Mo^{0+} $3d_{3/2}$, Mo^{4+} $3d_{5/2}$, Mo^{4+} $3d_{3/2}$, Mo^{5+} $3d_{5/2}$, Mo^{5+} $3d_{3/2}$, Mo^{6+} $3d_{5/2}$ and Mo^{6+} $3d_{3/2}$ respectively [4,27-29]. The concentration of different components has been given in Table 4.2. The O 1s spectrum, shown in Figure 4.10(b), can be fitted with three Gaussian components at 530.05 eV, 531.20 eV and 532.4 eV and attributed to the lattice oxygen (O_L) of MoO_2, oxygen deficiency (O_V) and the oxidation of the Si substrate (O_{SiO2}), respectively [30-32].

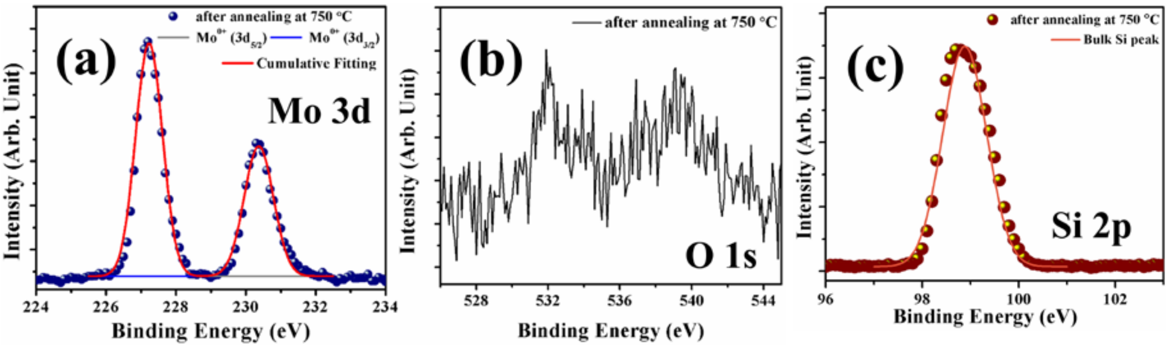

Figure 4.11: *XPS core level spectra of (a) Mo 3d, (b) O 1s and (c) Si 2p from the sample after PA at 750 °C for 30 min [1].*

Next, we annealed the sample to 650 °C for 30 min and measured core level spectrum after allowing to cool to room temperature. Figure 4.10(c) shows peaks consistent with the core level spectrum of Mo 3d. Here also Mo^{4+} is dominating similar to the previous measurements but Mo^{5+} and Mo^{6+} concentrations decrease with increasing annealing temperature. The small contributions coming from Mo^{5+} and Mo^{6+}could be due to residual MoO_3 which is not totally converted to MoO_2. One can decompose Mo 3d peak into eight Gaussian distributions at the same peak positions as for 550 °C temperature case. The concentration of Mo^{0+}, Mo^{4+}, Mo^{5+}, Mo^{6+} components are 27%, 46.4%, 21.8%, 4.7% respectively which can be observed from Table 2 [4,27,28,32]. O 1s core level is presented in Figure 4.10(d). This can be deconvoluted into three Gaussian peaks centered at 530.05 eV, corresponding to lattice oxygen (O_L) with the concentration of 22.6%, 531.20 eV corresponding to O_V with 6% concentration and 532.55 eV related to O_{SiO2} with 71.4% concentration [29-31]. Comparing the intensity and concentration of O_L and O_{SiO2} peaks at 550 °C and 650 °C, we can see that the O_L peak intensity decreases and O_{SiO2} peak intensity increases with increasing temperature. The cause of this likely to be a combination of enhanced exposure of the Si substrate as the coverage area of the nanostructures decreases with increasing temperature together with oxidation of the exposed areas which can be depicted from Si 2p peak (shown in Figure 4.10(e)). In Si 2p broad level spectrum (shown in Figure 4.10(e)), the peak centered at 99.1 eV corresponds to bulk Si whereas the peak at 103.5 eV could be assigned to Si_{SiO2} [30-32]. Direct comparison between XPS and SEM/TEM measurements are not possible due to temperature constraints in our MBE system.

After annealing the sample to 750 °C for 30 min and allow to cool down to room temperature, only two components exist in the Mo 3d core level spectrum (Figure 4.11(a)). After fitting with two Gaussian distributions, the peaks centered at 227.25 eV and 230.37 eV correspond to Mo^{0+} $3d_{5/2}$ and Mo^{0+} $3d_{3/2}$, respectively [29]. The O 1s core level (Figure 4.11(b)) confirms that there is no lattice oxygen, no oxygen deficiency or SiO_2. The lack of SiO_2 is further confirmed in the Si 2p core level (Figure 4.11(c)) spectrum. It clearly shows only one component centered at 99.1 eV attributed to bulk Si. An investigation from Ishizaka *et. al*, has shown that at annealing to 750 °C a thin oxide film will be removed by the following equation in UHV [33]:

$$Si + SiO_2 \rightarrow 2SiO \uparrow \qquad (4.1)$$

Thus, after annealing at 750 °C we are left with only Mo on the surface.

To sum up the XPS results, MoO_3 has been reduced to metallic Mo in two step processes ($MoO_3 \rightarrow MoO_2 \rightarrow Mo$) with the formation of Mo^{5+} state during the first step reduction process (@ 550 °C) due to the UHV annealing. With increasing temperature, the Mo 3d core level shifts towards lower binding energy. A summary of the XPS analyses at different temperatures are tabulated in Table 4.2 including the oxidation state of molybdenum.

Table 4.2: XPS analysis of the sample annealed at different temperatures [1]

Temperature (°C)	**Core levels**	**Binding Energy (eV)**	**FWHM (eV)**	**Concentration (%)**
350	Mo^{5+} $3d_{5/2}$	230.45	1.50	8
	Mo^{5+} $3d_{3/2}$	233.65	1.80	
	Mo^{6+} $3d_{5/2}$	232.35	1.10	92
	Mo^{6+} $3d_{3/2}$	235.55	1.27	
	O_L	530.06	1.20	93.1
	O_V	531.20	1.40	6.9
500	Mo^{0+} $3d_{5/2}$	227.25	0.77	0.9
	Mo^{0+} $3d_{3/2}$	230.37	0.84	
	Mo^{4+} $3d_{5/2}$	228.77	1.17	55.1

	Mo^{4+} $3d_{3/2}$	231.96	1.27	
	Mo^{5+} $3d_{5/2}$	230.45	1.50	36.8
	Mo^{5+} $3d_{3/2}$	233.65	1.80	
	Mo^{6+} $3d_{5/2}$	232.35	1.10	7.2
	Mo^{6+} $3d_{3/2}$	235.55	1.27	
	O_L	530.05	1.20	53.6
	O_V	531.20	1.40	15.9
	O_{SiO2}	532.4	1.45	30.5
550	Mo^{0+} $3d_{5/2}$	227.25	0.77	2.5
	Mo^{0+} $3d_{3/2}$	230.37	0.84	
	Mo^{4+} $3d_{5/2}$	228.77	1.17	59.5
	Mo^{4+} $3d_{3/2}$	231.96	1.27	
	Mo^{5+} $3d_{5/2}$	230.45	1.50	31.2
	Mo^{5+} $3d_{3/2}$	233.65	1.80	
	Mo^{6+} $3d_{5/2}$	232.35	1.10	6.8
	Mo^{6+} $3d_{3/2}$	235.55	1.27	
	O_L	530.05	1.20	50.9
	O_V	531.20	1.40	13.9
	O_{SiO2}	532.40	1.45	35.2
650	Mo^{0+} $3d_{5/2}$	227.25	0.77	27
	Mo^{0+} $3d_{3/2}$	230.37	0.84	
	Mo^{4+} $3d_{5/2}$	228.77	1.17	46.4
	Mo^{4+} $3d_{3/2}$	231.96	1.27	
	Mo^{5+} $3d_{5/2}$	230.45	1.50	21.8
	Mo^{5+} $3d_{3/2}$	233.65	1.80	
	Mo^{6+} $3d_{5/2}$	232.35	1.10	4.7
	Mo^{6+} $3d_{3/2}$	235.55	1.27	
	O_L	530.05	1.20	22.6
	O_V	531.20	1.40	6.0
	O_{SiO2}	532.40	1.45	71.4
750	Mo^{0+} $3d_{5/2}$	227.25	0.77	100
	Mo^{0+} $3d_{3/2}$	230.37	0.84	
	Bulk Si	99.1	1.07	

Subsequent to XPS measurements, the sample was removed from vacuum for microscopy measurements. Figure 4.12(a) displays a SEM micrograph revealing two types of NPs (smaller and bigger). The size distribution of the particles from different SEM frames has been evaluated and fitted with two Gaussian distributions giving average sizes ≈ 16.9 ±0.3 nm and 44.5 ± 0.4 nm for smaller and larger NPs (Figure 4.12(b)).

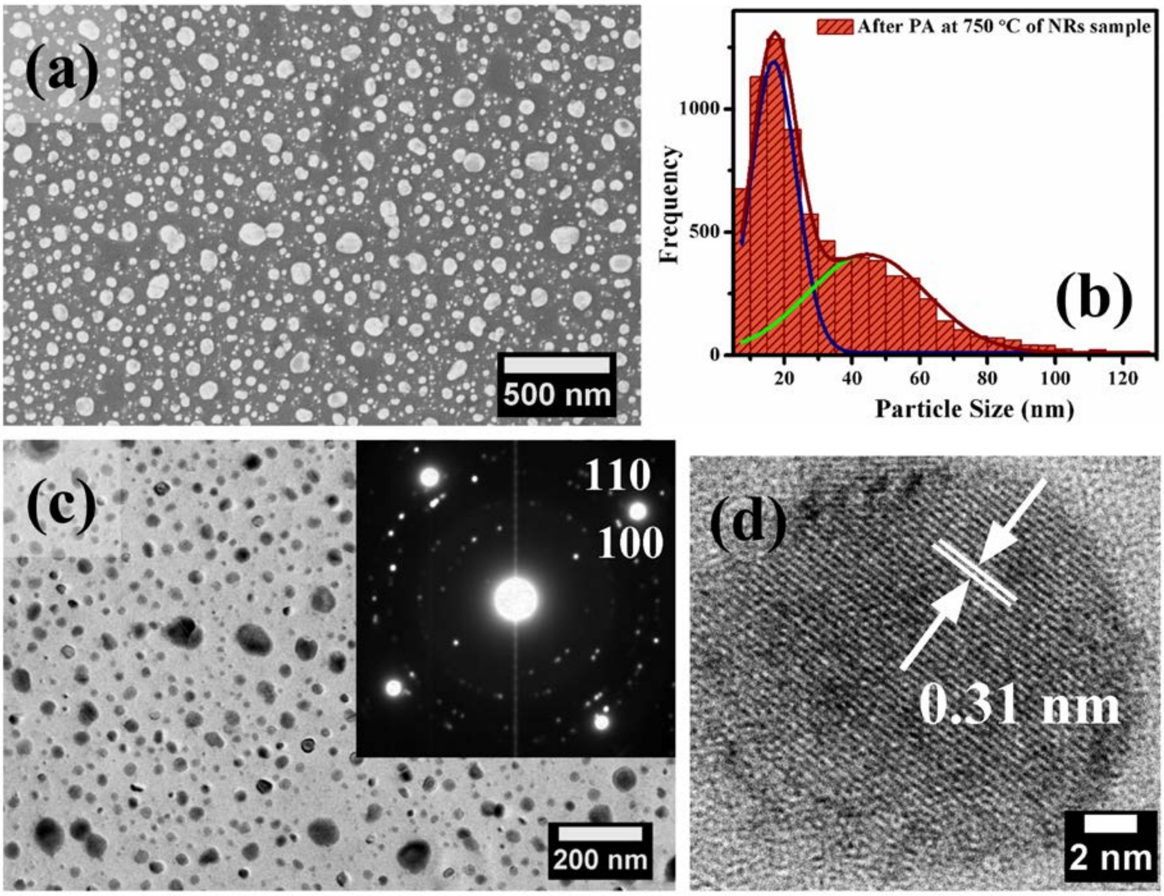

Figure 4.12: *(a) High magnification SEM micrograph of β-MoO_3 nanoribbons (NRs) post annealed at 750 °C for 30 min in ultra-high vacuum (UHV) and (b) corresponding particle size distribution. (c) Planar TEM micrograph of corresponding sample; inset of (c) represents selected area electron diffraction (SAED) pattern. (d) High resolution TEM (HRTEM) image, representing NPs are Mo, and the corresponding d-spacing 0.31 nm of <100> has shown [1].*

Figure 4.12(c) depicts a planer TEM image with a SAED pattern inset showing circular rings of the (100) and (110) planes of cubic Mo. Other spots seen in the SAED pattern are likely to correspond to molybdenum silicide. C. M. Doland *et al* [34] reported that the tetragonal $MoSi_2$ phase was thermodynamically favored in the presence of excess silicon after annealing to 788 °C in UHV. The lattice spacing of ≈ 0.31 nm calculated from HRTEM (see Figure 4.12(d)) represents $d_{(100)}$ of Mo. The reason for the bimodal distribution could result from the following mechanism. From kinetic Monte Carlo simulations, Yu *et al* have shown two growth mechanisms for the formation of Si nanocrystals (NCs) in the Si sub-oxide matrix. They appear to grow through coalescence or via pseudo-Ostwald ripening, both processes having very different time constants. At the early stage of annealing where the clusters are close to each other the growth follows the coalescence mechanism. When the cluster density is low i.e., they are separated by large distances, pseudo-Ostwald ripening becomes important. These two different mechanisms lead to the formation of two types of Si-NCs with different sizes [35, 36]. Similarly, in our case we have already seen from Table 4.1 that the particle density increases with increasing substrate temperature from 400 °C to 600 °C. With a further increase in temperature, the density was probably enough for the coalescence like mechanism to dominate and at 750 °C both growth mechanisms give two different sized NPs. This is possibly due to the chemical phase separation, controlled by diffusion of O atoms.

4.3.2 KPFM Results

We have experimentally measured the local work function of three samples: MoO_3 NRs (β-MoO_3 grown at 350 °C), MoO_2 NPs (β-MoO_2 grown at 550 °C) and Mo NPs (NRs sample annealed to 750 °C) by Kelvin probe force microscopy (KPFM) technique. When an AFM tip is brought close to the sample surface, due to the difference in their work function values, an electric force will be acted between tip and the sample surface. To nullify the generated electrostatic force, an external DC voltage V_{DC} whose amount is equal but the polarity is opposite to contact potential difference V_{CPD} has to be applied for the compensation of the work function difference. So the mapping of this nullifying V_{DC} with the lateral position coordinate composes work function mapping image of the sample surface called KPFM image. So the work function of the sample surface can be calculated by the following equation [4]

$$V_{DC} = V_{CPD} = (\Phi_{tip} - \Phi_{sample})/q \tag{4.2}$$

Where, Φ_{tip} and Φ_{sample} are work function of the tip and sample respectively. The work function of the tip has been calibrated with respect to standard HOPG sample and comes out to be Φ_{tip}= 5.2eV. So Φ_{sample} will be

$$\Phi_{sample} = \Phi_{tip} - qV_{CPD} = 5.2 \text{ eV} - qV_{CPD} \tag{4.3}$$

So, larger the value of V_{CPD}, lower the work function of the sample.

Figure 4.13(a), (b) and (c) represent work function mapping images of β-MoO_3 NRs, β-MoO_2 NPs and Mo NPs samples, respectively and the work function values are found to be ≈ 5.27 ± 0.05 eV, ≈ 5.10 ± 0.05 eV, and ≈ 4.83 ± 0.05 eV for the respective samples consistent with the literature [37,38]. It is clear from the experimental results that with the reduction from MoO_3 to Mo, the work function decreases from 5.27 eV to 4.83 eV. This reduction in work function with decreasing cation oxidation state can be attributed to (i) lower electronegativity of lower oxidation state of cation and (ii) increase in valence donor states with decreasing cation oxidation states [39].

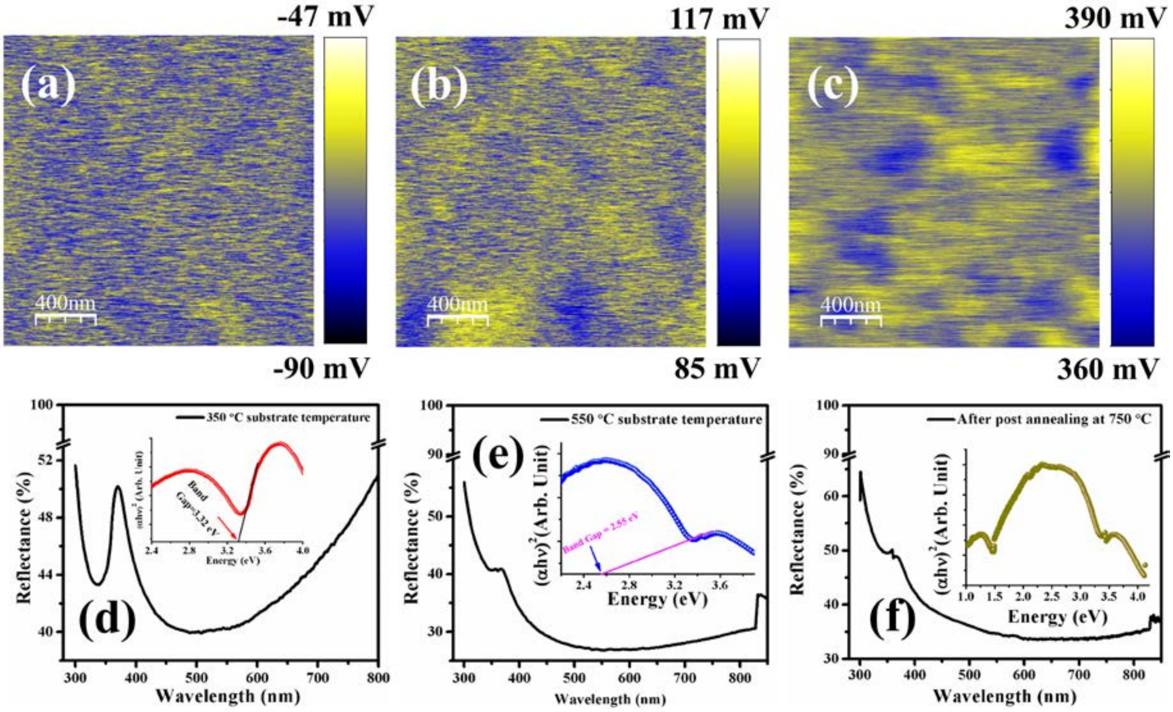

Figure 4.13: *(a-c) Work function mapping by Kelvin probe force microscopy (KPFM) technique and (d-f) UV-Vis reflectance spectra from* MoO_3 *nanoribbons (NRs) sample (at 350 °C),* MoO_2 *NPs sample (at 550 °C) and Mo NPs sample (at 750 °C) respectively; insets of (d-f) are the corresponding* $(\alpha h\nu)^2$ *vs.* $(h\nu)$ *plots [1].*

4.3.3 UV-Vis-NIR Spectroscopy

To measure the band gap of these three types of morphologies, we have performed UV-Vis-NIR spectroscopy in reflectance mode. Kubelka-Munk equation has been used to get the absorbance from the reflectance data and made a Tauc plot to get the band gap.

Kubelka-Munk equation [40]:

$$\text{Absorbance } (\alpha) = (100-R)^2/(2\times R) \qquad (4.4)$$

Where, R is the reflectance.

Tauc plot:

$$\alpha h\nu = \text{Constant } (h\nu - E_b)^n \qquad (4.5)$$

Where hν: photon energy, E_b: band gap of the material, n is a parameter determined by the type of transition. Here we use n=1/2 for direct allowed transition of MoO_3; [41]. So,

$$(\alpha h\nu)^2 = \text{Constant}\ (h\nu - E_b) \qquad (4.6)$$

Figures 4.13(d), (e), and (f) show reflectance spectras and their insets depict the $(\alpha h\nu)^2$ as a function of photon energy (hν) taken from the previously mentioned three samples i.e., β-MoO_3 NRs, β-MoO_2 NPs and Mo NPs, respectively. We observe the band gap of β-MoO_3 NRs to be ≈ 3.32 eV [42] whereas the band gap of β-MoO_2 NPs is found to be ≈ 2.55 eV which matches to the earlier reports [15]. The post-annealed (@ 750 °C) sample in the XPS chamber did not show any band gap because it was in the pure metal molybdenum phase. With increasing degree of reduction, the lattice collapses leading to strong changes in the electronic density of states due to the filling of Mo 4d states. As a result, the initial wide band gap (MoO_3) has reduced to semi metallic (MoO_2) and then to metallic Mo [42]. We have tabulated band gaps for the different phases and morphologies in Table 4.3.

Table 4.3: Band gap for different substrate temperatures [1]

Type of morphology (Phase)	Band gap (eV)
350 °C (NRs) (β-MoO_3)	3.32
550 °C (NPs) (β-MoO_2)	2.55
750 °C (Mo)	--

4.4 Conclusion

In summary, this chapter reported a simple thermal reduction from MoO_3 to Mo in UHV using MBE. XRD data has revealed that NRs, grown at 350 °C substrate temperature, are in the β phase of MoO_3. At 400 °C substrate temperature, the morphology changes from nanoribbons to nanoparticles and the phase changes from monoclinic MoO_3 to monoclinic MoO_2. β-MoO_2 phase persists up to 600 °C substrate temperature. We have described the possible reduction process by *in-situ* XPS study, where we have started with β-MoO_3 nanoribbon sample and ended up with Mo nanoparticles after annealing at 750 °C via β-MoO_2 phase with detailed elemental quantification for the different temperatures. The results showed that the phase transition from β-MoO_2 to Mo had initiated at 650 °C. We experimentally measured the work function of the different phases of molybdenum oxide and molybdenum by KPFM. The reduction in Φ value with increasing temperature can be understood by the decreasing oxidation state of Mo during the phase transition from MoO_3 to MoO_2 to Mo. The band gaps of β-MoO_3 and β-MoO_2 are found to be 3.32 eV and 2.55 eV, respectively. Next chapter, we will discuss the effect of film thicknesses and different substrate on the growth and characteristics of NRs.

4.5 References

[1] P. Maiti, P. Guha, H. Hussain, R. Singh, C. Nicklin and P. V. Satyam, *Surf. Sci.* 2019, 682, 64.

[2] L. Kihlborg, *Arkiv. Kemi*. 1964, 21, 357.

[3] I. A. Castro, R. S. Datta, J. Z. Ou, A. C. Gomez, S. Sriram, T. Daeneke, and K. Kalantar-zadeh, *Adv. Mater.* 2017, 1701619.

[4] P. Guha, A. Ghosh, R. Thapa, E. M. Kumar, S. Kirishwaran, R. Singh, and P. V. Satyam, *Nanotechnology* 2017, 28, 415602.

[5] T. Siciliano, A. Tepore, E. Filippo, G. Micocci, and M. Tepore, *Mater. Chem. Phys.* 2009, 114, 687.

[6] A.J. M. Mendoza, J. L. Lado, J. O. Island, M. A. Nino, L. Aballe, M. Foerster, F. Y. Bruno, A. L. Moreno, L. V. Garzon, H. S. J. van der Zant, G. R. Bollinger, N. Agraït, E. M. Pérez, J. F. Rossier, and A. C. Gomez, *Chem. Mater.* DOI: 10.1021/acs.chemmater.6b01505.

[7] R. Sivakumar, R. Gopalakrishnan, M. Jayachandran, and C. Sanjeeviraja, *Curr. Appl. Phys.* 2007, 7, 51.

[8] S. H. Mohamed and S. Venkataraj, *Vacuum* 2007, 81, 636.

[9] A. A. Bolzan, B. J. Kennedy, and C. J. Howard, *Aust. J. Chem.* 1995, 48, 1473.

[10] M. Ferroni, V. Guidi, G. Martinelli, M. Sacerdoti, P. Nelli, and G. Sberveglieri, *Sens. Actuator B* 1998, 48, 285.

[11] Z. C. Xiang, Q. Zhang, Z. Zhang, X. J. Xu, and Q. B. Wang, *Ceram. Int.* 2015, 41, 977.

[12] S. Wanga, C. Anb, Y. Zhanga, Z. Zhanga, and Y. Qiana, *J. Cryst. Growth* 2006, 293, 209.

[13] Y. Liang, Z. Yi, S. Yang, L. Zhou, J. Sun, and Y. Zhou, *Solid State Ion*. 2006, 177, 501.

[14] X. Liu, Y. He, S. Wang, and Q. Zhang, *J. Alloys. Compd.* 2011, 509S, S408.

[15] N. Dukstiene, D. Sinkeviciute, and A. Guobiene, *Cent. Eur. J. Chem.* 2012, 10(4), 1106.

[16] F. C. Nix, and D. MacNair, *Phys. Rev.* 1942, 61, 74.

[17] J. Dang, G-H. Zhang, and K-C. Chou, *Int. J. Refract. Metals Hard Mater* 2013, 41, 356.

[18] J. Dang, G. -H. Zhang, and K. -C. Chou, *High Temp. Mater. Proc.* 2014, 33(4), 305.

[19] D. Wang, D.S. Su, and R. Schlögl, *Z. Anorg. Allg. Chem.* 2004, 630, 1007.

[20] B. Hu, L. Mai, W. Chen, and F. Yang, *ACS Nano.* 2009, 3, 478.

[21] https://www.diamond.ac.uk/Instruments/Magnetic-Materials/I06/status.html

[22] J. B. Parise, E. M. McCarron, R. V. Dreele, and J. A. Goldstone, *J. Solid State Chem.* 19991, 93, 193.

[23] T. Mizushima, Y. Moriya, N. H. H. Phuc, H. Ohkita, and N. Kakuta, *Cetal. Commun.* 2011, 13, 10.

[24] P.F. Carcia, and E.M. III McCarron, *Thin Solid Films* 1987, 155, 53.

[25] T. Ressler, R. E. Jentoft, M.M. Gunter, and O. Timpe, *J. Phys. Chem. B* 2000, 104, 6360.

[26] E. Comini, G. Faglia, G. Sberveglieri, C. Cantalini, M. Passacantando, S. Santucci, Y. Li, W. Wlodarski, and W. Qu, *Sens. Actuator B* 2000, 68, 168.

[27] X. Zhao, M. Cao, B. Liu, Y. Tian, and C. Hu, *J. Mater. Chem.* 2012, 22, 13334.

[28] Y. Jin, and P. K. Shen, *J. Mater. Chem. A* 2015, DOI: 10.1039/C5TA06018D.

[29] G. E. Buono-Core, A. H. Klahn, C. Castillo, E. Muñoz, C. Manzur, G. Cabello, and B. Chornik, *J. Non-Cryst. Solids* 2014, 387, 21.

[30] T. A. Dang, and C. N. Chau, *J. Electrochem. Soc.* 1996, 143, 302.

[31] D. S. Jensen, S. K. Kanyal, N. Madaan, M. A. Vail, A. E. Dadson, M. H. Engelhard, and M. R. Linford, *Surf. Sci. Spectra* 2013, 20.

[32] A. Bensalem, F. Bozon-Verduraz, M. Delamar, and G. Bugli, *Appl. Catal. A: General* 1995, 121, 81.

[33] A. Ishizaka, and Y. Shiraki, *J. Electrochem. Soc.* 1986, 133, 666.

[34] C. M. Doland, and R. J. Nemanich, *J. Mater. Res.* 1990, 5, 12.

[35] D. Yu, S. Lee, and G. S. Hwang, *J. Appl. Phys.* 2007, 102, 084309.

[36] K. Wei-Wei, F. Xue, and H. Yi-Dong, *Chin. Phys. Lett.* 2012, 29, 016402.

[37] Irfan; F. So, and Y. Gao, *Int. J. of Photoenergy* 2011, Article ID 314702.

[38] S. Berg, P. O. Gartland, and B. J. Slagsvold, *Surf. Sci.* 1974, 43, 275.

[39] M. T. Greiner, L. Chai, M. G. Helander, W. M. Tang, and Z. -H. Lu, *Adv. Funct. Mater.* 2012, DOI: 10.1002/adfm.201200615.

[40] J. Klaas, G. Schulz-Ekloff, and N. I. Jaeger, *J. Phys. Chem. B* 1997, 101, 1305.

[41] C. Julien, A. Khelfa, O. M. Hussain and G. A. Nazri, *J. Cryst. Growth* 1995, 156, 235.

[42] K. Inzani, M. Nematollahi, F. Vullum-Bruer, T. Grande, T. W. Reenaas, and S. M. Selbach, *Phys. Chem. Chem. Phys.* 2017, DOI: 10.1039/C7CP00644F.

Chapter 5

Optical Band Gap, Local Work Function and Field Emission Properties of MBE Grown β-MoO_3 Nanoribbons

5.1 Introduction

In the previous chapter, we have discussed on the growth and characteristics study of defect free, mixed phase free metastable molybdenum trioxide (β-MoO_3) and MoO_2 and then the phase transition from β-MoO_3 to MoO_2 to Mo by simple thermal reduction process in ultra-high vacuum (UHV) condition by molecular beam epitaxy (MBE) technique. In this current chapter, detailed report is given on determination of the optical band gap, local work function and field emission properties of thickness-dependent MBE grown β -MoO_3 nanoribbons using UV-Vis, KPFM and other associated methods. Emphasis is also given to understand the growth of MoO_3 on the various substrates (such as, Si(100), Si(5512) and fluorine-doped tin oxide (FTO)) by MBE technique under UHV conditions. The dependence of substrate conditions and the effective thickness of MoO_3 films on the morphology of nanostructures and their structural aspects have also been reported. The electron microscopy measurements show that the length and the aspect ratio of nanostructures increased by, 260% without any significant change in the width for a change in effective thickness from 5 nm to 30 nm. NRs are grown along <011> for all the effective thickness of MoO_3 films.

The work presented in this chapter has been published in "P. Maiti, P. Guha, R. Singh, J. K. Dash and P. V. Satyam, *Appl. Surf. Sci.* 2019, 476, 691".

Similarly, when we increased the film thickness from 5 nm to 30 nm, the optical band gap decreased from 3.38± 0.01eV to 3.17± 0.01eV and the local work function increased from 5.397 ± 0.025 eV to 5.757 ± 0.030 eV. Field emission turn-on field decreased from 3.58 V/μm for 10 μA/cm^2 to 2.5 V/μm and field enhancement factor increased from 1.1×10^4 to 5.9×10^4 for effective thickness variation of 5 nm to 30 nm β-MoO_3 structures. The β-MoO_3 nanostructures found to be much better than the α-MoO_3 nanostructures due to low work function, low turn on field and high field enhancement factor, and are expected to be useful applications [1].

In this study, we report on the growth and application of β-MoO_3, usually possible in the clean environment (like UHV-MBE) condition, which is found to have superior properties compared to α-MoO_3 nanostructures. While many reports found β-MoO_3 to be meta-stable, our results show a consistently stable growth of this phase using molecular beam epitaxy (MBE) under ultra-high vacuum condition. The enhanced field emission characteristics of self-assembled grown β-MoO_3 NRs of different thickness have been studied in this chapter and compared the results with previously addressed values and shown that β-MoO_3 NRs are better in field emission than α-MoO_3 nanostructures. Details of β-MoO_3 crystal structure, transition temperature from β-MoO_3 to α-MoO_3 have been described in the previous chapters.

Though there are different techniques to grow β-MoO_3 but many of these processes are found to be unsuccessful because of the proper molybdic source, metastable state of β-MoO_3 and the final product detected as stable α-MoO_3. E. M. McCarron et al. showed the formation of β-MoO_3 from the thermal treatment of spray-dried powders of aqueous molybdic acid solutions [2]. I. Jua´ rez Ramı´rez described that β-MoO_3 was prepared by ion exchange of an aqueous solution of Na_2MoO_4. $2H_2O$ passed through a cation-exchange resin (Dowex 50WX8-200) [3]. Other research groups reported the synthesis of β-MoO_3 from peroxo-polymilybdate [4], commercial α-MoO_3 [5], and sodium molybdate solution [6]. However, very few reports are seen on MoO_3 nanostructures grown by molecular beam epitaxy (MBE) technique. Like Kazuto Koike et al. have showed the growth of amorphous, (100) β phase and (010) α phase of MoO_3 films at 150, 200, and 350 °C respectively on sapphire substrates by MBE technique. They also reported β to α-MoO_3 transformation at 600 °C. They used RF plasma cell for oxygen radicals to terminate the surface by oxygen atoms before deposition of MoO_3 films on the substrate surface at different temperature [7]. Recently, epitaxial β-MoO_3 film has been grown on lattice matched $SrLaAlO_4$(001) substrate by oxygen plasma assisted MBE [8]. Lu Wang et al. reported in their paper almost spherical particle of β-MoO_3 with average particle size less than 1 μm [9]. Davide Mariotti et al. showed 0.3 mm wide and up to 2 mm long β-MoO_3

nanosheets produced by atmospheric micro plasma [10]. Thi Thuy Phuong Pham et al. described in their paper that prepared β-MoO_3 was composed of small primary particles in the range 50–100 nm [11]. *In this study, highly crystalline β-MoO_3 nanoribbons (NRs) were grown in an ultra-high vacuum chamber using commercially available α-MoO_3 powder as source material without passing any oxygen gas to maintain the stoichiometry by molecular beam epitaxy (MBE) technique.*

Scanning electron microscope (SEM), transmission electron microscope (TEM) and grazing incidence X-ray diffraction (GIXRD) techniques were utilized for structural characterizations of as-synthesized nanostructures. We employed UV-Visible-NIR spectroscope for optical properties and Kelvin probe force microscope (KPFM) for local work function measurements of the as-grown material.

5.2 Experimental Details

Growth of molybdenum trioxide was carried out in Omicron based MBE system and details of the setup are given in earlier chapters. The properties of materials, such as, surface morphology, shape and size, structural characterizations of as-grown samples had been determined using the microscopy facilities, such as, FEGSEM, TEM and GIXRD. Ultraviolet-visible-near infrared (UV-Vis-NIR) spectrophotometer was used to measure the optical properties of the as-grown samples at room temperature. To measure the local work function of as-prepared NRs, Kelvin probe force microscopy (KPFM) technique was employed with atomic force microscope (AFM) in lift mode, with a lift height of 100 nm, using conductive Ir/Pt tip (AC240TM, Electric-Lever, Olympus) of ≈ 30 nm radius of curvature, ≈ 2 N-m^{-1} stiffness, and a resonance frequency of ≈ 70 kHz. The change in contact potential difference (V_{CPD}) with the lift height (up to 3 μm) was carried out.

To measure field emission (FE) properties of as-grown samples, a high vacuum (≈ 2.3×10^{-7} mbar) chamber by Excel Instruments, FE System-150, was used. In diode configuration, a copper plate of ≈ 2.5 mm tip diameter acts as anode and the NRs samples of different thickness were used as cathode. To secure the samples we have used copper tape. To measure FE we put anode-sample separation of ≈ 50 μm (5 nm), ≈ 40 μm (10 nm), ≈ 50 μm (20 nm), and ≈ 40 μm (30 nm) for NRs samples.

5.3 Results and discussion

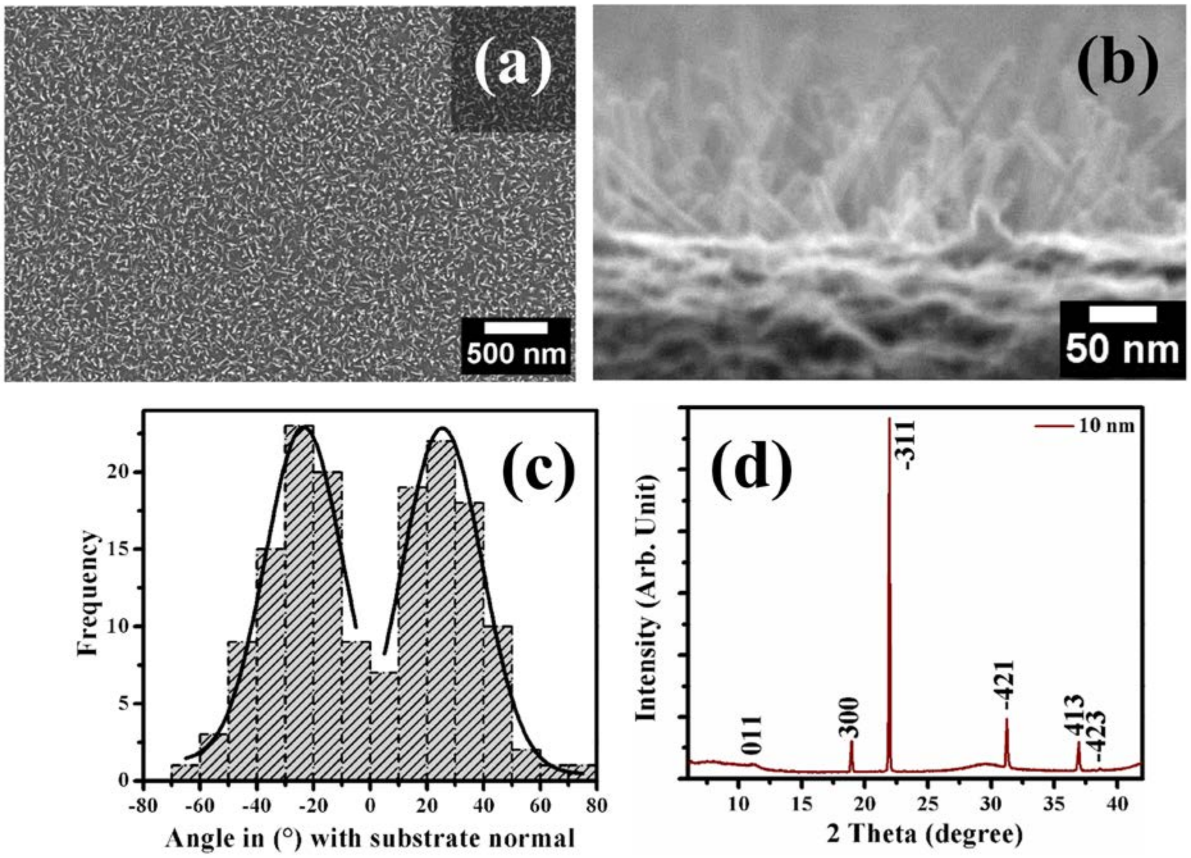

Figure 5.1: *(a) High magnification and (b) cross sectional SEM micrographs of 10 nm MoO_3 grown on cleaned Si(100) substrate at substrate temperature 350 °C, (c) angular distribution corresponding to the size of the nanoribbon structures with substrate normal, (d) GIXRD spectrum of corresponding sample [1].*

Figure 5.1(a) depicts SEM micrograph from the surface of 10 nm MoO_3 film deposited on cleaned Si(100) at 350 °C substrate temperature under ultra-high vacuum condition. Here, cleaned Si(100) surface refers to the removal of native oxide by two step process, often known as reconstructed surface (as explained in section 5.2). The micrograph shows the presence of nanoribbon (NRs) like structures. Cross-sectional view of the sample (Figure 5.1(b)) shows that NRs oriented in two directions with respect to substrate normal. Measuring the angle of NRs with substrate normal, angular distribution curve is shown in Figure 5.1(c). Most of the NRs are oriented at an average angle of ± 24° with the substrate normal.

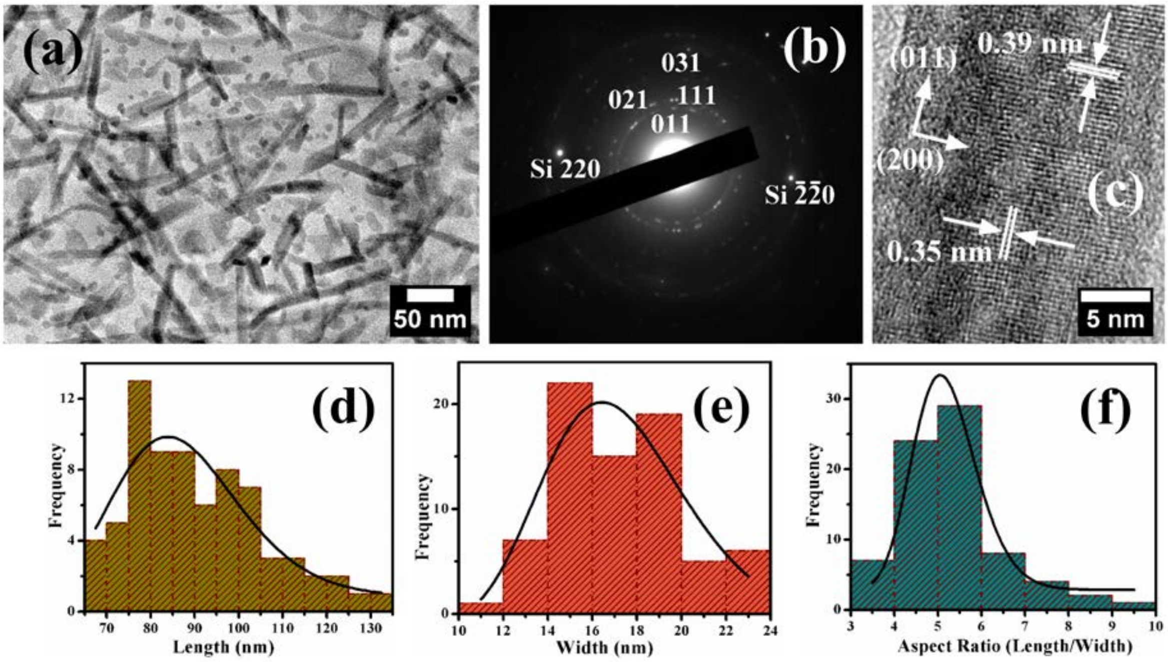

Figure 5.2: *(a) Planar TEM micrograph of 10 nm MoO_3 deposited on cleaned Si(100) substrate at 350 °C and the corresponding selected area electron diffraction (SAED) pattern has been shown in (b). (c) High resolution TEM (HRTEM) image, representing preferential growth along <011>. Typical size distributions i.e., length, width and aspect ratio of NRs are shown in (d), (e), (f) respectively [1].*

To get the macro-scale crystalline information, the grazing incidence X-ray diffraction (GIXRD) measurement was carried out using synchrotron X-rays at Photon Factory, Japan (Indian beam line) and shown in Figure 5.1(d). All the peaks could be indexed to monoclinic phase of MoO_3 (β-MoO_3) (JCPDS card, #89-1554) [12]. From XRD spectrum, stronger intensities are observed for the reflection peaks of (011), (300), (-311), (-421), (413), (-423) and the data is found to be in good agreement with Thi Thuy Phuong Pham et al. [11] and Lu Wang et al. [9]. The XRD data confirms the formation of β-MoO_3 phase. Figure 5.2(a) shows a planar TEM image of 10 nm MoO_3 deposited on cleaned Si(100) substrate at 350 °C substrate temperature. Selected area electron diffraction (SAED) shown in Figure 5.2(b) corresponds to the area shown in Figure 5.2(a). The circular rings indicated in Figure 5.2(b) correspond to the (011), (111), (021), (031) planes of β-MoO_3. The high-resolution TEM (HRTEM) image shown in Figure 5.2(c) confirms the β-MoO_3 structure. The inter-planar lattice plane spacing of 0.39 nm and 0.35 nm, corresponds to the d spacing (d_{011} and d_{200}) of (011) and (200) planes of β-MoO_3 respectively and represents the preferential growth of NRs along <011>. Typical size histograms shown in Figure 5.2(d), 5.2(e), and 5.2(f) represent length, width and aspect ratio of the above NRs sample respectively. For calculating the average length, width and aspect ratio of the NRs, corresponding histograms have been fitted with log-normal distribution; the average value of length and width come out to be 86.0 ± 2.0 nm and 17.1 ± 0.9 nm respectively with the mean aspect ratio 5.2 ± 0.1. All the error bars describe here are fitting error.

5.3.1 Substrate dependent effect

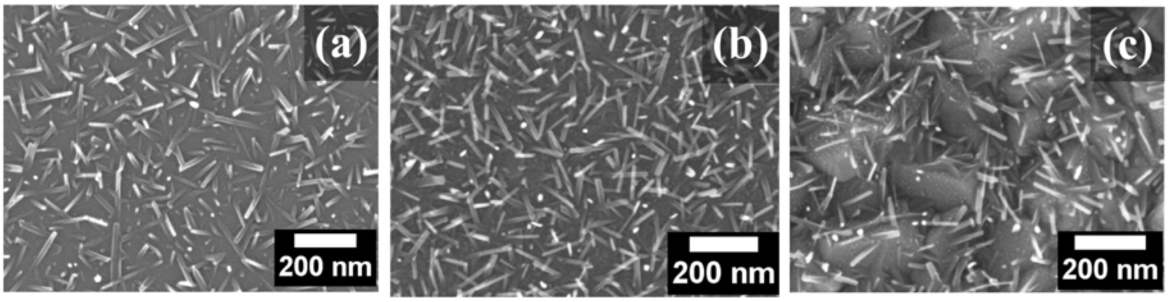

Figure 5.3: *10 nm MoO_3 deposition on (a) Si(100) with native oxide layer, (b) atomically cleaned Si(5512) and (c) FTO at 350 °C substrate temperature [1].*

Furthermore, β-MoO_3 NRs were also synthesized on different commercially available substrates like Si(100) with native oxide (i.e., SiO_x/Si(100)), higher index Si substrates like Si(5512) and FTO keeping the same growth parameters as for cleaned Si(100) substrate (i.e., 10 nm MoO_3 deposition at 350 °C substrate temperature by RH) and their morphologies are shown in Figure 5.3(a), (b), (c) respectively. No significant change in the morphology, affected by the substrates was observed. For Si(100) with native oxide layers shown in Figure 5.3(a), measured length, width and aspect ratio of the NRs are 74.0 ± 6.0 nm, 12.3 ± 0.4 nm and 6.1 ± 0.3 respectively. NRs with 98.0 ± 1.0 nm length, 15.2 ± 0.7 nm width and aspect ratio of 6.4 ± 0.3 are found for cleaned Si(5512) substrate (see Figure 5.3(b)). Figure 5.3(c) depicts the same morphology i.e., NRs, grown on the FTO substrate. Even though the surface roughness is very high, it does not effect on the growth of the NRs. Length, width and aspect ratio of the NRs grown on FTO substrate are 95.0 ± 1.0 nm, 15.7 ± 0.4 nm and 5.6 ± 0.2 respectively. Tabulated structural dimensions of NRs grown on various substrates have been shown in Table 5.1. Here, we can say that growth of β-MoO_3 NRs are almost independent of substrates; furthermore out of plane unidirectional growth of the NRs structures is also substrate independent phenomena for this particular case.

Table 5.1: Structural dimensions of the NRs grown on different substrates [1]

Substrates	Length (nm)	Width (nm)	Aspect Ratio
Cleaned Si(100)	86.0±2.0	17.1±0.9	5.2±0.1
Si(100) with native oxide	74.0±6.0	12.3±0.4	6.1±0.3
Cleaned Si(5512)	98.0±1.0	15.2±0.7	6.4±0.3
FTO	95.0±1.0	15.7±0.4	5.6±0.2

5.3.2 Thickness dependent effect

From the above substrate dependent study, one can observe that the native oxide layers on Si(100), do not play any role in the growth of β-MoO_3 NRs. Hence for the thickness dependent study, Si(100) with native oxide layers has been used as substrate. A thickness of 5, 10, 15, 20 and 30 nm MoO_3 were deposited at 350 °C substrate temperature on SiO_x/Si(100) substrates (i.e., having ≈ 2-3 nm native oxide layer) and the morphology of these various thickness films is shown in the Figure 5.4(a), (b), (c), (d) and (e), respectively. In each case, the length, width and aspect ratio of the NRs were measured as mentioned before and then fitted with log-normal least square fitting procedures (refer: Table 5.2). For 5 nm case, length of the NRs is 57.9±0.3 nm, width is 14.9±0.3 nm and aspect ratio is 3.9±0.1. Length, width and aspect ratio of NRs in 10 nm case (see Figure 5.4(b)) are 74.0±6.0 nm, 12.3±0.4 nm and 6.1±0.3 respectively. Figure 5.4(c) depicts for 15 nm thickness of MoO3 deposition. In this case, length, width and aspect ratio of NRs are 102.0±3.0 nm, 14.1±0.2 nm and 7.7±0.4, respectively. Length and aspect ratio are gradually increasing but width is almost unchanged. In similar fashion, length, width and aspect ratio of NRs for 20 nm thickness deposition have been calculated and found to be 158.0±1.0 nm, 14.5±1.5 nm and 11.8±0.1. For the last case i.e., 30 nm deposition, length of NRs is 195.0±3.0 nm, width is 13.7±0.6 nm, and aspect ratio becomes 14.1±0.5. Cross sectional view of NRs from 30 nm thickness sample have been shown in Figure 5.4(f). Length, width and aspect ratio for each thickness have been tabulated in Table 5.2 and graphically presented in Figure 5.5.

Length of the NRs is gradually increasing from 57.9±0.3 nm to 195.0±3.0 nm (see Figure 5.5(a)) whereas the width is not changing much. As the width is almost constant (Figure 5.5(b)); aspect ratio will definitely follow length and is gradually increasing from 3.9±0.1 to 14.1±0.5 with increase of thickness from 5 nm to 30 nm (shown in Figure 5.5(c)). From thickness dependent study, we can say that the growth rate is quite higher in <011> than other perpendicular directions like <200>.

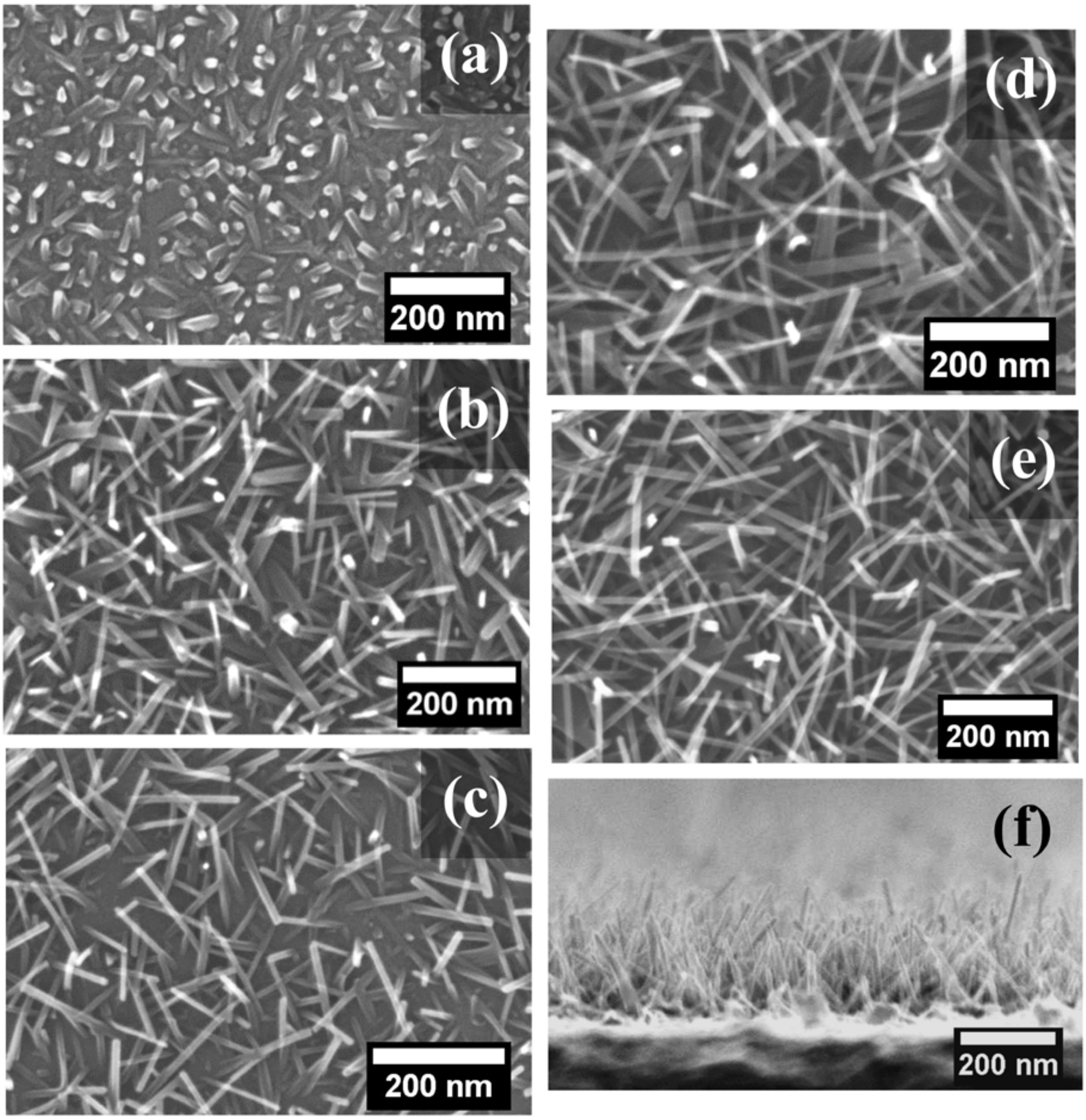

Figure 5.4: *(a) 5 nm, (b) 10 nm, (c) 15 nm, (d) 20 nm, (e) 30 nm* MoO_3 *deposition on Si(100) substrates with native oxide at 350 °C substrate temperature and (f) the cross sectional SEM micrographs of (e) [1].*

Table 5.2: Dimensions of β-MoO_3 NRs with different thicknesses [1]

Thickness (nm)	Length (nm)	Width (nm)	Aspect Ratio
5	57.9±0.3	14.9±0.3	3.9±0.1
10	74.0±6.0	12.3±0.4	6.1±0.3
15	102.0±3.0	14.1±0.2	7.7±0.4
20	158.0±1.0	14.5±1.5	11.8±0.1
30	195.0±3.0	13.7±0.6	14.1±0.5

To validate our argument, TEM characterization on 30 nm deposited MoO_3 sample have been carried out and presented in Figure 5.6. For TEM characterization in this case; the as-prepared samples were scrapped off from the substrates and dispersed into methanol and then drop casted on commercially available carbon coated copper grids. Figure 5.6(a) shows TEM micrograph of MoO_3 NRs; 5.6(b) represents selected area electron diffraction (SAED) pattern from yellow marked region of 5.6(a). The high resolution TEM (HRTEM) image of corresponding NR is presented in Figure 5.6(c), depicting the preferential growth along <011>.

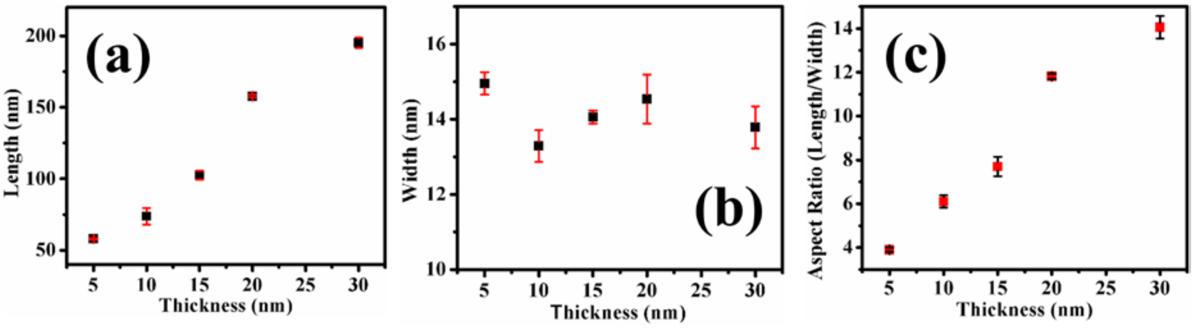

Figure 5.5: *(a) Length, (b) width and (c) aspect ratio of NRs with different thickness of* MoO_3 *deposited on Si(100) with native oxide layer at 350 °C substrate temperature [1].*

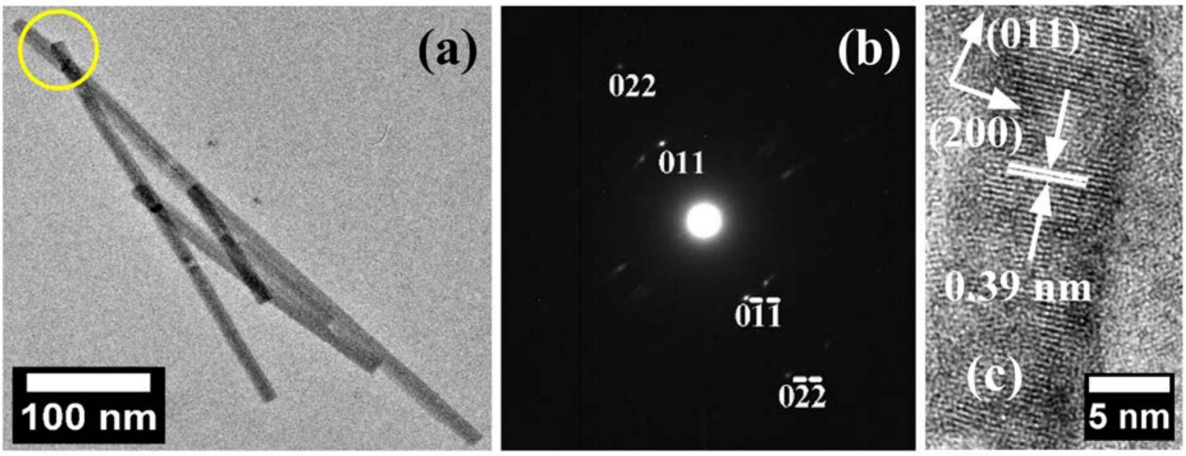

Figure 5.6: *(a) TEM micrograph of* MoO_3 *NRs for the case of 30 nm* MoO_3 *deposition. (b) Selected area electron diffraction (SAED) pattern from yellow marked region of (a). (c) High resolution TEM (HRTEM) image of corresponding NRs, representing preferential growth along <011> [1].*

5.3.3 UV-Vis-NIR spectroscopy data

UV-Vis-NIR spectroscope in reflectance mode was used to measure the band gap of the NRs from different thickness samples. Kubelka-Munk equation [13] and Tauc plot [14] (described in chapter 4) have been used to get absorbance from reflectance data and band gap of the corresponding sample.

Figure 5.7(a) shows the reflectance spectra of NRs for five different thicknesses i.e., 5, 10, 15, 20 and 30 nm. The reflectance decreases with the increase of MoO_3 thickness. This is due to the increment in aspect ratio of NRs with increasing thickness (or size of nanostructures) [14,15]. Hence increase in absorption which is reflected in Figure 5.7(b) where absorption coefficient (α) was calculated using equation (4.4) and its dependence on wavelength has been plotted. For wavelength, $\lambda \geq 700$ nm, no appreciable change was observed and the value of the absorption coefficient is quite low but for wavelength < 700 nm, α is strongly dependent on wavelength [16]. Next in Figure 5.7(c) we have plotted $(\alpha h\nu)^2$ as a function of photon energy ($h\nu$). Band gap which has been determined from the extrapolation of the linear portion with the photon energy axis and its dependence on different thickness of β-MoO_3 NRs shown in Figure 5.7(d).

Table 5.3: Band gap (E_g) for β-MoO_3 NRs of different thicknesses [1]

Thickness (nm)	**Band gap (E_g)**
5	3.38± 0.01
10	3.25± 0.01
15	3.21± 0.01
20	3.19± 0.01
30	3.17± 0.01

For thickness dependent band gap study it is observed that band gap value is affected by thickness and with the increase of thickness from 5 nm to 30 nm, band gap decreases from ≈ 3.38 ± 0.01 eV to ≈ 3.17± 0.01 eV. We have tabulated band gap of NRs for each thickness in Table 5.3.

It is reported that this can be due to any one or combined effect of the following reasons: 1) due to the grain size in polycrystalline film, barrier height changes, 2) large density of dislocations and 3) quantum size effect [17]. More details are given below. Slater [18] proposed that energy berries are associated with grain boundaries and due to the charge accumulation at grain boundaries, barrier height varies. Accordingly, the increased barrier height is given by

$$H = H0 + C\,(X - f\,D)^2 \tag{5.1}$$

Where, H0 is the original barrier height. C related to charge carrier density, electronic charge, and dielectric constant of the material

X is the barrier width

f is a fraction depending on charge accumulation and carrier concentration

D is the dimension of grain

Gran size effect: K. L. Chopra [19] reported that grain size is approximately proportional to thickness and increases with increasing thickness. Replacing D by thickness (t) in equation (5.1) then H proportional to (X – f t)2. But from the inset of Figure 5.7(d), it has been seen that the band gap is inversely proportional to the square of thickness of the film. This confirms that the band gap variation with thickness cannot be assigned to the first reason.

Effect of dislocations: For the discussion on the role of dislocations, during the formation of films, dislocations are created and density of dislocations increases with the film thickness upto a certain thickness and constant beyond this specific thickness. But the exact relationship between the dislocation density and the change in band gap is unknown. So due to the complex nature of dislocation density with thickness, the variation of band gap with dislocation density is also complex [17]. But here we got a liner relationship between band gap and $1/t^2$. In this way we can ignore the second cause.

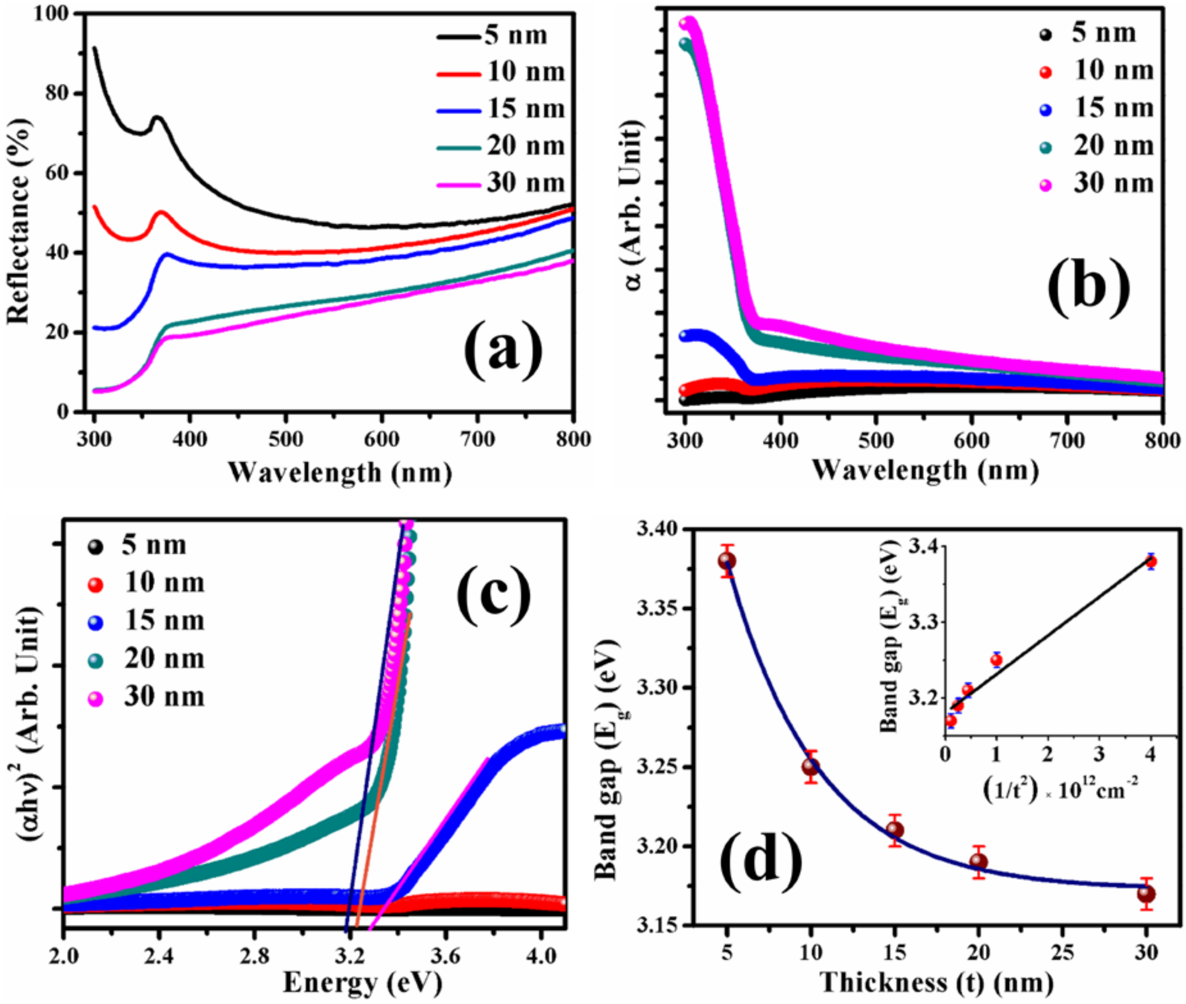

Figure 5.7: *(a) UV-Vis reflectance spectrum, (b) corresponding absorbance (α) spectra with wavelength and (c) $(\alpha h\nu)^2$ versus photon energy (hν) of MoO_3 NRs of different thickness. (d) Plot of band gaps with different thickness and inset of figure (d) shows band gap with $1/t^2$ plot [1].*

Quantum size effect: Sandomirskii [20] reported on the role of effective thickness of structures, their de Broglie wavelength of conduction electrons/holes and mean free path of the charge carriers, to the quantum size effect observation. Then momentum component of electron/hole normal to the film and the kinetic energy of the charge carriers are found to be quantized:

$$E_z = (\hbar^2 \Pi^2 / 2m^*) (1/t^2) n^2, n = 1, 2, 3\ldots \quad (5.2)$$

where, E_z = Kinetic energy contribution due to motion normal to the film plane.

$\hbar = h/2\Pi$, h is Planck’s constant

m^* = effective mass of the charge carrier

t = thickness of the film

From the above equation, it can be observed that E_z decreases with the increase of film thickness. By plotting the band gap versus $1/t^2$, and from the slop of such a graph, one can calculate effective mass of the electron in MoO_3. Here, it is assumed that the hole mass to be very large and the band separation is only due to conduction band shifting. Theoretical calculations by A. H. Reshak reported the values for effective electron mass ratio (m_e^*/m_e), heavy holes (m_{hh}^*/m_e) and light holes (m_{lh}^*/m_e) effective mass ratio of α- MoO_3 compounds to be 0.0194, 0.0984 and 0.1034 respectively [21]. We found the effective electron mass in β-MoO_3 to be 0.0191m_e. As the effective mass of hole is larger than electron, this would imply that the hole mobility is lesser than electron mobility and hence the conductivity would be mainly due to electrons. This implicates that the material β-MoO_3 is of n-type. The de Broglie wavelength of the electron can be calculated by the following equation [17]

$$\lambda = h / p = h / \mathrm{Sqrt}\,(2\, m_e^*\, E_F) \quad (5.3)$$

where, λ is the de Broglie wavelength

p is the momentum

m_e^* is the electron effective mass

E_F is the Fermi energy of the electron

The value of λ for 30 nm MoO_3 found to be 7 nm (using the value of m_e^* = 0.0191m_e, obtained from the slope of band gap versus $1/t^2$ plot). It is reported the mean free path of inelastic scattering in MoO_3 is 111 nm [22]. So according to Sandomirskii, the two conditions required for quantum size effect i.e. 1) film thickness is of the order of de Broglie wavelength (here different film thickness like 5 nm, 10 nm, 15 nm, 20 nm and 30 nm are of the order of de Broglie wavelength of 7 nm), and 2) film thickness is much less than the mean free path of the charge carrier (hare different thickness are less than the mean free path of 111 nm) are satisfied in the case of β- MoO_3 NRs.

5.3.4 KPFM results

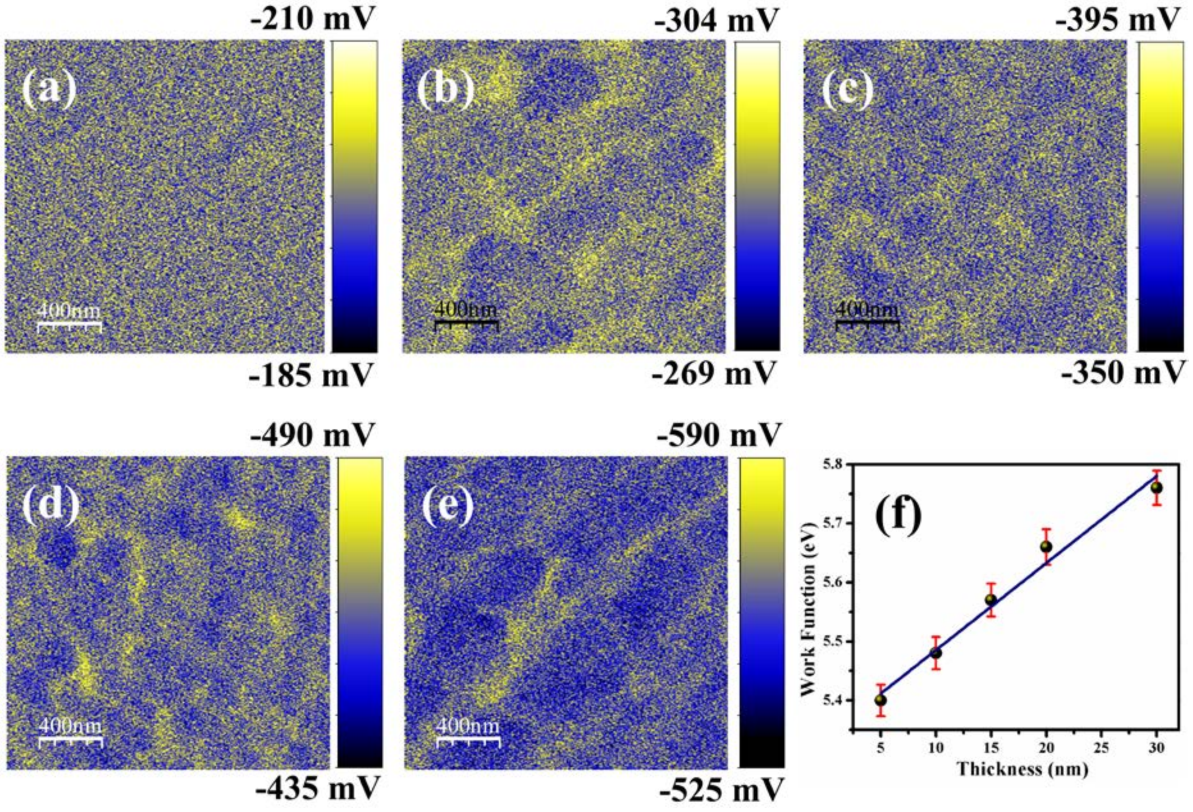

Figure 5.8: *Work function mappings by Kelvin probe force microscopy (KPFM) from nanoribbons (NRs) samples at different thickness of (a) 5nm, (b) 10 nm, (c) 15 nm, (d) 20 nm, (e) 30 nm. (f) Plot of work functions with different thickness [1].*

To measure the local work function of NRs samples for different thickness, Kelvin probe force microscopy (KPFM) technique has been used. The working principle of this technique have been described in chapter 2 and chapter 4. The work function of the sample is calculated by the following equation [23]

$$V_{DC} = V_{CPD} = (\Phi_{tip} - \Phi_{sample})/q \tag{5.4}$$

where, Φ_{tip} and Φ_{sample} are the work function of the AFM tip and the sample under investigation, respectively.

The work function of the tip has been calibrated with respect to standard *highly oriented pyrolytic Graphite (HOPG)* sample and is determined to be 5.2 eV. So from equation (5.4) we can calculate

$$\Phi_{sample} = \Phi_{tip} - qV_{CPD} = 5.2 \text{ eV} - qV_{CPD} \tag{5.5}$$

Figures 5.8(a)-(e) depict the work function mapping images of nanoribbon structures (NRs) from different thickness of MoO_3, 5 nm, 10 nm, 15 nm, 20 nm, 30 nm respectively. The Table 5.4, represents the experimentally determined work function values for the various thickness samples. We have prepared a chart for the work function of different thickness in Table 5.4 and represented a graph in Figure 5.8(f).

Table 5.4: Work function of β-MoO_3 NRs for different thickness [1]

Thickness (nm)	Work Function (eV)
5	5.397 ± 0.025
10	5.486 ± 0.027
15	5.572 ± 0.028
20	5.662 ± 0.029
30	5.757 ± 0.030

From Figure 5.8(f) and Table 5.4 one can observe that with increasing thickness, the local work function of β-MoO_3 NRs increases. Mark T. Greiner also observed the similar behavior that work function increases with MoO_3 film thickness [24].

5.4 Field emission properties:

Field emission (FE) process involves emission of electrons from the target specimen when high electric field is applied across a small areas and the emission of electrons is known to be the tunneling process. FE process depends mainly on two factors (i) work function (Φ) of the emitter and (ii) field enhancement factor (FEF) (B). FEF defined as the ratio of local to applied electric field and it also depends on morphology and structure of the emitters. In this report we have shown on how the thickness (or in the present case, the size) of NRs will play a role on FEF.

Figure 5.9 (a) depicts the field emission current density (J) versus applied electric field (E) for the cases of 5 nm, 10 nm, 20 nm and 30 nm β-MoO_3 NRs samples. Turn-on-field (E_{to}) is defined as the electric field required to draw 10 µA/cm^2 current density. The experimentally determined values of the turn-on voltage found to be ≈ 2.50 V/µm, ≈ 2.77 V/µm, ≈ 3.03 V/µm and ≈ 3.58 V/µm for 30, 20, 10 and 5 nm thickness of β-MoO_3 NRs. The FE behavior (J-E plot) can be analyzed theoretically by FN equation [25]

$$J = (aB^2E^2/\Phi) \exp(-b\Phi^{3/2}/BE) \tag{5.6}$$

Or,

$$\ln(J/E^2) = \ln(aB^2/\Phi) - (b\Phi^{3/2}/B) \times (1/E) \tag{5.7}$$

where, a and b are constants with a= 1.54×10^{-6} A-eV/V^2 and b= 6.83×10^3 eV$^{-3/2}$ –V μm^{-1}, B is the field enhancement factor (FEF), Φ is the work function of the emitter. By plotting ln (J/E^2) versus (1/E) (called F-N plot), from the slop ($b\Phi^{3/2}/B$), we can calculate B, i.e. field enhancement factor by knowing the constant b and work function value.

$$B = -b\Phi^{3/2}/\text{slope} \tag{5.8}$$

So, for smaller slope values, the FEF (B) will be high.

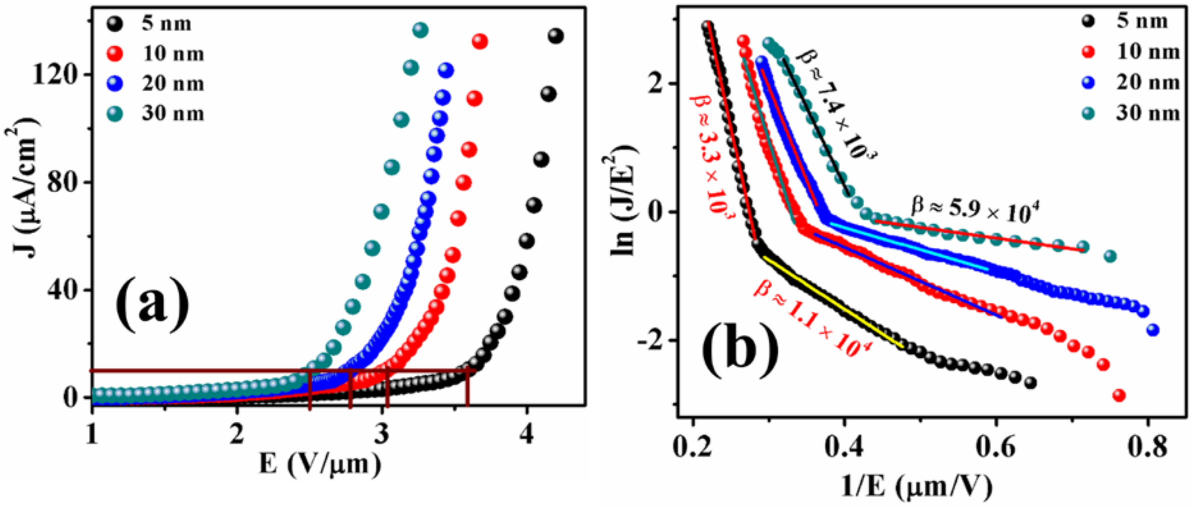

Figure 5.9: *(a) Field emission current density as a function of applied field (J–E) for the β-MoO$_3$ NRs samples with different thickness and the corresponding F–N plots in (b) [1].*

We have shown F-N plots of the same samples in Figure 5.9(b). This two slopes arise due to the emission of electrons from different energy levels [23,26]. In the low field region, electrons come from only conduction band but in the high field region electrons come from both conduction band as well as valence band. So for calculating FEF, one can assume the effective work function (Φ_{eff}) is the addition of material band gap (E_b) with the work function of the emitters (Φ) in the high field regime. We have already shown before the work function and band gap of different thickness β-MoO$_3$ NRs experimentally by KPFM and UV-Vis-NIR spectroscopy techniques. Hence, Φ_{eff} will be ~ 5.76 eV and ~ 8.93 eV (taking E_b = 3.17 eV) for 30 nm β-MoO_3 NRs sample in low field and high field regions, respectively and similarly for other thickness samples. Now from equation (5.8) we can calculate FEF (Β) as Φ_{eff} and slope values are known. The values of FEF (Β) for different thickness β-MoO_3 NRs sample in the low field and high field regions are tabulated in Table 5.5.

Table 5.5: Electron field emission performances of as-grown NRs samples having various thicknesses [1]

Thickness	Turn-on field (V/µm) for 10 µA/cm^2	Anode-sample separation	Slope		Field Enhancement Factor (FEF) (β)	
			Low Field	High Field	Low Field	High Field
5 nm	3.58	50 µm	-7.68	-54.48	1.1×10^4	3.3×10^3
10 nm	3.03	40 µm	-5.07	-38.46	1.7×10^4	4.6×10^3
20 nm	2.77	50 µm	-3.03	-29.51	3.0×10^4	6.1×10^3
30 nm	2.50	40 µm	-1.6	-24.48	5.9×10^4	7.4×10^3

We showed above that with increasing NRs thickness from 5 nm to 30 nm, aspect ratio (length/width) also increases from 3.9±0.1 to 14.1±0.5 respectively. So the FEF increases from 1.1×10^4 to 5.9×10^4 in the low field region and from 3.3×10^3 to 7.4×10^3 in high field regime. *To the best of our knowledge, there are no such reports on the thickness dependent FE study of monoclinic phase of MoO_3 (β-MoO_3). Our self-assembled grown β-MoO_3 NRs sample exhibit lowest turn-on field and highest FEF among all the previously reported other types of molybdenum oxide nanostructures as summarized in Table 5.6.*

Table 5.6: Representative results on field emission performances of various MoO_3 nanostructures [1]

Emitter	Turn-on field (V/µm) for specific emission current density	Gap between anode and sample	Field Enhancement Factor (FEF) (β)	Reference
MoO_3 Nanoflakes	11.0 V/µm for 10 µA/cm^2	-	2.5×10^3	[27]
MoO_3	3.5 V/µm for 10 µA/cm^2	70 µm	2.3×10^3 for high field	[23]

			1.0×10^4 for low field	
MoO_3 Nanowires	3.5 MV/m for 10 μA/cm^2	300 μm	-	[28]
MoO_3 Nanobelts	13.2 V/μm for 10 μA/cm^2 8.7 V/μm for 10 μA/cm^2	50 μm 80 μm	-	[29]
MoO_3 Nanoflowers	4.3 V/μm for 10 μA/cm^2	80 μm	0.7×10^3	[30]
β-MoO_3 Nanoribbons (from 30 nm thickness sample)	2.5 V/μm for 10 μA/cm^2	40 μm	7.4×10^3 for high field 5.9×10^4 for low field	Present work

5.5 Conclusion

In summary, we have reported self-assembled MoO_3 NRs structures grown on varied substrates by molecular beam epitaxy technique. XRD and TEM data revealed the monoclinic phase of MoO_3 (β-MoO_3) grown along <011>. As-grown NRs were oriented in two directions with respect to substrate normal. The transmission electron microscopy measurements confirmed that the growth of the NRs is unidirectional along <011>. It has been found that, with the increase in the thickness of MoO_3 films (and hence the dimension of the nanostructures), the band gap decreases, supported by UV-Visible spectroscopy measurements. The effective mass of electron in NRs structures (calculated from the slope of E_g vs $1/t^2$ graph) and de Broglie wavelength, β-MoO_3 is found to be n-type material. Local work function of the NRs structures measured by KPFM, found to increase with increasing thickness (or size of nanostructures) of MoO_3 films. Thickness dependent field emission study has also been studied and found to be better than the α-MoO_3 films grown by chemical vapor deposition. The reason behind low turn-on field (2.5 V/μm) and high FEF (Β) (7.4×10^3 and 5.9×10^4 for high and low field respectively) for 30 nm β-MoO_3 NRs has been attributed to high aspect ratio (~ 14.1 ± 0.5) of emitters. In the next chapter, we will discuss the role of catalyst (noble metal like Au, Ag) to control the growth of MoO_3 NRs.

5.6 References

[1] P. Maiti, P. Guha, R. Singh, J. K. Dash and P. V. Satyam, *Appl. Surf. Sci.* 2019, 476, 691.

[2] Mc Carron, E. M, *J. Chem. Soc., Chem. Commun.* 1986, 336.

[3] I. Juárez Ramírez and A. Martínez-de la Cruz, *J Solid State Electrochem* 2003, 7, 259.

[4] T. M. McEvoy and K. J. Stevenson, Langmuir 2003, 19, 4316.

[5] T. Mizushima, Y. Moriya, N. H. H. Phuc, H. Ohkita, and N. Kakuta, *Catal. Commun.* 2011, 13, 10.

[6] D. D. Yao, J. Z. Ou, K. Latham, S. Zhuiykov S, A. P. O'Mullane and K. Kalantar-zadeh *Cryst. Growth Des.* 2012, 12, 1865.

[7] K. Koike, R. Wada, S. Yagi, Y. Harada, S. Sasa, and M.Yano, *Jpn. J. Appl. Phys.* 2014, 53, 05FJ02.

[8] E. I. Altman, T. Dr oubay, S. A. Chambers, *Thin Solid Films* 2002, 414, 205.

[9] L. Wang, G.-H. Zhang, Y.-J. Sun, X.-W. Zhou and K.-C. Chou, *J. Phys. Chem. C* 2016, 120, 19821.

[10] D. Mariotti, H. Lindstr¨om, A. C. Bose and K. (Ken) Ostrikov. *Nanotechnology* 2008, 19, 495302.

[11] T. T. P. Pham, P. H. D. Nguyen, T. T. Vo, H. H. P. Nguyen and C. L. Luu, *Adv. Nat. Sci.: Nanosci. Nanotechnol.* 2015, 6, 045010.

[12] J. B. Parise, E. M. McCarron, R. V. Dreele, and J. A. Goldstone, *J. Solid State Chem.* 1991, 93, 193.

[13] J. Klaas, G. Schulz-Ekloff and N. I. Jaeger, *J. Phys. Chem. B* 1997, 101, 1305.

[14] R. Singh, M. Kumar, M. Saini, A. Singh, B. Satpati and T. Som, *Appl. Surf. Sci.* 2017, 418, 225.

[15] H. Sai, Y. Kanamori, K. Arafune, Y. Ohshita and M. Yamaguchi, *Prog. Photovoltaics Res. Appl.* 2007, 15, 415.

[16] S. A. Aly, A. A. Akl, *Chalcogenide Lett.* 2015, 12, 489.

[17] V. D. Das and D. Karunakaran, *J. Appl. Phys.* 1983, 54.

[18] J. C. Slater, *Phys. Rev.* 1956, 103.

[19] K. L. Chopra, Thin Film Phenomena (McGraw-Hili, New York, 1969).

[20] V. B. Sandomirskii, SOVIET PHYSICS JETP 1967, 25.

[21] A. H. Reshak, *RSC Adv.* 2015, 5, 22044.

[22] K. Iakoubovskii and K. Mitsuishi, *Phys. Rev. B* 2008, 77, 104102.

[23] P. Guha, A. Ghosh, R. Thapa, E. M. Kumar, S. Kirishwaran, R. Singh and P. V. Satyam, *Nanotechnology* 2017, 28, 415602.

[24] M. T. Greiner, L. Chai, M. G. Helander, W.-M. Tang, and Z.-H. Lu, *Adv. Funct. Mater.* 2012, DOI: 10.1002/adfm.201200615.

[25] R. H. Fowler and L. Nordheim, *Proc. R. Soc. A* 1928, 119, 173.

[26] A. Ghosh, P. Guha, R. Thapa, S. Selvaraj, M. Kumar, B. Rakshit, T. Dash, R. Bar, S. K. Ray and P. V. Satyam, *Nanotechnology* 2016, 27, 125701.

[27] B. Yan, Z. Zheng, J. Zhang, H. Gong, Z. Shen, W. Huang and T. Yu, *J. Phys. Chem. C* 2009, 113, 20259.

[28] J. Zhou, S. Z. Deng, N. S. Xu, J. Chen and J. C. She, *Appl. Phys. Lett.* 2003, 83, 2653.

[29] Y. B. Li, Y. Bando, D. Golberg and K. Kurashima, *Appl. Phys. Lett.* 2002, 81, 5048.

[30] G. Wei, W. Qin, D. Zhang, G. Wang, R. Kim, K. Zheng and L. Wang, *J. Alloys Compd.* 2009, 481, 417.

Chapter 6

Growth of molybdenum trioxide nanoribbons on oriented Ag and Au nanostructures: a scanning electron microscopy (SEM) study

6.1 Introduction

In the previous chapters, we have discussed on the growth of monoclinic molybdenum trioxide (β-MoO_3) nanostructures on various substrates and reported their physical properties. One of the challenging problem in nanoscience and nanotechnology is a proper understanding of self-assembled growth of nanostructures on pre-designed patterned surfaces. It also helps to fabricate hetero-nanostructure junctions as well. It is known that noble metal nanostructures, in particular, Au nanostructures are found to act as very good catalysts to from nanowires [1]. In this chapter, it would be shown experimentally that, well oriented Au nanostructures act as good catalyst particles for the growth of MoOx structures while Ag nanostructures are not. Here, we report on the growth of molybdenum trioxide (MoO_3) nanoribbons (NRs) on epitaxial Ag and oriented Au nanostructures using an UHV-MBE technique at different substrate temperatures. For oriented Ag nanostructures, a ≈2 nm silver

---

“P. Maiti, A. Mitra, R. R. Juluri, A. Rath and P. V. Satyam, *Micros. Microanal.* 2019, DOI: 10.1017/S1431927619014648.

(Ag) film has been deposited at different growth temperatures (using UHV-MBE) on reconstructed Si(100), Si(110) and Si(111) substrates. For oriented Au nanostructures, a ≈50 nm Au film has been deposited (using high vacuum thermal evaporation) on a Si(100) substrate with a native oxide layer at the interface and the sample was annealed in low vacuum ($\approx 10^{-2}$) and at high temperature (≈975 °C). Both procedures allowed oriented Ag and Au nanostructures. These nanostructure substrates have been used as substrates for the growth of MoO_3 using MBE methods. Scanning electron microscopy (SEM) measurements were performed to determine the morphology of MoO_3/Ag and MoO_3/Au composite films. From energy dispersive X-ray spectroscopy (EDS) elemental mapping and line scan it is found that faceted Au nanostructures are more favorable for the growth of MoO_3 NRs than the oriented Ag microstructures [2].

Well-ordered, highly crystalline, defect free nanostructures (NSs) are very important field of research due to their interesting physical, chemical and mechanical properties at the nanometer scale and a wide range of technological applications [3,4]. However, synthesis of well-ordered and oriented 1-D or 2-D NSs (e.g. nanorods, nanobelts, nanotubes, nanoribbons and nanoplates) by simple growth methods have proven to be a great challenge over the last two three decades [5,6]. Recently, molybdenum oxide NSs have attracted interest in nanoscience and nanotechnology for their unique structural, electrical, optical, mechanical properties and diverse applications in gas sensing [7,8], solar cells [9] Li-ion batteries [10], photochromic [11], photoelectrochromic windows and display [12] resistive switching [13] and field emission [14].

Recently, hybrid semiconductor-metal nanostructures have attracted attention because of their tunable physical and chemical properties that are superior to their individual properties [15, 16]. It has been reported that metal NSs, particularly Au, enhance visible light absorption and populate conduction band of oxide semiconductors by transferring electrons utilizing their surface plasmon resonance (SPR) properties. The transferred electrons are assembled at the interface and the work function of the heterostructure (HS) reduces by lifting the Fermi energy level of semiconductor towards vacuum [17-19]. Besides, Au and Ag have a great scientific interest and a vast range of applications in optical, electrical and biological research due to their low resistance, high transmittance, electrical conductivity, plasmonic and catalytic properties [20,21]. Ag is a good applicant for electrical characterizations due to its highest electrical conductivity ($\sigma_{Ag} = 6.30 \times 10^7$ S/m at ≈ 20 °C), detecting organic dye-molecules and biomolecules via surface enhanced Raman spectroscopy (SERS) technique [22-24]. Chai et al. reported that nucleation sites of MoO_3 nanobelts can be controlled by lowering the MoOx vapor concentration and introducing Au nanoparticles to the growth substrate, leading to the growth of flower like MoO_3 nanostructures [25].

In this chapter we have grown MoO_3 NRs on Si substrates using Ag and Au as nucleation sites/catalysts. Using FEGSEM combined with and energy dispersive X-ray spectroscopy (EDS) mapping suggests that Au is a better nucleation site as compared to Ag to control the growth of MoO_3 NRs.

6.2 Experimental Details

A custom-built MBE system (M/S Omicron GmbH, Germany) (base pressure: 2.1×10^{-10} mbar) equipped with effusion cells, integrated cooling shroud and shutter was used to grow silver (Ag) and molybdenum oxide nanostructures in UHV condition, whereas gold (Au) thin films were deposited in a high vacuum (HV) condition. MoO_3 powder (Alfa Aesar) with 99.995% purity and Ag wire were used as source material. Cleaned Si(100), Si(110) and Si(111) with 1-20 ohm-cm resistance were used as substrates. To remove the native oxide layer, Si substrates were degassed at 600 °C by direct heating (DH) for 12-15 hours. Then the substrates were repeatedly flashed at ~ 1200 °C for 5 minutes. The deposition rates of MoO_3 and Ag were ≈ 0.1nm/min, ≈ 0.2nm/min and the chamber base pressure went to ~ 6.9×10^{-9} mbar and ~7.5×10^{-10} mbar during deposition respectively. The substrate temperature was measured by a type-K thermocouple and cross-checked with an optical pyrometer. The thickness of the films was measured by a quartz crystal microbalance (QCM) which was calibrated by cross-sectional transmission electron microscopy (XTEM) and Rutherford backscattering spectrometry (RBS). For oriented Au nanostructures, Si(100) with native oxide layer was used as substrate and Au wire as source material. A 50 nm thick Au film was deposited in HV condition (~2.3×10^{-6} mbar) by physical vapor deposition (PVD) technique. Rath et al. reported the synthesis of highly oriented Au nanostructures by annealing the Au/SiOx/Si(100) system under low vacuum and at high temperature condition [26]. Following this procedure, the gold deposited sample was annealed in low vacuum (~10^{-2} mbar) in a horizontal tube (length ≈ 100 cm, inner diameter ≈ 4.5 cm) furnace with single zone side entry. The furnace was ramped up to 975 °C from room temperature with a ramping rate of 7 °C/min and kept for 30 min at 975 °C.

Ex-situ surface structure characterizations such as, morphology, shape, size of the as-grown samples as well as post annealed (PA) samples were performed by FEGSEM (with 20 keV electrons). Elemental analysis was performed using an Oxford INCA X-Act energy dispersive X-ray spectroscopy system equipped with the FEGSEM.

6.3 Results and discussion

6.3.1 Surface modification by Ag

A 2 nm Ag film was deposited on reconstructed Si(110) substrates at different substrate temperatures as discussed in section 6.2. Figure 6.1(a) depicts topographic SEM image of 2 nm Ag grown at 400 °C substrate temperature on a clean Si(110) substrate. Wire like nanostructures of Ag are observed, following the twofold symmetry of the underlying Si(110) substrate. The Ag wire-like structures try to align along the substrate plane, which indicates an epitaxial growth of Ag. After increasing the substrate temperature to 500 °C (Figure 6.1(b)), micron size wires (~10 µm) with large aspect ratio and islands (~1-2 µm) are formed. The number of islands is much higher than the number of microwires. At 600 °C substrate temperature shown in Figure 6.1(c), more and more islands connect to the wires to make them longer (~20 µm). When the substrate temperature is increased to 650 °C (Figure 6.2(a)), only microwires are found on the surface, which follow the substrate 2-fold symmetry (i.e for Si(110)) and orientation. A magnified image of one microwire is shown in the inset of Figure 6.2(a).

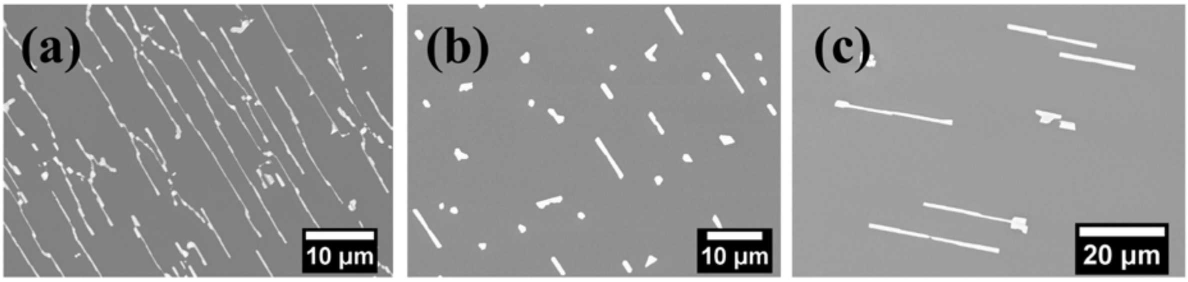

Figure 6.1: *SEM image of 2 nm Ag deposited on cleaned Si(110) substrate at the substrate temperature of (a) 400 °C, (b) 500 °C, (c) 600 °C.*

Similarly, a 2 nm Ag has been deposited at 650 °C substrate temperature on the other low index Si(hkl) substrates such as Si(100) and Si(111). Prior to Ag deposition, the substrates were cleaned in a similar way as discussed earlier for Si(110) substrates. Figure 6.2(b) shows the morphology of 2 nm Ag deposited on an ultra-cleaned Si(100) substrate at 650 °C substrate temperature where large aspect ratio micro wires are grown along two orthogonal directions. An enlarged view of two micro-wires are shown in the inset of Figure 6.2(b). Below a certain critical size, the length and the width of the nanostructures are increased proportionally which results in the formation of square-shaped nanostructures due to the four-fold symmetry of the substrate. But above the critical size, dimensions of the nanostructures are predominantly influenced by the length increment, whereas the width of the nanostructures is a slow varying dimension and remain nearly constant. As a result, anisotropic growth is observed for large size nanostructures and micro wires are formed. A topographic image of 2 nm Ag deposition on a reconstructed Si(111) substrate is shown in Figure 6.2(c) where triangular and hexagonal shaped microstructures are observed. This is due to the three-fold symmetry of the underneath substrate. Insets of Figure 6.2(c) show the enlarged view of one of the triangular and hexagonal microstructures. These measurements show that ordered and shape controlled Ag structures can be grown successfully using MBE conditions. The SEM measurements confirm the presence of oriented Ag nanostructures.

In this study, we have performed morphological study, elemental concentration analysis and mapping after metal oxide deposition on the oriented Au and Ag microstructures. First, we have studied the morphology separately i.e. MoO_3 on Si(100), Au on Si(100) and Ag on Si(100), next we have combined both i.e. MoO_3/Au/Si(100) and MoO_3/Ag/Si(100). The main focus of this study is to succeed in growing MoO_3 in a controlled manner using either Ag or Au as nucleation sites for the growth.

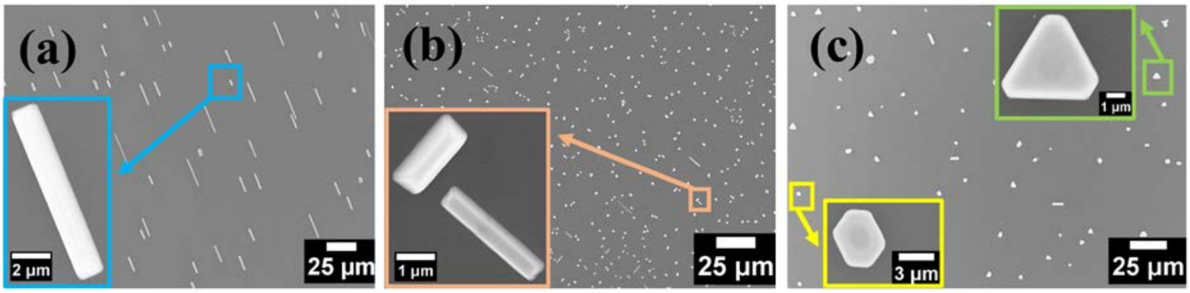

Figure 6.2: *SEM images of 2 nm Ag deposited at 650 °C substrate temperature on cleaned (a) Si(110), (b) Si(100) and (c) Si(111) substrates and corresponding magnified images of nanostructures at the insets.*

The morphology of a ≈10 nm thick MoO_3 deposited on an ultra-cleaned Si(100) substrate at room temperature (RT) followed by a post anneal (PA) at 350 °C for 30 minutes is shown in Figure 6.3(a). The SEM image depicts in-plane leaf-like thin film. Figure 6.3(b) represents out of plane NRs like structures, when ≈10 nm MoO_3 was deposited at 350 °C substrate temperature and they are grown along <011> [14,27].

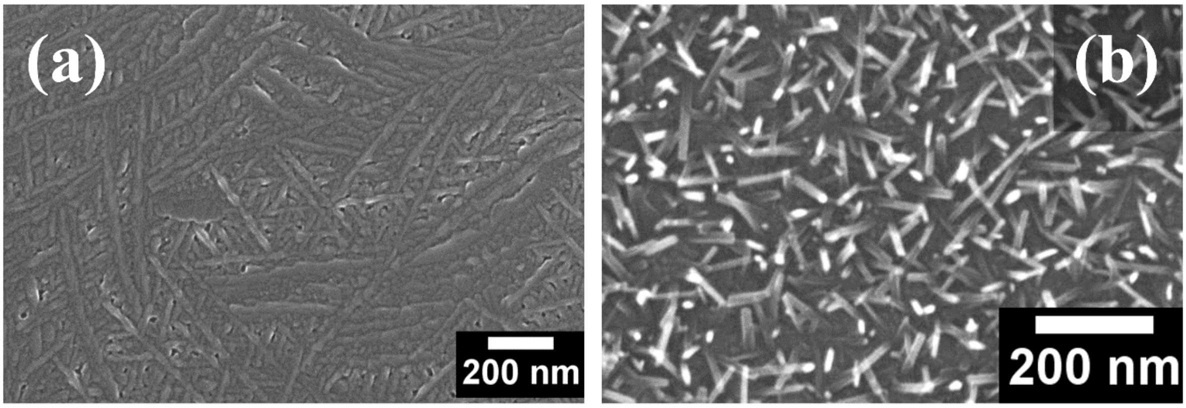

Figure 6.3: *10 nm MoO_3 deposited on cleaned Si(100) substrate at (a) RT followed by post annealing at 350 °C for 30 minutes and (b) 350 °C substrate temperature.*

6.3.2 Microscopy study of MoO_3 with Au

Formation of oriented gold nanostructures on Si(100) substrate with an oxide layer at the interface by annealing at high temperature and in the low vacuum has already been reported by Rath et. al. [26]. The interfacial oxide layer plays an important role in the formation of faceted Au nanoparticles. Here, the substrate with oriented Au nanostructures is used as the template to grow MoO_3 NRs. Figure 6.4(a) shows faceted Au nanostructures (NSs) formed by annealing of 50 nm Au/SiOx/Si(100) at ≈ 975 °C in low vacuum (≈10^{-2} mbar). An image at higher magnification of a faceted Au nanostructure has been shown in the inset of Figure 6.4(a). After annealing at ≈ 975 °C, various sizes of oriented Au NSs (starting from ≈ 5 nm to ≈ 500 nm) are formed [26]. On this substrate that has oriented Au nanostructures, a ≈10 nm MoO_3 (effective thickness as shown by quartz thickness monitor) was deposited at 350 °C on the substrate in UHV-MBE condition and the morphology has been displayed in Figure 6.4(b). It has been observed that number density of MoO_3 NRs grown on the faceted Au nanostructures is higher than the Si substrate (see inset of Figure 6.4(b)). Due to the high contact angle (≈

126°) [26] between faceted Au nanostructures and the substrate, MoO_3 NRs covered Au faceted nanostructures can be easily scrubbed for future applications.

Chemical composition analysis of MoO_3-Au nanostructure:

The EDS measurements were carried out for MoO_3/Au/Si system. A 5 keV electron energy and 450 pA probe current were used to get elemental concentration and the EDS spectrum from the nanostructure marked in Figure 6.5(a) is shown in Figure 6.5(b). Elemental concentrations have been tabulated in Table 6.1. The peak positioned at 0.52 keV, 1.74 keV, 2.12 keV, 2.29 keV represent characteristic X-ray lines of O, Si, Au, and Mo respectively.

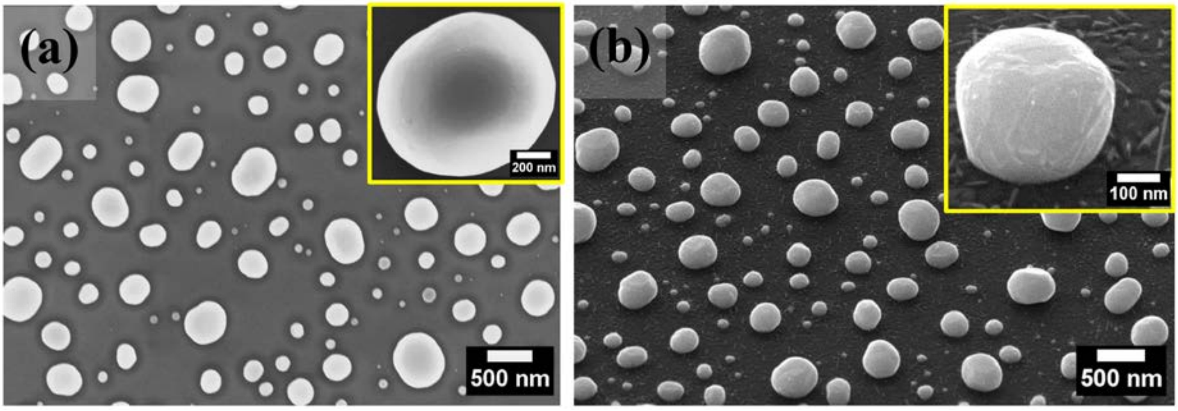

Figure 6.4: *(a) 50 nm Au deposited on Si(100) substrate with native oxide layer followed by post annealing at 975 °C in low vacuum and inset shows the magnified image of Au nanoparticle, (b) 10 nm* MoO_3 *deposited at 350 °C substrate temperature on sample (a).*

Elemental mapping of the region marked as yellow box in Figure 6.5(a) has also been done for 5 keV electron energy and dwell time was 100 μs per pixel. Constituent elements have been represented in Figure 6.5(c) – (f). EDS line spectra was also recorded along the green line shown in Figure 6.5(a). Mo, O, Au spectra have been depicted in Figure 6.5(g) and Si in Figure 6.5(h). Si signal is detected from those places where Au nanostructures are not present (see Figure 6.5(f) and 6.5(h)) and from the nanostructures, signals of Mo, O and Au are recorded. It can be observed from Figure 6.5(c), 6.5(d) and 6.5(g) that the Mo and O concentration is much higher on the faceted Au nanostructure as compared to the Si substrate. The density of MoO_3 NRs varies from Au nanostructures to Si substrate.

Table 6.1: Elemental concentration of MoO_3-Au nanostructure

Element	Atomic%
O K	6.7
Si K	83.2
Mo L	2.0
Au M	8.1

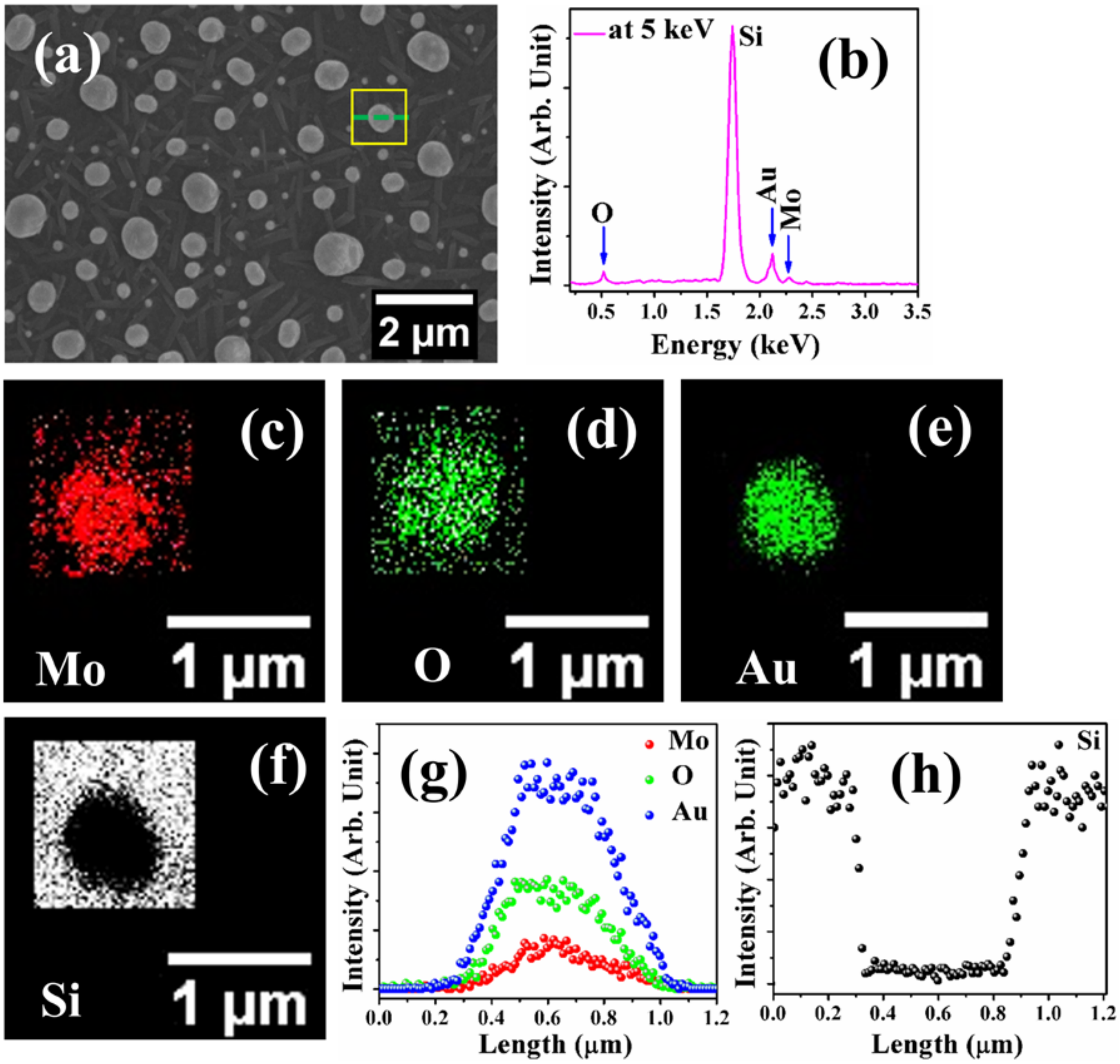

Figure 6.5: *(a)SEM image from MoO_3-Au-Si(100) sample, (b) EDS spectrum at 5 keV electron energy and EDS elemental map of (c) Mo, (d) O, (e) Au and (f) Si from the nanostructure marked in (a), EDS line spectrum (taken along green line in (a)) of Mo, O, Au in (g) and Si in (h).*

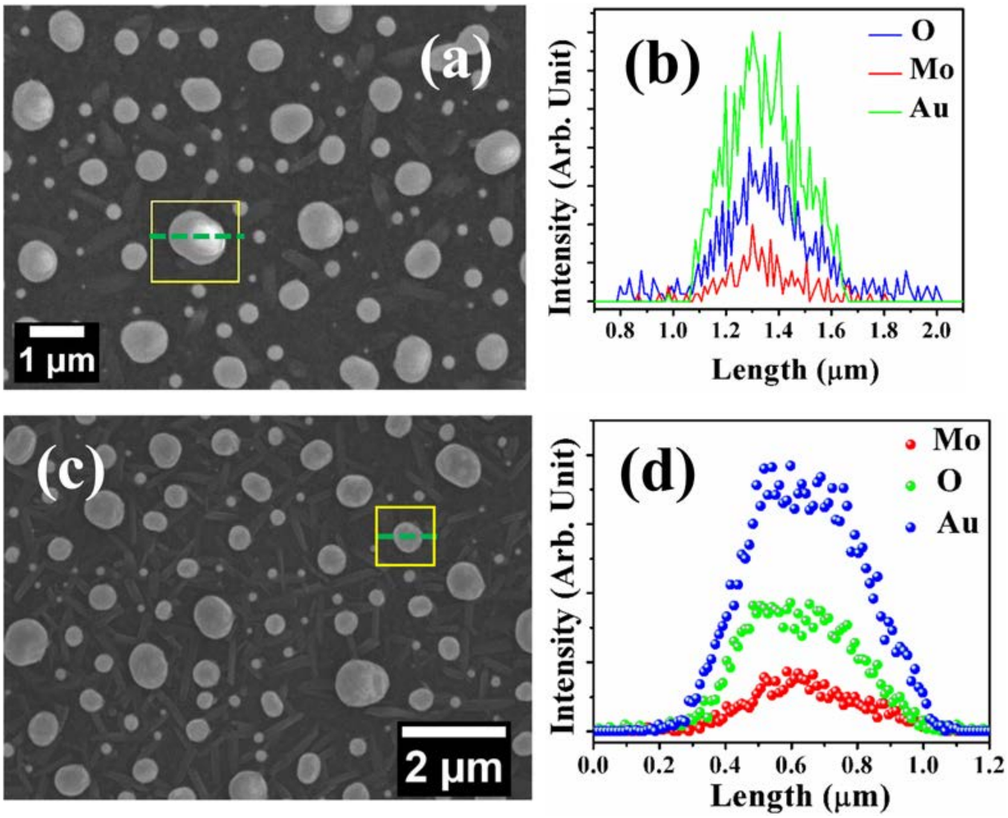

Figure 6.6: *EDS line spectra of Mo, O and Au, taken from (b) only one frame (marked the line shown in (a)), (d) five similar frames (marked the line depicted in (c)).*

To make sure that, the same area is mapped and to avoid any drift in the images, we have carried out five scans of duration 900 s for each EDS elemental mapping. Following this, a line scan has been taken through the selected region for the each of the frames, and the signals are added. This improves the counting statistics as compared with the line scan taken from only one frame (see Figure 6.6) and helps in better semi-quantitative analysis. Total live-time was 2955 sec after adding the live-time for the corresponding five frames (576,603,594,585,597 sec). Cai et al. reported that when the MoOx vapor concentration is low, the nucleation rate and the growth rate of MoO_3 nanobelts are reduced, as well. With small nucleation rates, nucleation occurs preferentially at surface defects rather than smooth surfaces because the former has a lower activation energy barrier. Therefore, when Au nanoparticles are present on the Si substrate, they are the preferred nucleation sites for the MoOx vapor [25]. Similarly in our study, the Mo signal follows exactly the Au signal because oriented gold nanostructures are the preferred nucleation sites for the growth of MoO_3 NRs. A more fundamental understanding of this interesting phenomenon is being studied.

6.3.3 Microscopy study of MoO_3 with Ag

Figure 6.7(a) and 6.7(b) shows the SEM images of a 2 nm Ag deposited on an ultra-cleaned reconstructed Si(100) substrate at RT followed by PA at 350 °C for 30 minutes and at 350 °C substrate temperature respectively. In the RT and Post Anneal case (see Figure 6.7(a)), nanoparticles are formed and the typical particle size histogram is shown in the inset of Figure 6.7(a). After fitting a Gaussian distribution, the average value of nanoparticle size has been found to be 45.4 ± 0.3 nm. Square and elongated microstructures are formed when a 2 nm of Ag is deposited at 350 °C substrate temperature on a cleaned Si(100) substrate and the enlarged view of the microstructure is shown in the inset of Figure 6.7(b). Comparing Figure 6.2(b) and Figure 6.7(b), we observe square and elongated micro structures are formed at lower substrate temperature (at 350 °C shown in Figure 6.7(b)). With increasing substrate temperature, only elongated nanostructures i.e micro wires exist, which have been observed at 650 °C (in Figure 6.2(b)). A 10 nm MoO_3 at RT was deposited on a clean Si(100) substrate modified by a 2 nm of Ag at RT. The MoO_3/Ag/ Si(100) sample (at (RT)) was annealed at 350 °C for 30 minutes and the morphology is shown in Figure 6.7(c). It is clear from the image that the morphology is totally different from Figure 6.3(a) and 6.7(a). Neither leaf-like MoO_3 thin films nor Ag nanoparticles have been observed in Figure 6.7(c). In case of sample grown at 350 °C substrate temperature (i.e. MoO_3/Ag/ Si(100) at 350 °C) shown in Figure 6.7(d), both the materials retain their own morphology. From the inset of Figure 6.7(d), we observe MoO_3 NRs (similar to Figure 6.3(b)) as well as square and elongated Ag micro structures (similar to Figure 6.7(b)).

Chemical composition analysis of MoO_3-Ag nanostructure:

To get the elemental concentration, EDS measurements are carried out at 5 keV electron energy and 450 pA probe current. EDS spectrum from the microstructure marked in SEM image (Figure 6.8(a)) has been shown in Figure 6.8(b). The atomic percentage of different elements have been tabulated in Table 6.2. The peaks represent at 0.52 keV for O, 1.74 keV for Si, 2.29 keV for Mo and 2.98 keV for Ag.

Elemental mapping is performed to identify the constituents of microstructure which have been shown in Figure 6.8(c) – (f). Mapping has been taken with a 100 μs dwell time per pixel. EDS line spectra (along red line marked in Figure 6.8(a)) of Mo, O, Ag and Si have been shown in Figure 6.8(g) and 6.8(h) respectively

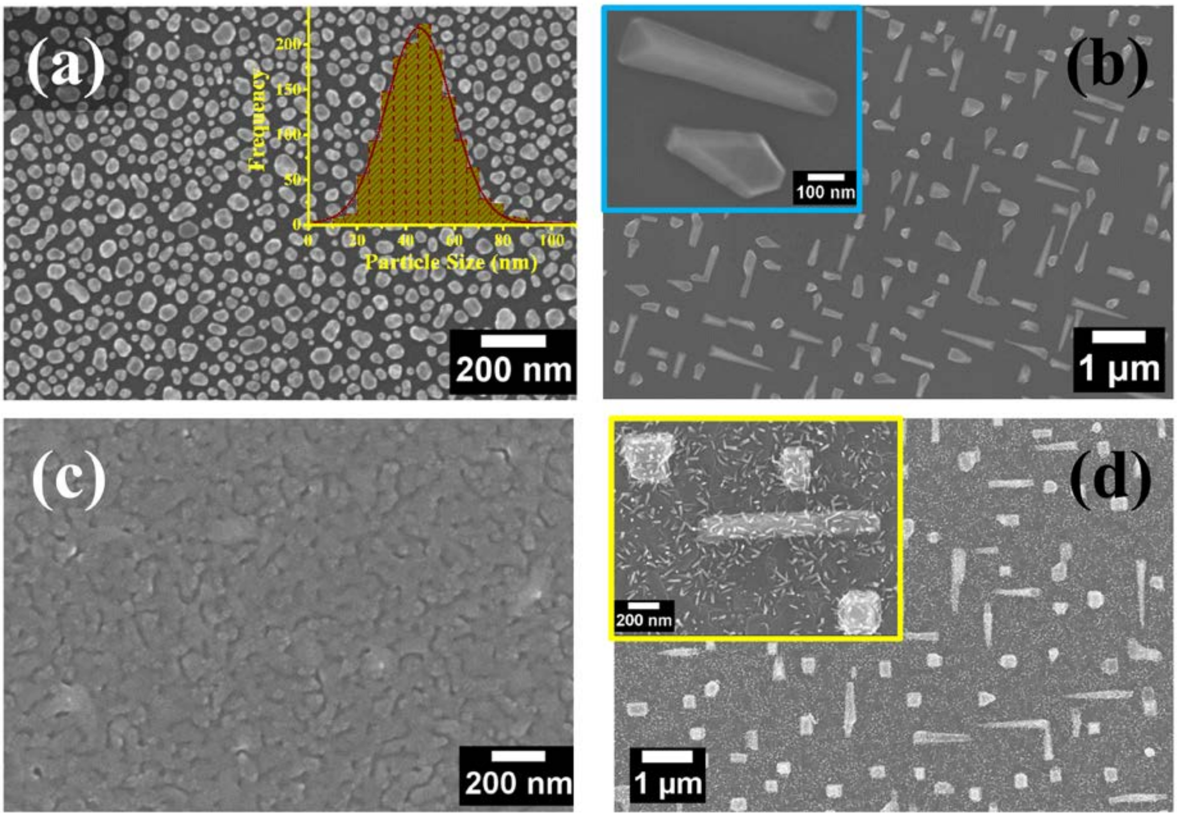

Figure 6.7: *2 nm Ag deposited on cleaned Si(100) substrate at (a) RT followed by post annealing at 350 °C for 30 minutes and (b) 350 °C substrate temperature. 10 nm* MoO_3 *and 2 nm Ag deposited on cleaned Si(100) substrate i.e 10 nm* MoO_3*/ 2 nm Ag/ Si(100) at (c) RT followed by post annealing at 350 °C for 30 minutes and (d) 350 °C substrate temperature.*

Table 2: Elemental concentration of MoO_3-Ag microstructure

Element	Atomic%
O K	8.3
Si K	84.8
Mo L	2.7
Ag L	4.2

The nanostructures are composed of Mo, O and Ag and we get Si signal from those places where Ag microstructures are not present (see Figure 6.8(f) and 6.8(h)). Figure 6.8(c), (d) and (g) indicate that unlike the MoO_3/Au films, the distribution of Mo and O in MoO_3/Ag films do not depend on the presence of Ag microstructures. Here also we have added line scan intensity for five frames to get better statistics (similar to Au case). Total live-time for all the scans was 3134 sec (630s, 639s, 621s, 612s, and 632s). There is no preferred growth on Ag microstructures whereas density of MoO_3 NRs varies from Au nanostructures to Si substrate

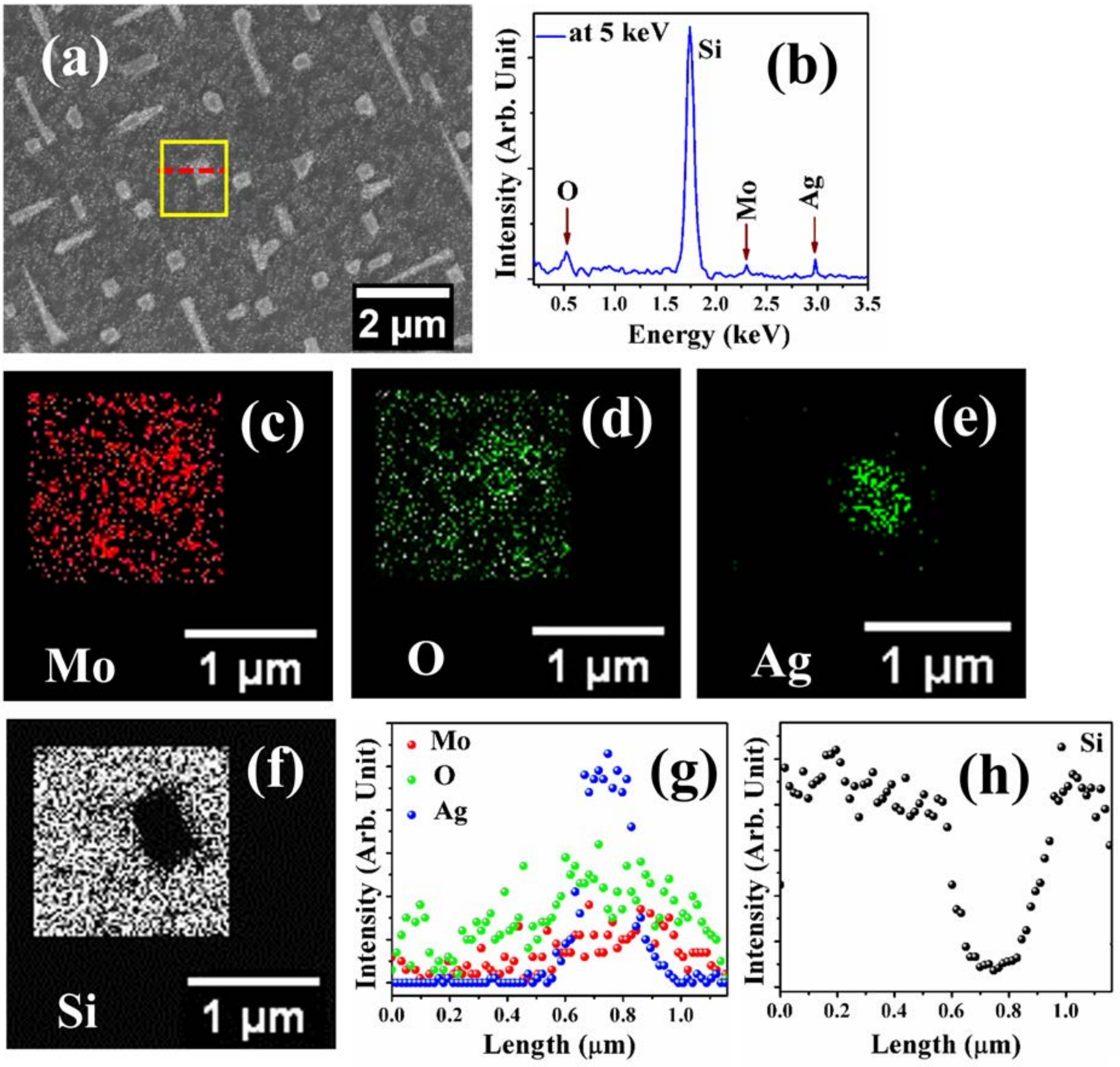

Figure 6.8: *(a) SEM image of* MoO_3*/ Ag/ Si(100) grown at 350 °C substrate temperature sample, (b) EDS spectrum at 5 keV electron energy and EDS elemental map of (c) Mo, (d) O, (e) Ag and (f) Si from the microstructure marked in (a). EDS line spectrum (taken along red line in (a)) of Mo, O, Ag in (g) and Si in (h).*

For further confirmation, we have simulated Mo X-ray intensity using CASINO [28,29] software for both $MoO_3/Ag/Si$ and $MoO_3/Au/SiO_2/Si$ systems to check if there is any contribution of backscattered electron from Au in Mo signal. We have found almost same Mo intensity for both the cases [I_{Mo} (MoO_3/Au/SiO_2/Si) / I_{Mo} (MoO_3/Ag/Si) = 1.06]. Therefore, the increased Mo signal with Au particle is due to the preferential growth of MoO_3 NRs on Au nanostructures.

Similarly, we have also grown MoO_3 NRs on reconstructed Si(110) and Si(111) substrates modified by Ag microstructures. Figure 6.9(a) represents the SEM image of MoO_3/Ag/ Si(110) sample. EDS has been carried out from the region marked in Figure 6.9(a), at 5 keV electron energy with 450 pA probe current and 100 μs per pixel dwell time. An EDS spectra is shown in Figure 6.9(b) and mapping of the constituent elements is shown in Figure 6.9(c) - (f). Mapping was done for 3010 sec live-time. EDS line spectra of Mo, O, Ag and Si, taken along the red line marked in Figure 6.9(a), is presented in Figure 6.9(g) and (h) respectively. Here also distribution of Mo and O does not depend on the Ag microstructures as well as Si substrates (see Figure 6.9(c), (d) and (g)). Therefore, we can conclude from substrate dependent study that Ag modified ultra-clean reconstructed Si(hkl) substrate does not control the growth of β-MoO_3 NRs. Ag is not a good nucleation site for β-MoO_3 NRs growth. Previously we have also reported that Si substrate with a native oxide layer, higher index vicinal substrate like Si(5512), FTO do not play any role on the growth of β-MoO_3 NRs [14].

6.4 Conclusion

We have reported the synthesis of Molybdenum trioxide nanoribbons on oriented Au and epitaxial Ag nanostructures using UHV-MBE. We showed that a minimum temperature of 650 °C is necessary to grow epitaxial Ag film on various reconstructed Si substrates and the growth of β-MoO_3 depends on the oriented Ag and Au nanostructures. In case of MoO_3/Ag samples, MoO_3 nanostructures are uniformly distributed on Ag microstructures as well as on the Si substrate, whereas in case of MoO_3/Au, the density of MoO_3 nanostructures is very high on top of the faceted Au structures as compared to the silicon substrate. As the MoO_3/Au structures can be easily removed from the substrate due to the high contact angle of faceted Au, these structures can be used as a potential material for the device as well as energy applications.

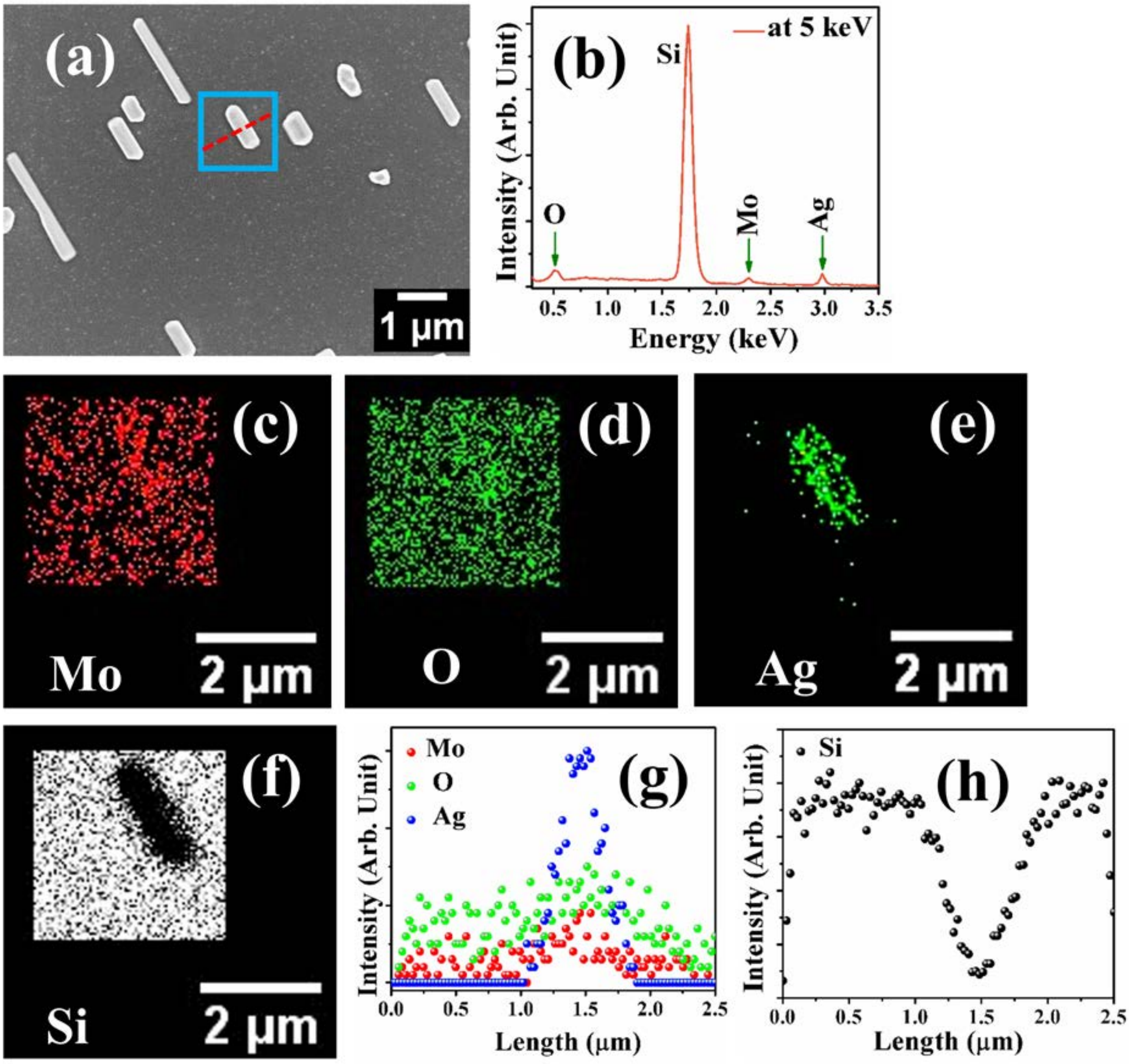

Figure 6.9: *(a) SEM image of* MoO_3 *NRs / Ag (450°C) / Si(110) sample, (b) EDS spectrum at 5 keV electron energy and EDS elemental map of (c) Mo, (d) O, (e) Ag and (f) Si from the microstructure marked in (a). EDS line spectrum (taken along red line in (a)) of Mo, O, Ag in (g) and Si in (h).*

6.5 References

[1] R. S. Wagner and W. C. Ellis, Appl. Phys. Lett. 1964, 4, 89.

[2] P. Maiti, A. Mitra, R. R. Juluri, A. Rath and P. V. Satyam, *Micros. Microanal. 2019, (under review).*

[3] A. P. Alivisatos, *Science* 1996, 271, 933.

[4] X. Fang, Y. Bando, U. K. Gautam, C. Ye and D. Golberg, *J. Mater. Chem.* 2008, 18, 509.

[5] S. Balendhran, S. Walia, H. Nili, J. Z. Ou, S. Zhuiykov, R. B. Kaner, S. Sriram, M. Bhaskaran and K. Kalantar-zadeh, *Adv. Funct. Mater.* 2013, 23, 3952.

[6] S. Cong, T. Sugahara, T. Wei, J. Jiu, Y. Hirose, S. Nagao and K. Suganuma, *Cryst. Growth Des.* 2015, DOI: 10.1021/acs.cgd.5b00790.

[7] M. Ferroni, V. Guidi, G. Martinelli, N. Paolo, M. Sacerdoti and G. Sberveglieri, *Thin Solid Films* 1997, 307, 148.

[8] E. Comini, G. Faglia, G. Sberveglieri, C. Cantalini, M. Passacantando, S. Santucci, Y. Li, W. Wlodarski and W. Qu, *Sens. Actuators, B* 2000, 68, 168.

[9] Z. Su, L. Wang, Y. Li, G. Zhang, H. Zhao, H. Yang, Y. Ma, B. Chu and W. Li, *ACS Appl. Mater. Interfaces* 2013, 5 12847.

[10] D. Mariotti, H. Lindström, A. C. Bose, and K. Ostrikov, *Nanotechnology* 2008, 19,495302.

[11] L. Zheng, Y. Xu, D. Jin and Y. Xie, *Chem. Mater.* 2009, 21, 5681.

[12] J. N. Yao, K. Hashimoto and A. Fujishima, *Nature* 1992, 355, 624.

[13] D. Lee, D-J. Seong, I. Jo, F. Xiang and R. Dong, *Appl. Phys. Lett.* 2007, 90, 122104.

[14] P. Maiti, P. Guha, R. Singh, J. K. Dash and P. V. Satyam, *Appl. Surf. Sci.* 2019, 476, 691.

[15] M. D. L. R. Peralta, U. Pal and R. S. Zeferino, *ACS Appl. Mater. Interfaces* 2012, 4, 4807.

[16] W. He, H-K Kim, W. G. Wamer, D. Melka, J. H. Callahan and J-J. Yin, *J. Am. Chem. Soc.* 2014, 136, 750.

[17] L. Zhang, J. C. Yu, H. Y. Yip, Q. Li, K. W. Kwong, A-W. Xu and P. K. Wong, *Langmuir* 2003, 19, 10372.

[18] M. Wu, W-J. Chen, Y-H. Shen, F-Z. Huang, C-H. Li and S-K. Li, *ACS Appl. Mater. Interfaces* 2014, 6, 15052.

[19] A. Ghosh, P. Guha, A. K. Samantara, B. K. Jena, R. Bar, S. K. Ray and P. V. Satyam, *ACS Appl. Mater. Interfaces* 2015, 7, 9486.

[20] C. J. Murphy, T. K. Sau, A. M. Gole, C. J. Orendorff, J. Gao, L. Gou, S. E. Hunyadi, and T. Li, *J. Phys. Chem. B* 2005, 109, 13857.

[21] Y-C. Yeh, B. Creran and V. M. Rotello, *Nanoscale* 2012, 4, 1871.

[22] K. G. Stamplecoskie, J. C. Scaiano, V. S. Tiwari, and H. Anis, *J. Phys. Chem. C* 2011, 115, 1403.

[23] A. H. Alshehri, M. Jakubowska, A. Młożniak, M. Horaczek, D. Rudka, C. Free, and J. D. Carey, *ACS Appl. Mater. Interfaces* 2012, 4, 7007.

[24] B. Sharma, R. R. Frontiera, A-I. Henry, E. Ringe, and R. P. V. Duyne, *Mater. Today* 2012, 15, 16.

[25] L. Cai, P. M. Rao, and X. Zheng, *Nano Lett.* 2011, 11, 872.

[26] A. Rath, J. K. Dash, R. R. Juluri, A. Rosenauer, M. Schoewalter and P. V. Satyam, *J. Appl. Phys.* 2012, 111, 064322.

[27] P. Maiti, P. Guha, H. Hussain, R. Singh, C. Nicklin and P. V. Satyam, *Surf. Sci.* 2019, 682, 64.

[28] P. Huvington, D. Drouin and R. Gauvin, *Scanning* 1997, 19(1), 1.

[29] Y. Yuan, H. Demers, S. Rudinsky and R. Gauvin, *Microsc. Microanal.* 2019, DOI: l0.1017 /51431927618016215

Chapter 7

Vacuum dependent annealing effect on structural, optical, local work function and field emission properties of Molybdenum oxide thin films

7.1 Introduction

A major part of the thesis was on the growth, characterization and application of MoO_x nanostructures (in particular β-MoO_3) under ultra-high vacuum (UHV) conditions by molecular beam epitaxy (MBE) process. For comparison with the other growth procedures, the molybdenum oxide thin films were also grown on Si(100) substrates by physical vapor deposition (PVD) technique and the results are reported in this chapter. Following the growth using PVD method, the resultant α-MoO_3 thin films have been annealed (≈600 °C for 30 minutes) under various controlled condition: Atmospheric (in air), low vacuum (LV) ($\approx 10^{-2}$ mbar) and UHV ($\approx 10^{-10}$ mbar) conditions. The dependence of the vacuum annealing on morphological and structural aspect studies by using experimental methods, such as, SEM, EDS, AFM and XRD are reported. Morphology changes from layered like orthorhombic α-MoO_3 to granular like monoclinic MoO_2 nanostructures when we increased the vacuum level during annealing from air to UHV. Optical band gap decreased from 3.22 ± 0.01 eV to 2.60 ± 0.01 eV and local work function also decreased from 5.764 ± 0.029 eV to 5.123 ± 0.026 eV

The work presented in this chapter will be published as P Maiti et al. (*To be submitted*, 2019) with increasing vacuum level from air to UHV. Field emission (FE) turn-on field increased from 4.78 V/μm to 6.62 V/μm for 10 μA/cm^2 and field enhancement factor (FEF) (b) decreased from 3.8×10^4 to 3.3×10^3 for effective variation of vacuum level from air to UHV during annealing. Air anneal α-MoO_3 nanostructures found to be best field emitter due to the low work function, low turn-on field and high FEF among three different cases [1].

Molybdenum oxide is a wide band gap material whose band gap varies from insulating MoO_3 (≈3.2 eV) to more conducting MoO_{3-x} to semi-metallic MoO_2 (≈2.55 eV) [2]. It shows several phases such as MoO_3 (orthorhombic, monoclinic, hexagonal), Mo_4O_{11} (monoclinic, orthorhombic), Mo_5O_{14} (tetragonal), Mo_8O_{23} (monoclinic), Mo_9O_{26} (monoclinic), MoO_2 (monoclinic) depending upon the oxygen concentration and oxidation state (+6, +5, +4, +2) of Mo. It has been already reported that thermal annealing [2], film thickness [3], hybridization with a noble metal such as Au, Ag and creation of oxygen vacancies [4] can change the material properties of molybdenum oxide. Here, we have reported different vacuum level (air, LV, UHV) annealing effect on structural, optical, local work function, and field emission properties of molybdenum oxide thin films.

We have already discussed in chapter 4 and 5 that there exists mainly three different polymorphs of MoO_3, (i) thermodynamically most stable orthorhombic structure (α-MoO_3), [4] (ii) metastable monoclinic structure (β-MoO_3) [2,3] and (iii) metastable hexagonal structure (h-MoO_3) [5]. Crystal structure of α-MoO_3, β-MoO_3, transition temperature from β-MoO_3 to α-MoO_3 [6], their different growth techniques and applications have been discussed in the previous chapters. Due to the high melting point, high chemical and thermal stability, metallic conductivity; monoclinic MoO_2 has attracted much attention to the research community. The lattice parameters of MoO_2 crystal structure, different types of MoO_2 morphologies [7-11] and growth techniques [12-14] are describes in chapter 4.

In this chapter we have reported different molybdenum oxide NSs after annealing MoO_3 thin films (deposited by thermal evaporation) in the air, LV and UHV conditions and further explore their potential in FE application. Room temperature (RT) AFM measurements provide the surface roughness of the above mentioned three types of NSs.

7.2 Experimental Details

MoO_3 thin films were grown at room temperature (RT) by physical vapor deposition (PVD) system that was kept at a base pressure of ≈ 10^{-6} mbar. We used Si(100) (*n-type*, phosphorus doped, resistivity ≈ 1-20 Ω–cm) with a native oxide layer of ≈ 2-3 nm thickness on top as a substrate and commercially available molybdenum trioxide (α-MoO_3) powder (99.995% purity from Alfa-aeser) as source material for the growth. Mo boat was used to keep the source material for deposition and a quartz crystal microbalance was used to measure the real-time thickness of the deposited thin films. Prior to thin film deposition, the substrates were cleaned by acetone and methanol in an ultrasonic bath (to remove the contaminations on the surface) and put in the growth chamber. A ≈ 250 nm thick molybdenum trioxide film was deposited on Si(100) substrates with a native oxide layer at ≈ 1 Å/sec deposition rate. The chamber base pressure was 2.8×10^{-6} mbar during the deposition. After the deposition, the sample was annealed at 600 °C in air, low vacuum (LV) and ultra-high vacuum (UHV) conditions to understand the effect of vacuum level on molybdenum oxide thin films. A horizontal tube furnace with single zone side entry was used for annealing the sample in air and LV conditions. The furnace was ramped up to 600 °C from room temperature with a ramping rate of 7 °C/min and kept for 30 min at 600 °C. For LV case, a rotary pump was attached with the furnace to create $\approx 1.2 \times 10^{-2}$ mbar pressure inside the tube. A custom-built MBE system (M/S Omicron GmbH, base pressure $\approx 2.3 \times 10^{-10}$ mbar) was used to anneal the thin film deposited sample in UHV condition. In this system the sample was heated by resistive heating (RH) mode and type-K thermocouple attached with the sample stage was used to measure the heated sample temperature. The samples were collected from both the systems after cooling down to room temperature for characterizations.

Ex-situ structure characterizations like surface morphology, shape, size of the as grown and post annealed samples were examined by FEGSEM (M/S Carl Zeiss GmbH, Neon 40 cross-beam system) with 20 keV electrons and atomic force microscopy (AFM) (MFP3D, Asylum Research, USA). We used WSxM [15] software to analyze AFM images. To obtain large crystalline information from the samples, X-ray diffraction (XRD) measurements were performed using a Bruker DA VINCI D8 ADVANCE diffractometer equipped with Cu-Kα source ($\lambda = 0.154$ nm). The optical properties of the samples were measured at RT using ultraviolet- visible- near infrared (UV-Vis-NIR) spectrometer (Shimadzu Corporation, UV-3101PC). Kelvin probe force microscopy (KPFM) was employed to measure the local work function of the post annealed samples by ex situ atomic force microscope in lift mode with 60 nm lift height, using conductive Ir/Pt tip (AC240TM, Electric-Lever, Olympus) having ≈ 30 nm radius of curvature, ≈ 2 $N\text{-}m^{-1}$ stiffness, and a resonance frequency of ≈ 70 kHz.

The field emission (FE) performance was determined by a diode configuration in a custom made high vacuum ($\approx 2.7 \times 10^{-7}$ mbar) chamber (Excel Instruments, FE System-150) and Keithley 2410 voltage source meter was used to record current versus voltage (I-V) data. The post annealed samples, fixed at the bottom plate with copper tape act as the cathode and a copper plate having ≈ 2.5 mm tip diameter was used as the anode.

7.3 Results and discussion

7.3.1 Structural Characterization

MoO_3 film with thickness of ≈ 250 nm (as shown by quartz thickness monitor) was deposited on Si(100) substrates with a native oxide layer by physical vapor deposition technique. Figure 7.1 shows the cross sectional view of the as deposited MoO_3 thin film sample. The cross sectional SEM imaging was carried (as shown in Figure 7.1) to determine the thickness of the MoO_3 film and is found to be about ≈ 252 nm. This is in close agreement with the quartz thickness monitor values.

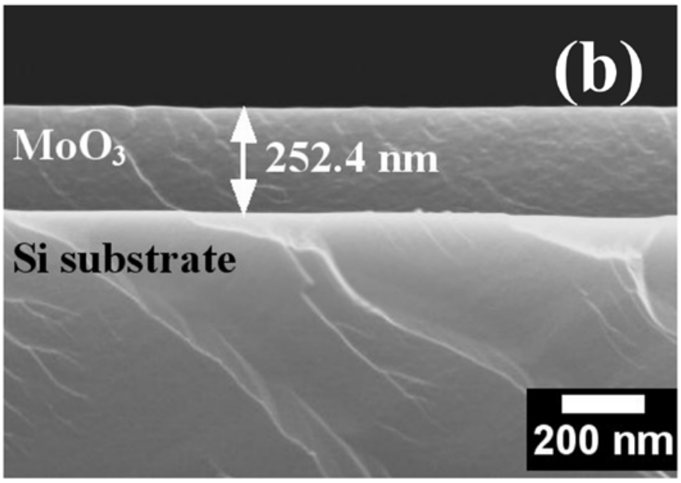

Figure 7.1: *Cross-sectional SEM (XSEM) image from the as deposited 250 nm MoO_3 film grown on Si(100) substrate.*

The *MoO_3* deposited samples were annealed at 600 °C for 30 minutes in different vacuum level. After cooling down to room temperature, SEM images were taken from the samples and depicted in Figure 7.2. Figure 7.2(a) displays the morphology of a sample that was annealed in air. From the inset of Figure 7.2(a), it is clear that, the layered like structures are formed. But the morphology is totally different when we annealed the thin film deposited sample at low vacuum (LV: ≈ 10^{-2} mbar). Plate like microstructures are formed in the LV case which has been depicted in Figure 7.2(b). Granular structures are formed after annealing the thin film deposited sample in UHV (≈ 10^{-10} mbar) condition at 600 °C for 30 minutes (figure 7.2(c)).

For macro scale crystal strucchture information, we have carried out X-ray diffraction (XRD) measurements on the as deposited sample for different vacuum annealed samples. As deposited sample did not show any characteristic XRD peaks (see figure 7.3(a) (i)). Only a broad hump has been observed at $2\theta \approx 27.29$. This confirms that the as deposited films were amorphous in nature. When we annealed the as deposited sample in air at 600 °C for 30 minutes, layered like structures are formed. All the peaks observed in the XRD are indexed to the orthorhombic phase of MoO_3 (α-MoO_3) (see Figure 7.3(a) (ii)). Stronger intensities are observed for the reflection peaks of (020), (110), (040), (021), (131) and (142) (JCPDS card, #35-0609).

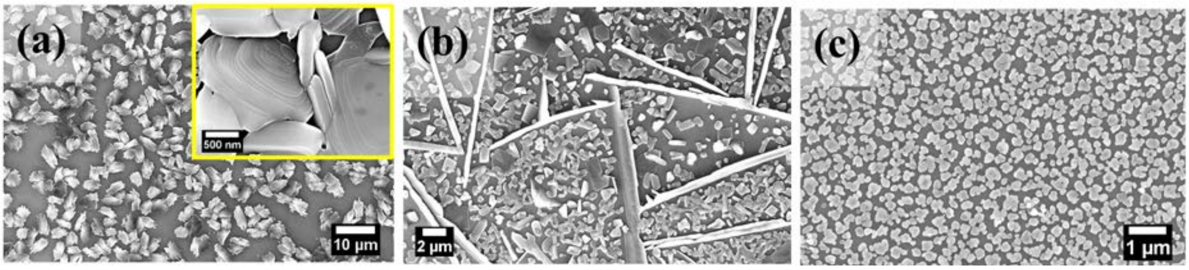

Figure 7.2: *250 nm MoO_3 deposited on Si(100) substrate with a native oxide layer by PVD followed by post anneal at 600 °C for 30 min in (a) air using a tube furnace, (b) LV using a tube furnace and (c) UHV using MBE.*

Interestingly, after annealing in LV, the crystal structure of the plate like microstructures is transformed to β-MoO_3 and η-Mo_4O_{11} (in Figure 7.3(a) (iii)). Both of these structures are in monoclinic phase. Strong intensity comes from (100) planes of β-MoO_3. In the inset, we have marked the peaks correspond to β-MoO_3 (JCPDS card, #89-1554) and η-Mo_4O_{11} (JCPDS card, #86-1269). It has already been reported that the growth of α-MoO_3 and β-MoO_3 depends on the oxygen partial pressure during the annealing proccess. When the oxygen partial pressure is high (50%), α-MoO_3 is formed similar to the air annealed sample. But at low oxygen partial pressure (5% -10%), β-MoO_3 is formed, as seen in the sample annealed in LV [16]. After annealing in UHV, granular structures of monoclinic MoO_2 are formed which have been confirmed by XRD spectrum shown in Figure 7.3(a) (iv). In our previous report, we have already observed that the samples grown at substrate temperature between 400 °C to 600 °C, exhibit nanoparticles (NPs) of monoclinic MoO_2 phase [2]. Using FWHM value of the preferred orientation, crystallite size (D) is estimated by Scherrer formula (Eq. 7.1) [17] and the lattice strain (ε), dislocation density (δ) are calculated by the following Eq. 7.2 and Eq. 7.3, respectively [49]. The dislocation density (δ) which measures the amount of defects in a crystal defined as the length of dislocation lines per unit volume [18]

$$\text{Crystallite size (D)} = K\lambda / \{(\cos\theta) \times (\text{FWHM})\} \tag{7.1}$$

$$\varepsilon = (\text{FWHM}) / (4 * \tan\theta) \tag{7.2}$$

$$\delta = 1/ D^2 \tag{7.3}$$

where, K is a dimensionless shape factor (close to unity), λ is the X-ray source wavelength, FWHM represents full width half maxima (in radian) and θ is the Bragg angle (in degree). We have tabulated the calculated crystallite size, ε and δ for all the samples annealed under different vacuum conditions in Table 7.1. Crystallite size changes with varying the vacuum level, and lowest crystallite size has been observed for UHV annealed sample (see Table 7.1).

7.3.2 Elemental Analysis

To obtain the quantitative analysis of the film we have used EDS attached with FESEM with 20 keV electrons and plotted the graph in Figure 7.3(b). The peaks positioned at 0.52 keV, 1.74 keV, 2.29 keV represent O K, Si K and Mo L signals, respectively. Insets of Figure 7.3(b) display the enlarged view of Mo and O signal. The obtained atomic percentages for Mo, O and Si have been tabulated in Table 7.2. It can be observed from Table 7.2 and the insets of Figure 7.3(b) that with increasing vacuum level, Mo and O intensity decreases and Si intensity increases. This can happen mainly due to evaporation of material from the substrate and the phase transition from MoO_3 to MoO_2 during annealing. We have measured the thickness of the material, O/Mo atomic ratio, Mo, O concentration after annealing the thin film deposited samples in different vacuum level by Rutherford backscattering spectrometry (RBS) under resonance condition (Chapter 3). There we have seen that with increasing vacuum level from air to UHV, thickness decreases from 242.9 nm to 200.7 nm to 87.4 nm.

Table 7.1: Calculated values for three different vacuum annealed samples.

Vacuum Level	Crystallite size (D) in nm	Lattice strain (ε) in (10^{-3})	Dislocation density (δ) in (10^{14} lines/m^2)
Air	52.00	6.86	3.70
Low vacuum (LV)	57.38	6.19	3.04
Ultra-high vacuum (UHV)	34.64	8.33	5.00

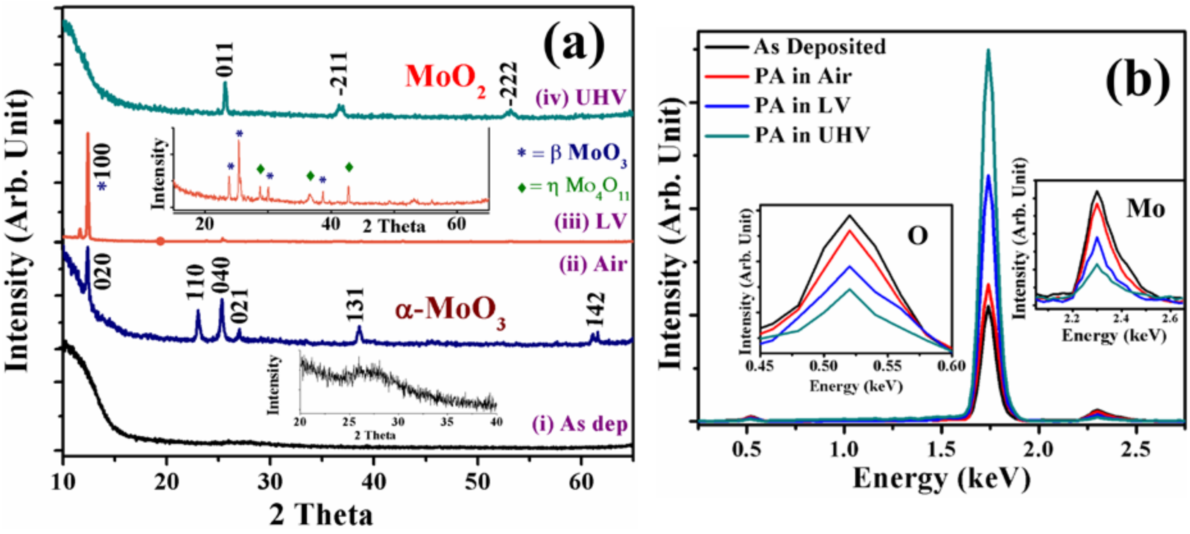

Figure 7.3: *(a) XRD data from the samples of 250 nm MoO_3 deposition at RT on Si(100) substrate with a native oxide layer by PVD followed by post anneal at 600 °C for 30 min in (i) air using a tube furnace, (ii) LV using a tube furnace, (iii) UHV using MBE and (b) EDS spectra from the as deposited and post annealed samples at 600 °C for 30 min in air, LV and UHV.*

Table 7.2: Elemental concentration of different vacuum annealed nanostructures

Vacuum Level	**Elemental Atomic %**		
	Mo L	**O K**	**Si K**
As deposited	7.3	36.2	56.5
Air	6.6	26.8	66.6
Low vacuum (LV)	4.3	20.1	75.6
Ultra-high vacuum (UHV)	1.1	7.4	91.5

7.3.3 AFM study

To get the root mean square (RMS) roughness, we have studied the surface morphology by atomic force microscope (AFM) in tapping mode. Figure 7.4(a), (c), (e) represent AFM topographic images of the samples after post annealing at 600 °C for 30 minutes in the air, LV and UHV respectively. Their corresponding line profiles have been depicted in Figure 7.4(b), (d) and (f) respectively.

Table 7.3: RMS roughness values for three different vacuum annealed samples.

	Vacuum Level		
	Air	**Low vacuum (LV)**	**Ultra-high vacuum (UHV)**
RMS roughness (nm)	278	261	159

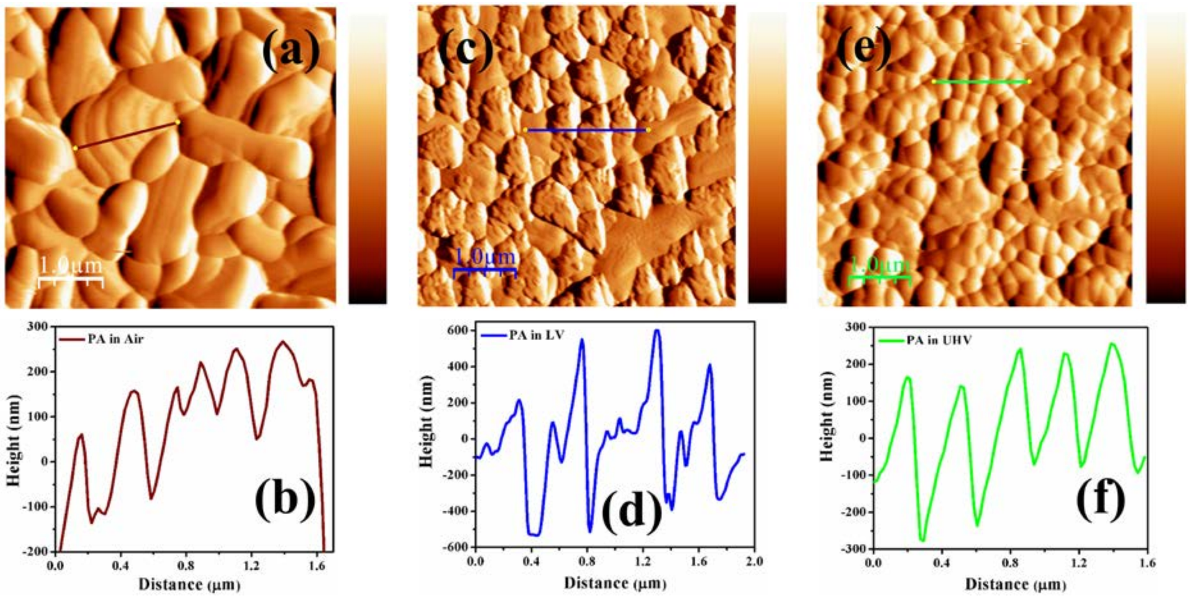

Figure 7.4: *AFM topographic data from 250 nm MoO_3 deposited on Si(100) substrate with a native oxide layer by PVD followed by post anneal at 600 °C for 30 min in (a) air, (c) LV and (e) UHV by MBE and their corresponding line profile shown in (b), (d), (f) respectively.*

We have calculated RMS roughness from AFM micrograph for all these three samples by WSxM software and tabulated in Table 7.3. From Table 7.3, we can observe that with increasing vacuum level from air to UHV, surface roughness decreases which matches with the previous result [19]. From SEM images we have already seen that in UHV annealing, granular structures are formed whereas in air annealing, layered like microstructures are formed. Hence the RMS roughness is highest in air anneal sample and lowest in UHV anneal sample.

7.3.4 UV-Vis-NIR Spectroscopy

The band gap of Molybdenum oxide nanostructures depends on the different oxidation states of Molybdenum. It starts from a wide band gap of MoO_3 (+6) to more conducting MoO_{3-x} (+5) to semi-metallic MoO_2 (+4). UV-Vis-NIR spectroscopy in reflectance mode has been used to measure the band gap of different vacuum annealed samples. We have already discussed in the previous chapters (chapter 4, 5), Kubelka-Munk equation [3] to get absorbance (α) from reflectance data and Tauc plot to calculate band gap of the corresponding samples.

Figure 7.5(a), (b), (c) depict UV-Vis reflectance spectra taken from the sample after post annealing at 600 °C in air, LV and UHV conditions respectively. Insets of Figure7.5 (a), (b) and (c) display corresponding $(\alpha h\nu)^2$ versus photon energy (hν) graph. We have tabulated band gaps for different vacuum annealed samples in Table 7.4. We can observe from Table7. 4 that with increasing vacuum level from air to UHV, band gap of the annealed Molybdenum oxide films has been decreased from 3.22 eV to 2.6 eV. This is due to the phase changes from MoO_3 to MoO_2.

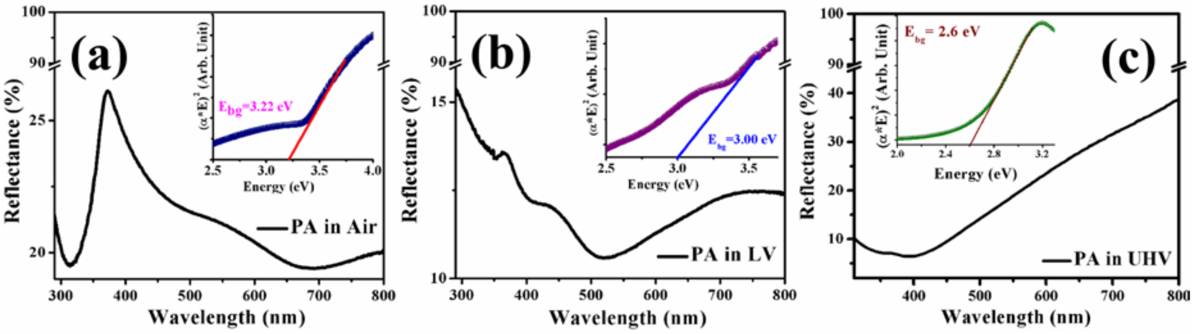

Figure 7.5: *UV-Vis reflectance spectra taken from the sample after post annealing at 600 °C in (a) air, (b) low vacuum (LV), (c) ultra-high vacuum (UHV) conditions respectively. Insets of (a), (b) and (c) depict corresponding* $(\alpha h\nu)^2$ *versus photon energy (hν) graph.*

Table 7.4: Band gap for different vacuum annealed samples

Vacuum level	**Band gap (eV)**
Air	3.22 ± 0.01
Low vacuum (LV)	3.00 ± 0.01
Ultra-high vacuum (UHV)	2.60 ± 0.01

7.3.5 KPFM Results

Kelvin probe force microscopy (KPFM) is a technique that enables nanometer scale imaging and measures the potential difference between the tip and the sample. This technique is based on the atomic force microscopy (AFM) in non-contact mode. We have used this technique to measure the local work function of three annealed samples in different vacuum conditions. The principle of this technique has been described in the previous chapters [2,3]. The Work function of the sample surface can be determined by the following equation:

$$\Phi_{\text{sample}} = 5.2 \text{ eV} - qV_{\text{CPD}} \qquad (7.4)$$

Where, V_{CPD} is the apparent contact potential difference which forms when an AC voltage is applied to the tip to generate an oscillating electrostatic force between the tip and the sample. Φ_{sample} is the work function of the sample and q is the electronic charge. 5.2 eV is the tip work function which has been calibrated with respect to HOPG sample.

Figure 7.6(a), (b), (c) display work function mapping images (mapping of V_{DC} with the lateral position coordinates) from the samples annealed at 600 °C in air, LV and UHV respectively. Experimentally determined local work function values (calculated from Eq. 7.4) for those three annealed samples have been charted in Table 7.5.

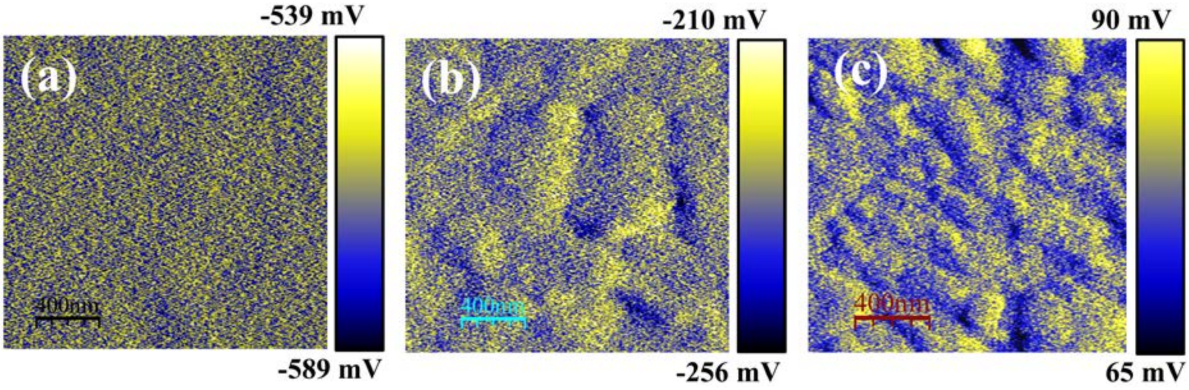

Figure 7.6: *Work function mapping by Kelvin probe force microscopy (KPFM) technique from the sample after post annealing at 600 °C for 30 min in (a) air, (b) LV and (c) UHV conditions respectively.*

It is clear from Table 7.5 that with increasing vacuum level from air to UHV, work function decreases. This is expected due to the decreasing of cationic oxidation states (+6 to +4). Electronegativity decreases and valance donor states increase with decreasing cationic oxidation states [20].

Table 7.5: Work function of different vacuum annealed samples.

Vacuum level	**Work Function (eV)**
Air	5.764 ± 0.029
Low vacuum (LV)	5.433 ± 0.027
Ultra-high vacuum (UHV)	5.123 ± 0.026

7.3.6 Field Emission Results

Field emission (FE) is the process to emit electrons from the material under high applied electric field. Electron density depends on the radius of curvature and for a small radius of curvature, the electron density is higher. According to Fowler-Nordheim (FN) theory [21], FE not only depends on work function (Φ) of the emitters but also on field enhancement factor (B), which is defined as the ratio of local to applied electric field. The structure of the emitters like morphology, aspect ratio highly influence B. Earlier, a large number of attempts have been made to grow various shape of MoO_3 nanostructures with high aspect ratio and studied their FE properties. Here we have successfully grown different nanostructures, analyzed their FE properties and compared the results with previous reports.

We investigated the FE properties of air, LV and UHV annealed nanostructures and displayed field emission current density (J) versus applied electric field (E) in Figure 7.7(a). For air annealed sample we put anode-sample separation of ~ 65µm, for LV annealed sample ~ 54 µm and ~ 50 µm for UHV annealed sample. Turn-on-field (E_{to}) is defined by the electric field required to draw 10 $\mu A/cm^2$ current density. So from Figure 7.7(a) we obtained turn-on voltage of ~ 4.78 V/µm for layered like structures (air annealed), ~ 5.20 V/µm and ~ 6.62 V/µm for plate like microstructures (LV annealed) and granular (UHV annealed) structures respectively. The FE behavior (J-E plot) can be analyzed theoretically by FN equation (Eq. 5.6 in chapter 5).

So, if we plot $\ln(J/E^2)$ versus (1/E) (F-N plot) (see Eq. 5.7 in chapter 5) , then from the slop ($b\Phi^{3/2}/B$) we can calculate B i.e. field enhancement factor. Hence

$$B = - b\Phi^{3/2}/ \text{slope} \tag{7.5}$$

where, b is the constant with $b= 6.83 \times 10^3\ eV^{-3/2}\ –V\ \mu m^{-1}$, B is the field enhancement factor (FEF) and Φ is the work function of the emitter.

FEF is higher for smaller slope value. We have shown F-N plots for three different cases in Figure 7.7(b). Interestingly, there are two slopes for low field and high field region in each case. The slopes are found to be -68.26 and -2.52 for air annealed, -78.84 and -7.62 for LV annealed, -89.27 and -23.77 for UHV annealed samples for higher and lower field regions, respectively. As the slopes for air annealed sample are lowest among three different cases in both the field regions, the FEF will be highest for layered like structures. These two slopes arise due to the emission of electrons from different energy levels [4,22]. In the low field region electrons come from only conduction band but in the high field region electrons come from both conduction band as well as valence band. So for calculating FEF, one can assume the effective work function (Φ_{eff}) is the addition of material band gap (E_b) with the work function of the emitters (Φ) in the high field regime.

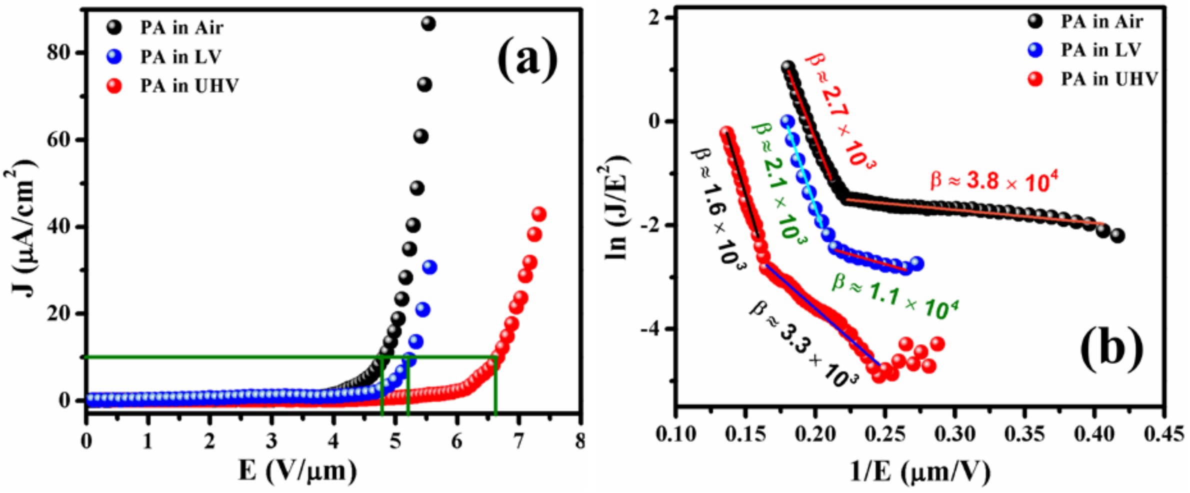

Figure 7.7: *(a) Field electron emission current density as a function of applied field (J–E) for PA in air sample (black), LV sample (red) and UHV sample (blue) after 250 nm* MoO_3 *deposition by PVD and their corresponding F–N plots in (b) respectively.*

We have already shown the work function and band gap of these three types of samples experimentally by KPFM and UV-Vis-NIR spectroscopy techniques. Hence, the values of Φ_{eff} are ~ 5.76 eV and ~ 8.98 eV (taking E_b = 3.22 eV) for air annealed sample, ~ 5.43 eV and ~ 8.46 eV (taking E_b = 3.03 eV) for LV annealed sample and ~ 5.10 eV and ~ 7.70 eV (taking E_b = 2.60 eV) for UHV annealed sample in low field and high field regions, respectively. Now one can easily calculate FEF (B) from Eq. 7.5 as Φ_{eff} and slope values are known. Calculated FEF (B) values are ~ 3.8×10^4 and ~ 2.7×10^3 for air annealed sample, ~ 1.1×10^4 and ~ 2.1×10^3 for LV annealed sample, ~ 3.3×10^3 and ~ 1.6×10^3 for UHV annealed sample in the low field and high field regions respectively. We have already mentioned FEF depends on both work function as well as structural geometry of the emitters. As the slope values are lowest in both the field regions and work function is highest for air annealed sample, therefore the FEF is highest for air annealed sample among three different cases. We have summarized the FE results for three different samples in Table 7.6 and compared with previously reported FE properties of other types of Molybdenum oxide nanostructures in Table 7.7.

Table 7.6: Electron field emission properties of different vacuum annealed nanostructures.

Vacuum level	Turn-on field (V/µm) for 10 µA/cm^2	Anode-sample separation	Slope		Field Enhancement Factor (FEF) (b)	
			Low Field	High Field	Low Field	High Field
Air	4.78	65 µm	-2.52	-68.26	3.8×10^4	2.7×10^3
LV	5.20	54 µm	-7.62	-78.84	1.1×10^4	2.1×10^3
UHV	6.62	50 µm	-23.77	-89.27	3.3×10^3	1.6×10^3

Table 7.7: Representative results on field emission performances of various molybdenum oxide and Mo nanostructures.

Emitter	Turn-on field (V/µm) for specific emission current density	Gap between anode and sample	Field Enhancement Factor (FEF) (b)	Reference
MoO_3				
MoO_3 Nanowires	3.5 MV/m for 10 µA/cm^2	300 µm	-	[23]
MoO_3 Nanobelts	13.2 V/µm for 10 µA/cm^2 8.7 V/µm for 10 µA/cm^2	50 µm 80 µm	-	[24]
MoO_3 Nanoflakes	11.0 V/µm for 10 µA/cm^2	-	2.5×10^3	[25]
MoO_3 Nanoflowers	4.3 V/µm for 10 µA/cm^2	80 µm	0.7×10^3	[26]
MoO_3	3.5 V/µm for 10 µA/cm^2	70 µm	2.3×10^3 for high field 1.0×10^4 for low field	[4]
α-MoO_3 Nanostructures	4.78 V/µm for 10 µA/cm^2	65 µm	2.7×10^3 for high field 3.8×10^4 for low field	Present work
MoO_2				
MoO_2 Nanostars	11.3 V/µm for 10 µA/cm^2	100 µm	2.3×10^3	[11]

	4.2 V/µm for 10 µA/cm^2	150 µm	3.9 × 10^3	
	3.2 V/µm for 10 µA/cm^2	200 µm	4.3 × 10^3	
	2.7 V/µm for 10 µA/cm^2	250 µm	5.3 × 10^3	
	1.9 V/µm for 10 µA/cm^2	300 µm	8.1 × 10^3	
	1.8 V/µm for 10 µA/cm^2	350 µm	9.5 × 10^3	
	1.4 V/µm for 10 µA/cm^2	400 µm	1.29 × 10^4	
	1.3 V/µm for 10 µA/cm^2	450 µm	1.34 × 10^4	
	1.0 V/µm for 10 µA/cm^2	500 µm	1.91 × 10^4	
MoO$_2$ Nanorods	4.0 V/µm for 10 µA/cm^2	200 µm	-	[24]
Pinaster-like MoO$_2$ Nanoarrays	2.4 V/µm for 10 µA/cm^2	500 µm	3.59 × 10^3	[27]
MoO$_2$ granular structures	6.62 V/µm for 10 µA/cm^2	50 µm	3.3 × 10^3 for high field 1.6 × 10^4 for low field	Present work

7.4. Conclusion

In summary, we have reported the effect of annealing in different vacuum conditions on PVD grown Molybdenum oxide thin films. SEM and AFM images show that layered, plate and granular like microstructures are formed after annealing the as deposited thin films at 600 °C in air, LV and UHV, respectively. XRD data reveals that with increasing the vacuum level from air to UHV, structural and phase changes from orthorhombic MoO$_3$ (α- MoO$_3$) to MoO$_{3-x}$ to monoclinic MoO$_2$. Crystallite size, lattice strain and dislocation density have been determined from XRD data. Elemental concentration decreases with increasing vacuum level which has been confirmed by EDS spectrum. Local work function and optical band gap decrease with increasing the vacuum level from air to UHV supported by KPFM and UV-Vis spectroscopy. Field emission properties have also been studied and found that the air anneal sample shows lowest turn-on field (4.78 V/µm) and highest FEF (B) (2.7 × 10^3 for high field and 3.8 × 10^4 for a low field) among three different vacuum annealed samples.

7.5 References

[1] P. Maiti, R. Singh and P. V. Satyam, *(to be submitted).*

[2] P. Maiti, P. Guha, H. Hussain, R. Singh, C. Nicklin, P. V. Satyam, *Surf. Sci.* 2019, 682, 64.

[3] P. Maiti, P. Guha, R. Singh, J. K. Dash and P.V. Satyam, *Appl. Surf. Sci.* 2019, 476, 691.

[4] P. Guha, A. Ghosh, R. Thapa, E.M. Kumar, S. Kirishwaran, R. Singh, P.V. Satyam, *Nanotechnology* 2017, 28, 415602.

[5] Z. Yin, X. Zhang, Y. Cai, J. Chen, J.I. Wong, Y.–Y. Tay, J. Chai, J. Wu, Z. Zeng, B. Zheng, H.Y. Yang, H. Zhang, *Angew. Chem. Int. Ed.* 2014, 53, 1.

[6] I.A. Castro, R.S. Datta, J.Z. Ou, A.C. Gomez, S. Sriram, T. Daeneke, K. Kalantarzadeh, *Adv. Mater* 2017, 1701619.

[7] X. Zhang, Z. Hou, X. Li, J. Liang, Y. Zhu and Y. Qian, *Electrochim. Acta* 2016, 213, 416.

[8] L. Zeng, X. Huang, X. Chen, C. Zheng, R. Liu, G. Chen, Q. Qian, Q. Chen and M. Wei, *RSC Adv.* 2016, 6, 105558.

[9] X. Liu, Y. He, S. Wang and Q. Zhang, *J. Alloys Compd.* 2011, 509S, S408.

[10] J. Zhou, N. S. Xu, S. Z. Deng, J. Chen, J. C. She and Z. L. Wang, *Adv. Mater.* 2003, 15, 1835.

[11] A. Khademi, R. Azimirad, A. A. Zavarian and A. Z. Moshfegh, *J. Phys. Chem. C* 2009, 113, 44.

[12] H. Hu, J. Xu, C. Deng and X. Ge, *J. Nanosci. Nanotechnol.* 2014, 14, 4462.

[13] L. Zheng, Y. Xu, D. Jin and Y. Xie, *J. Mater. Chem.* 2010, 20, 7135.

[14] P. Guha, A. Ghosh, A. Sarkar, S. Mandal, S. K. Ray, D. K. Goswami, and P. V. Satyam, *Nanotechnology* 2018, DOI: 10.1088/1361-6528/aaeadc.

[15] I. Horcas, R. Fernández, J. M. Gómez-Rodríguez, J. Colchero, J. Gómez-Herrero and A. M. Baro, *Rev. Sci. Instrum.*2007, 78, 013705.

[16] P.F. Carcia, E.M. McCarron III, *Thin Solid Films* 1987, 155, 53.

[17] P Scherrer, *Gött. Nachr.* 1918, 2, 98.

[18] A. Boukhachem, C. Bouzidi, R. Boughalmi, R. Ouerteni, M. Kahlaoui, B. Ouni, H. Elhouichet and M. Amlouk, *Ceram. Int.* 2014, 40, 13427.

[19] A. Arfaoui, B. Ouni, S. Touihri, A. Mhamdi, A. Labidi, T. Manoubi, *Opt. Mater.* 2015, 45, 109.

[20] M.T. Greiner, L. Chai, M.G. Helander, W.M. Tang and Z.-H. Lu, *Adv. Funct. Mater.* 2012, DOI:10.1002/adfm.201200615.

[21] R. H. Fowler and L. Nordheim, *Proc. R. Soc. A* 1928, 119, 173.

[22] A. Ghosh, P. Guha, R. Thapa, S. Selvaraj, M. Kumar, B. Rakshit, T. Dash, R. Bar, S.K. Ray and P.V. Satyam, *Nanotechnology* 2016, 27, 125701.

[23] J. Zhou, S. Z. Deng, N. S. Xu, J. Chen and J. C. She, *Appl. Phys. Lett.* 2003, 83, 2653.

[24] Y.B. Li, Y. Bando, D. Golberg and K. Kurashima, *Appl. Phys. Lett.* 2002, 81, 5048.

[25] B. Yan, Z. Zheng, J. Zhang, H. Gong, Z. Shen, W. Huang and T. Yu, *J. Phys. Chem. C* 2009, 113, 20259.

[26] G. Wei, W. Qin, D. Zhang, G. Wang, R. Kim, K. Zheng and L. Wang, *J. Alloys Compd.* 2009, 481, 417.

[27] J. –Y. Zhang, Y. –G. Liu, S.-L. Shi, Y.-G. Wang and T.-H. Wang, *Chin. Phys. B* 2008, 17, 4333.

Chapter 8

Summary and Conclusions

The thesis work involves an extensive study on the growth of molybdenum oxide (MoO_x) nanostructures (NSs) by molecular beam epitaxy (MBE) technique under ultra-high vacuum (UHV) conditions with varying parameters, such as, substrates, substrate temperature, film thickness, etc. and their applications. Any materials system development involves growth, characterization and applications. The thesis work focuses on these three parts related to MoO_x nanostructures. One of the idea was to grow MoO_x nanostrcutures under clean environment (like using MBE under UHV) and look at possibility of growing ordered 2D layered structures, such as, MoO_x nanostructures under MBE conditions. It is a challenging task as often there is a large amount of lattice mismatch with the substrate besides weak inter-planar forces in the 2D layered structures.

The growth and characteristics of defect free, mixed phase free metastable molybdenum trioxide (β-MoO_3) on varied substrates and MoO_2 and then the structural phase transformation from β-MoO_3 to MoO_2 and then to Mo by simple thermal reduction process in UHV condition were covered in detail. A part of the thesis work was devoted to structural characterization of MoO_x nanostructures, such as, elemental composition, thickness, shape and size, order in the organization using several experimental methods. The effective thickness, composition and the oxygen concentration of the molybdenum oxide thin films and nanostructures were determined by using the resonant Rutherford backscattering spectrometry (RBS). In resonant RBS measurements, 3.05 MeV alpha particles were used to probe, as it is known that the Rutherford cross-section is enhanced from the Oxygen atoms. Extensive use of electron microscopy methods, such as, scanning electron microscopy (SEM) and transmission electron microscopy (TEM) were used for size, shape, ordering, crystalline structure and composition of the grown nanostructures. UV-Vis spectroscopy and Kelvin probe force microscopy (KPFM) methods were used to determine the band gap and work function of the structures. X-ray photoelectron spectroscopy was used to determine the chemical bonding information. The effect of different film thickness of molybdenum oxide nanostructures on the optical band gap, local work function and field emission was discussed in detail. The role of noble metal (Au and Ag) nanostructures acting as catalyst for the growth of MoO_3 was studied. The experimental investigations using SEM - EDS method, showed that the Au nanostructures are better catalyst particles for MoO_x nanostructure growth. The role of annealing environment on structural, optical, field emission properties of MoO_3 thin films was also presented in this thesis.

In chapter 1, a brief introduction to the need of growing molybdenum oxide NSs in UHV condition and their intrinsic properties with possible applications are outlined. This chapter also includes the motivation of the work being carried out for this thesis. Different growth modes, working principles and instrumentations of all the major experimental techniques involved in this thesis work for the materials growth, characterizations and applications are briefly narrated in the 2nd chapter.

Chapter 3 focuses about the oxygen concentration determination in different molybdenum oxide NSs by resonant RBS studies. The thickness, composition, growth mode and structural aspects of the molybdenum oxide thin films deposited on the surface either at different substrate temperature and thicknesses or post annealed at different ambience have been studied using RBS method. We have shown the use of ion scattering under resonance conditions (using 3.04 MeV He ions from 1.7 MV Tandetron Accelerator) to determine the concentration of oxygen in thin film oxide nanostructures, such as, MoO_x and compare the same with TEM, XRD and XPS measurements. Based on the experimental observations, compositional depth profile analysis and the thickness of the films were investigated using RBS measurements and comparing the experimental profile with simulation (using SIMNRA software).

In the chapters 4 and 5, structural phase transformation under annealing conditions and the role of substrate and the film thickness of the structure have been studied. In chapter 4, nanostructural phase and morphology transformation from molybdenum tri-oxide (β-MoO_3) nanoribbons (NRs) to MoO_2 nanoparticles (NPs) and then to Mo (elemental), have been studied. The β-MoO_3 nanoribbons were grown on reconstructed Si(100) substrate by thermal annealing in UHV condition using MBE technique. Grazing incident X-ray diffraction (GIXRD), selected area electron diffraction (SAED) pattern, high resolution TEM (HRTEM) results reveal that the monoclinic phase of MoO_3 (β-MoO_3) is grown under ultra-high vacuum conditions. After raising the substrate temperature to 400 °C, morphology changes from larger size nanoribbons to smaller size nanoparticles. From electron microscopy measurements, we have observed that all the as-grown samples having substrate temperature ranging from 400 °C to 600 °C, exhibit similar morphology (i.e. monoclinic MoO_2). A decrease in average particle size, coverage area and an increase in areal density with increasing the substrate temperature have been observed. For in-situ XPS study, NRs sample has been taken. After measuring XPS of NRs sample, the sample was annealed at subsequent temperatures and XPS data was taken after cooling down to room temperature. From this experiment, it is found that Mo 3d peak shifts from 232.35 eV (for Mo^{6+} $3d_{5/2}$) to 228.77 eV (for Mo^{4+} $3d_{5/2}$) to 227.25 eV (for Mo^{0+} $3d_{5/2}$) whereas lattice oxygen peak generated for MoO_3 cases gradually decreases with increasing temperature and vanishes when MoO_3 converts to Mo at 750°C. The *ex-situ* KPFM measurements show a decrease in the local work function (Φ) from $\approx 5.27 \pm 0.05$ eV (for β-MoO_3 NRs) to $\approx 4.83 \pm 0.05$ eV (for Mo bimodal NPs) with increasing substrate temperature. A gradual reduction of the band gap from ≈ 3.32 eV for β-MoO_3 NRs to zero band gap for Mo NPs is also observed from UV-Vis-NIR spectrometry during the annealing up to 750 °C.

In chapter 5, growth of defect free, mixed phase free metastable monoclinic molybdenum trioxide (β-MoO_3) NRs on various substrates, such as, on Si(100), Si(5512) and fluorine-doped tin oxide (FTO) by MBE technique under UHV condition has been studied. The dependence of substrate conditions and the effective thickness of MoO_3 films on the morphology of nanostructures and their structural aspects have been examined. From electron microscopy observations, all NRs are found to be out of plane, oriented with an average angle of ±24° with the substrate normal along <011>, preferentially growth direction and restricted in <200>. From the growth of NRs on different substrates, it has been observed that out of plane unidirectional growth of the NRs structures is a substrate independent phenomenon. Different effective thickness of MoO_3 films, starting from 5, 10, 15, 20 and 30 nm have been deposited on Si(100) with a native oxide layer substrate. With increasing effective thickness, length and the aspect ratio of nanostructures increase by 260% without any significant change in the width. We have also shown how quantum size effects and thickness dependency play a role on band gap, local work function and field emission properties of β-MoO_3 NRs. With increasing effective film thickness from 5 nm to 30 nm, the optical band gap decreases from $3.38\pm$ 0.01eV to $3.17\pm$ 0.01eV. A liner relationship exists between band gap (Eg) and $1/(\text{thickness (t)})^2$. From the slope of band gap versus $1/t^2$ plot, the effective mass of electron in MoO_3 has been calculated and found to be $0.0191m_e$ which is same as the previously reported theoretical value. By knowing electron effective mass, de Broglie wavelength (λ) =7 nm is obtained which is of the order of effective film thickness. Local work function increases from 5.397 ± 0.025 eV to 5.757 ± 0.030 eV with an increase of film thickness from 5 nm to 30 nm. Field emission (FE) behavior is strongly influenced by two parameters, one is structure (composition, tip diameter and aspect ratio) and the other is work function (Φ) of the emitters. Here, with increasing film thickness from 5 nm to 30 nm, aspect ratio (length/width) increases from 3.9±0.1 to 14.1±0.5. So the FEF increases from 1.1×10^4 to 5.9×10^4 in the low field region and from 3.3×10^3 to 7.4×10^3 in high field regime. The self-assembled grown β-MoO_3 NRs sample (30 nm thickness) exhibits lowest turn-on field (2.5 V/μm for10 $\mu A/cm^2$) and highest FEF among all the previously reported other types of molybdenum oxide nanostructures.

Growth of molybdenum trioxide NRs on oriented silver (Ag) and gold (Au) nanostructures, to find a good catalyst for fabricating aligned and ordered NSs have been covered in chapter 6. For the growth of Ag nanostructures, silver films of an effective thickness of about 2 nm have been deposited at different growth temperatures (using UHV-MBE) on atomically cleaned Si(100), Si(110) and Si(111) substrates. The experiments reported in this chapter show that a minimum temperature of 650 °C is necessary to grow epitaxial Ag film on various reconstructed Si substrates. For faceted Au NSs, a ≈50 nm Au has been deposited (using high vacuum thermal evaporation) on Si(100) substrate with a native oxide layer at the interface and followed by annealing in low vacuum (≈ 10^{-2} mbar) and at high temperature (≈ 975 °C). Either Ag nanostructures grown in UHV conditions or oriented Au nanostructures grown in high vacuum condition are used as catalysts for the growth of MoO_3 nanostructures. From energy dispersive X-ray spectroscopy (EDS) elemental mapping and line scan it is found that MoO_3 nanostructures are uniformly distributed on Ag microstructures as well as Si substrate for MoO_3/Ag films, whereas interestingly, in case of MoO_3/Au films the density of MoO_3 nanostructures is very high on top of the faceted Au structures. Thus, SEM-EDS measurements have confirmed that Au nanostructures act as better catalysts for the growth of MoO_3 nanostructures.

The vacuum level of the system also plays a very important role in the growth and different properties of molybdenum oxide nanostructures. A ≈ 250 nm thick molybdenum trioxide film was deposited at room temperature (RT) on Si(100) substrates with a native oxide layer by physical vapor deposition (PVD) technique. Then the films were annealed at 650 °C under different conditions ie. air, low vacuum (LV) and ultra-high vacuum (UHV) and their resultant outcomes have been discussed in chapter 7. SEM and atomic force microscopy (AFM) images depict layered like structures after annealing in the air whereas plate like microstructures and granular structures are formed for post anneal (PA) in LV and UHV respectively. X-ray diffraction (XRD) confirms the orthorhombic phase of molybdenum trioxide (α-MoO_3) for layered like and monoclinic phase of MoO_2 for granular structures. Mixed states of β-MoO_3 and η-Mo_4O_{11} exist for microplates after annealing in LV. The main focus of this chapter is how the ambience plays an important role on the morphology and phase of different oxidation states of molybdenum. To study the optical band gap, UV-VIS spectroscopy measurements are done for the annealed samples. Optical band gap decreases from 3.22 ± 0.01 eV (for α-MoO_3, PA in Air) to 3.03 ± 0.01 eV (for a mixed phase of β-MoO_3 and η-Mo_4O_{11}, PA in LV) to 2.6 ± 0.01 eV (for MoO_2, PA in UHV). The *ex-situ* KPFM measurements show a decrease in the local work function (Φ) from $\approx 5.764 \pm 0.029$ eV for layered α-MoO_3 microstructures to $\approx 5.123 \pm 0.026$ eV for granular MoO_2 structures. With increasing vacuum level from air to UHV, aspect ratio (length/width) decreases. So the FEF decreases from 3.8×10^4 to 3.3×10^3 in the low field region and from 2.7×10^3 to 1.6×10^3 in high field regime.

Looking at more generalized view for future, it would be both fascinating and beneficial to grow other oxide materials such as WO_3, MnO_2, SnO_2, and ZnO_2 in UHV condition by MBE technique. How growth rate, temperature, vacuum level, film thickness affect the properties of other oxide materials can be studied systematically. At the present scenario, hybrid metal-semiconductor NSs have a great scientific significance in optical, electrical and biological applications. It would be interesting to study the catalytic and surface enhanced Raman spectroscopy (SERS) applications of Au-MoO_3 hybrid NSs.